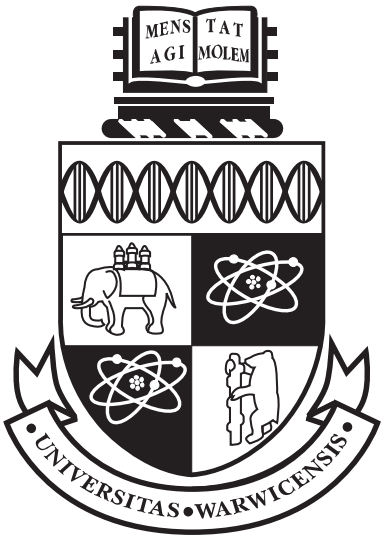

Low Order Modelling of Flow-Control Techniques for Turbulent Skin-Friction Reduction

by

Carlos Alberto Duque-Daza

Mech.Eng., MSc.Eng.

A thesis submitted in partial fulfilment

of the requirements for the degree of

Doctor of Philosophy

School of Engineering

October 2012

THE UNIVERSITY OF
WARWICK

Contents

List of Tables

List of Figures

Acknowledgments

I would like to dedicate this thesis to Professor Peter Carpenter, who believed that one stranger from Colombia could be guided by him. Unfortunately the destiny chose otherwise and we never met personally, but thanks to him I am at the end of this exciting road.

It would be difficult to thank everyone who has helped or supported me, directly or indirectly, during my doctoral studies. To all of them, who know who they are, a very special thank you.

I would like to say thanks to Dr Chris Davies from Cardiff University for many helpful discussions on mathematical and numerical aspects of this research; I would like to say thanks to Dr Mirza Baig for the helpful discussions around the topic and different aspects of this work; to Dr Yongmann Chung for his helpful support, advice in computational and theoretical matters, and his warm friendship; and very especial thanks to my supervisor Dr Duncan Lockerby because thanks to all his support, our discussions and his friendly guidance this thesis came to a successful ending.

Last but not least, I would like to lovingly thank my wife Andrea and my son Joseph. Their love, patience and companionship always helped me to overcome difficult situations. Their blind love was always a light in the road. Dear An, I will always remember your courage on all the decisions you made to keep our family together. I am infinitely grateful for that.

This research thesis was supported by the Programme Alban, the European Union Programme of High Level Scholarships for Latin America, scholarship No E07D402100CO. I would also like to acknowledge the partial financial support from EPSRC through grant EP/G060215/1, together with Airbus Operations Ltd and EADS UK Ltd.

This thesis was typeset with LaTeX 2_ε[1]

[1] LaTeX 2_ε is an extension of LaTeX. LaTeX is a collection of macros for TeX. TeX is a trademark of the American Mathematical Society. The style package *warwickthesis* was used by the author.

Declarations

This thesis is submitted to the University of Warwick in support of my application for the degree of Doctor of Philosophy in Engineering. It has been composed by myself and has not been submitted in any previous application for any degree.

The work presented (including data generated and data analysis) was carried out by the author.

Parts of this thesis have been published by the author: An alternative method to that discussed in chapter § 3 to calculate the Blasius layer profile, has been published in the paper of appendix B; some findings presented in chapter § 5 related to skin-friction drag reduction/increase have been published in a paper presented in appendix C

Abstract

In the present thesis a linearized formulation of the Navier-Stokes equations is used to study two main subjects: the generation of near-wall streaks in turbulent boundary layers and the response of turbulent wall-bounded flows to streamwise-travelling waves of spanwise oscillations of the bounding walls. For the purposes of the present work, these oscillations of the wall have been considered as a flow control mechanism.

A mathematical model, based on a velocity-vorticity formulation linearized around a turbulent mean base flow, is adopted to simulate the fluid flow equations. A hybrid spectral-finite differences solver has been employed to numerically implement the linearized system.

A review on turbulent streak generation is presented and the concepts of exponential growth, algebraic growth and viscous dissipation of small-scale perturbations are linked to the concept of transient growth. Mechanisms of generation of near-wall streaks are explored using a large set of sources of excitation for the linearized Navier-Stokes equations (LNSE). Two types of sources, here labelled as Excitation Mechanisms (EM), are employed: a body-force source and an initial condition. The selection of parameters for the excitation mechanisms is performed based on the definition of a multi-step optimization problem. The different EMs studied consist of a restricted number of parameters, and therefore can be considered as a Low Order Model (LOM) for the generation of streaks. It is shown that both types of EM produce satisfactory results for the streak generation process evaluated in terms of experimentally expected optimal spanwise scales.

Finally, a large set of numerical experiments are conducted to evaluate the response of the LNSE with optimised EM, to the flow control by a spanwise oscillating wall. By comparing the results between the response of the LNSE considered here to this type of flow control against a drag-reduction map obtained by DNS in other studies, it is possible to assess the correlation between streak evolution and disruption of the skin-friction drag. A good agreement between these two responses is found for the parameter space of the streamwise-travelling spanwise oscillation waves.

Chapter 1

Introduction and Background

1.1 Motivation

Modern engineering and technological developments are becoming increasingly driven by concepts like efficiency and environmental impact. In the eyes of the general public climate change has become one of the major motivations for improvements in different technological areas; the aeronautical industry is not an exception. In this case, it is highly probable that these concerns will translate into ever-tougher regulatory actions over the next few years. This new interest in environment-friendly-designed aircrafts sets one of the toughest challenges for airframe manufacturers. The need for greatly reduced emissions, particularly of greenhouse gases such as carbon dioxide and nitrogen oxides, will establish new paradigms in aircraft design. Two main approaches to achieve this reduction can be highlighted: 1) to improve the efficiency of the aeroengines, and 2) to improve the aerodynamic design of airframes. An efficient design in aeroengines, as discussed by Carpenter et al. [1], can make a significant contribution towards a reduction of the levels of pollution produced. However, ultimately emissions can only be significantly reduced by burning less fuel, which could be achieved by reducing the drag created during flight.

Considering the problem of reduction of drag associated with aeronautical applications, two different aspects must be observed. Firstly, most flows in aeronautical applications involve high Reynolds numbers, and therefore exhibit turbulent flow characteristics. Secondly, given that the main component of the total drag is the skin-friction drag, any reduction strategy will be probably required to focus the attention on the region close to the wall where the friction drag is being generated. As such, a flow control methodology targeting the Turbulent Boundary Layer (TBL) arises as the most obvious option to achieve significant skin-friction drag reduction

and ultimately to produce lower levels of pollution. In spite of the extensive amount of investigation and work accumulated over the years, the study of turbulent boundary layers is still an active area of research, recently propelled by this interest in drag-reduction and new clean technologies.

The main motivation of this thesis is to study the near-wall region of a turbulent boundary layer and, by using an efficient Low-Order Model (LOM), to explore flow control strategies that have been the focus of attention in recent years.

1.2 Turbulent skin friction and streaks

Skin friction arises from the interaction, due to relative displacement, between the surface of a body and the fluid adjacent to the surface [2]. This interaction is essentially dominated by the viscosity of the fluid. A common way to quantify the skin-friction drag is by estimation of the generation of wall shear stress. Härtel and Kleiser [3] suggest a useful measure to relate the wall shear stress with the near wall energy, providing a way to establish the level of loss of energy and drag in the very-near wall region. What it is important to note is that the level of wall shear stress, and therefore of skin-friction drag, increases at high Reynolds numbers. In flow conditions of large Reynolds numbers, usually existing in regular aerospace applications, the flow within the boundary layer becomes seemingly chaotic. Large temporal and spatial fluctuations appear and are observed at a wide range of scales, usually associated with eddy-like flow structures.

In spite of such an apparently chaotic nature, in regions closest to the surface of wall-bounded flows (the near-wall region, depicted in figure 1.1[1]) coherent flow structures exhibiting a deterministic behaviour have been found. These structures are not confined to a precise scale, in terms of velocity or spatial location, but instead they are spread over a set of scales relevant to the overall flow.

Early experimental and numerical evidence has made clear that a close relationship between turbulence and those coherent structures exist, as discussed by Bonnet [4] and Robinson [5]. A number of authors (Kim [6], Landahl [7], Kiesow and Plesniak [8]) have argued that a good understanding of the flow physics of the near-wall region in turbulent flows is required if modelling of techniques aiming to control and reduce the drag produced by the near-wall turbulence are to be successful.

It is convenient at this point to provide a definition for *'Coherent Structure'*. As it is described by Bonnet [4], "the term itself is controversial". Although there is not universal agreement on this definition, in general

[1] The near-wall region is usually defined as the closest portion of a wall-bounded flow to the bounding surface, which is considered to be consisting of the viscous sublayer, the transitional or buffer layer and the inner part of the log-law region, all part of the boundary layer.

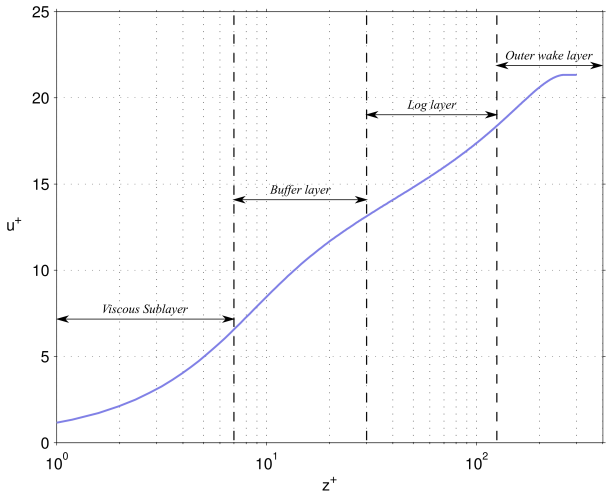

Figure 1.1: Schematic representation of a Turbulent Boundary Layer.

it is considered to denote events characterised by an organised motion persistent in time which repeatedly appear and undergo a characteristic temporal life cycle. Some authors consider the coherent structures as the region of flow where a two point correlation[2] is able to detect the passage or presence of certain specific coherent events (Bonnet [4], Adrian [9], Jakirlic and Hanjalic [10]). Not all researchers fully agree with this definition, so other group tends to think of a coherent structure as a structure present in the flow for a relatively long time. This last definition requires a proper generalised time-scale correlation and an adequate time scale definition (Baudet et al. [11]). A quite comprehensive review on coherent structures was presented by Robinson [5], where the author establishes that the most important vortical elements of all exist within the boundary layer. However, since such work was published, the number of acknowledged structures has grown substantially (Adrian [9], Savill and Mumford [12], Asai et al. [13]).

Robinson [5] established a general classification for the main works dealing with the structure of turbulence and coherent structures: 1) research dealing with quasi-streamwise vortices; 2) research dealing with spanwise vortices; and 3) research focused on vortex structures. The first type of flow structure historically identified was the *hairpin vortex* proposed by Theodorsen [14] in 1952. A few years later, Kline et al. [15] were able to reveal the presence of surprisingly well-organised spatially and temporally dependent motions, which were called low-speed streaks, nowadays also known as sub-layer streaks, near-wall streaks or just simply *streaks* (see figure 1.2).

These streak-like structures are narrow regions in the spanwise and wall-normal directions, although elongated in the streamwise direction; streaks are characterised by streamwise velocities that alternate in the spanwise direction between higher or lower values than that of the mean velocity. A remarkable feature of these streaks

[2] Two-point correlation is a statistical method employed to obtain correlation between two different events in the same flow, separated in distance and time, using only information available at one spatial point and characteristics of the structure to detect.

is their coherence, which is defined by their persistent appearance and consistency in the range of values of their features: their length is often observed to be about 1000 viscous units, and their spanwise separation (or spacing) about 100 ± 30 viscous units[3], as reported in several works (Smith and Metzler [16], Landahl [17], Zacksenhouse et al. [18], Schoppa and Hussain [19], Hwang and Cossu [20]). It is these streaks that are generally thought to be of critical importance to the near-wall flow physics.

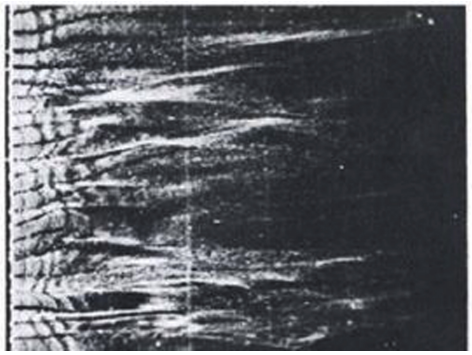

Figure 1.2: Sublayer streaks: Hydrogen-bubble flow visualisations of horizontal slices of a turbulent boundary layer. Taken from [15]

Initially Kline et al. postulated that the streaks are created by a vertical 'lift-up' mechanism produced by the induced velocity due to the legs of structures like the hairpin vortices of Theodorsen. More recently, Chernyshenko and Baig [21] have shown that, in fact, even a randomised field of wall-normal velocity perturbations can create these low-speed streaks. Nonetheless, in turbulent boundary layers, streamwise vortices are usually considered to be one of the most important elements responsible for the generation of streaks.

A question remains: What is the relationship between streaks and skin-friction drag? It is reasonable to expect that the skin-friction drag in turbulent boundary layers is governed by, or at least extremely dependent on, the near-wall dynamics of the flow and therefore, ultimately, on the low-speed streaks. Arguably, a good amount of evidence and modern consensus agree on the idea that skin-friction drag is intricately linked to the coherent structures, especially to the low-speed streaks.

1.3 The regeneration cycle of turbulence

The process of generation of streaks is known to be quasi-periodic, part of what is widely referred to as the near-wall cycle, even though there is not a common agreement on its precise nature. Several theoretical models have been proposed by Hamilton et al. [22], Jiménez and Pinelli [23], and Schoppa and Hussain [24],

[3] The viscous wall or inner units are a dimensionless representation based on variables associated to the viscosity and a local wall-shear-stress. Properties referred to inner units are usually represented by a '+' superscript. This will be explained in further detail in §2.3.3.

among many others, for this near wall cycle. In all of these works it is acknowledged that the coherent structures, the so-called streaks discovered by Kline et al., play a central role. Moreover, evidence of the existence of a cycle, which is local to the near-wall region, is presented by Jiménez and Pinelli [23]. Jiménez and Pinelli suggests that this cycle involves the formation of velocity streaks from the streamwise vortices in the mean profile, and then the generation of the vortices from the instability of the streaks. It is argued, in this work, that the presence of a wall seems to be only necessary to maintain the mean shear, suggesting a universal nature in the small scale structure of turbulence. Hamilton et al. [22], propose a quasi-cyclic process composed of three distinct phases: formation of streaks, breakdown of the streaks, and finally a regeneration of the streamwise vortices.

In a more recent study by Schoppa and Hussain [19], a different mechanism is proposed to explain the generation of near-wall streamwise vortices. Their arguments are based on a linear perturbation analysis, by direct numerical simulation, of a turbulent channel flow. In their case, however, the flow already consists of a mean velocity profile and low-speed streaks, and therefore is not concerned with the initial growth of streaks. In the mechanism proposed therein [19], called *streak transient growth*, the streamwise vortices are generated from the normal-mode-stable streaks. This cycle consists of three main stages: *i.* formation of a sheet of streamwise vorticity ω_x; *ii.* growth of sinuous streak waviness; and *iii.* collapse of the ω_x sheet into streamwise vortices. Results of this study are claimed to be in agreement with the (*ensemble-averaged*) coherent structures obtained in a fully turbulent flow by other experimental studies.

In another theoretical model for the near-wall cycle, proposed by Carpenter et al. [1], the cycle consists of the following main stages: (*i*) in an initial process, essentially linear, streamwise and other vortical structures in the buffer layer simultaneously generate streamwise velocity streaks and quasi-plane waves in the viscous sublayer; (*ii*) these waves and streaks interact non linearly to generate oblique waves, characterised by a periodic modulation and a later explosive growth that generates high levels of wall shear stress; (iii) as a final stage, oblique and plane waves interact non linearly to regenerate streamwise vortices, hence regenerating the cycle.

As indicated early, the list of works acknowledging the relevance of the near-wall physics and the coherent structures in the regeneration cycle is even longer than those presented above, including works presented by Smith and Metzler [16], Hamilton et al. [22], Toh and Itano [25], Sanghi and Aubry [26], Schoppa and Hussain [27, 28].

What it is really key to note is that, despite being only a theory, it is widely accepted that these low-speed streaks are in some way critical to the regeneration of turbulence.

1.4 Flow control and drag reduction

Different approaches have been suggested to reduce levels of drag, though there are two distinguishable tendencies. The first aims to reduce the skin-friction drag in fully turbulent flows by acting over the boundary layer using passive or active means. The second approach is focused on seeking to maintain laminar flow over aerodynamic surfaces, as this flow regime has a far weaker skin-friction. Despite its conceptual simplicity, the latter approach has proven to be extremely demanding in practise, due to the inherently unstable nature of the regime [29–31]. Amongst the efforts aiming to maintain laminar flow over a wing surface, it is worth mentioning the use of laminar-flow control in the form of boundary-layer suction discussed in Braslow [32], and the concept of compliant walls; although this latter alternative has not shown to be practical for use in aeronautical applications [33]. Both techniques, boundary-layer suction and compliant walls, are reviewed in more depth by Gad-el-Hak [34].

However, a general flow-control strategy arises from the link between the turbulence regeneration cycle and the near-wall streaks. By affecting the boundary layer, a suppression of any phase of the regeneration cycle should lead to a strong reduction in wall shear stress, and therefore will force a significant reduction in the skin-friction drag. It has been proposed, then, that in stopping the near-wall streaks, by cancelling or subduing them in some way, it might be possible to control the levels of turbulence and thus reduce the amount of skin-friction drag. Accepting this view, the natural step is to look for strategies to control or reduce the streak generation process. Previous attempts explored ways to control the streaks, including passive or active techniques, or combinations of these. In this group it is worth mentioning techniques involving actuation by suction/blowing, roughness modification by riblets, or alteration of near-wall dynamics by spanwise oscillations.

Regarding the active suction/blowing technique, some noteworthy efforts include: the study performed by Tardu [35], where the influence of the effect of periodical blowing through a spanwise slot in the near-wall turbulence is investigated; the work by Asai et al. [36], where an experimental exploration of the influence of active control by a two-dimensional local wall suction is performed and the cyclic nature of the turbulence in the near-wall region and the associated influence of the low-speed streaks influence are reaffirmed; and the research explored and presented by Lockerby [37], Lockerby et al. [38, 39], where the effects of MEMS actuators on turbulent boundary layers are investigated. In most of these works the idea is that as the streaks travel over the actuators, a form of resonance or a perturbation of the near-wall structure may occur, which in turn may disrupt the early-stage development of streaks in the viscous sublayer.

A successful passive method that has already been used on commercial airliners is the use of riblets. This technique was first investigated and developed by Walsh and Weinstein [40] in the U.S.A., and extended by

Walsh [41], and was also proposed independently in Germany by Reif and Dinkelacker [42] in a the study of the fluid dynamics over sharks' skin. These riblets "essentially consist of minute streamwise ridges and valleys"[4] on the aircraft's surface, as illustrated in figure 1.3.

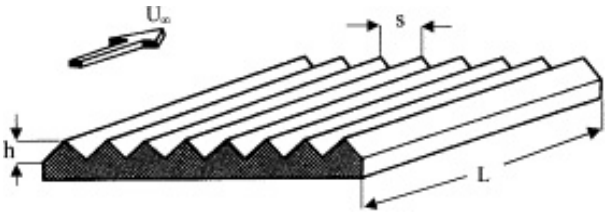

Figure 1.3: Schematic illustration of a riblets configuration (taken from [43])

Johansson et al. [44] proposed that, essentially, riblets reduce turbulent skin-friction drag by inhibiting spanwise movement of coherent flow structures. Park [45] performed experimental studies, in the wall region of a turbulent boundary layer with zero pressure gradient, documenting statistical properties of the fluctuating velocity components and the Reynolds stress from data obtained over the valley of a riblet plate; investigations on the influence of surface roughness-type treatments and on the spatial configuration of riblets have also been carried out by Sirovich and Karlsson [46], Nourmohammadi et al. [47], Jiménez [48] and Fransson et al. [49]; some investigations on the effects of riblets on the regeneration cycle and the near-wall structures include the works by Baron and Quadrio [50], and Choi [51, 52], amongst many others. Nevertheless, despite the great quantity of work focused on passive flow control, in particular those dealing with riblets, the maximum value reported in skin-friction drag reduction was just around $10 - 12$ % when applied to actual commercial aircrafts [2].

1.4.1 Turbulent flow control by spanwise oscillations

Flow control by oscillating walls has been investigated under several experimental and numerical approaches (for instance, see [53–56, 56–58]). Recent studies of wall-bounded turbulence have shown that spanwise oscillations of the bounding wall (perpendicular to the direction of the flow), and streamwise-travelling waves of spanwise wall velocity (STWSV) can deliver a substantial reduction in skin-friction drag. Choi et al. [59] demonstrated, experimentally, drag reduction of up to 45 % using pure wall oscillations in the spanwise direction; an optimum period of around $T^+ = 100 - 125$ was shown to be independent of the wall-oscillation amplitude (here, again, '$^+$' denotes viscous wall units). More recently Quadrio et al. [57] investigated, numerically, streamwise-travelling waves of spanwise wall velocity of the form $V_{wall} = A\,\sin(\kappa_x x - \omega t)$ with A being a velocity amplitude, κ_x a streamwise wavenumber and ω the oscillation frequency of the wave. This form of forcing generates waves of spanwise velocity moving (backward or forward) in the streamwise

[4] Text taken from reference [2], page 520.

direction with a phase speed $c = \omega/\kappa$. This forcing represents a generalised form of spanwise-wall actuation which includes two extreme cases: pure spanwise oscillation ($\kappa_x = 0$) as investigated by Choi et al. [59]; and stationary streamwise waves of spanwise velocity ($\omega = 0$). In particular, Quadrio et al. [57] found a range of wave parameter combinations for which drag reduction was of the order of 48 %. This value of drag reduction is evidently greater than that achievable using pure spanwise oscillations or standing streamwise waves of spanwise velocity alone.

It has been found that this wall-oscillation control approach has a strongly disruptive/inhibitive effect on the near-wall streak structures (Jung et al. [60], Karniadakis and Choi [61], and Ricco and Quadrio [58]). Consequently, due precisely to such strong effect, this is the flow control technique explored in this thesis. A more detailed and precise discussion on the mathematical model and numerical implementation adopted to explore this flow control is presented in §5.

1.5 Simulation methods for streak generation and flow control

A number of the drag-reduction studies mentioned above have been performed numerically using either Direct Numerical Simulations (DNS) or Large-Eddy Simulations (LES), and hence they have been mostly restricted to relatively low Reynolds number simulations, especially in the DNS case. Different approaches have been attempted to model, efficiently, flows at higher Reynolds numbers. Two of these approaches, not mutually exclusive, are the reduction of the level of complexity in the governing Navier-Stokes equations and the use of spectral or pseudo-spectral methods.

In the first case, many numerical investigations have attempted to "reduce this level of complexity by proposing alternative reduced-order models, that eventually will allow to produce approximate solutions" [62]. One of such approaches is to reduce the complexity of the fluid-flow governing relations by linearization of the Navier-Stokes equations. The idea of using linearized Navier-Stokes (LNS) equations to solve nonlinear turbulent flows stems from the initial work of Landahl [7] who showed that near-wall turbulence is a linear driven system and who also argued that turbulence forcing is produced by vorticity bursts originating in the viscous sublayer which are intermittent in space and time. A numerical exploration on generation of near-wall streaks in turbulent flows using a linearized approach was performed by Butler and Farrell [63] who investigated the relationship between optimal perturbations and near-wall coherent structures. The response of the linearized Navier-Stokes equations with respect to the generation of near-wall streaks was also analysed by Chernyshenko and Baig [64] and by the low-order model proposed by Lockerby et al. [38].

In the second approach a family of numerical methodologies employed to reduce the memory requirements and

to increase computational speed, aiming to cope more efficiently with high Reynolds number flows, is based on the construction of numerical models for the NS equations using a special set of orthogonal functions, for instance using Fourier expansions or Chebyshev polynomials. Depending on the type of test functions used to assess the accuracy of the solutions obtained with these kind of numerical approaches, such methodologies can fall into these three main categories: Galerkin methods, Tau-approximations, and Collocation or Pseudo-spectral methods.

Although not directly akin to the aim of reducing complexity or improving numerical accuracy, another interesting approach is that which aims to exploit the remarkable importance of vortical structures in the near-wall region. As mentioned above, a significant amount of evidence has been provided attesting the major role of vortices and vortical structures on the streak generation process. If the idea of a strong correlation between streaks and skin-friction drag is assumed to be true, then it is also obvious that these vortical structures strongly influence the turbulent drag production. Therefore, either considering the streak generation aspect or the skin-friction drag control, it seems appropriate to express the NS equations in terms of vorticity and velocity variables. This approach is usually referred to as a Velocity-Vorticity formulation. Amongst the works dealing with turbulence simulation using a velocity-vorticity formulation it is worth highlighting those performed by Clercx [65], Young et al. [66], Speetjens and Clercx [67], Shen and Loc [68], Lo et al. [69] and Dennis and Hudson [70].

Formulations based on velocity and vorticity variables are just simply restatements of the traditional Navier-Stokes equations in primitive variables form. Hence, the approaches mentioned above to achieve higher Reynolds numbers are also applicable to these velocity-vorticity strategies. For instance, Clercx [65] based its model in a Chebyshev expansion in two dimensions, applying Tau corrections to eliminate the effects of discretization errors.

In an alternative velocity-vorticity formulation presented and discussed by Davies and Carpenter [71] the order of the system of equations can be reduced by using relationships between integral expressions of the vorticity and velocity for a given flow field. Furthermore, the flow is modelled indirectly by a reduced group of variables using a new methodology particularly suitable to model the evolution of three-dimensional disturbances in boundary layers [71]. They overcame two major drawbacks inherent to basic velocity-vorticity formulations: the use of six dependent variables and the lack of proper boundary conditions on vorticity. It is this approach that has been adopted in the present thesis. This model is presented in far greater detail in chapter §2.

1.6 Current research project

As mentioned above, given that it is commonly accepted that near-wall streak structures play a major role in the turbulent regeneration mechanism, it might be expected that an explanation for the efficacy of spanwise oscillation control methods would be readily forthcoming. However, there is still a lack of clarity in the understanding of the physical mechanism(s) underpinning this type of control strategy, which stands in the way of efficient prediction and engineering application. In this way, the main aims in this thesis are to explore and study the generation of near-wall streaks in turbulent boundary layers and the response of turbulent wall-bounded flows to streamwise travelling spanwise oscillations of the bounding walls.

The starting point of the present work is the LOM employed by Lockerby et al. [38] and Carpenter et al. [1], whereby the generation of turbulent streaks is produced by introducing a Lorentz-type body force to the LNSE; a coarse-grained optimization over a small set of forcing parameters is then performed to find a near-optimal streak. This approach to generating streaks is particularly convenient as it is relatively easy, and computationally efficient, to incorporate the streak disturbance into an otherwise conventional computational fluid dynamics simulation. Given this advantage, this approach has been successfully employed in a variety of flow-control applications, such as: 'closed-loop' streak control using micro jet actuators, Lockerby et al. [38]; 'open-loop' streak control using a spanwise-oscillating wall, Togneri [72]; and passive streak control using compliant surfaces, Carpenter et al. [1]. Despite its convenience and efficiency over full DNS and other linear streak models, the method as it currently stands has a number of less satisfactory aspects. The functional form of the forcing required to generate the streaks has a number of parameters which are either set empirically, or in a seemingly arbitrary way. This can give the impression that tuning of the free parameters is required to generate streaks, and that the body force is intended to represent some specific physical distribution. In fact, it is not well known how these parameters and the particular forcing form affect the streaks generated from such models. This thesis aims also to shed light in this particular aspect.

This thesis aims to perform a numerical study on a turbulent boundary layer using linearized Navier-Stokes (LNS) equations, with the base flow corresponding to an open-loop control in the form of streamwise travelling waves of spanwise wall velocity (STWSV). Due to the high computational efficiency of the LNS solver adopted in this work, high Reynolds number flow simulations, corresponding to cruise flight conditions, are investigated regarding both phenomena (streaks generation and drag reduction). This would be otherwise not possible using the current DNS/LES capabilities. Moreover, this thesis attempt to shed light on the fundamental physics of turbulent DR by exploring the effect of STWSV on near-wall structures in shear-driven flows.

1.7 Chapter list

A summary of the general structure and organisation of this thesis.

Chapter §2 The mathematical model in terms of velocity and vorticity variables and the formulation employed to track the evolution of small perturbations are presented and discussed; the mathematical model used to generate the mean base profiles, used in the applications explored herein, is also introduced. Advantages and limitations of the methodology are also elicited and discussed.

Chapter §3 A full description of the numerical methods employed to implement the models presented in §2 are discussed in this chapter. Tests aiming to validate the numerical methodologies adopted are also discussed and their results presented.

Chapter §4 In this chapter a brief discussion on concepts associated with transient growth and non-normality of the general LNS operator is presented. Afterwards a short description of the physics of the near-wall streaks, as well as different aspects associated with their measurement, are discussed. Then the concept of a low-order numerical model of streak development is outlined, and the two methods for generation of streaks studied in this work are introduced. Finally, the results of the exploration of mechanisms to generate streaks along with a discussion of the different measures of streak growth investigated are presented.

Chapter §5 In this chapter a modified version of the mathematical model for the LNSE, to account for the spanwise oscillation, is introduced. A short description of the generalised Stokes layer profile, as well as the types of analytical and mathematical models considered here to simulate such a profile, are discussed. The results of the numerical experiments of this thesis, using both types of excitation mechanisms discussed in §4, are presented and compared against values obtained for drag-reduction by Quadrio et al. [57].

Chapter §6 In this final chapter the general conclusions, elicited from the different results in the thesis, are presented and ideas for future work are included.

Chapter 2

Theoretical and mathematical models

One of the main focus of the current work is to investigate the self-organisation and development of structures in the near-wall region of turbulent wall-bounded flows, such as those described in §1.2. Specifically, to investigate the generation and development of streamwise low-speed streaks, in the form of instabilities of the flow, to small perturbations or disturbances[1].

It is also of interest to study the relationship between these structures and skin-friction drag. An approach based on a viscous initial value approximation of the Navier-Stokes equations has been adopted. In particular, a velocity-vorticity formulation of the incompressible Navier-Stokes equations has been employed. Such a formulation was originally described and presented by Davies and Carpenter [71]. This formulation and its application to different problems (including stability analysis and compliant-wall control of disturbances in flat-plate and rotating-disc boundary layers), is described in Davies [73, and references therein]. Nevertheless, as that methodology is at the core of the present project, and due to its relevance and importance as well as for completeness, a detailed exposition of the formulation is given here.

The present chapter exposes the basic formulation for incompressible flows, discusses the mathematical model in terms of vorticity, the formulation employed to track the evolution of such small perturbations, and the underlying model of the base mean flows to be used in the applications explored herein. Advantages and limitations of the methodology are also presented and discussed.

[1] From here onwards *disturbance* or *perturbation* will have the same meaning, a small amplitude deviation from a mean base flow, and will be used indistinctly throughout this document.

2.1 Governing equations. Incompressible fluid flow

The general law of conservation of mass can be written as,

$$\frac{\partial \rho}{\partial t} + \boldsymbol{\nabla} \cdot (\rho \mathbf{u}) = 0 \tag{2.1}$$

where ρ is the density of the fluid. For incompressible flows with constant density this relationship can be expressed as,

$$\boldsymbol{\nabla} \cdot \mathbf{u} = 0 \tag{2.2}$$

or in scalar Cartesian form,

$$\frac{\partial u}{\partial x} + \frac{\partial v}{\partial y} + \frac{\partial w}{\partial z} = 0 \tag{2.3}$$

where u, v and w stand for the velocity components in the x, y and z directions, respectively. In the model here adopted such components correspond to x-streamwise, y-spanwise and z-wall-normal directions. An illustrative scheme of the parallel flow under consideration and the coordinate system adopted hereafter is shown in Figure 2.1, with U_∞ representing the velocity of the flow outside the boundary-layer region.

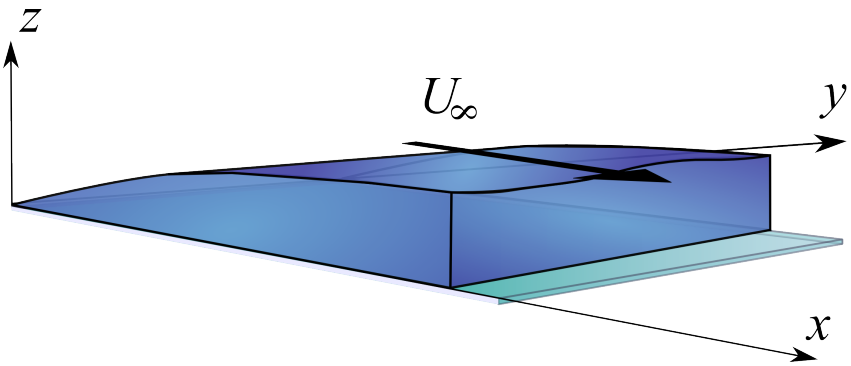

Figure 2.1: Flow direction and coordinate system adopted: x-streamwise , y-spanwise and z-wall-normal directions.

The incompressible Navier-Stokes or momentum conservation equations can be expressed in terms of velocity and pressure as

$$\frac{\partial \mathbf{u}}{\partial t} + \mathbf{u} \cdot \nabla \mathbf{u} = -\frac{\nabla p}{\rho} + \frac{\mu}{\rho} \nabla^2 \mathbf{u} + \mathbf{f} \tag{2.4}$$

where $\mathbf{u}$ is the flow velocity field vector, p is pressure, μ is the fluid dynamic viscosity, ∇ is the gradient operator, ∇^2 is the laplacian operator and $\mathbf{f}$ stands for any body force acting on the fluid. Owing to the fact that the coherent structures of interest for this work are confined within an incompressible region of flow, no additional relations to equations (2.1) and (2.4) are required (in a compressible flow an additional equation accounting for the conservation of energy is required). The momentum conservation equation for an

incompressible Newtonian fluid can be expressed in an extended scalar form as a system of three equations,

$$\frac{\partial u}{\partial t} + u\frac{\partial u}{\partial x} + v\frac{\partial u}{\partial y} + w\frac{\partial u}{\partial z} = -\frac{1}{\rho}\frac{\partial p}{\partial x} + \boldsymbol{\nu}\left(\frac{\partial^2 u}{\partial x^2} + \frac{\partial^2 u}{\partial y^2} + \frac{\partial^2 u}{\partial z^2}\right) + f_x \tag{2.5}$$

$$\frac{\partial v}{\partial t} + u\frac{\partial v}{\partial x} + v\frac{\partial v}{\partial y} + w\frac{\partial v}{\partial z} = -\frac{1}{\rho}\frac{\partial p}{\partial y} + \boldsymbol{\nu}\left(\frac{\partial^2 v}{\partial x^2} + \frac{\partial^2 v}{\partial y^2} + \frac{\partial^2 v}{\partial z^2}\right) + f_y \tag{2.6}$$

$$\frac{\partial w}{\partial t} + u\frac{\partial w}{\partial x} + v\frac{\partial w}{\partial y} + w\frac{\partial w}{\partial z} = -\frac{1}{\rho}\frac{\partial p}{\partial z} + \boldsymbol{\nu}\left(\frac{\partial^2 w}{\partial x^2} + \frac{\partial^2 w}{\partial y^2} + \frac{\partial^2 w}{\partial z^2}\right) + f_z \tag{2.7}$$

with every vector field variable expressed in its own Cartesian-coordinates components and $\boldsymbol{\nu}$ being the kinematic viscosity. It is more convenient to deal with non-dimensional expressions instead of their dimensional form in order to benefit from similarities present at different flow conditions for the same application. The present work is concerned with phenomena occurring within the boundary layer, and thus an appropriate characteristic length is the displacement thickness δ_* of the boundary layer (defined explicitly later in §2.3.3). Equally, a suitable characteristic velocity is the free stream or mean flow velocity U_∞ (i.e. the velocity of flow outside the boundary layer), which for simplicity is being considered as non-variable in time and space location. The following dimensionless quantities can now be introduced:

$$\begin{aligned} x^* &= \frac{x}{\delta_*} & y^* &= \frac{y}{\delta_*} & z^* &= \frac{z}{\delta_*} & t^* &= \frac{t\,U_\infty}{\delta_*} \\ u^* &= \frac{u}{U_\infty} & v^* &= \frac{v}{U_\infty} & w^* &= \frac{w}{U_\infty} & p^* &= \frac{p - p_0}{\rho\,U_\infty^2} \\ & & f_i^* &= \frac{f_i\,\delta_*}{U_\infty^2} & Re_{\delta_*} &= \frac{U_\infty \delta_*}{\boldsymbol{\nu}} & & \end{aligned} \tag{2.8}$$

with p_0 being a reference pressure, Re_{δ_*} the Reynolds number based on displacement thickness δ_* and the free-stream velocity U_∞, and f_x^* as a dimensionless body force component. Equation (2.4) can now be expressed as:

$$\frac{\partial \mathbf{u^*}}{\partial t^*} + \mathbf{u^*}\cdot\nabla\mathbf{u^*} = -\nabla p^* + \frac{1}{Re_{\delta_*}}\nabla^2\mathbf{u^*} + \mathbf{f^*} \tag{2.9}$$

2.2 Governing equations. Velocity-vorticity formulation

In the present work a formulation based on vorticity variables, rather than primitive variables, is adopted. Considering that in turbulent flows the advection of vorticity is one of the most important processes determining the flow dynamics, to study this type of flows in terms of vorticity and velocity is arguably a more convenient approach to model the physical reality [65]. Additionally, as discussed in §1.2 and §1.3, it is thought that

vortical dynamics is essential to the near-wall physics in wall-bounded flows and central to the mechanisms of the self-sustaining cycle of turbulence. Moreover, since there is no explicit mechanism for advancing the pressure term in time in the original incompressible Navier–Stokes equations, major efforts have been dedicated to remove the pressure gradient from all or part of the computational process solving the NSEs. The implementation of suitable boundary conditions for pressure has also been deemed to be particularly difficult. In any case, they must be derived from velocity boundary conditions [74]. Thus by studying the fluid flow in terms of vorticity variables the pressure term is eliminated from the original system of equations[2], so surpassing any inconvenience with time integration for the pressure term. For schemes based on vorticity variables, pressure recovery is achieved by using the solenoidal nature of the velocity field, which is imposed for incompressible flows. In general, as in projection methods, a Poisson equation obtained by taking the divergence of the momentum equation allows the recovery of the pressure field from the velocity field.

A vector vorticity transport equation can be obtained by taking the curl of the momentum equation (2.9), which can then be rewritten (after some manipulation) as

$$\frac{\partial \boldsymbol{\omega}^*}{\partial t^*} + (\mathbf{u}^* \cdot \nabla)\,\boldsymbol{\omega}^* - (\boldsymbol{\omega}^* \cdot \nabla)\,\mathbf{u}^* = \frac{1}{Re_{\delta_*}} \nabla^2 \boldsymbol{\omega}^* + \mathbf{S}^* \tag{2.10}$$

with $\mathbf{S}^* = \boldsymbol{\nabla} \times \mathbf{f}^*$. To obtain expression (2.10), the following definitions have been employed

$$\boldsymbol{\nabla} \cdot \mathbf{u}^* = 0 \qquad \text{and} \qquad \boldsymbol{\nabla} \cdot \boldsymbol{\omega}^* = 0, \tag{2.11}$$

The first relationship in (2.11) represents the continuity equation for incompressible flows expressed for the dimensionless velocity field $\mathbf{u}^*$, which accounts for those terms not appearing in (2.10) compared to the more general vorticity transport equation. The second expression in (2.11) solely corresponds to a vector calculus identity, independent of the assumptions on the fluid flow. Definitions (2.11) also impose a more general characteristic: both velocity and vorticity fields are enforced to be solenoidal or divergence-free, preserving the conservative nature of the original continuity and momentum equations.

Although this approach represents an advantage over the original NSEs by overcoming issues associated with pressure and providing the dynamics of the flow in terms of vortical structures directly, it poses some inconveniences too. Firstly, velocity-vorticity methods, like some pressure-based methods, have suffered from the difficulty in imposing boundary conditions; specifically on the vorticity perturbation field, particularly at walls. Secondly, in these methods the number of unknowns to be solved goes from four in the primitive-variable form (three components of velocity plus pressure), to six in the velocity-vorticity formulations (three components of velocity and three components of vorticity). To circumvent these inconveniences, especially

[2]The velocity-vorticity form generated by taking the curl of the momentum equations eliminates the pressure gradient term.

for simulations of the evolution of small perturbations in known or predefined boundary layer solutions, Davies and Carpenter [71] have proposed rigorous integral conditions to be imposed on the vorticity perturbations, given some general conditions are satisfied by the boundary layer disturbances on the upper boundary of the computational domain employed. This approach was employed in this work and is presented in the next section.

2.2.1 Vorticity formulation for small perturbations

Owing to the interest in small-scale structures existent in the near-wall region of a wall-bounded flow, a distinction between a base flow and a perturbed flow is introduced. Previous methodologies based on linear stability analysis (as presented by Kawahara et al. [75] as well as the studies on streak generation by Schoppa and Hussain [19]) have prescribed a base flow composed of a known parallel mean base flow plus a streaky background flow. This background flow is then incorporated in the corresponding fluid flow model. For instance, this could be the Orr-Sommerfeld equation in the case of stability analysis. In the methodology hereby adopted the velocity and vorticity fields are decomposed into two independent fields: a mean base flow field and a first-order perturbation field, as presented in [71]. In the present case, however, without any particular assumption about an inherent streaky nature of the perturbation. Both approaches for modelling the near-wall structures (with and without a streaky base flow), are valid considering that experimentally observed streaky flows have a weak dependence on time and more importantly on streamwise variation. In fact this kind of analysis is fully justified as a valid approximation to the dynamics of small-scale perturbations (in this case the streamwise streaks), because actual near-wall streaks have much larger time and streamwise length scales than those typically found in turbulence, making suitable the adoption of a streamwise homogeneous mean base flow as background flow condition.

Accordingly, in the approach followed in this work, the total velocity and vorticity fields are decomposed into a mean base flow and a perturbation field from the prescribed base flow as,

$$\mathbf{u}^{*} = \mathbf{U}^{\mathbf{B}}\left(x,y,z\right) + \mathbf{u}'\left(x,y,z,t\right) \tag{2.12}$$

$$\boldsymbol{\omega}^{*} = \boldsymbol{\Omega}^{\mathbf{B}}\left(x,y,z\right) + \boldsymbol{\omega}'\left(x,y,z,t\right) \tag{2.13}$$

with $\mathbf{U}^{\mathbf{B}}$ and $\boldsymbol{\Omega}^{\mathbf{B}}$ representing vector fields for velocity and vorticity of the mean flow. In cartesian coordinates

these fields are expressed as

$$\mathbf{U}^B = [U^B, V^B, W^B] \tag{2.14a}$$

$$\mathbf{u'} = [u', v', w'] \tag{2.14b}$$

$$\boldsymbol{\Omega}^{\mathbf{B}} = [\Omega_x^B, \Omega_y^B, \Omega_z^B] \tag{2.14c}$$

$$\boldsymbol{\omega'} = [\omega_x', \omega_y', \omega_z'] \tag{2.14d}$$

where, as noted before, velocity and vorticity components are defined in the streamwise (x), spanwise (y) and wall-normal (z) directions, respectively, and non-dimensionalised in accordance with the definitions in (2.8). By substituting definitions (2.12) and (2.13) into (2.10), the transport equation can be recast (after some manipulation) as:

$$\begin{aligned} \frac{\partial \boldsymbol{\omega}}{\partial t} + \mathbf{U^B} \cdot \boldsymbol{\nabla}\ \boldsymbol{\Omega^B} - \boldsymbol{\Omega^B} \cdot \boldsymbol{\nabla}\ \mathbf{U^B} + \mathbf{U^B} \cdot \boldsymbol{\nabla}\ \boldsymbol{\omega} - \boldsymbol{\omega} \cdot \boldsymbol{\nabla}\ \mathbf{U^B} + \mathbf{u} \cdot \boldsymbol{\nabla}\ \boldsymbol{\Omega^B} \\ - \boldsymbol{\Omega^B} \cdot \boldsymbol{\nabla}\ \mathbf{u} + \mathbf{u} \cdot \boldsymbol{\nabla}\ \boldsymbol{\omega} - \boldsymbol{\omega} \cdot \boldsymbol{\nabla}\ \mathbf{u} = \frac{1}{Re_{\delta_*}} \nabla^2 (\boldsymbol{\Omega^B} + \boldsymbol{\omega}) + \mathbf{S} \end{aligned} \tag{2.15}$$

where for simplicity, primes indicating perturbation variables and asterisks indicating dimensionless quantities have been dropped [3]. In a first approach, for the streaks generation study presented here, the base flow is being considered essentially steady, at least compared to the time scales of the perturbations, and so the time derivative of the mean base flow is zero. In the numerical experiments on skin friction drag reduction in this thesis the mean base flow is time-dependent; which is explained in §5. Here, using definitions (2.11) and noticing that the same expressions are applicable also for mean flow variables, equation (2.15) can be rewritten as

$$\frac{\partial \boldsymbol{\omega}}{\partial t} + \boldsymbol{\nabla} \times \mathbf{M}^\star = \frac{1}{Re_{\delta_*}} \nabla^2 \boldsymbol{\omega} + \frac{1}{Re_{\delta_*}} \nabla^2 \boldsymbol{\Omega^B} + \mathbf{S} \tag{2.16}$$

with convective term $\mathbf{M}^\star$ defined as

$$\mathbf{M}^\star = \boldsymbol{\Omega^B} \times \mathbf{U^B} + \boldsymbol{\Omega^B} \times \mathbf{u} + \boldsymbol{\omega} \times \mathbf{U^B} + \boldsymbol{\omega} \times \mathbf{u} \tag{2.17}$$

The first term of $\mathbf{M}^\star$ corresponds exclusively to the mean or base solution flow. It is relatively straightforward to see that if the mean flow is a solution to the governing equations (2.2) and (2.10), then

$$\boldsymbol{\nabla} \times (\boldsymbol{\Omega^B} \times \mathbf{U^B}) = \frac{1}{Re_{\delta_*}} \nabla^2 \boldsymbol{\Omega^B} \tag{2.18}$$

[3] From here onwards perturbation variables will be indicated by lowercase symbols without prime or any other indication. Mean flow variables will in turn be indicated by uppercase symbols, unless otherwise stated. Equally, all quantities will be dimensionless unless noted differently.

for which there is no source term; equation (2.16) finally can be expressed as

$$\frac{\partial \boldsymbol{\omega}}{\partial t} + \boldsymbol{\nabla} \times \mathbf{M} = \frac{1}{Re_{\delta_*}} \nabla^2 \boldsymbol{\omega} + \mathbf{S} \tag{2.19}$$

with $\mathbf{M}$ defined as

$$\mathbf{M} = \boldsymbol{\Omega}^{\mathbf{B}} \times \mathbf{u} + \boldsymbol{\omega} \times \mathbf{U}^{\mathbf{B}} + \boldsymbol{\omega} \times \mathbf{u} \tag{2.20}$$

As mentioned before, this formulation provides in fact only three equations for the six unknowns in the perturbation fields, $\{\mathbf{u}, \boldsymbol{\omega}\}$. However, an additional set of three equations are obtained by taking the curl of the vorticity, which leads to

$$\nabla^2 \mathbf{u} = -\boldsymbol{\nabla} \times \boldsymbol{\omega} \tag{2.21}$$

These relations complete the system of equations required to solve the velocity and vorticity perturbation fields. So far it appears that it is required to solve a system of six equations to completely resolve the evolution of the disturbances. However, as it is shown in [71, 73], if the components of the perturbation fields $\mathbf{u}$ and $\boldsymbol{\omega}$ are grouped into two distinct sets, namely the *primary* variables $\{\omega_x, \omega_y, w\}$, and the *secondary* variables $\{u, v, \omega_z\}$, it is possible to determine the evolution of the former independently from the latter variables. After a full solution for the primary variables is achieved, it is possible to recover the secondary variables by using rigorous integral conditions. A simplified exposition of the full methodology as described in [71], is presented below.

Taking the streamwise and spanwise vorticity definitions

$$\omega_x = \frac{\partial w}{\partial y} - \frac{\partial v}{\partial z}$$
$$\omega_y = \frac{\partial u}{\partial z} - \frac{\partial w}{\partial x}$$

and using the second theorem of calculus, it is possible to express the streamwise perturbation velocity u as

$$u(x, y, z_2, t) - u(x, y, z_1, t) = \int_{z_1}^{z_2} \left(\omega_y(x, y, z, t) + \frac{\partial w}{\partial x}(x, y, z, t) \right) dz$$

and the spanwise perturbation velocity v as

$$v(x, y, z_2, t) - v(x, y, z_1, t) = \int_{z_1}^{z_2} \left(\frac{\partial w}{\partial y}(x, y, z, t) - \omega_x(x, y, z, t) \right) dz$$

Similarly, the definition of the wall-normal component of the vorticity perturbation can be obtained from the

solenoidal condition on the vorticity (2.11), i.e. $\boldsymbol{\nabla}\cdot\boldsymbol{\omega}=0$, which gives

$$\omega_z(x,y,z_2,t)-\omega_z(x,y,z_1,t)=\int_{z_1}^{z_2}\left(-\frac{\partial\omega_x}{\partial x}(x,y,z,t)-\frac{\partial\omega_y}{\partial y}(x,y,z,t)\right)dz$$

It is clear at this point that the secondary set of variables can be fully described by the primary variables, provided that some conditions can be ensured. In order to get a valid closure between sets of variables, and given the interest in this work on disturbances with vanishingly small amplitude, particularly away from the wall bounding the flow, the following simplification (or assumption) is made for every primary perturbation variable

$$\lim_{z\to\infty}\phi(x,y,z,t)=0 \tag{2.22}$$

strongly implying now that the formulation adopted here is valid only for small perturbations, in a simply connected semi-infinite domain, which are vanishing as $z\to\infty$. This particular assumption does not pose any problem for the study of the near-wall structures of interest, but rather pinpoint the formulation as model for boundary layer flows and particularly for the structures within the near-wall region. It is not difficult to see that by extension this is equivalent to assume that (2.22) is also valid for the secondary variables. By using (2.22), then, a rigorous definition of u, v and ω_z in terms of primary variables can be obtained as follows:

$$u=-\int_z^\infty\left(\omega_y+\frac{\partial w}{\partial x}\right)dz' \tag{2.23}$$

$$v=\int_z^\infty\left(\omega_x-\frac{\partial w}{\partial y}\right)dz' \tag{2.24}$$

$$\omega_z=\int_z^\infty\left(\frac{\partial\omega_x}{\partial x}+\frac{\partial\omega_y}{\partial y}\right)dz' \tag{2.25}$$

Since the flow considered here is bound by a wall at $z=0$, these integral conditions not only allow to obtain the full perturbation field but also help to enforce no-slip conditions on the velocity at the wall solely using the primary variables. Additional considerations on the boundary conditions employed will be further discussed in §2.2.3.

In this way, with the secondary set of variables completely defined in terms of the primary, the complete mathematical model to study the evolution of small perturbations using only three equations in three variables can be formulated as

$$\frac{\partial\omega_x}{\partial t}+\frac{\partial M_z}{\partial y}-\frac{\partial M_y}{\partial z}=\frac{1}{Re_{\delta_*}}\nabla^2\omega_x+S_x \tag{2.26}$$

$$\frac{\partial\omega_y}{\partial t}+\frac{\partial M_x}{\partial z}-\frac{\partial M_z}{\partial x}=\frac{1}{Re_{\delta_*}}\nabla^2\omega_y+S_y \tag{2.27}$$

$$\nabla^2 w=\frac{\partial\omega_x}{\partial y}-\frac{\partial\omega_y}{\partial x} \tag{2.28}$$

where any reference to the secondary variables $\{u, v, \omega_z\}$ in the system equations (2.26) to (2.28) is then substituted by an adequate definition in equations (2.23) to (2.25). Equally, the terms S_x and S_y correspond to the streamwise and spanwise components of the source or forcing term $\mathbf{S}$. Assuming that the original body force term $\mathbf{f}$ in (2.15) obey some minor technical conditions, it is valid to assume that this body term vanishes from the Poisson equation. The two convection-diffusion transport equations for vorticity plus the fully elliptic Poisson equation for the wall-normal velocity dictate the appropriate numerical schemes to be adopted, which are further discussed in §3

2.2.2 Linearization of the Navier-Stokes equations for small perturbations

In order to further simplify the model described by equations (2.26) to (2.28), and given that the flow perturbations are assumed to be of small amplitude compared to the mean undisturbed flow, a linearization is performed by intentionally omitting nonlinear terms of perturbations in equation (2.20). If this equation is rewritten as:

$$\mathbf{M} = \mathbf{\Omega^B} \times \mathbf{u} + \boldsymbol{\omega} \times \mathbf{U^B} + \mathbf{N} \tag{2.29}$$

with $\mathbf{N} = \boldsymbol{\omega} \times \mathbf{u}$, thence the linearity of the perturbation fields can be attained from the equation (2.29) by dropping $\mathbf{N}$.

The linearized methodology has been chosen in the present research project precisely because of the high computational efficiency achieved by approaches based on linearized Navier-Stokes equations. In this study, equally, the linear operator is regarded as a key element in the process of generation and coupling of vortical structures responsible for the increase or reduction of skin friction drag. There is also documentation that highlights the strengths and insights provided for such linearized approaches ([21, 64, 73, 76]). Last but not least, the interest of this project is to explore recent mechanisms for drag reduction on high-speed flight regimes. Such requirement immediately points towards a low computational cost methodology, in this case a linearization of the perturbation terms in the vorticity transport equation.

However, even though such linearization offers obvious advantages, for instance a simplification of the numerical implementation and therefore a reduction in the overall computational cost, other aspects of linearization can be considered as drawbacks. Several sources in the literature identify the nonlinear terms in the NSEs as a key element in the self-sustaining process of turbulence (see also §1.2). For instance Kim and Lim [77], motivated by evidence that a linear process may play a key role in such self-generation process, examined the implications of altering the linear operator in a fully nonlinear turbulent flow. In that work a direct correlation between omission of the nonlinear terms and response to different initial conditions was found. Therefore, they

were able to explicitly show that non linearity is responsible for part of a cycle maintaining levels of turbulence present in a given flow. Davies and Carpenter [71] also highlights how ignoring non-parallel and nonlinear terms weakens any coupling between streamwise perturbation velocity and spanwise perturbation vorticity. An ill-posed scheme could result if such false decoupling is not properly tackled using adequate boundary conditions. In the present work such strong coupling is achieved via the integral boundary conditions imposed on the primary variables.

In any case, for those situations where numerical simulations are required to explore phenomena connected to fully nonlinear turbulence, as could be desired in self-sustaining turbulence studies, the linear approach would require a further development in order to be used as mathematical model. On the other hand, and as stated above, given the purposes of the present thesis the linear approach offers certain advantages supporting its selection as mathematical framework for the study of the near-wall structures target of this study.

An additional aspect must be briefly discussed when linearization of the NSEs is performed. Once the non-linear terms are absent from the system of equations (2.26) - (2.46) (as the model adopted here), such a system lacks of any ability to self-generate perturbations. In the model here adopted the tracking of a single perturbation is performed, which would be considered as a single representation of the multi-event structures present, and self-regenerating in the fully non-linear case. nevertheless, an initial condition or initial perturbation state must be prescribed, just like in the non-linear case. Source terms in the system of equations need to be used to generate that initial perturbation. In the present study the implications of the selection of this source term (or its projection as an initial disturbance) are studied in §4.

2.2.3 Spatial domain and boundary conditions

In accordance with the selected flow of this study (a parallel boundary layer), corresponding to a parallel flow over a flat plate, the development and evolution of small-scale perturbations are studied in a semi-infinite Cartesian domain over an adequately-long flat plate, as depicted in figure 2.1. Accordingly, four types of boundaries are required to be prescribed. The conditions in the upper boundary far from the wall are covered by the assumption of infinitesimal or vanishingly small amplitudes as $z \to \infty$, as described above in equation (2.22). The upstream and downstream boundaries of the domain are considered, essentially, as inflow and outflow regions, respectively. The adopted treatment of the boundary on the limiting wall ensures the no-slip condition. Likewise, a methodology has been introduced to numerically deal with the semi-infinite domain. Furthermore, given the periodicity of the near-wall structures, the spanwise direction is treated using a Fourier expansion approach. In the following sections a further examination of each of the last four boundaries is presented.

In order to bring clarity to this discussion and for illustration purposes figure 2.2 shows a schematic representation of the domain Ω and boundaries which will be referenced later on. Specifically, boundaries Γ_1 and Γ_2 are the inlet and outlet of the domain Ω, for non-streamwise-periodic simulations, respectively. Γ_3 represents the location of the wall bounding the flow at $z = 0$, and Γ_4 represents the upper boundary located at an asymptotic location $z \to \infty$. The spanwise direction has been intentionally omitted as it will be treated as periodic and, as discussed in §2.2.3, expanded in independent Fourier modes.

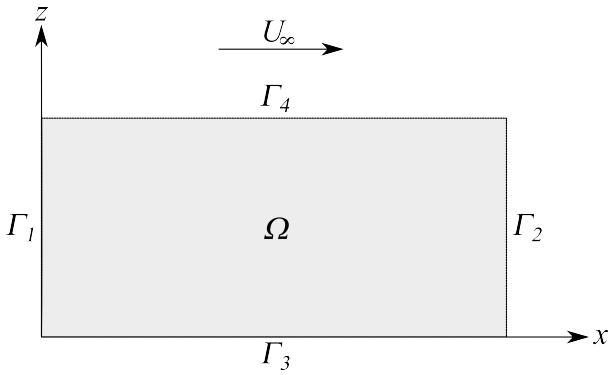

Figure 2.2: Two-dimensional side visualisation of the physical domain Ω.

Boundary conditions on the streamwise direction

For the numerical simulations, the streamwise domain was kept long enough to roughly cover two to three times the anticipated streamwise length of the near-wall streaks. Letting the total domain length in the streamwise direction be represented by L_x, every streamwise location is bounded by $x \in [0, L_x]$. The limits in this range define the inlet or upstream inflow boundary at $x = 0$ (boundary Γ_1 in figure 2.2), and the outlet or downstream outflow boundary at $x = L_x$ (boundary Γ_2 in figure 2.2).

The numerical code employed in this work focused on two different type of numerical experiments: short-time evolutions (non-periodic simulations) and long-time evolutions (periodic simulations). Depending upon such a criteria different type of boundary conditions were considered for these inlet and outlet regions.

Non-periodic simulations For those cases where the interest was set upon relatively short simulation times, non-periodic simulations were setup. In this case the inlet or inflow boundary has been set as a zero value boundary condition for primary variables, so

$$\phi(x = 0, y, z, t) = 0 \tag{2.30}$$

with the upstream influence of the perturbations considered to be negligible, as long as the downstream location of such perturbations remains reasonably far from the inlet. In cases where intentionally a source of perturbation was located nearby the inlet, a simple non-reflective boundary condition was used, ensuring first derivatives equal to zero,

$$\frac{\partial \phi(x=0,y,z,t)}{\partial x} = 0 \tag{2.31}$$

and so establishing a non-reflective nature for the inlet region.

For the farthest downstream boundary, the outlet region in the non-periodic simulations, a non-reflecting boundary condition has been defined for all cases as

$$\frac{\partial^2 \phi(x=L_x,y,z,t)}{\partial x^2} = 0 \tag{2.32}$$

This condition has proved to be extremely satisfactory, especially for transient growth-decay type phenomena. Equally, it contributes to subdue the presence of any spurious oscillation and limits reflections of numerical information back into the domain.

Periodic simulations A slight change in the code allowing periodicity in the streamwise direction has been performed when long periods of simulation have been required, so avoiding excessively long computational domains. Thus, a periodic boundary condition has been set to the upstream boundary as

$$\phi(x=0,y,z,t) = \phi(x=L_x,y,z,t) \tag{2.33}$$

Wall-normal direction and boundary conditions at the wall

A detailed discussion on aspects associated with boundary conditions at the wall for the methodology hereby adopted are thoroughly discussed in Davies and Carpenter [71]. Nevertheless, in such work the main focus was on compliant walls and boundary conditions for moving surfaces. In this thesis, the study these boundary conditions for wall-normal direction are simpler because all applications explored in here correspond to flows over rigid walls. The interest is focused on the stability of different parallel unperturbed mean base flow profiles to small disturbances with no moving walls. In this case the boundary conditions for perturbations

are given by

$$\underset{\sim}{u} = u(x, y, z = 0, t) = 0 \tag{2.34}$$

$$\underset{\sim}{v} = v(x, y, z = 0, t) = 0 \tag{2.35}$$

$$\underset{\sim}{w}(x, y, z = 0, t) = \eta(x, y, t) \tag{2.36}$$

where (2.34) and (2.35) account for no-slip condition and (2.36) allows us to prescribe any transpiration condition, if it is required. In cases where no transpiration velocity is present, $\eta = 0$ satisfies incompressibility at the wall. In the formulation adopted here, boundary conditions for perturbations of wall-normal velocity, as prescribed by (2.36), can be applied directly to the Poisson equation (2.28). In this way any prescription of w can be used directly as a Dirichlet condition on this equation.

On the other hand, the prescription of boundary conditions for vorticity is usually a nontrivial issue in this kind of formulation. In the formulation here adopted, however, such imposition may be carried out easily using the definition of the secondary variables. Such definitions would also allow to naturally associate boundary conditions $\underset{\sim}{u}$ and $\underset{\sim}{v}$ with the vorticity transport equations, if needed. In any case, for the formulation in this thesis the vorticity boundary conditions are replaced by integral constraints obtained directly from the definitions of the secondary variables

$$\int_{z=0}^{\infty} \omega_y \, dz = -\underset{\sim}{u} - \int_{z=0}^{\infty} \frac{\partial w}{\partial x} dz \tag{2.37}$$

$$\int_{z=0}^{\infty} \omega_x \, dz = \underset{\sim}{v} + \int_{z=0}^{\infty} \frac{\partial w}{\partial y} dz \tag{2.38}$$

These expressions evidently act as constraints on the vorticity transport equations, ensuring at the same time the no-slip condition and incompressibility.

Dealing with the wall-normal semi-infinite domain

Since the wall-normal extension of the physical domain is semi-infinite, with the solid boundary surface located at $z = 0$ (Γ_3 in figure 2.2), it is necessary to adopt a numerical strategy that can deal with such domain. For numerical purposes different approaches to mapping or truncating the semi-finite domain have been presented in [78–81]. Asaithambi [79] highlights problems related to stability and convergence when attempting to directly solve the equation for the entire mapped semi-infinite domain. In order to deal with such a semi-infinite domain, the present work follows the method presented in [38, 82, 83], where a coordinate

transformation defined as

$$\zeta = \frac{L_\infty}{z + L_\infty} \tag{2.39}$$

is employed to transform the physical region $z \in [0, \infty)$ on to the bounded computational domain $\zeta \in (0, 1]$ with the parameter L_∞ being a stretching factor. In general, the stretching factor can be any value such that the minimum mapped coordinate ζ corresponds to a sufficiently large coordinate z enough to be greater than the boundary layer thickness. At this location it is safe to assume that the mean velocity profile asymptotically approaches the free stream limit and that, as it was previously defined, primary and secondary variables asymptotically approach zero and effectively vanish. An additional effect of the mapping defined by (2.39) is that every derivative in the wall-normal direction must be modified to account for such re-mapping. As such, z-derivatives must be expressed now as

$$\frac{\partial \phi}{\partial z} = -\frac{\zeta^2}{L_\infty} \frac{\partial \phi}{\partial \zeta} \tag{2.40}$$

$$\frac{\partial^2 \phi}{\partial z^2} = \frac{\zeta^4}{L_\infty^2} \frac{\partial^2 \phi}{\partial \zeta^2} + \frac{2\,\zeta^3}{L_\infty^2} \frac{\partial \phi}{\partial \zeta} \tag{2.41}$$

for every field variable ϕ. It can be appreciated from (2.40) and (2.41) that this mapping also ensures that if derivatives in ζ remain bounded as $\zeta \to 0$, then derivatives in z vanish as $z \to \infty$. In other words, if $\partial\phi/\partial\zeta$ is bounded then $\partial\phi/\partial z$ vanishes approaching the upper boundary for any field ϕ.

Spanwise direction. Fourier modes expansion.

In the spanwise direction, in the present formulation, one of the main features of the near-wall structures it is exploited: their coherent periodicity and relative spanwise uniformity. Owing to the well-known characteristic of the structures under study, a spectral Fourier representation of the perturbations in the spanwise direction has been incorporated and defined in the model as:

$$\phi(x, y, z, t) = \frac{1}{2\pi} \int_{-\infty}^{\infty} \hat{\phi}_\beta(x, z, t)\, e^{\mathbf{i}\beta y} d\beta \tag{2.42}$$

for every field variable ϕ, with β denoting a spanwise wavenumber defined also by a spanwise wavelength λ_y as

$$\beta = \frac{2\pi}{\lambda_y} \tag{2.43}$$

An attractive compensation of this assumption in the model is that, once the governing equations have been linearized, each spanwise or Fourier mode is independent of all others. This allows to study stability of any

chosen laminar or turbulent profile to small perturbations at individual spanwise modes in an independent manner. In this case no boundary conditions are required for the spanwise direction. Two- and three-dimensional simulations can be implemented straightforwardly using the same mathematical model with a proper selection and superposition of β modes; though in both cases it is required to use a parallel, spanwise uniform mean flow. Finally, advantage of modern parallel computing techniques, as discussed later in §3.1.3, can be taken with relative ease in the numerical implementation.

2.3 Prescribing base flow: Mean velocity profiles

As part of the mathematical model, and in accordance with previous discussion a mean base flow must be prescribed which will determine the nature and stability of the mathematical operators defined in equations (2.26) to (2.28). As one of the main purposes in this study is to characterise the near-wall streaks, initially an undisturbed, semi-empirical, parallel, known and homogeneous velocity profile is chosen. This flow is defined in general terms as

$$\mathbf{U^B} = [U(z), 0, 0] \tag{2.44}$$

$$\mathbf{\Omega^B} = [0, \Omega_y(z), 0] \tag{2.45}$$

Throughout this work this known base-flow can represent either a laminar or turbulent mean velocity profile, depending upon specific application of the model. A laminar profile is required for validation purposes in §3.5, but turbulent profiles are the main target in this work. For both profiles, given the streamwise scales involved, a reasonable approximation of near-constant boundary-layer thickness is made.

In this thesis the main interest is the stability and response of a different type of mean base profile with a spanwise component, which is further discussed in §5 . In that case the base profile can be represented as

$$\mathbf{U^B} = [U(z), V(x, z, t), 0] \tag{2.46}$$

$$\mathbf{\Omega^B} = [\Omega_x(x, z, t), \Omega_y(x, z, t), \Omega_z(x, z, t)] \tag{2.47}$$

A short description of the mathematical models chosen to represent a flow condition given by (2.44) and (2.45) is discussed in §2.3.2 and §2.3.3, for laminar and turbulent cases, respectively. However, the more general flow form defined by equations (2.46) and (2.47) will be discussed in §5. In this work the selection of a particular type of profile is a key element as it allows to pinpoint the specific flow whose near-wall structures are to be

characterised, for instance a turbulent boundary layer or a turbulent channel flow, and also differentiates the specific flow-control techniques discussed in §5.

Throughout this document recurrent mention is made of some characteristic lengths of the boundary layer (mainly the boundary layer thickness and the displacement thickness); and so a brief description of these concepts is presented first.

2.3.1 Characteristic lengths of boundary layers

To facilitate the quantification of lengths involved at the region of interest, different conceptual values have been established. In this work two of them are often used. Although there is not a precise value for the *boundary layer thickness*, owing mainly to the asymptotic reduction of viscous effects towards the free stream, it is customary to define such a limit as the point within the boundary layer where the streamwise component of velocity is 99% of the free stream velocity (see also [84]). This can be explicitly expressed as

$$\delta_{99} = \kappa_1 \, \delta_N \tag{2.48}$$

where κ_1 is a proportionality constant usually taken as 3.6 for laminar boundary layers, and δ_N is a reference scale defined as

$$\delta_N = \sqrt{\frac{2\,\boldsymbol{\nu}\,x}{U_\infty\,(\gamma+1)}} \tag{2.49}$$

with U_∞ as the usual free stream velocity, $\boldsymbol{\nu}$ the kinematic viscosity, x the streamwise location from starting up point of boundary layer and γ representing a dimensionless pressure-gradient parameter defined as

$$\gamma = \frac{x}{U_\infty}\frac{d\,u}{d\,x} \tag{2.50}$$

In general, factor κ_1 can be estimated by locating the wall-normal location at which u reaches 99% of U_∞, and therefore it is not a firm fixed value. For abbreviation, from here onwards this boundary layer thickness is simply indicated as δ, unless otherwise noted.

On the other hand, another important characteristic length is the *displacement thickness*, which is considered as that thickness by which the outer "inviscid" outer portion of the flow is displaced outwards owing to the drop in velocity within the boundary layer itself. This can be stated mathematically as

$$\delta_* = \int_0^\infty \left(1 - \frac{u}{U_\infty}\right) dz \tag{2.51}$$

These definitions are used in the following discussion on both laminar and turbulent velocity profiles.

2.3.2 Laminar boundary layers

One of the main important results of linearized approaches, associated to stability theory, is the ability to predict an instability that is thought to be responsible for, or at least to lead to, the transition from laminar to turbulent flow: the Tollmien-Schlichting wave instability. In this way an important validation test for the model adopted here is its ability to accurately capture such phenomenon. Another well-known phenomenon associated with a transitional boundary layer is the Klebanoff mode. In this phenomenon the laminar boundary layer responds in a large-scale motion to observable spanwise streaks, which are thought to be caused by low-frequency vortical disturbances. Both phenomena are well documented in the literature ([1, 30, 76, 85, 86]) which makes them useful validation test cases. Equally, in both cases the important underlying mean flow is a laminar profile of Blasius type. To model this transition from laminar to turbulent flow it is necessary then to have a valid laminar velocity profile. Such a profile is provided by the Blasius equation for the case of a zero pressure gradient flow, or by the Falkner-Skan equation for the more general case. In this section a general treatment for obtaining such a profile from the Falkner-Skan equation is presented.

Laminar boundary layers exhibiting self similarity have been the subject of a large body of research as they provide useful insight into many key features of wall-bounded flows, as well as being the basis of approximate methods for calculating more complex, non-similar boundary-layer problems [84]. The Falkner-Skan equation is obtained when a similarity analysis is performed on the two-dimensional, steady, incompressible Navier-Stokes equations for a one-sided bounded flow. The simplified continuity and momentum equations for such case are as follows:

$$\frac{\partial u}{\partial x} + \frac{\partial w}{\partial z} = 0 \tag{2.52}$$

$$u\,\frac{\partial u}{\partial x} + w\,\frac{\partial u}{\partial z} = -\frac{1}{\boldsymbol{\rho}}\,\frac{d\,p}{d\,x} + \boldsymbol{\nu}\,\frac{\partial^2 u}{\partial z^2} \tag{2.53}$$

where, as above, x is the streamwise and z is the wall-normal coordinate, $\boldsymbol{\rho}$ is the fluid density, $\boldsymbol{\nu}$ is the kinematic viscosity, and u and w are the x- and z-components of velocity, respectively. For the boundary layer these equations are subjected to a simple set of boundary conditions:

$$\text{at } z = 0: \;\; u = 0\,, \;\; w = 0 \tag{2.54}$$

$$\text{at } z \to \infty: \;\; u = U_\infty \tag{2.55}$$

where U_∞ is the free-stream velocity, which is assumed to be a function of x. Hereby, only walls with non-transpiration and no-slip conditions are considered, hence both components of velocity at the wall are zero. In order to perform a similarity analysis on eqs. (2.52) and (2.53), Falkner and Skan [87] proposed the following transformation:

$$\xi = \sqrt{\frac{U_\infty}{\boldsymbol{\nu}\, x}}\; z \tag{2.56}$$

or simply

$$\xi = \frac{z}{\delta_{ref}} \tag{2.57}$$

with $\delta_{ref} = \sqrt{\boldsymbol{\nu}\, x/U_\infty}$ being a similarity variable. Using (2.56) and an implicit dimensionless stream function $g[\xi(x,z)]$ such that

$$\psi[x,\xi(x,z)] = \delta_{ref}\, U_\infty(x)\; g\left[\xi\,(x,z)\right] \tag{2.58}$$

where ψ is a conventional stream function used to define the two-dimensional velocity field:

$$u = \frac{\partial \psi}{\partial z} \quad \text{and} \quad w = -\frac{\partial \psi}{\partial x}.$$

The two velocity components can be expressed in terms of $g(\xi)$ as follows:

$$u \;=\; U_\infty\, g' \qquad \text{and} \qquad w = \frac{1}{2}\,\frac{\boldsymbol{\nu}}{\delta_{ref}}\;(\xi\, g' - g) - \frac{1}{2}\,\delta_{ref}\,\frac{d\,U_\infty}{d\,x}\,g \tag{2.59}$$

with the prime symbol denoting a derivative with respect to ξ. Using equations (2.57) to (2.59), the momentum equation (2.53) can be rewritten, after some algebraic manipulation, as:

$$\frac{\mathrm{d}^3 g}{\mathrm{d}\xi^3} + \frac{\gamma+1}{2}\, g\, \frac{d^2\, g}{d\,\xi^2} + \gamma\left[1 - \left(\frac{d\, g}{d\,\xi}\right)^2\right] = 0, \tag{2.60}$$

where γ is the dimensionless pressure-gradient parameter defined in (2.50).

For zero pressure gradient γ=0 and therefore equation (2.60) reduces to the Blasius equation. The boundary conditions (2.54) and (2.55) can now be rewritten using definitions for the velocity components given in equation (2.59):

$$\begin{aligned} &\text{at}\;\; \xi = 0: \qquad g = 0, \qquad g' = 0 \\ &\text{at}\;\; \xi \to \infty: \qquad g' = 1 \end{aligned} \tag{2.61}$$

Hartree [88] introduced an additional simplification to the equation (2.60), defining the following linear

transformation:

$$\eta = \sqrt{\left(\frac{\gamma+1}{2}\right)}\,\xi \qquad \text{and} \qquad f = \sqrt{\left(\frac{\gamma+1}{2}\right)}\,g \tag{2.62}$$

such that the Falkner-Skan equation (2.60) can now be rewritten in its most known form, and indeed as the model employed in this work, as

$$\frac{\mathrm{d}^3 f}{\mathrm{d}\eta^3} + f\,\frac{d^2 f}{d\,\eta^2} + \beta_{fs}\left[1 - \left(\frac{d\,f}{d\,\eta}\right)^2\right] = 0, \tag{2.63}$$

where β_{fs} is the dimensionless pressure-gradient parameter:

$$\beta_{fs} = \frac{2\,\gamma}{\gamma+1}. \tag{2.64}$$

The range of values for which β_{fs} is physically meaningful is approximately $-0.2 \leqslant \beta_{fs} < \infty$ (corresponding to $-0.09 \leqslant \gamma < \infty$), range defined by the limits on existence of a solution for this equation, as presented by Hartree [88]. For $0 \leqslant \beta_{fs} \leqslant 2$, the physical interpretation of the solution of the Falkner-Skan equation is the laminar boundary layer over an infinite wedge of vertex angle $\pi\beta_{fs}$ (β_{fs}=0 corresponds to the Blasius boundary layer). In this manner using Hartree's transformation eq. (2.62), the boundary conditions can be rewritten as

$$\text{at } \eta = 0: \qquad f = 0, \qquad f' = 0 \tag{2.65}$$

$$\text{at } \eta \to \infty: \qquad f' = 1, \tag{2.66}$$

with the prime symbol denoting now a derivative with respect to η. It is important to highlight that using the definitions shown in equations (2.57), (2.59) and (2.62) the displacement thickness presented in eq. (2.51) can be expressed in a more compact expression as

$$\delta_* = \delta_N \int_0^\infty (1 - f')\,d\eta \tag{2.67}$$

Transformations related to similarity analysis like the one proposed by Falkner and Skan are appropriate for two-dimensional boundary layers. In cases where it is required to deal with three-dimensional boundary layers, a different transformation to the formulation hereby presented must be used. The primary aim of these methodologies is to reduce the partial differential formulation into an ordinary differential by reducing in one the number of spatial variables. In the three-dimensional case, though the transformation is slightly different, it produces a system of two ODEs instead of just one equation as in the present case. A simple example of such a transformation and the system obtained can be found in Hogberg and Henningson [89].

2.3.3 Turbulent boundary layers

Turbulent flows are characterised by a two-layer structure. In the inner wall portion of the boundary layer, where viscous effects are dominant, velocities and lengths scale are discussed in terms of inner wall units, or simply inner units. In the outer region, where inertial effects are dominant, velocity and length scales are discussed in terms of outer units. In this outer portion of the boundary layer characteristic lengths are the same order of magnitude as the displacement thickness δ_* or the boundary layer thickness δ with the free stream velocity U_∞ being an appropriate scaling parameter for velocity. However, in inner units the pertinent scaling parameters are the wall friction velocity

$$u_\tau = \sqrt{\frac{\tau_w}{\rho}} \tag{2.68}$$

with τ_w being the wall shear stress, and the viscous length which is defined as

$$\delta_{\boldsymbol{\nu}} = \frac{\boldsymbol{\nu}}{u_\tau}. \tag{2.69}$$

However, this two-layer structure can in turn be subdivided into four fairly well defined regions: the viscous sublayer, the buffer layer, the logarithmic layer and the outer wake layer. Such structure for a zero pressure gradient turbulent boundary layer at $Re_{\delta_*} = 1000$ is presented in Fig. 2.3.

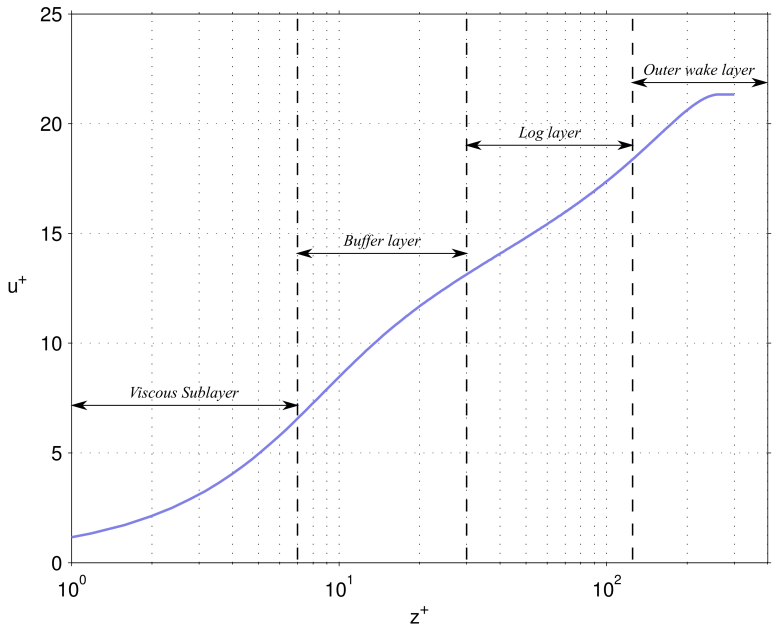

Figure 2.3: Layer structure of a turbulent velocity profile for $Re_{\delta_*} = 1000$.

The solution of the mean base flow is based on an asymptotic matching of the inner and outer layers. This

yields the very well known result of the logarithmic law of the wall for the turbulent velocity profile in the region where inner and outer regions overlap,

$$u^+ = \frac{u}{u_\tau} = \frac{1}{\kappa} \ln z^+ + B \tag{2.70}$$

where z^+ is the distance from the wall in inner units[4], i.e. normalised using δ_ν, and u^+ is the streamwise velocity normalised using u_τ. In equation (2.70) κ and B denote the Von-Karman and additive intercept at $z^+ = 1$, respectively.

In order to use (2.70) to model the outer layer, it must be corrected in the final external portion to account for a slight deviation of actual profiles from the log profile, particularly in non-equilibrium boundary layers with a pressure gradient. Coles [90] noted that the deviation or excess velocity above the log law resembled a wake-like shape relative to the free stream and proposed a correction for the log law,

$$u^+ = \frac{1}{\kappa} \ln z^+ + B + \frac{\Pi}{\kappa} f\left(\frac{z^+}{\delta^+}\right) \tag{2.71}$$

where f should be some S-shape function with $f(0) = 0$ and $f(1) = 2$, and Π is a parameter related to the local friction coefficient and therefore to the pressure gradient. As noted by Musker [91] and references therein, this correction alone to the log law leads to a discrepancy in the slope condition at the edge of the boundary layer, $du/dz = 0$. An additional correction function Γ is then adopted accordingly as proposed in [91]

$$\Gamma = \left(\frac{z}{\delta}\right)^2 \left(1 - \frac{z}{\delta}\right) \tag{2.72}$$

Nagib and Chauhan [92] highlight that though extensive literature can be found both against and in favour of the logarithmic law of the wall, such a law has been extensively tested and employed to represent accurately experimental data points for three different canonical turbulent flows: flow past a smooth surface, flow within a channel and flow within a pipe. In the "classical" approach similar relations have been universally applied to all type of wall bounded flows. In fact, it has been common to use the same logarithmic law and parameters as equally valid for different wall bounded flows; for instance, zero pressure gradient boundary layers (ZPG TBL), pipes, and channels alike. This classical approach has been recently re-evaluated, as more rigorous and precise experiments in canonical wall bounded flows have been carried out. Abundant evidence now indicates that parameters κ, B and Π are not as universal as originally thought [93].

In a more recent approach, the general form of the law of the wall, though preserved, is adjusted by changing the values of the Von Karman constant κ, additive constant B and wake parameter Π for each canonical

[4] From here onwards a superscript '+' will denote a non-dimensionalisation in terms of the inner wall variables δ_ν and u_τ.

flow. This in turn affects also the inner region by changing its asymptotic behaviour. Nagib and Chauhan [92] offers alternative values for the log-law parameters, which are presented in table 2.1.

Canonical wall bounded flow	**Asymptotic value proposed by [92]**			**Classical value**		
	Π	κ	B	Π	κ	B
ZPG TBL	0.480	0.384	4.13	0.45-0.55	0.41	5.00
Channel	0.055	0.370	3.70	0.00		
Pipe	0.220	0.410	5.00			

Table 2.1: Comparison of classical against adopted values of the log-law parameters.

On the other hand, though there is a fairly wide agreement on the logarithmic law of the wall as a valid model for most of the outer region, for the inner region there is not, strictly speaking, such a thing as a universal model. Although the linear behaviour in the inner viscous sublayer is known to be Reynolds number independent, this criteria does not conform by itself a universal inner model. One of the most celebrated analytical expressions to obtain a turbulent velocity profile is a formula proposed by Spalding [94] with which the viscous, buffer, and log layers of the turbulent boundary layer can be modelled using a single expression given by

$$z^+ = u^+ + e^{-\kappa B}\left[e^{\kappa u^+} - 1 - \kappa u^+ - \frac{(\kappa u^+)^2}{2} - \frac{(\kappa u^+)^3}{6}\right] \tag{2.73}$$

Spalding's expression presents two particular problems. First, it is an implicit expression for u^+ which makes difficult its direct use to estimate a velocity profile. Secondly, Spalding's expression eq. (2.73) fails to reproduce an "overshoot" near the buffer layer observed in both boundary layer data as well as in velocity profiles obtained by Direct Numerical Simulation (DNS) [95]. A totally different expression to produce a velocity profile for turbulent boundary layers from the wall up to the log layer was developed by Musker [91]. Later, Musker's expression was improved by Nagib and Chauhan [92] in order to produce turbulent profiles also for flows in channels and pipes (the other two canonical flows). Given the interest in this thesis in near-wall structures in different potential applications, the modified Musker model presented in [92] is adopted here, which can be rewritten as

$$\frac{d\,u^+}{d\,z^+} = \frac{\dfrac{1}{s} + \dfrac{z^{+2}}{\kappa} - \dfrac{z^+}{s\,Re_\tau}}{\dfrac{1}{s} + \dfrac{z^{+2}}{\kappa} + z^{+3}} \tag{2.74}$$

where s is a parameter to be found depending on the type of flow and Reynolds number. More details on the specific procedure to determine this s-parameter are presented in §3.4.2. Nevertheless, since a combination of type of flow and Reynolds number offers a unique log-law profile, it is noteworthy that this parameter s must be adjusted such that the ending portion of the inner profile described by equation (2.74) matches the final

or ending portion of the profile described by the logarithmic model. Re_τ is the Reynolds number defined as

$$Re_\tau = \frac{\delta\, u_\tau}{\boldsymbol{\nu}} \tag{2.75}$$

also called the *friction Reynolds number* which, due to its definition equation (2.75), is equal to δ^+.

Thus, the complete model to generate the turbulent velocity profile adopted in the present work can be stated as a composite profile with the inner region obtained by solving

$$\frac{d\, u^+_{inner}}{d\, z^+} = \frac{\dfrac{1}{s} + \dfrac{{z^+}^2}{\kappa} - \dfrac{z^+}{s\, Re_\tau}}{\dfrac{1}{s} + \dfrac{{z^+}^2}{\kappa} + {z^+}^3} \tag{2.76}$$

with the value for s adjusted depending on κ, B and Re_{δ_*}, and the outer region modelled by incorporating equation (2.72) in (2.71) as

$$u^+_{outer} = \frac{1}{\kappa}\ln z^+ + B + \frac{\Pi}{\kappa}\left[6\left(\frac{z^+}{\delta^+}\right)^2 - 4\left(\frac{z^+}{\delta^+}\right)^3\right] + \frac{1}{\kappa}\left(\frac{z^+}{\delta^+}\right)^2\left(1 - \frac{z^+}{\delta^+}\right) \tag{2.77}$$

Further explanation about numerical implementation of the model given by eqs. (2.76) and (2.77) is presented in §3.4.2.

Conversion between inner and outer units

A final issue must be tackled in order to use the turbulent velocity profiled described above. The numerical and computational implementation is based in outer units, i.e. using as velocity and length scales U_∞ and δ_*, respectively. However, owing to the definition above of the turbulent profile in inner units, with u_τ as a velocity scale and $\delta_{\boldsymbol{\nu}}$ as a length scale, it must be obtained a valid conversion between these two sets of variables. This can be accomplished by associating the definition of Re_{δ_*} with δ^+ for the model described before.

If the free-stream velocity and displacement thickness are non-dimensionalised using inner units

$$\begin{aligned} U^+_\infty &= \frac{U_\infty}{u_\tau} \\ \delta^+_* &= \frac{\delta_*}{\delta_{\boldsymbol{\nu}}} \end{aligned}$$

a simple modified definition for Reynolds number in outer units is

$$Re_{\delta_*} = \delta_*^+ \, U_\infty^+ \tag{2.78}$$

Additionally any length variable χ normalised with outer units can be converted into inner units by

$$\chi^+ = \chi^* \, \delta_*^+ \tag{2.79}$$

and time t can be converted using

$$t^+ = t^* \, \frac{\delta_*^+}{U_\infty^+} \tag{2.80}$$

In particular, by using (2.79), the previous definition of the displacement thickness can be rewritten in terms of u_{outer}^+ as

$$\delta_*^+ = \int_0^{\delta^+} \left(1 - \frac{u^+}{U_\infty^+}\right) dz^+ \tag{2.81}$$

and if u^+ is replaced by u_{outer}^+ in equation (2.77) then, after performing integration, it leads to[5]

$$\delta_*^+ = \frac{\delta^+}{U_\infty^+} \left[U_\infty^+ - B - \frac{\ln \delta^+}{\kappa} - \frac{\Pi}{\kappa} + \frac{11}{12\,\kappa}\right] \tag{2.82}$$

Since the log law evaluated at the boundary-layer thickness produces

$$U_\infty^+ = \frac{\ln \delta^+}{\kappa} + B + \frac{2\Pi}{\kappa} \tag{2.83}$$

then, by replacing (2.83) into (2.82), a full expression is obtained as

$$\delta_*^+ = \frac{\delta^+}{U_\infty^+} \left[\frac{12\,\Pi + 11}{12\,\kappa}\right] \tag{2.84}$$

Finally, using eq. (2.78), a complete relationship between Re_{δ_*} and δ^+ (or its equivalent Re_τ) is obtained as

$$Re_{\delta_*} = \delta^+ \left(\frac{12\,\Pi + 11}{\kappa}\right) \tag{2.85}$$

or simply

$$\delta^+ = \frac{12\,Re_{\delta_*}\,\kappa}{12(\Pi + 1) - 1} \tag{2.86}$$

In this manner two conversion scales can be defined as the main basis for the entire model. For the velocity

[5] Note that this expression is only valid for turbulent boundary layers using the wake correction presented before.

scale a conversion between outer and inner units is defined as

$$u_i^+ = u_i^* \, U_\infty^+ \tag{2.87}$$

with u_i^* as a velocity u_i non-dimensionalised using free-stream velocity U_∞, and u_i^+ being a non-dimensionalisation with respect to u_τ. For length scale a conversion is then defined as

$$d_i^+ = d_i^* \, \delta_*^+ \tag{2.88}$$

with d_i^* being a length scale non-dimensionalised using the displacement thickness δ_*, and d_i^+ being such length scale, but non-dimensionalised using the viscous length $\delta_{\boldsymbol{\nu}}$. In both cases, for length as well as for velocity conversions, U_∞^+ and δ_*^+ are related by equation (2.78).

2.4 Complete mathematical model

Using the system of equations (2.26) - (2.28), and incorporating the criteria described above the main mathematical model can now established and expressed it in an expanded form. First, it is written down the operator $\mathbf{M}$ with the non-linear term included, eq. (2.29), by components and with mean flow vorticity replaced by its definition in terms of velocity as

$$\mathbf{M_x} = \left(\frac{\partial U^B}{\partial z} - \frac{\partial W^B}{\partial x}\right) w - \left(\frac{\partial V^B}{\partial x} - \frac{\partial U^B}{\partial y}\right) v + \left(\omega_y W^B - \omega_z V^B + \omega_y w - \omega_z v\right) \tag{2.89}$$

$$\mathbf{M_y} = \left(\frac{\partial V^B}{\partial x} - \frac{\partial U^B}{\partial y}\right) u - \left(\frac{\partial W^B}{\partial y} - \frac{\partial V^B}{\partial z}\right) w + \left(\omega_z U^B - \omega_x W^B + \omega_z u - \omega_x w\right) \tag{2.90}$$

$$\mathbf{M_z} = \left(\frac{\partial W^B}{\partial y} - \frac{\partial V^B}{\partial z}\right) v - \left(\frac{\partial U^B}{\partial z} - \frac{\partial W^B}{\partial x}\right) u + \left(\omega_x V^B - \omega_y U^B + \omega_x v - \omega_y u\right) \tag{2.91}$$

By introducing two-dimensional homogeneous parallel flow assumptions for the mean flow velocity components[6],

$$\begin{array}{lll} U^B = U(z) & V^B = 0 & W^B = 0 \\ \dfrac{\partial U^B}{\partial x} = 0 & \dfrac{\partial V^B}{\partial x} = 0 & \dfrac{\partial W^B}{\partial x} = 0 \\ \dfrac{\partial U^B}{\partial y} = 0 & \dfrac{\partial V^B}{\partial y} = 0 & \dfrac{\partial W^B}{\partial y} = 0 \\ \dfrac{\partial U^B}{\partial z} = \dfrac{d\,U^B}{d\,z} & \dfrac{\partial V^B}{\partial z} = 0 & \dfrac{\partial W^B}{\partial z} = 0 \end{array} \tag{2.92}$$

[6]For the time being only a streamwise parallel flow is being considered. However, in §5 a spanwise base flow will be introduced and therefore properly explained

the components of $\mathbf{M}$ can be re-written as

$$\begin{aligned}\mathbf{M_x} &= \frac{d\,U^B}{d\,z}\,w + \omega_y\,w - \omega_z\,v \\ \mathbf{M_y} &= U^B\,\omega_z + \omega_z\,u - \omega_x\,w \\ \mathbf{M_z} &= -\frac{d\,U^B}{d\,z}\,u - \omega_y\,U^B + \omega_x\,v - \omega_y\,u\end{aligned} \tag{2.93}$$

For instance, by substituting these expressions in equations (2.26) and (2.27), and introducing U' as a shorthand for the wall-normal derivative of the mean base profile, the vorticity transport equation in streamwise direction becomes

$$\begin{aligned}\frac{\partial \omega_x}{\partial t} = U'\omega_z + U^B\frac{\partial \omega_z}{\partial z} + U'\frac{\partial u}{\partial y} + U^B\frac{\partial \omega_y}{\partial y} + \frac{1}{Re_{\delta_*}}\nabla^2\omega_x \\ - \frac{\partial(\omega_x\,v - \omega_y\,u)}{\partial y} + \frac{\partial(\omega_z\,u - \omega_x\,w)}{\partial z} + S_x\end{aligned} \tag{2.94}$$

where S_x is the streamwise component of any non-vanishing source term in (2.10). However, previous expression is still in terms of six variables. After some straightforward manipulation a "reduced" expression in terms of only primary variables $\{\omega_x, \omega_y, w\}$ can be obtained

$$\frac{\partial \omega_x}{\partial t} = U'\int_z^\infty \left(\frac{\partial \omega_x}{\partial x} - \mathbf{i}\beta\frac{\partial w}{\partial x}\right) dz - U\frac{\partial \omega_x}{\partial x} + \frac{1}{Re_{\delta_*}}\nabla^2\omega_x + f_x \tag{2.95}$$

where the Fourier expansion in the spanwise direction has been applied. Due to the linearity of terms other than f_x, and for the sake of simplicity, only an individual spanwise mode is represented in eq. (2.95). The non-linear terms present in equation (2.95) have been grouped together with the source term into a single element f_x defined then as

$$f_x = S_x + \frac{\partial(\omega_z\,u - \omega_x\,w)}{\partial z} - \frac{\partial(\omega_x\,v - \omega_y\,u)}{\partial y} \tag{2.96}$$

Equally, using same the methodology for the spanwise vorticity a transport equation can also be obtained as,

$$\begin{aligned}\frac{\partial \omega_y}{\partial t} = -U''\,w + U'\,\frac{\partial v}{\partial y} - U\,\frac{\partial \omega_y}{\partial x} + \frac{1}{Re_{\delta_*}}\nabla^2\,\omega_y \\ + \frac{\partial(\omega_x\,v - \omega_y\,u)}{\partial x} - \frac{\partial(\omega_y\,w - \omega_z\,v)}{\partial z} + S_y\end{aligned} \tag{2.97}$$

and again, after substituting definitions of secondary variables and condensing non-linear and source terms into f_y, it is obtained for the spanwise vorticity transport equation the following expression,

$$\frac{\partial \omega_y}{\partial t} = -U''\,w + U'\int_z^\infty \left(\mathbf{i}\,\beta\,\omega_x + \beta^2\,w\right) dz - U\,\frac{\partial \omega_y}{\partial x} + \frac{1}{Re_{\delta_*}}\nabla^2\,\omega_y + f_y \tag{2.98}$$

with U'' representing $\dfrac{d^2\,U}{d\,z^2}$.

For the model adopted here to be complete only the Poisson equation for the wall normal velocity is required, which can be written in a similar fashion as

$$\left\{\underset{\sim}{\Delta} - \beta^2\right\} w = \frac{\partial \omega_x}{\partial y} - \frac{\partial \omega_y}{\partial x} \tag{2.99}$$

with $\underset{\sim}{\Delta} = \dfrac{\partial^2}{\partial x^2} + \dfrac{\partial^2}{\partial z^2}$.

The mathematical model is now complete, and fully determined by equations (2.95), (2.98) and (2.99). Finally, a full recovery of the remaining secondary flow field variables can be attained by a simple replacing of primary fields into the integral definitions given by equations (2.23) to (2.25).

2.5 Chapter summary

A general overview of important concepts required for the theoretical model used in this work has been presented. The main elements of the mathematical model to be used have been elicited and a discussion about the implications of several assumptions has been presented. A complete description of the model also required relationships for semi-empirical velocity profiles to be used, both as validation background flow and as a key component of the Linearized Navier-Stokes (LNS) operator to study. These have been elaborated and explained in the last section. Important relations required to outline the numerical implementation have also been presented.

Chapter 3

Numerical model and code validation

In the present work a numerical methodology based on that presented in Davies and Carpenter [71] for solving the velocity-vorticity formulation of the Navier-Stokes equations is adopted. Here some features of the technique are adopted directly, although in some cases with differences. For instance, where like in Davies and Carpenter [71], Chebyshev expansions in the wall-normal direction are used, and therefore the current numerical implementation benefits from a double integration of the vorticity transport equations (2.26) and (2.27) and the Poisson equation (2.28) with respect to the mapped variable ζ, introduced in §2.2.3. Nevertheless, some changes in the streamwise direction discretization and in a parallel MPI implementation are worthy of mention. Additionally, a semi-implicit predictor-corrector time-stepping technique was adopted. A full description of the methods employed to perform numerical simulations of the models presented in §2 is discussed in the present chapter. Tests aiming to validate the numerical methodologies implemented are also discussed and their results presented.

3.1 Spatial Discretization

A hybrid spectral and high-order finite difference scheme has been exploited to discretise the governing equations. In the streamwise direction, fourth-order schemes are implemented; in the spanwise direction the flow fields are expanded using Fourier modes, and in the wall-normal direction there is an expansion in terms of Chebyshev polynomials. Integral conditions are used to implement boundary conditions as outlined in §2.2.3, ensuring also no-slip at the walls.

3.1.1 Streamwise discretization. Numerical details.

Even though in previous implementations of the methodology centered finite differences have been satisfactorily employed, for some cases the use of centered schemes requires caution. For instance, in equations with large advective terms, like in hyperbolic systems, spurious oscillations can appear in the solution due entirely to a central difference approximation ([see 96, pg. 200]). For this reason, even though the system of interest here has elliptic-parabolic features, depending upon Reynolds number, supported by different numerical tests, a semi-backwards finite differences scheme instead of a centered scheme, is adopted. Numerical tests were performed to ensure that not extra dissipation was introduced by these schemes, compared to a centred scheme.

As an example, in numerical simulations of the generation of Tollmien-Schlichting waves (see §3.5.1), the centered schemes generated spurious oscillations in the streamwise direction. An example of such results for spanwise vorticity is presented in figure 3.1, though a more detailed discussion follows later. In this particular case, for instance, small oscillations like those depicted in figure 3.1a appeared at upstream locations. Equally undesired spurious oscillations like those illustrated in figure 3.1b appeared at downstream stations when centered schemes were in place. In both cases such oscillations were completely subdued or heavily damped by the implementation of semi-backwards finite differences, as discussed below.

Owing to the diffusive nature of the system, particularly of the wall normal velocity, it is necessary to preserve numerical information at both sides of every grid point, along with a high level of accuracy. Moreover, in order to capture most of the advective nature of the system, primarily at high Reynolds number flows, preference was given to the upstream direction. The model adopted here only features first and second order streamwise derivatives. Both of these were then estimated using unbalanced semi-backwards finite differences. Accordingly, first derivatives were numerically estimated with a fourth-order approximation as

$$\frac{d\,\phi_i}{d\,x} = \frac{-\phi_{i-3} + 6\,\phi_{i-2} - 18\,\phi_{i-1} + 10\,\phi_i + 3\,\phi_{i+1}}{12\,\Delta x} + \mathsf{O}\left(-\frac{\phi_i^{(5)}}{20}\,h^4\right) \tag{3.1}$$

whereas for second derivatives a third order-approximation was used, given by

$$\frac{d^2\,\phi_i}{d\,x^2} = \frac{-\phi_{i-3} + 4\,\phi_{i-2} + 6\,\phi_{i-1} - 20\,\phi_i + 11\,\phi_{i+1}}{12\,\Delta x^2} + \mathsf{O}\left(-\frac{\phi_i^{(5)}}{12}\,h^3\right) \tag{3.2}$$

for all $i-$th streamwise locations in the cases with streamwise periodicity. For those cases with inlet/outlet boundary conditions, these schemes were used in all streamwise locations except near the boundaries. In those cases, near the inlet boundary one-sided finite differences were used. The outlet boundary was prescribed, and presented no problems. In the different tests and applications performed in this thesis those schemes proved

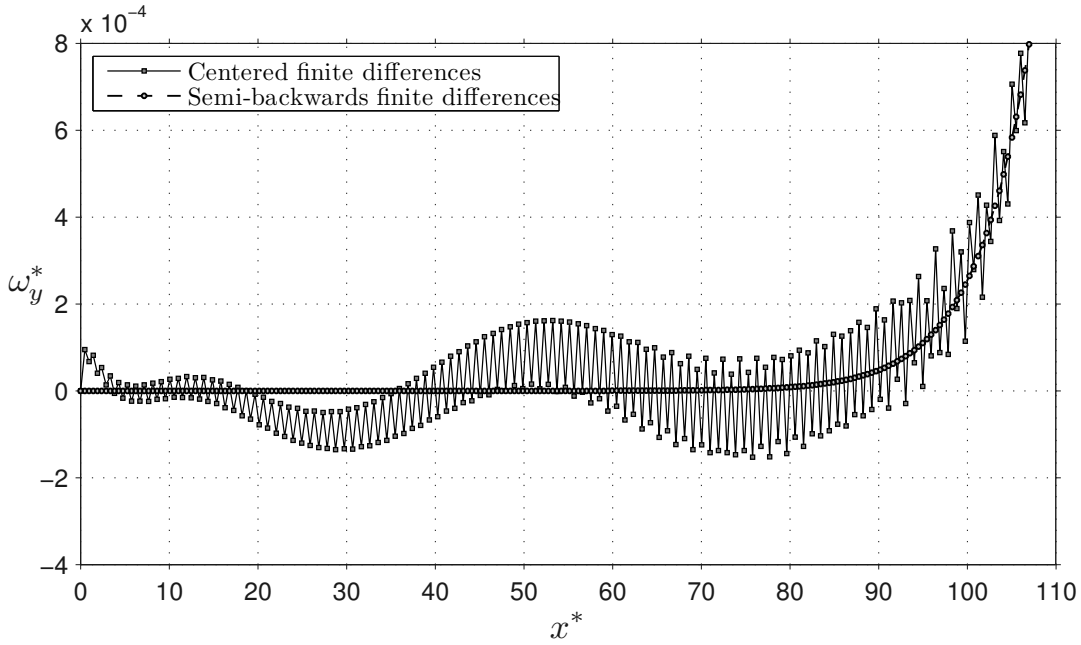

(a) Comparison at $0 < x^* < 110$

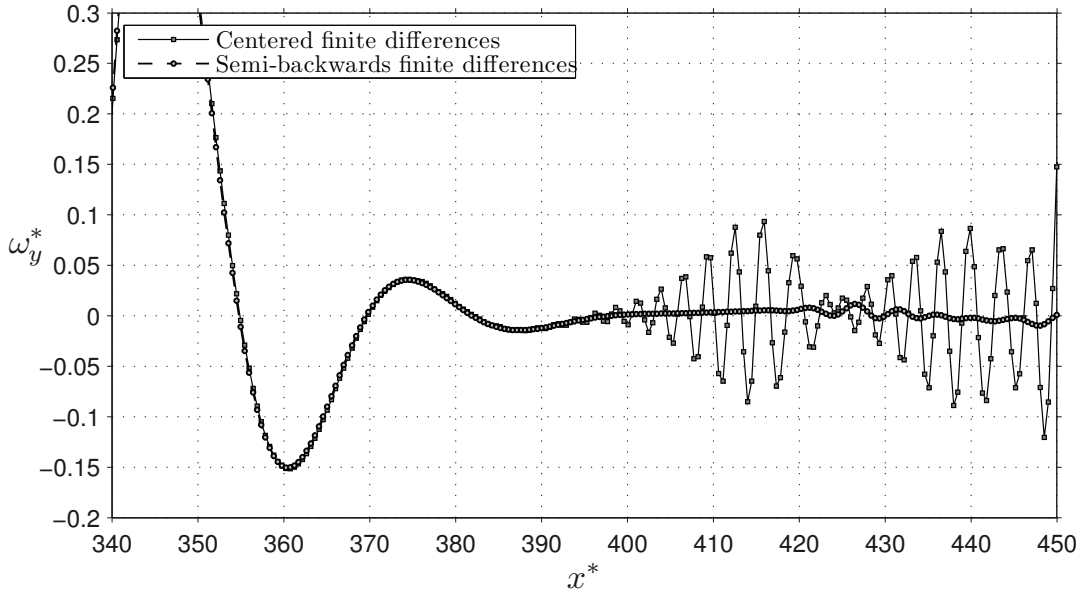

(b) Comparison at $340 < x^* < 450$

Figure 3.1: Comparison of response for a Tollmien-Schlichting (TS) wave numerical experiment using centered and backwards finite differences. TS wave of spanwise vorticity excited at a frequency $\omega^* = 0.03$. (a) Upstream station; (b) Downstream station. Simulation parameters: $Re_{\delta_*} = 10000$, total time simulation $\tau_t^* = 863$, snapshot taken at $t^* = 190$.

to be successful in capturing the complete set of features of the flow without the appearance of spurious numerical results.

It is noteworthy that owing to the interest of this work in exploring several forms of generation of streaks, some of them including prescription of arbitrary initial conditions or forcing fields (as detailed in §4) and

therefore not necessarily related to physically possible distributions, then sharp gradients in the streamwise direction can be generated. To avoid an acute distortion on the streamwise gradients of velocity and vorticity flow fields due to such artificial prescriptions, a slope limiter was implemented. Acting as flux limiters, these functions are sometimes used in high resolution schemes to also avoid the spurious oscillations or wiggles that would otherwise occur with high-order spatial discretization schemes (Rionero and Romano [97]). In any case, for the purposes of this work such discontinuities are mainly due to sharp changes in the prescribed field. Different types of flux limiters exist, but here it is decided to adopt one of the simplest called *minmod limiter*, which is defined as

$$\Xi(\varpi_1, \varpi_2) = \begin{cases} \text{sign}(\varpi_1)\ \min(|\varpi_1|\,|\varpi_2|) & \text{if } \varpi_1\,\varpi_2 > 0 \\ 0 & \text{if } \varpi_1\,\varpi_2 \leq 0 \end{cases} \tag{3.3}$$

In general, the mathematical form of both slope and flux limiters have the effect of limiting the solution gradient near discontinuities. However, the term flux limiter is used when the function operates over system fluxes, and slope limiter is used when it acts on system states, as in this case. Using function Ξ, streamwise gradients of any prescribed field are refined by filtering it as

$$\phi'_i = \Xi(\phi_{i+1} - \phi_i, \phi_i - \phi_{i-1})$$

which is usually done before any derivative approximation.

3.1.2 Wall-normal discretization

In the wall-normal direction, as described in Davies and Carpenter [71], a representation in terms of a series of odd Chebyshev polynomials $T_{2\,k-1}(\zeta)$ is employed for the primary variables. Secondary variables are then represented by even Chebyshev polynomials $T_{2\,k}(\zeta)$. Given that the semi-infinite physical domain $z \in [0, \infty]$ is mapped into variable $\zeta \in (0, 1]$, both primary and secondary variables are defined only on half of the interval of Chebyshev polynomials.

Let us assume linearity for the perturbation fields, and consider only one individual spanwise mode. Denoting any primary field variable as ϕ_A, then its expansion in terms of odd Chebyshev polynomials can be written as,

$$\phi_A\,(x, y, z, t) = \left\{ \sum_{k=1}^{N_z} \hat{\phi}_{A_k}(x, t)\, T_{2k-1}(\zeta) \right\} e^{\mathbf{i}\beta y} \tag{3.4}$$

with $\hat{\phi}_{A_k}$ representing the $k-th$ coefficient of the Chebyshev series, T_k the $k-th$ Chebyshev polynomial

and N_z the total number of polynomials used as the base of expansion; the mapping variable ζ was defined previously in 2.2.3. As in [71], it is assumed that disturbances decay exponentially as $z \to \infty$. By using odd Chebyshev expansions it is guaranteed that the primary variables and all of their even-order derivatives in ζ also vanish as $\zeta \to 0$. Given the integral definitions made for the secondary variables in terms of primary variables, any secondary variable ϕ_B can be expanded in terms of even Chebyshev polynomials as

$$\phi_B\,(x,y,z,t) = c_0\,\hat{\phi}_{B_0} + \left\{\sum_{k=1}^{N_z} \hat{\phi}_{B_k}(x,t)\,T_{2k}(\zeta)\right\} e^{\mathbf{i}\beta y} \tag{3.5}$$

with $\hat{\phi}_{B_0}$ representing the zeroth-order expansion coefficient and c_0 usually taken as $1/2$. This expansion coefficient is adjusted so vanishing conditions are also ensured for secondary variables at $\zeta = 0$, i.e. as $z \to \infty$. With the aid of equations (3.4) and (3.5) along with equations (2.23) to (2.25) it is possible to obtain tridiagonal relations between the Chebyshev coefficients of primary variables and the Chebyshev coefficients of the secondary variables; specifically, for the streamwise and spanwise velocities and for the wall-normal vorticity, these relations are

$$(k-1)\hat{u}_{k-1} + 2k\hat{u}_k + (k+1)\hat{u}_{k+1} = -L_\infty\left(\hat{\omega}_{y,k} - \hat{\omega}_{y,k+1} + \frac{\partial \hat{w}_k}{\partial x} - \frac{\partial \hat{w}_{k+1}}{\partial x}\right) \tag{3.6}$$

$$(k-1)\hat{v}_{k-1} + 2k\hat{v}_k + (k-1)\hat{v}_{k-1} = -L_\infty\left(\hat{\omega}_{x,k} - \hat{\omega}_{x,k+1} - \mathbf{i}\,\beta(\hat{w}_k - \hat{w}_{k+1})\right) \tag{3.7}$$

$$(k-1)\hat{\omega}_{z,k-1} + 2k\hat{\omega}_{z,k} + (k-1)\hat{\omega}_{z,k-1} = -L_\infty\left(\frac{\partial \hat{\omega}_{x,k}}{\partial x} - \frac{\partial \hat{\omega}_{x,k+1}}{\partial x} + \mathbf{i}\,\beta(\hat{\omega}_{y,k} - \hat{\omega}_{y,k+1})\right) \tag{3.8}$$

with L_∞ being the stretching factor defined in §2.2.3. More details on the obtainment of these relations can be found in Davies and Carpenter [71].

Spectral accuracy is reached by choosing a suitable number of expansion functions, in this case the Chebyshev polynomials, to perform the representation of primary or secondary variables. Nevertheless in the implementation followed in this work a set of collocation points is defined, so the number of polynomials is directly dictated by the number of collocation points taken to expand such polynomials. Different types of collocation points exist which determine the accuracy of each particular methodology [98]. In this work, for practicality and to take advantage of specific available FFT routines, the collocation points selected for the mapped variable ζ are defined as

$$\zeta_k = \cos\left[\frac{(k-1)\,\pi}{2\,N_z}\right] \qquad k = 1,\ldots,N_z \tag{3.9}$$

which effectively allow the variable ζ to be defined in the range $(0,1]$. Such definition of collocation points together with proper FFT routines allow transformations between Chebyshev space and physical space to be

performed in a swift and accurate manner.

As remarked in [71], it is more convenient to work with the integral operators of Chebyshev coefficients rather than with its derivatives. As such, the governing equations of the mathematical model are integrated twice with respect to the variable ζ. In doing so all z-derivatives present in the governing equations are replaced by ζ-integral operators, and so facilitating the adoption of an efficient line iterative procedure along the streamwise direction, achieving spectral accuracy without computational penalty.

Specifically, the integrated form of the governing equations may be re-written after some re-arrangement as

$$\mathbf{I}\left[\frac{\partial \omega_x}{\partial t}\right] = \mathbf{I}\left[-U\,\frac{\partial \omega_x}{\partial x} + \frac{1}{Re_{\delta_*}}\left(\frac{\partial^2 \omega_x}{\partial x^2} - \beta^2\,\omega_x\right) + U'\left(\frac{\partial \omega_x}{\partial x} - \mathbf{i}\beta\frac{\partial w}{\partial x}\right)\right] + \mathbf{K}\left[\frac{\omega_x}{Re_{\delta_*}}\right] \tag{3.10}$$

$$\mathbf{I}\left[\frac{\partial \omega_y}{\partial t}\right] = \mathbf{I}\left[-U''\,w - U\,\frac{\partial \omega_y}{\partial x} + \frac{1}{Re_{\delta_*}}\left(\frac{\partial^2 \omega_y}{\partial x^2} - \beta^2\,\omega_y\right) + U'\left(\mathbf{i}\beta\omega_x + \beta^2 w\right)\right] + \mathbf{K}\left[\frac{\omega_y}{Re_{\delta_*}}\right] \tag{3.11}$$

$$\mathbf{I}\left[\frac{\partial^2 w}{\partial x^2} - \beta^2\,w\right] + \mathbf{K}\left[w\right] = \mathbf{I}\left[\mathbf{i}\beta\omega_x - \frac{\partial \omega_y}{\partial x}\right] \tag{3.12}$$

with the integral operators $\mathbf{I}$, $\mathbf{J}$ and, $\mathbf{K}$ defined as

$$\mathbf{I}\left[\phi(\zeta)\right] = \int^{\zeta}\int^{\zeta'} \phi(\zeta'')d\zeta' d\zeta'' \tag{3.13}$$

$$\mathbf{J}\left[\phi(\zeta)\right] = \frac{1}{L_\infty}\left(\int^{\zeta} \zeta'^2\phi(\zeta')d\zeta' - 2\int^{\zeta}\int^{\zeta'} \zeta''\phi(\zeta'')d\zeta' d\zeta''\right) \tag{3.14}$$

$$\mathbf{K}\left[\phi(\zeta)\right] = \frac{1}{L_\infty^2}\left(\zeta^4\phi(\zeta) - 6\int^{\zeta} \zeta'^3\phi(\zeta')d\zeta' + 6\int^{\zeta}\int^{\zeta'} \zeta''^2\phi(\zeta'')d\zeta' d\zeta''\right) \tag{3.15}$$

Integral operators $\mathbf{I}$, $\mathbf{J}$, and $\mathbf{K}$, when applied to adequate expansions in terms of odd or even Chebyshev polynomials give place to banded matrices. Specifically, operator $\mathbf{I}$ can be represented by a tri-diagonal matrix, operator $\mathbf{K}$ by a pentadiagonal matrix, and operator $\mathbf{J}$ by a matrix of bandwidth four. This operator $\mathbf{J}$ is only required when using the full non-linear formulation, and therefore is absent from the equations shown above. As mentioned before, such structure of the integral operators facilitates the use of efficient line matrix solvers. However, in order to incorporate the integral boundary conditions discussed above, these operators must be slightly modified, "breaking" the original banded structure. In particular, the first row of every operator is filled with the proper coefficients relating to the boundary condition to be applied. Thus, in order to solve such systems efficiently, a modified version of the efficient Thomas algorithm has been adopted. A careful and detailed exposition of the modified Thomas algorithm for the tridiagonal case, as used in this implementation, is available in [82].

3.1.3 Spanwise discretization

Flow field perturbations have been assumed to be periodic in the spanwise direction and thus can be adequately represented by Fourier expansions. This representation is exploited in the formulation of the mathematical model itself, and no further discretization would actually be required apart from the prescription of a particular spanwise mode β to be defined for every linear simulation carried out. In fact, the spanwise modes can be decoupled and calculated separately. This allows a highly-efficient parallelisation scheme to be implemented relatively simply for a full 3D flow field. Actually, once a Fourier expansion is defined over a finite set of spanwise modes, advantage of highly efficient FFT algorithms can be exploited in order to perform full three-dimensional reconstruction. In such a case, the accuracy of the method in the spanwise direction is spectral. For example, as originally suggested in [37], non-interactive control calculations could be performed for groups of modes which could be ascribed to individual processors and run completely independently of each other.

Following these ideas a computational parallelisation was implemented employing Message-Passing protocols aiming to speed-up simultaneous multiple spanwise modes simulations. In particular, this sort of parallel methodology was employed for two different situations: (*i*) Parametric optimisation of forcing and initial perturbation fields of the Linearised Navier-Stokes Equations (LNSE) and (*ii*) Three-dimensional simulations of boundary layer response to selected control cases. It is important to highlight that, strictly speaking, a full computational parallelisation is not a required or essential element in the linearized mathematical model adopted here, considering that every single spanwise mode can run independently on separate processors. However, such a parallel implementation makes it easier to manage and control the numerical information coming from all the different modes. However, although it was not explored in the present work, if a non-linear extension was desired for the present model, a real parallel computational implementation would be an efficient way to perform single-mode calculations, and using the parallel protocol to perform the non-linear part in those terms involving products of spanwise-modes.

MPI Parallelisation

Message-passing interface (MPI) is currently one of the most powerful and widely accepted parallelisation techniques (though at the time of writing, GPU-based[1] ones are a strong competitor). Since its inception, MPI protocol has been aimed at exploiting modern computational architectures. In past few years MPI has become a standard definition for message-passing libraries. For these reasons MPI has been adopted here to implement the parallelisation. Even more importantly, such protocol has been chosen because it aims to provide independence for each processor involved in a given computational task, a feature that is fully

[1] GPU: a *Graphics Processing Unit*.

compatible with the proposed methodology. A wide variety of texts and on-line resources are available to help any programmer to incorporate this protocol in his/her code. However, for more details than those provided here and for specific terminology, the reader is referred to Pacheco [99].

For this work, libraries based on Open MPI-2 were used as the MPI protocol. A single communicator, or group of cores, with no special topology has been employed. The number of processors required is read from an input file and therefore is set interactively at each simulation. For most of the cases studied the number of cores equals the number of spanwise modes to be simulated.

As in any MPI standard procedure, initially a master core performs the majority of I/O tasks on the disk, such as reading the simulation parameters from the same file. Although in some cases every processor stores its own data in a separate folder, at the very end of each simulation the master core saves in an output file information from a number of diagnostic checks. Equally, at the end of every simulation, every single core passes information specifically related to flow field variables to the master core to be saved. Any special post processing of data, like estimation of integrals in time or normalisation against maximum in time is performed for every individual processor. A short list of the MPI subroutines more intensively used, with a brief description of its use in the current implementation, is given directly below:

MPI_Bcast:	Used to transmit information from the master core to the rest members of the communicator.
MPI_Barrier:	Called for synchronisation between different cores.
MPI_Gather:	Required for the master core as a reduction task to gather data from the other cores at the end of the simulation.
MPI_Get_Address:	Employed to acquire memory allocation information to construct derived data types.
MPI_Type_Create_Struct:	This subroutine enables to create derived data types to efficiently transmit information between cores.
MPI_Type_Commit:	Final instruction to generate an identification code within the communicator for a particular data type.

In the present coding every processor can perform either a single-mode simulation or multiple-modes simulation depending upon the ratio of the spanwise-modes-required to cores available. Thanks to the inherent simplicity brought by linearization, along with the modal decomposition, it was possible to have a fully parallelised version of the serialised code with relative ease and a reduced set of MPI instructions. This feature was exploited with a minimal penalty on computational cost.

3.2 Time marching method

A semi-implicit predictor-corrector time-integration method was adopted. In particular, the well known Adams-Bashforth/Crank-Nicholson method was implemented. This procedure, also known as an IMEX scheme (Implicit/Explicit), has been comprehensively studied and its accuracy and stability conditions characterised [100, 101]. It has also been proven to be accurate and reliable enough to perform simulations of linearized fluid equations [38, 71]. Since the model here consists of two transport equations for vorticity and a diffusion equation for wall-normal velocity, time marching is strongly influenced by the structure of the vorticity transport equations. A brief discussion on the time marching method is presented below.

Let us assume a generic form of the transport equations (2.95) or (2.98) to be expressed for a vorticity primary variable ϕ as

$$\frac{\partial \phi}{\partial t} = F\left(\phi, \{\theta, w\}, x, y, z, t\right) \tag{3.16}$$

with θ being the complementary vorticity variable and function F consisting of both convective and diffusive terms. Then the time marching starts first with a projection obtained by a three-level Adams-Bashforth predictor as

$$\frac{\phi^*}{\Delta t} - G(\phi^*) = \frac{\phi^n}{\Delta t} + \frac{3}{2}\underset{\sim}{F}^n - \frac{1}{2}\underset{\sim}{F}^{n-1} \tag{3.17}$$

with superscripts n and $n-1$ indicating current and past time levels in the time integration, ϕ^* the projection into next time step and functions G and $\underset{\sim}{F}$ the diffusive and convective terms in F, respectively. It is noteworthy that not all diffusive terms are included in function G, but are left as part of $\underset{\sim}{F}$. Terms including streamwise derivatives are left in $\underset{\sim}{F}$ so they can be computed efficiently by high order schemes. This time step advancing is not complete until a correction over previous projection is made. Following previous notation, the corrector can be expressed as

$$\frac{\phi^{n+1}}{\Delta t} - G(\phi^{n+1}) = \frac{\phi^n}{\Delta t} + \frac{1}{2}\underset{\sim}{F}^* + \frac{1}{2}\underset{\sim}{F}^n \tag{3.18}$$

which completes a time advancement into the next time level $n+1$. In this way all the convective terms of $(\mathbf{M})$ in the transport equations (2.95) and (2.98) are computed explicitly using two previous time levels. Remaining terms are calculated implicitly in time. Though there is no explicit time derivative for the wall-normal velocity, thanks to the coupling provided by eq.(2.99), an estimation for such velocity field can be obtained from any currently available information on the vorticity field. Specifically, after a prediction is obtained for ω_x and ω_y, wall-normal and spanwise components of the Poisson equation for w are solved implicitly, whereas the streamwise component is treated explicitly.

It is necessary to make a final remark concerning the time marching method. Instead of explicit prescription of boundary conditions on the vorticity at the wall at each time step, the integral conditions discussed in §2.2.3, given by the equations (2.37) and (2.38), have been employed to prescribe boundary conditions at the wall at each time step. By using information from two previous time levels, and in accordance with the predictor-corrector scheme, it is possible to estimate adequate integral boundary conditions for the vorticity fields at every new time step. In the predictor step the time advancement of the integral conditions can be generalized, for any primary vorticity variable ϕ, as

$$\int \frac{\phi^{n+1} + \phi^{n}}{2} d\zeta = \int \mathcal{L}\left(\frac{3w^{n} - w^{n-1}}{2}\right) d\zeta \tag{3.19}$$

whereas in the corrector phase such advancement can be formulated as

$$\int \phi^{n+1} d\zeta = \int \mathcal{L}\left(w^{n+1}\right) d\zeta \tag{3.20}$$

with w^{n+1} representing the wall-normal perturbation velocity obtained by solving the appropriate Poisson equation (see §2.2.1). Using the corrector stage formulation into the predictor stage, after some rearrangement, the integral boundary condition for vorticity fields can be expressed as,

$$\int \phi^{n+1} d\zeta = \int (2\phi^{n} - \phi^{n-1}) d\zeta \tag{3.21}$$

or in discrete form as

$$f_i^{n+1} = 2\, f_i^{n} - f_i^{n-1}$$

with f being the integral function evaluated at the wall Γ_3 in figure 2.2 and i representing an arbitrary discrete streamwise location. An overall description of the complete algorithm is presented below.

3.3 General description of model solver

As discussed in §2.4, the original formulation of equations (2.94) and (2.97) can be restated using only primary variables. In this form, without reference to secondary variables, the whole system can be solved and advanced in time. In fact, as it is indicated by the reduced vorticity transport equations (RVTEs) (2.95) and (2.98), the representation in terms of Chebyshev coefficients of the secondary variables can be exchanged for integral relations using only coefficients of the primary variables. In the coding, such a transformation is done via application of an FFT routine on collocation values of the primary variables.

It is clear, then, that storage memory does not need to be allocated to the secondary variables at any point in the simulation. However, if required for purposes of post analysis, an explicit calculation of secondary variables can be done at regular intervals and stored on disk. This option is fully controlled by arguments in the input file.

It has been shown that products between primary variables (or their wall-normal integrals) and the mean-flow profile are required in the RVTEs as part of the evaluation of the convective function $\underset{\sim}{F}$. These multiplications are performed in physical space[2] and then transformed back to collocation values (in Chebyshev space) which are then used in the pseudo spectral evaluation of function $\underset{\sim}{F}$.

The general algorithm employed to solve the mathematical model can be outlined now. Initially, a prediction of spanwise and streamwise vorticity is obtained using the predictor given by (3.17). After an estimation is obtained for the vorticity fields the equation (2.99) is solved to provide an updated wall-normal velocity field. Such estimation of velocity field is achieved in between the predictor and corrector stage by solving the Poisson equation iteratively until some level of convergence is reached. This procedure usually takes a few iterations to provide a converged solution per time step, though for the first time steps the number of iterations can be slightly higher than in the rest of the simulation. In this implementation the terms of the Poisson equation are all solved implicitly using values of vorticity acquired from the predictor stage to estimate the velocity field at the next time level. Nevertheless, given that the streamwise term w_{xx} (the second derivative in streamwise direction of the wall-normal velocity) has been left in the right-hand-side of the equation (2.99), then this term is obtained iteratively and therefore its convergence dictates the speed of global convergence for estimation of the wall-normal velocity. With a converged velocity field the vorticity fields are then corrected using the information available from the updated velocity field and the values of vorticity from the past time step. This stage features the corrector given by (3.18). With this last computation the time loop is now complete and it is possible to advance to the next time step. A simplified flow chart with the main elements of the algorithm is presented in fig. 3.2.

3.4 Mean velocity profiles: numerical details

The mean base velocity profile defines the whole model and its selection brings about a distinctive response of the boundary layer to small perturbations. In this way it can be considered as one of the main elements of the whole linear operator defined by F in equation (3.16), and its prescription is then as important as any other element in the model. Specifically, a laminar velocity profile is employed for different validation

[2]Actually it is more appropriate to say Fourier space since if actual physical representation is desired, an additional conversion must be done, even for a single spanwise mode.

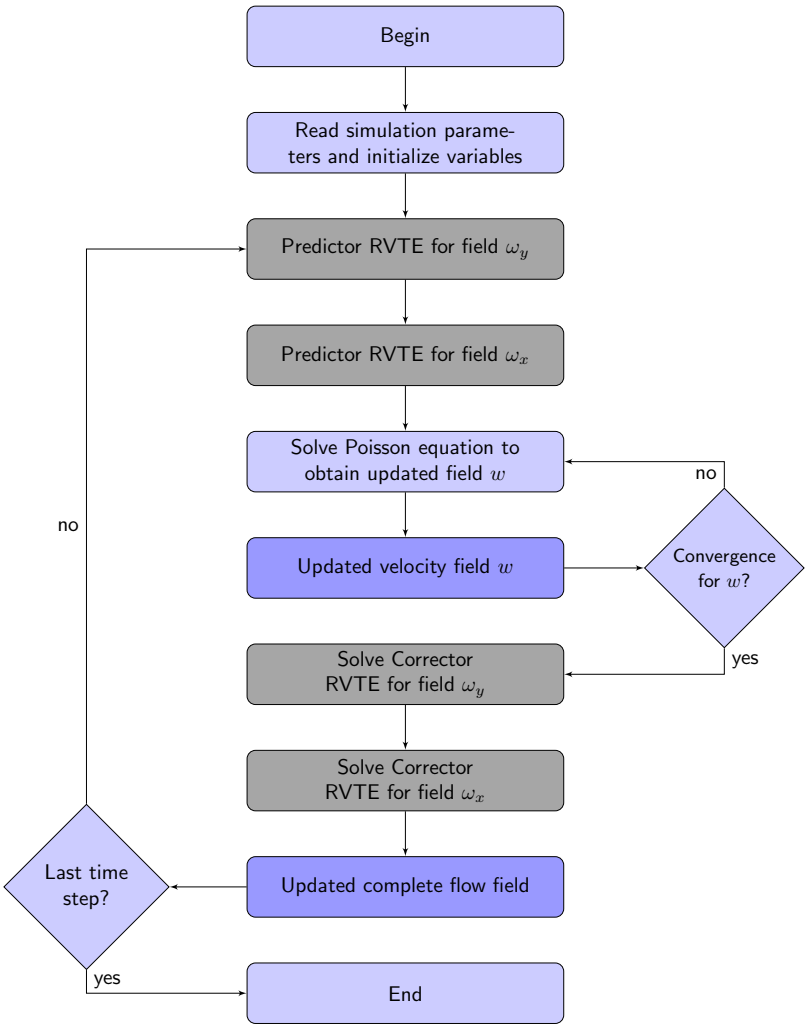

Figure 3.2: Schematic flow diagram with the main elements of solution algorithm for the Linearised Navier Stokes Equations.

tests of the code; a turbulent velocity profile is used for the numerical experiments that are the target of the present study. This section provides a few additional details to those discussed in §2.3 regarding the numerical methodologies followed for generating the mean base profiles.

3.4.1 Laminar profile

The current model for the laminar boundary layer is the Falkner-Skan equation obtained and presented in §2.3.2, which is reproduced here

$$\frac{\mathrm{d}^3 f}{\mathrm{d}\eta^3} + f\,\frac{d^2 f}{d\,\eta^2} + \beta_{fs}\left[1 - \left(\frac{d\,f}{d\,\eta}\right)^2\right] = 0, \tag{3.22}$$

This equation is a common benchmark case for methods of solution of non-linear ordinary differential equations. In this work two different approaches were undertaken. Initially, a high-order compact finite-difference scheme along with a non-linear optimization procedure, as detailed in appendix B, was implemented as a method of solution providing laminar profiles for a wide range of pressure gradient parameters γ (see §2.3.2). Nevertheless, a more standard method of solution also implemented in this thesis is briefly discussed here. Given that the validation tests chosen in this study deal only with zero pressure gradient cases, a profile obtained using a simplified version of equation (3.22) with $\beta_{fs} = 0$ is used in this section. As it has already been mentioned, such a profile is simply the Blasius profile.

The original ODE (3.22) is transformed into a system of three first order differential equations, using values of derivatives at the wall as boundary values for the new BVP. After the system is solved for a prescribed value of the second derivative f'' at $\eta = 0$, which is unknown and initially chosen arbitrarily[3], the values of the first derivative are checked at $\eta \to \infty$. If the derivative is $f' = 1$ then a correct solution has been obtained, otherwise the procedure is repeated, changing iteratively the value for $f''(\eta = 0)$ and verifying reduction on some error measure ϵ. Measure of convergence ϵ dictates if a solution has been reached or if additional iterations are required.

This method provides nodal values for the mean base profile U^B, as well as for its first and second derivatives U' and U'', which incidentally are also required in the current model. Finally, in order to make such a profile fully compatible with the code developed in this thesis, an interpolation must be carried out to generate the profile values at the collocation points given by (3.9). Figure 3.3 shows the velocity profile, and its first two derivatives, obtained with the methodology hereby discussed. Values in figure 3.3 have been normalized in outer units (for instance, velocity has been expressed as $U^* = U/U_\infty$). Coefficients κ_1, κ_2 and κ_3 appearing in this figure define a scaling due to transformation between the normalised function f and normalised profiles. These coefficients are defined as

$$\kappa_1 = \eta_\infty \qquad \kappa_2 = \eta_\infty^2 \sqrt{\frac{2}{\gamma+1}} \qquad \kappa_3 = \frac{2\,\eta_\infty^3}{\gamma+1}$$

3.4.2 Turbulent profile

As discussed before, the solution of the turbulent mean flow based on the asymptotic matching of the inner and outer layers yields the logarithmic mean velocity profile. In the case presented here the two layers are

[3] This problem has been so extensively studied that this value of the second derivative is well known and can be used as a criteria to gauge the success of any alternative methodology.

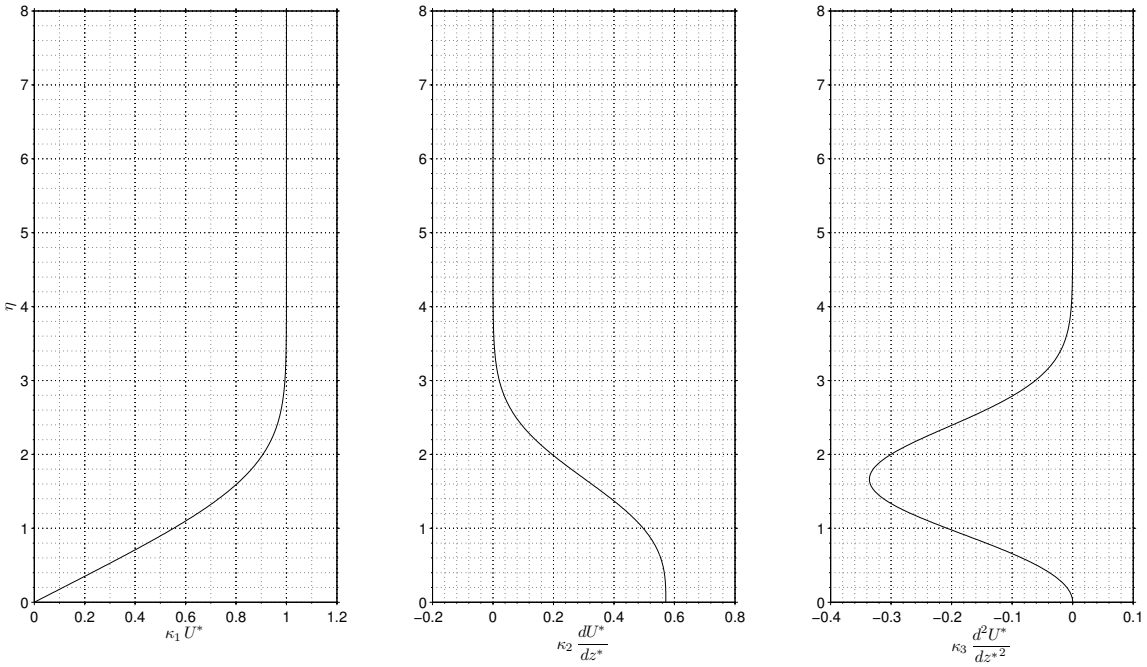

Figure 3.3: Laminar velocity profile obtained from the Falkner-Skan equation for $\beta_{fs} = 0$. Variables normalised using outer units: $U^* = U/U_\infty$, $z^* = z/\delta_*$

Canonical wall bounded flow	**Asymptotic value proposed by [92]**		
	Π	κ	B
ZPG TBL	0.480	0.384	4.13
Channel	0.055	0.370	3.70
Pipe	0.220	0.410	5.00

Table 3.1: Adopted values for the log-law parameters.

characterised by equations (2.76) and (2.77) which are reproduced again below

$$\frac{d\,u^+_{inner}}{d\,z^+} = \frac{\frac{1}{s} + \frac{z^{+2}}{\kappa} - \frac{z^+}{s\,Re_\tau}}{\frac{1}{s} + \frac{z^{+2}}{\kappa} + z^{+3}} \tag{3.23}$$

$$u^+_{outer} = \frac{1}{\kappa}\ln z^+ + B + \frac{\Pi}{\kappa}\left[6\left(\frac{z^+}{\delta^+}\right)^2 - 4\left(\frac{z^+}{\delta^+}\right)^3\right] + \frac{1}{\kappa}\left(\frac{z^+}{\delta^+}\right)^2\left(1 - \frac{z^+}{\delta^+}\right) \tag{3.24}$$

In a trade-off between simplicity and pertinence in the present work the asymptotic high Reynolds number values proposed in Nagib and Chauhan [92] are adopted for all the numerical experiments, including those proposed for the log-law parameters. These values are presented in table 3.1.

A similar methodology is followed to that proposed in [92] to generate a composite profile that covers the two-layer regions. It is noteworthy that the methodology for generating a turbulent velocity profile is valid

for the three canonical flows, although strictly speaking in this formulation only ZPG TBL profiles are fully compatible.

By incorporating the values in table 3.1 this methodology for the generation of a turbulent profile can be described as follows. Once a type of canonical flow and a Reynolds number Re_{δ_*} are prescribed, values for boundary layer thickness in inner units δ^+ are defined using equation (2.86),

$$\delta^+ = \frac{12\, Re_{\delta_*}\kappa}{12(\Pi+1)-1}$$

for ZPG TBL; or using the most common expression

$$\delta^+ = \frac{Re_{\delta_*}\kappa}{(\Pi+1)}$$

for Channel or Pipe flow. Using δ^+ and selected parameters κ and B in accordance with the type of flow, a specification of the asymptotic external velocity is obtained using equation (2.70) as,

$$U^+_{i,\infty} = \frac{1}{\kappa}\ln\delta^+ + B$$

This value of $U^+_{i,\infty}$ is used as an asymptotic limit for the inner profile given by (3.23). It is assumed that $Re_\tau = \delta^+$ when used in equation (3.23). Parameter s is chosen from an initial seed guess, which allows the solution of the ODE by standard methods, in this case by using a 4^{th} order Runge-Kutta integration scheme. After solution of the ODE for u^+_{inner} an error is estimated against an expected value of $U^+_{i,\infty}$ as,

$$E_1 = U^+_{i,\infty} - u^+_{inner}(\delta^+) \tag{3.25}$$

and then a decision about accuracy of the profile is made. If $|E_1|$ is less than a predefined ϵ, a correct inner profile is found. If this condition is not met, the value of s is iteratively changed using a secant method, until criteria $|E_1| < \epsilon$ is achieved. With an inner profile u^+_{inner} a composite profile is obtained as

$$U^+(z^+) = u^+_{inner}(z^+) + \frac{2\,\Pi}{\kappa}\left[3\left(\frac{z^+}{\delta^+}\right)^2 - 2\left(\frac{z^+}{\delta^+}\right)^3\right] + \frac{1}{\kappa}\left(\frac{z^+}{\delta^+}\right)^2\left(1-\frac{z^+}{\delta^+}\right) \tag{3.26}$$

thus giving

$$U^+_\infty = U^+(\delta^+) = u^+_{inner}(\delta^+) + \frac{2\,\Pi}{\kappa} \approx U^+_{i,\infty} + \frac{2\,\Pi}{\kappa} \tag{3.27}$$

Once a profile has been obtained, it is possible to get a verification of the accuracy of δ^+_* by numerical

integration, and so to confirm that it complies with the relation given by

$$Re_{\delta_*} = \delta_*^+ U_\infty^+$$

Note that the profile obtained with this procedure is normalised in inner units. For this reason, a final step is to convert the profile into outer units and generate interpolated values at the correct wall-normal collocation points. A profile for a ZPG TBL at $Re_{\delta_*} = 10000$ obtained using this methodology is shown in figures 3.4 and 3.5.

A final remark about the suitability of profiles other than the ZPG TBL (i.e. Channel and Pipe flows), is necessary at this point. The mathematical formulation adopted in this thesis is for semi-infinite domains and therefore it is strictly valid for boundary layers only. However, for some numerical experiments (in channel flows) the assumption is made that the flow disturbances are concentrated in the inner region and thus are not significantly affected by the outer form of the artificially large domain. In these cases the mean base profiles are used with some caution and it has been ensured that structures effectively remain in the inner region. In any case every profile has been provided with a phantom buffer (an additional portion of domain in wall-normal direction) that ensures a semi-infinite profile, at least from the inner region point of view. With the use of profiles for Channel or Pipe flow the aim is to study responses to small perturbations of other types of inner regions, that are different to each other. However, no claim is made that this method bears advantage over truly Channel or Pipe flow codes.

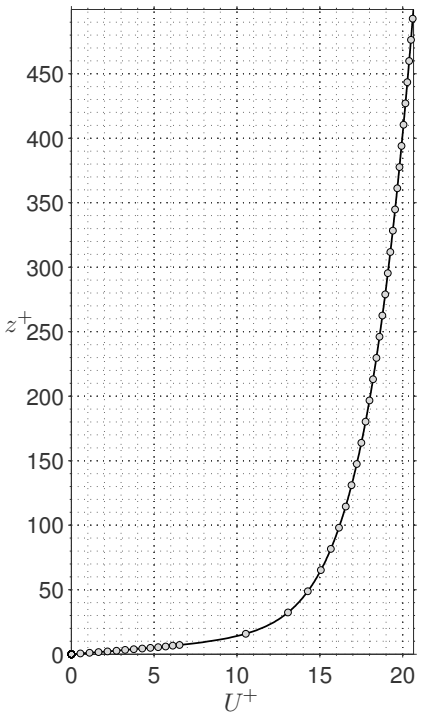

Figure 3.4: Inner and log-law regions of a turbulent velocity profile for ZPG TBL at $Re_{\delta_*} = 10000$

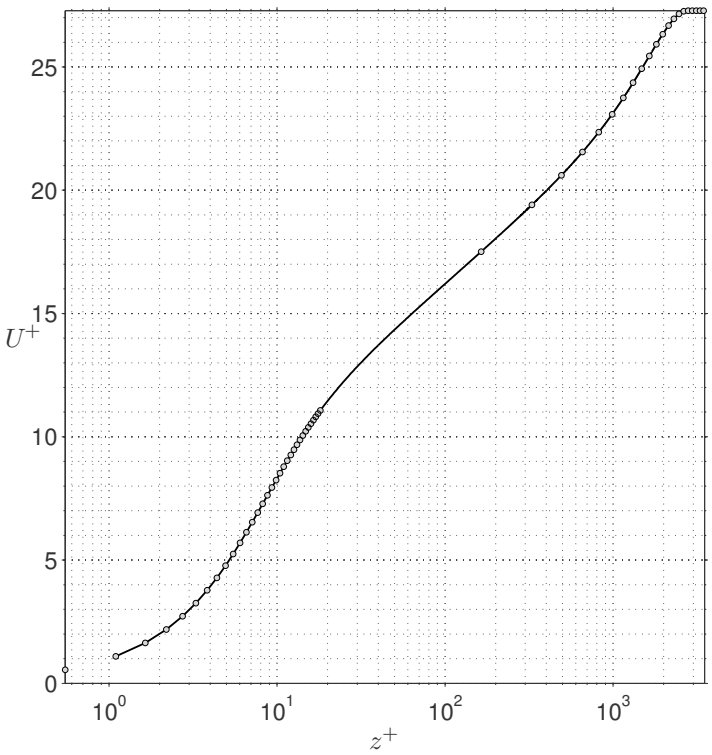

Figure 3.5: Composite turbulent velocity profile for a ZPG TBL at $Re_{\delta_*} = 10000$

3.5 Code Validation

Two cases from linear stability approach have been adopted for the validation tests: (i) generation and development of Tollmien-Schlichting waves and (ii) optimal perturbation of LNSEs. Such cases have been widely studied ([30, 63, 83, 86, 102]) and offer a set of results which are now part of mainstream LST. In the case of Tollmien-Schlichting waves a precise numerical comparison is obtained. For the optimal perturbation, quantitative and qualitative verifications are obtained. Results of these validation tests confirm the integrity of the numerical code and its ability to capture the phenomena associated with the boundary layer's response to small perturbations.

3.5.1 Tollmien-Schlichting waves: generation and development

One of the main results of primary stability theory is an analytical model to describe growing waves in a transitional boundary layer; the so-called Tollmien-Schlichting (TS) waves. Here, this analytical solution serve as a validation case to test the ability of the code to capture the response of laminar boundary layers to harmonic perturbations. Even more importantly, since a large number of results have been published for this phenomena for different flow conditions, the verification can also be done by comparison with published numerical results at different flow regimes.

Analytical model: Orr-Sommerfeld equation

A widely known analytical model that arises from LST is the Orr-Sommerfeld equation (see Schmid and Henningson [102]). To obtain such an equation a wavelike or modal solution of the form

$$w(x,y,z,t) = \tilde{w}(z)\, e^{\mathbf{i}(\alpha x+\beta y-\omega t)} \tag{3.28}$$

is introduced in the disturbance equation for the wall-normal velocity given as

$$\left[\left(\frac{\partial}{\partial t}+U^B\frac{\partial}{\partial x}\right)\nabla - U''\frac{\partial}{\partial x} - \frac{\nabla^4}{Re_\mu}\right] w = 0, \tag{3.29}$$

where Re_μ depends on the specific non-dimensionalisation, for instance $\mu = \delta_*$. This last expression can be obtained from the governing equations for infinitesimal disturbances in parallel flows by eliminating the pressure from the wall-normal component [102]. After this procedure the classical Orr-Sommerfeld equation

is obtained,

$$\left[(-\mathbf{i}\,\omega + \mathbf{i}\,\alpha U^B)(D^2 - \alpha^2 - \beta^2) - \mathbf{i}\,\alpha\,U'' - \frac{(D^2 - \alpha^2 - \beta^2)^2}{Re_\mu}\right]\tilde{w} = 0, \tag{3.30}$$

where D is a differential operator indicating differentiation with respect to z, α and β are the streamwise and spanwise wavenumbers, respectively; and ω is the temporal frequency. If a proper set of boundary conditions is coupled with equation (3.30), then a solution for this equation defines an eigenvalue problem.

There is no particular restriction on the values of α or ω, although as discussed in Schmid and Henningson [102], by prescribing and assuming α to be real, the eigenvalue problem is defined in terms of ω which is equivalent to studying the temporal evolution of a localised disturbance. Depending on the value of $\mathrm{Im}\{\omega\}$ such perturbation will grow if $\mathrm{Im}\{\omega\} < 0$ or decay if $\mathrm{Im}\{\omega\} > 0$. Though this analysis is valid, it is not as amenable as it would first appear in principle and it does not fully reflect the more frequently observed behaviour of disturbances in which spatially growing perturbations predominate over temporal growing perturbations, particularly at transition regimes. This has been studied and discussed by Watson [103], Gaster [104] for wall bounded flows, and by Michalke [105], Walker et al. [106] for free shear layers.

An alternative approach is to prescribe ω as real valued and seek for the most unstable mode in terms of α. In this way a flow state is prescribed by stipulating values of Re_μ, ω and β which brings about an eigenvalue problem in terms of a complex wavenumber α given by

$$\alpha = \alpha_r + \mathbf{i}\,\alpha_i \tag{3.31}$$

with real part α_r and imaginary part α_i. In any case, as briefly mentioned before, this procedure is closer to the observed development of physical perturbations [103–106]. Additionally, a more subtle advantage is gained by prescribing a perturbation with a given temporal frequency: it allows the analysis of the spatial wavenumber α to be performed at different time instants, by examining snapshots of the perturbation development within the domain. It is important to note that this decision increases the difficulty on solving the Orr-Sommerfeld equation. Nevertheless, since this method is so often followed and the amount of data available for this approach is relatively abundant, then it compensates for any difficulty by providing additional sources for results verification.

In this case, in order to perform validations against spatial Orr-Sommerfeld eigenvalues, both a flow condition and an excitation are prescribed. For a given Reynolds number Re_μ, spanwise wavenumber β and temporal frequency of a source of excitation ω, the form of a disturbance propagating from the oscillatory point source, i.e. the Tollmien-Schlichting wave, can be determined via solution of the Orr-Sommerfeld equations. In fact it can be distinguished between two-dimensional and three-dimensional TS waves by observing that if $\beta = 0$

in both the current model and equation (3.30), then both models automatically describe a two-dimensional TS wave. For the validation tests presented here the underlying base flow over which TS waves develop is the laminar boundary layer represented by the Falkner-Skan profile discussed in §2.3.2 and §3.4.1. In the present work, for those cases where numerical solutions to the Orr-Sommerfeld equation were required, the methodology proposed by Bridges and Morris [107] is followed. In this case the equation (3.30) is rewritten as a polynomial in α with matrix coefficients,

$$\mathbf{P}_4(\alpha) = \mathbf{C_4}\,\alpha^4 + \mathbf{C_3}\,\alpha^3 + \mathbf{C_2}\,\alpha^2 + \mathbf{C_1}\,\alpha + \mathbf{C_0} \tag{3.32}$$

and the eigenvalues are found using the 'companion matrix' method. For more details the reader is referred to Bridges and Morris [107] and Danabasoglu and Biringen [108].

Spatial wavenumbers extraction

Once a simulation has been performed with the present model, it is relatively straightforward to extract the real part α_r of the streamwise wavenumber. When a train of waves for any primary variable ϕ is formed and sufficiently separated from the excitation source, the distance between two consecutive maxima or two consecutive zeros is half the wavelength of the TS wave. From such observation, a relation to estimate α_r can be formulated as,

$$\alpha_r = \frac{\pi}{x_{e,i+1} - x_{e,i}} \tag{3.33}$$

where $x_{e,i}$ is the location of an extrema (or zero), and $x_{e,i+1}$ is the next extrema (or zero). Alternatively, a fast Fourier transform (FFT) can be performed over the data at regular periods of time, and then an asymptotic wavenumber obtained by examining the spectra at different time instants. This last method is much faster that previous one, although it can be relatively less accurate as it depends strongly on a large domain and a copious number of points in the streamwise direction. This is further explained in 3.5.2.

Obtaining the imaginary part α_i is more difficult. To find this value, it is possible to derive an expression correlating α_i and α_r as

$$\alpha_i^2 + \frac{2}{\phi}\frac{\partial \phi}{\partial x}\,\alpha_i + \left(\frac{1}{\phi}\frac{\partial^2 \phi}{\partial x^2} + \alpha_r^2\right) = 0 \tag{3.34}$$

which is a quadratic equation in α_i. By finding the roots of this polynomial, a value for α_i can be estimated.

Prescribing the oscillatory excitation source

Numerical experiments on the generation of TS waves were conducted using as a perturbation source a smooth, relatively local and oscillatory analytical function. This source was implemented as a wall-normal velocity boundary condition in the Poisson equation. Such a distribution, giving enough smoothness in the streamwise direction, producing both positive and negative values of wall-normal excitation at the same time and providing a zero net mass flux, is expressed as,

$$w(x,t) = \left(\frac{x-x_0}{l_0}\right)\left[1-e^{-\left(\frac{\omega\,t}{2}\right)^2}\right] e^{-\left(\frac{x-x_0}{l_0}\right)^2} \sin(\omega\,t) \tag{3.35}$$

where x is a streamwise location, x_0 the position of the centre of the distribution and l_0 a measure of the function extension. In this expression all quantities are non-dimensionalised using outer units.

3.5.2 Tollmien-Schlichting waves: numerical results

All numerical simulations on TS waves were conducted using a single spanwise Fourier mode. In the two-dimensional case the validation is made by comparison of the present code against the solution of the Orr-Sommerfeld equation and published data, whereas in the three-dimensional case only comparison against published data is performed. As explained earlier, in cases of three-dimensional TS waves, the values of β, ω and Re_{δ_*} were prescribed, whereas in the two-dimensional case only Re_{δ_*} and ω are required. In the numerical experiments on two-dimensional TS waves $\beta = 0$.

Numerical tests on two-dimensional waves were performed on laminar boundary layers at $Re_{\delta_*} = 1000$ and $Re_{\delta_*} = 3000$, with computational domains of length $L_x^* = 2360$. A grid of 5900×128 points was used in every case to resolve the domain, providing an effective grid resolution of $\Delta x^* = 0.4$ in the streamwise direction and 128 Chebyshev modes in the wall-normal direction. For these two-dimensional cases the source was located at $x_0^* = 140$. Figure 3.6 shows two different time instants of the train of two-dimensional TS waves obtained with the current model.

For the three-dimensional TS wave tests, the laminar boundary layers had Reynolds numbers of $Re_{\delta_*} = 1\times10^4$ and $Re_{\delta_*} = 1\times10^5$, with a computational domain covering $L_x^* = 2000$, in the streamwise direction. Grids of 4000×128 points were employed for these simulations, providing a resolution of $\Delta x^* = 0.5$ in the streamwise direction and 128 Chebyshev modes in the wall-normal direction. For these cases the source was located at $x_0^* = 100$. In all the numerical simulations, both for two- and three-dimensional TS waves, the computational domain extended at least 10 expected wavelengths of the TS wave (based on the real part of the wavenumber,

α_r). Figure 3.7 shows the spatial evolution in two time occurrences of a three-dimensional TS wave of spanwise vorticity at the wall $\omega_y(z = 0)$.

It can be seen that in both plots the excitation source produced a Tollmien-Schlichting wave train which emerged downstream from the source location ($x_0^* = 140$ and $x^* = 100$, for 2D and 3D TS waves, respectively). Equally, it is possible to appreciate a growth in the intensity or amplitude of the train of waves as they develop in time. This behaviour is in agreement with the expected response for these flow regimes. The real and imaginary parts of the streamwise wavenumbers obtained with the current model are now compared with theoretical and published values. As explained in the previous section, estimation of the real part α_r of the wavenumber for the TS waves obtained with the linearized model adopted here has been performed by two different techniques.

A first estimation of the spatial wavenumbers was obtained accurately by measuring the streamwise separation between two consecutive zeros or extrema, and averaging over a sample set of such points. The second technique consisted in looking for the strongest peak in a Fourier transformation of the spatial data once a train of TS waves was formed. In this latter case, in almost all simulations, as the TS wave evolves such a peak begins to concentrate around a single value, which is denominated here as the asymptotic wavenumber. This procedure was performed extremely quickly using a FFT subroutine. Owing to its practicality and speed, and the accuracy of results obtained using this second technique, all the values reported here for the real part of the streamwise wavenumber α_r are those attained using exclusively this methodology, although some of the results were corroborated using the first technique (not reported here). A first comparison is accomplished by using the spatial data of ω_y at $z = 0$ and looking for the asymptotic wavenumber in the spectra of energy obtained by an FFT. A sample of such asymptotic estimation is presented in figure 3.8. This plot shows a collection of four spatial spectra, attained at $t^* = 558.2, 774.2, 970.2,$ and 116.2, showing this asymptotic approach in time to a single value, in this case the streamwise wavenumber α_r is sought.

In order to establish the validity of the results for α_r, they are compared against data published by Jordinson [86] and also verified by an Orr-Sommerfeld equation solution generated here; see figure 3.9. From this comparison it is clear that the current code is able to perform, with high accuracy, calculations for small perturbations in two-dimensional domains. In all cases the relative error was less than 0.95%, as it can also be read from a summary of the numerical values involved in the validation process, presented in table 3.2.

In figure 3.10 are presented the results for the comparison of values of the imaginary part of the streamwise wavenumber α_i for the two-dimensional Tollmien-Schlichting waves generated with the current velocity-vorticity code. These results correspond to the same numerical experiments described above (laminar boundary layers at $Re_{\delta_*} = 1000$ and 3000). In this figure are also plotted the results obtained for α_i using the solution

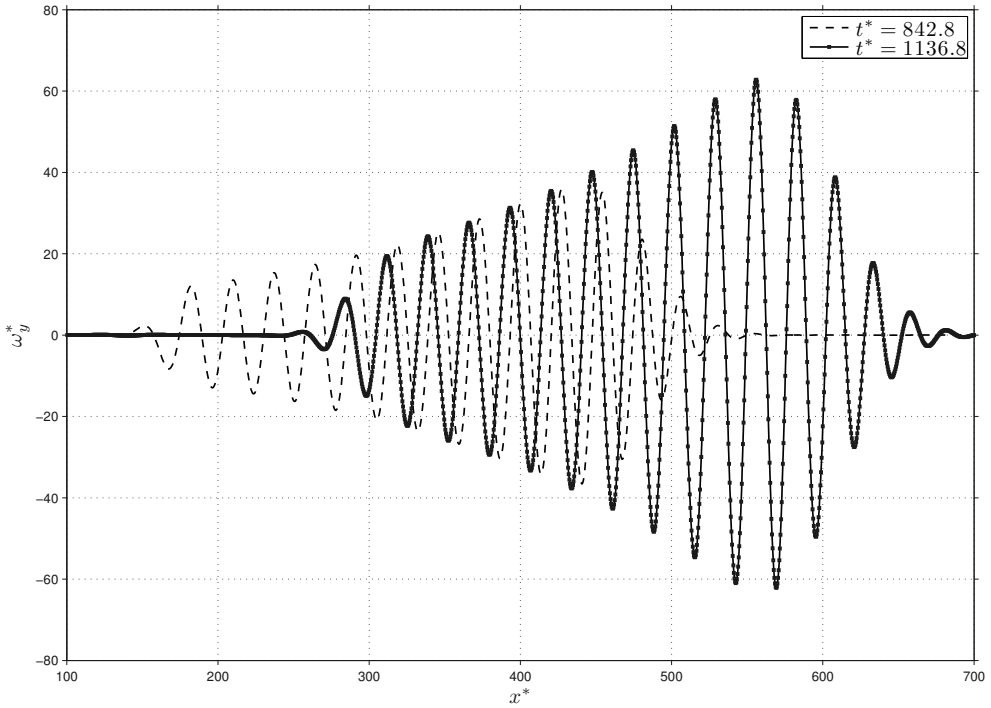

Figure 3.6: Spatio-temporal development of a two-dimensional TS wave for ω_y at $z = 0$ using a source located at $x^* = 140$. Snapshots taken at $t^* = 842.8$ and $t^* = 1136.8$; simulation parameters: $Re_{\delta_*} = 1000$, $\beta = 0.0$, $\omega = 0.08$, $N_x = 5900$, $N_z = 128$. Source activated only for a finite period of time.

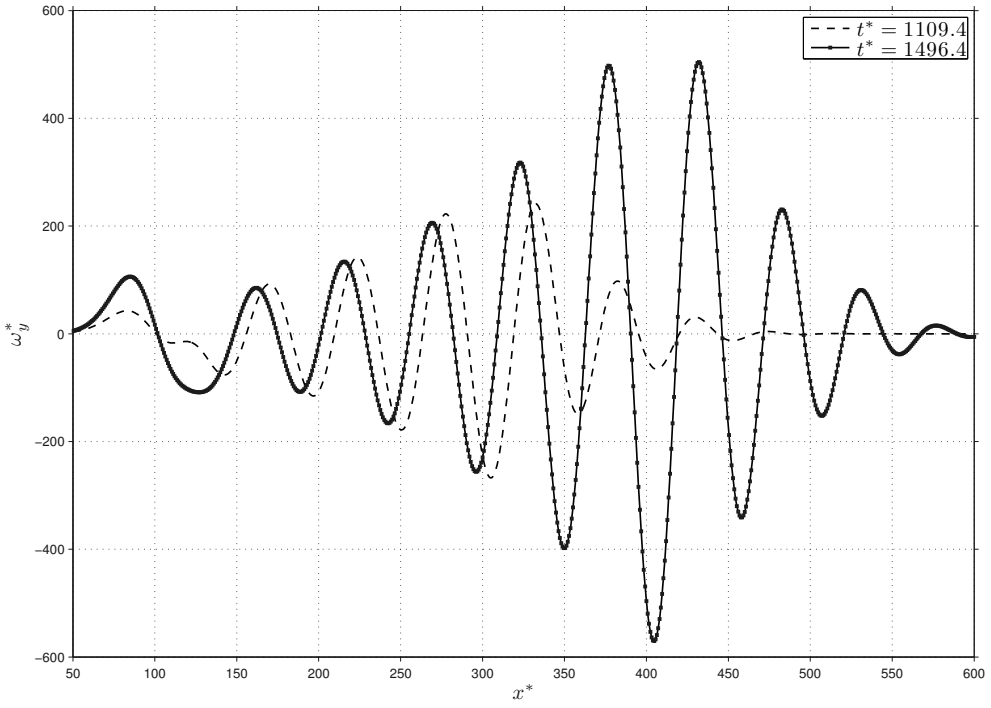

Figure 3.7: Spatio-temporal development of a three-dimensional TS wave for ω_y at $z = 0$ using a source located at $x^* = 100$. Snapshots taken at $t^* = 1109.4$ and $t^* = 1496.4$; simulation parameters: $Re_{\delta_*} = 10000$, $\beta = 0.15$, $\omega = 0.03$, $N_x = 4000$, $N_z = 128$.

of the Orr-Sommerfeld equation obtained in this work.

It is possible to appreciate that the numerical results obtained by the current linearized model are in good agreement with those generated by the current Orr-Sommerfeld solver, although some minor differences are present. A detailed examination of the specific numerical values, presented in table 3.3, reveals that in fact the values obtained here for the imaginary part with the velocity-vorticity formulation are less accurate than for the real part case. However, in all cases, including two-dimensional TS waves at $Re_{\delta_*} = 1000$ and 3000, the relative error between the current values and the one provided by the Orr-Sommerfeld solution is bounded by a 3% error, which can be deemed as a low level of error. These values are also in good agreement with the trend for α_i provided graphically by Jordinson [86] for the same range of frequencies ω and Reynolds numbers Re_{δ_*}.

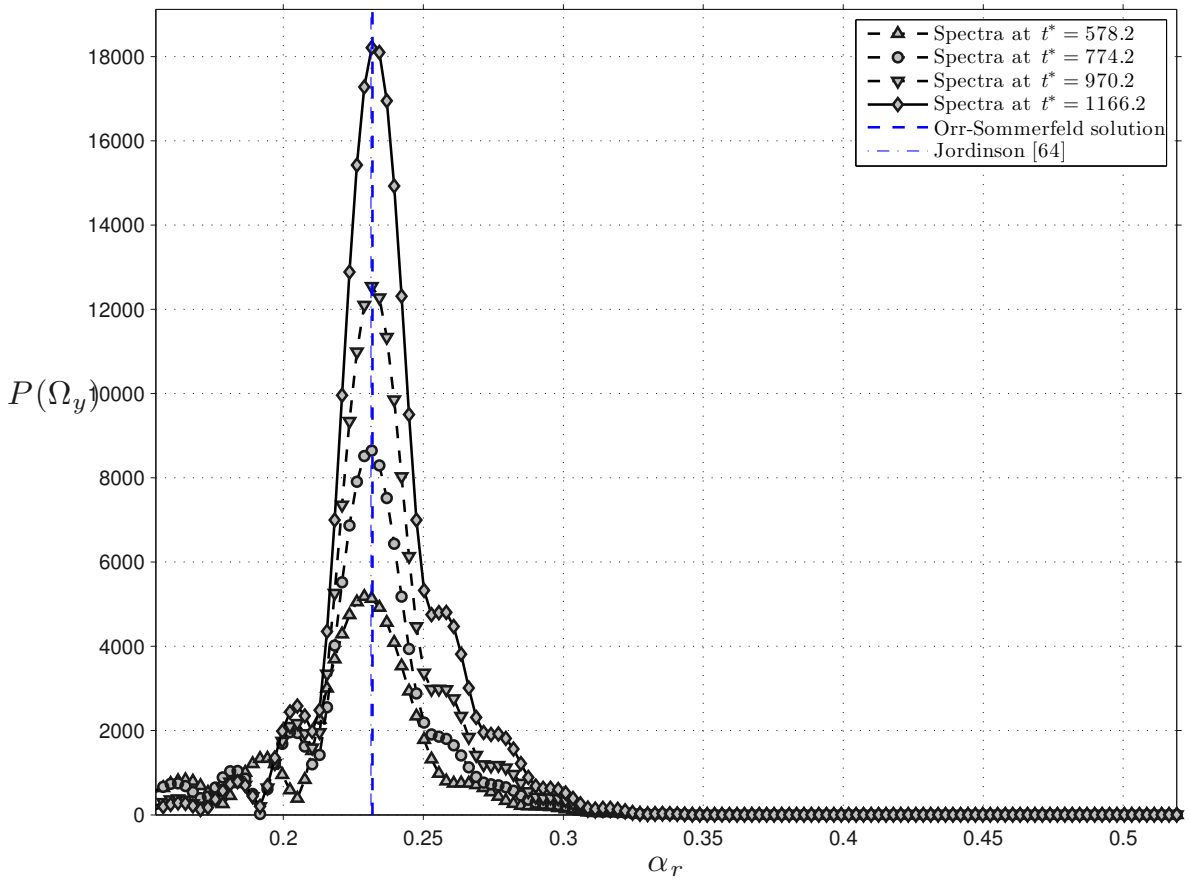

Figure 3.8: Evolution in time of spatial spectra of a two-dimensional TS wave providing the real part of streamwise wavenumber α_r. The values reported for this case by Jordinson [86] and the ones obtained by the solution of the O-S equation are indicated, for reference, as blue dashed lines without symbols; simulation parameters: $Re_{\delta_*} = 1000$, $\beta = 0.0$, $\omega = 0.08$.

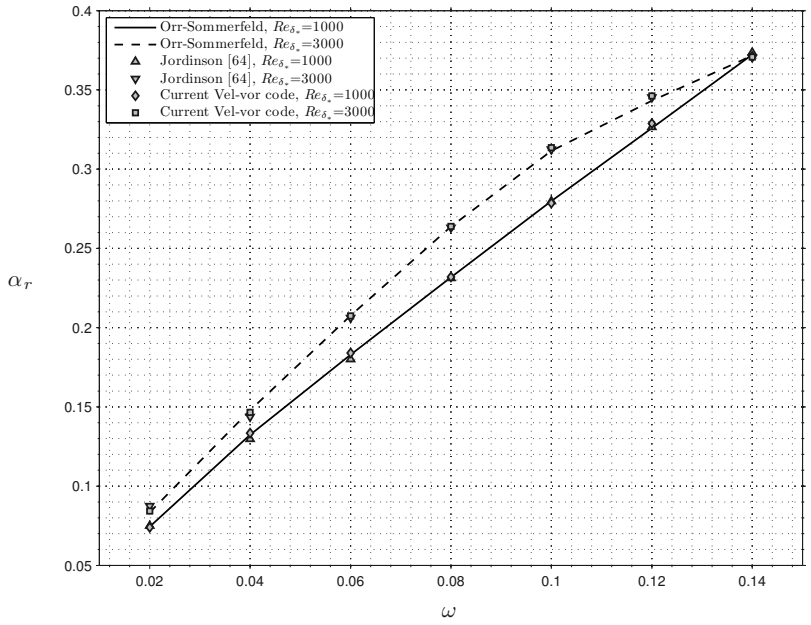

Figure 3.9: Comparison of results for α_r of two-dimensional T-S waves of spanwise vorticity, ω_y, for varying values of forcing frequency ω. Expected data taken from Jordinson [86] and solution of OS equation. See legend for specific details; simulation parameters: $Re_{\delta_*} = 1000$ and 3000, $\beta = 0$.

Re_{δ_*}	ω	α_r		Relative error (%)
		Orr-Sommerfeld equation	Velocity-vorticity code	
1000	0.02	0.07446	0.07400	0.6178
	0.04	0.13242	0.13350	0.8141
	0.06	0.18294	0.18400	0.5783
	0.08	0.23180	0.23198	0.0798
	0.10	0.27982	0.27857	0.4478
	0.12	0.32587	0.32875	0.8841
	0.14	0.37226	0.37120	0.2853
3000	0.02	0.08348	0.08429	0.9691
	0.04	0.14784	0.14649	0.9125
	0.06	0.20760	0.20760	0.0024
	0.08	0.26373	0.26380	0.0273
	0.10	0.31152	0.31350	0.6346
	0.12	0.34315	0.34615	0.8734
	0.14	0.37159	0.37080	0.2126

Table 3.2: Comparison of values obtained of α_r for two-dimensional TS waves. Values obtained with the current LNSE model (fourth column) are compared against and values from solution of the OS equation (third column). Percentage of relative error with respect to Orr-Sommerfeld solution shown in last column.

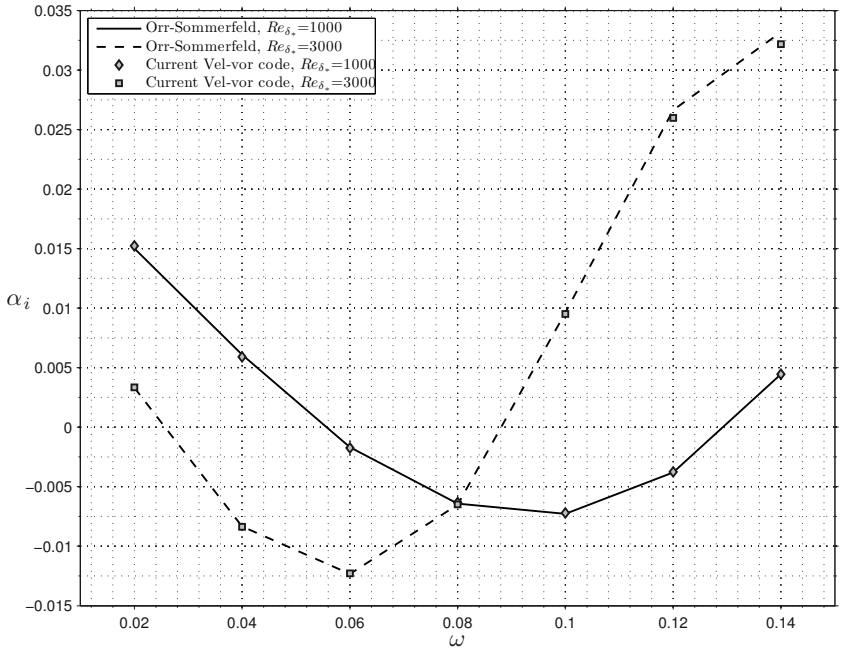

Figure 3.10: Comparison of results of the imaginary part of the streamwise wave number α_i for a 2D Tollmien-Schlichting wave of ω_y for varying ω values; simulation parameters: $Re_{\delta_*} = 1000$ and 3000, $\beta = 0.0$.

Re_{δ_*}	ω	α_i		Relative error (%)
		Orr-Sommerfeld equation	Velocity-vorticity code	
1000	0.02	0.01501	0.01523	1.46569
	0.04	0.00609	0.00590	3.03926
	0.06	-0.00168	-0.00174	3.32542
	0.08	-0.00642	-0.00633	1.40187
	0.10	-0.00729	-0.00721	1.05668
	0.12	-0.00381	-0.00375	1.44547
	0.14	0.00445	0.00450	1.05665
3000	0.02	0.00331	0.00334	0.75460
	0.04	-0.00834	-0.00836	0.28780
	0.06	-0.01233	-0.01228	0.40561
	0.08	-0.00651	-0.00648	0.47641
	0.10	0.00961	0.00951	1.10267
	0.12	0.02663	0.02598	2.42217
	0.14	0.03319	0.03217	3.08536

Table 3.3: Comparison of values obtained of α_i for two-dimensional TS waves. Values obtained with current LNSE model (fourth column) compared against values from solution of the OS equation (third column). Percentage of relative error with respect to OS solution shown in last column; simulation parameters: $Re_{\delta_*} = 1000$ and 3000, $\beta = 0.0$.

Another set of numerical experiments aiming to gauge the ability of the implementation and methodology adopted to predict accurately three-dimensional Tollmien-Schlichting waves, i.e. when $\beta \neq 0$, were conducted for flows at $Re_{\delta_*} = 10^4$ and $Re_{\delta_*} = 10^5$. The asymptotic spectra for one of this cases and the results of all the experiments are presented in figures 3.11 to 3.13.

Regarding the real part of the wavenumber, the trend shown in figure 3.11 is a collection of spectra at different time instants, in this case at $t^* = 1534, 2054, 2574$ and 2990, whose maxima location in the wavenumber axis tends asymptotically towards the expected value of α_r. Results of the computation of α_r for TS waves generated in a laminar boundary layer at $Re_{\delta_*} = 10^5$, excited at five different frequencies, are presented in figure 3.12. In table 3.4 the numerical values of the real part of the streamwise wavenumber α_r attained in this work are compared against theoretical values, i.e. solutions of the Orr-Sommerfeld equation, as well as versus values obtained from a high-order velocity-vorticity method similar to the method employed in this work, both reported by Togneri and Davies [83]. In this thesis the relative errors of the computed values for α_r, compared against the theoretical values reported in [83], are bounded always below 1.0% for the cases examined, $Re_{\delta_*} = 10^4$ and $Re_{\delta_*} = 10^5$, both for a wavenumber $\beta = 0.15$ in spanwise direction.

An examination of the results for the imaginary part of the wavenumber, α_i, presented in table 3.5, reveals a higher level of error on the estimated values. In all the numerical experiments on three-dimensional TS waves, this value presented a high sensitivity, and its elicitation was less trivial than for all previous cases. It is quite probably that the small values associated with this parameter (α_i) make its estimation more difficult, and therefore the computation of the relative error produces such large data in the error value.

Nevertheless, for most of the situations numerically tested, the predictions of the current model compare accurately to the benchmark data for this perturbation phenomenon. For instance, in figure 3.12 the results of the current model appear to be identically to those presented in [83], and and one has to look at the exact numerical data to appreciate differences against the benchmark data available.

From the complete set of figures and tables, it is possible to conclude that the current code is also able to capture the three-dimensional Tollmien-Schlichting waves without any complications (except for the relatively large errors in α_i for three-dimensional TS waves). In this manner, the ability of the formulation adopted here and of the current code to cope with wave like disturbances and instabilities has been established.

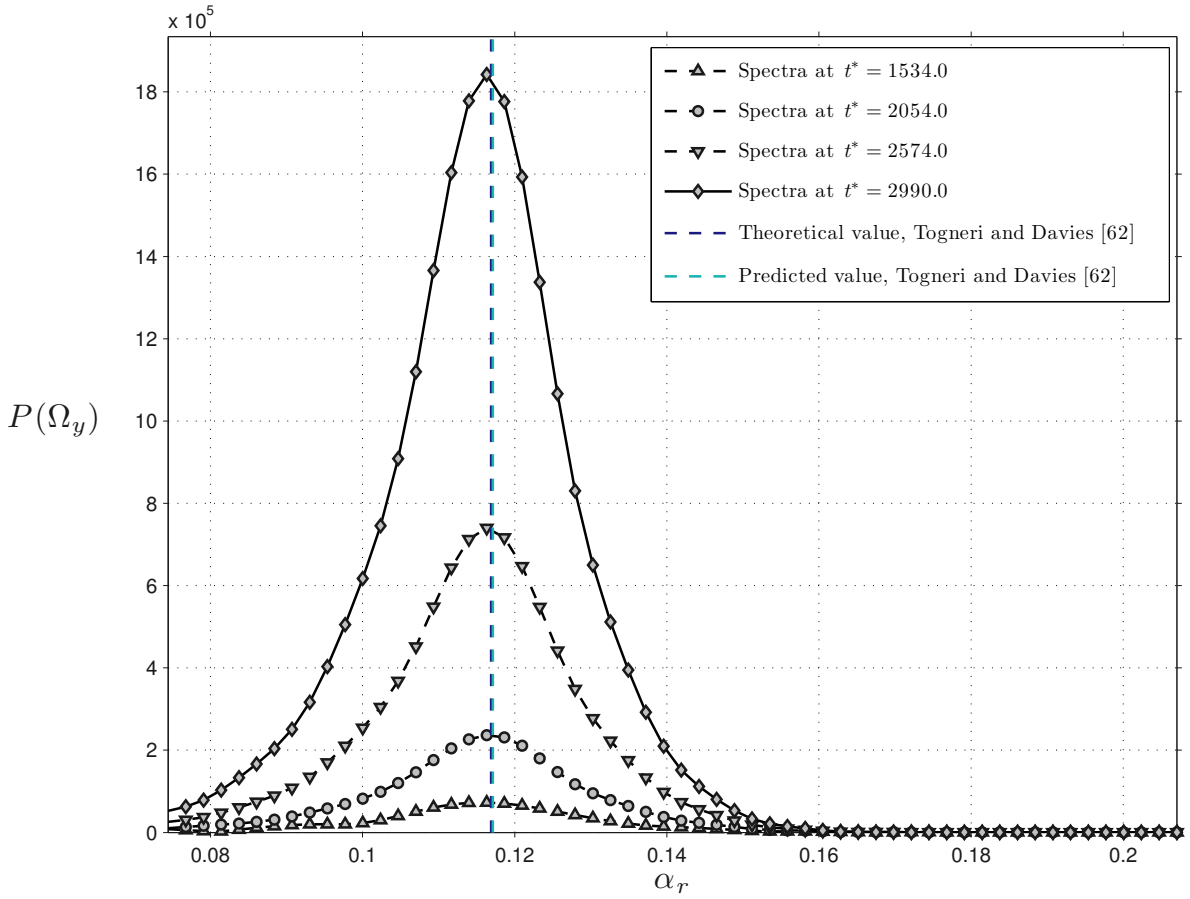

Figure 3.11: Evolution in time of spectra (spatial FFT transform) of a three-dimensional TS wave providing the real part of streamwise wavenumber α_r. Theoretical and computed values reported for this case by Togneri and Davies [83] are presented, for reference, as blue and cyan dashed lines, respectively. Simulation parameters: $Re_{\delta_*} = 10000$, $\beta = 0.15$, $\omega = 0.03$

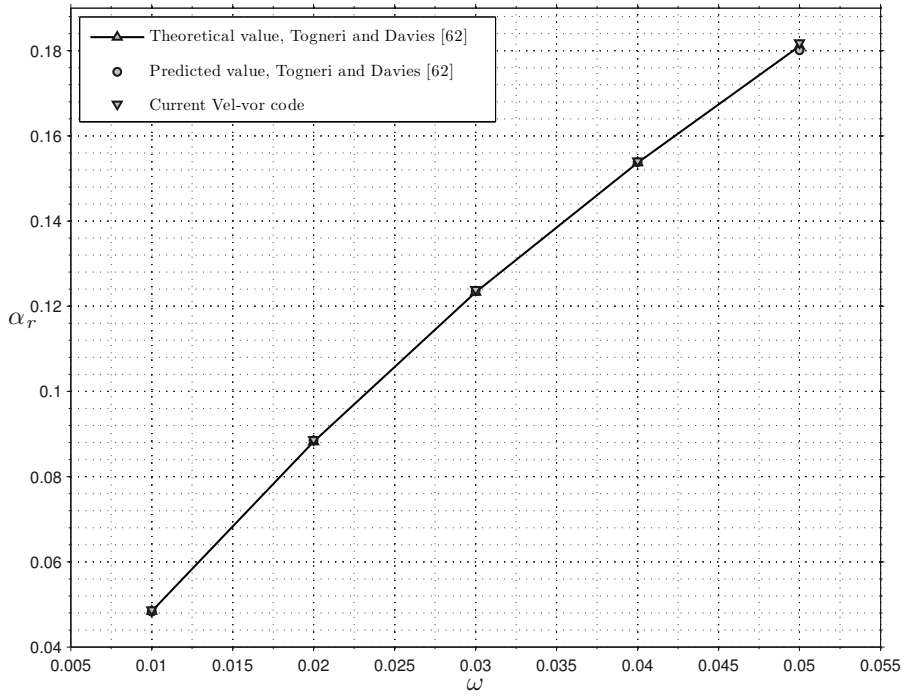

Figure 3.12: Results of numerical experiments on three-dimensional TS waves of spanwise vorticity, ω_y. Comparison of the real part of streamwise wave number, for varying ω values. Theoretical data taken from Togneri and Davies [83]. Simulation parameters: $Re_{\delta_*} = 10000$, $\beta = 0.15$.

Re_{δ_*}	ω	α_r			Relative error (%)
		Computed by [83]	Orr-Sommerfeld solution reported by [83]	Velocity-vorticity code	
10^4	0.03	0.11714	0.11691	0.11775	0.71
10^5	0.01	0.048332	0.04840	0.04870	0.62
	0.02	0.088496	0.08817	0.08870	0.59
	0.03	0.123520	0.12329	0.12392	0.55
	0.04	0.153770	0.15369	0.15411	0.26
	0.05	0.180090	0.18104	0.18185	0.52

Table 3.4: Comparison of results for real part of streamwise wavenumber α_r. Computed and theoretical wavenumbers reported by Togneri and Davies [83] are presented in third and fourth column, respectively. Values obtained in this study are located in the fifth column. Percentage of relative error, against theoretical values, are presented in last column. Simulations parameters: $\beta = 0.15$

Re_{δ_*}	ω	α_i			Relative error (%)
		Computed by [83]	Orr-Sommerfeld solution reported by [83]	Velocity-vorticity code	
10^4	0.03	-0.008783	-0.008845	-0.008399	5.03
10^5	0.01	-0.000003	-0.000011	-0.000013	18.61
	0.02	0.001478	0.001486	0.001248	16.03
	0.03	0.003489	0.003613	0.003230	10.60
	0.04	0.006240	0.005940	0.006392	7.61
	0.05	0.008471	0.008449	0.008378	0.83

Table 3.5: Comparison of results for imaginary part of streamwise wavenumber α_i. Computed and theoretical wavenumbers reported by Togneri and Davies [83] are presented in third and fourth column, respectively. Values obtained in this study are located in the fifth column. Percentage of relative error, against theoretical values, are presented in last column. Simulations parameters: $\beta = 0.15$

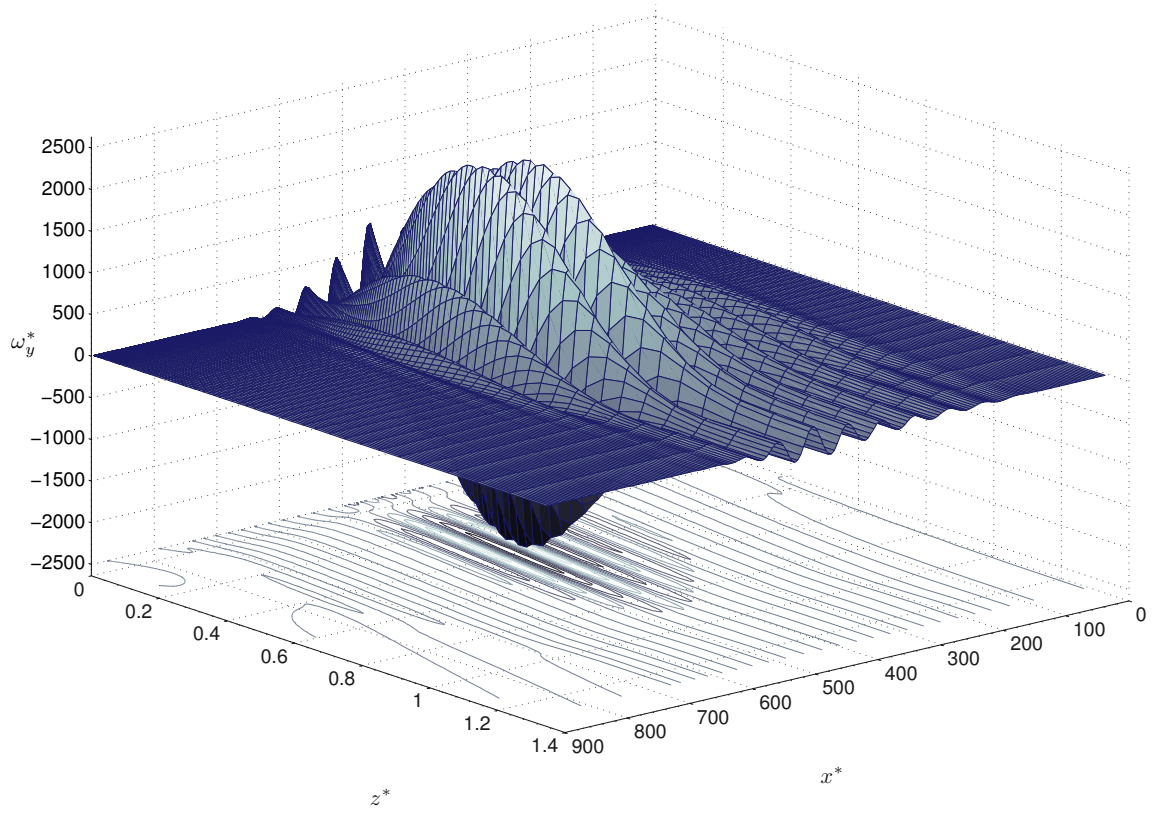

Figure 3.13: Spanwise vorticity, ω_y, for a three-dimensional Tollmien-Schlichting. Simulation parameters: $Re_{\delta_*} = 10000$, $\beta = 0.15$, $\omega = 0.03$

3.5.3 Linear Stability Theory: Optimal perturbation

A significant result in linear stability theory, first presented by Butler and Farrell [63], is the correlation between two-dimensional optimal perturbations to the turbulent mean velocity profile and the dynamics of small scale coherent structures. Owing to the nature of the methodology, it has been dubbed as Optimal Perturbation (OP) approach. One noteworthy result is the estimation of a spanwise streak spacing $\lambda_y^+ \approx 100$, which is consistently observed in physical experiments as well as in DNS studies, in wall-bounded turbulent shear flows. Here an attempt is made to reproduce, with the current methodology, the results presented in [63]. The mean base flow adopted was the turbulent velocity profile described in 3.4.2.

Butler and Farrell [63] performed an optimisation of the energy growth, i.e. the amplification of energy with respect to some initial value of perturbation energy. The objective function was defined in terms of spanwise wavelength for different optimisation times, namely $\tau^+ = 40, 80, 120$, over which the energy growth was maximised. For comparison, the results of this work are reproduced without any modification in figure 3.14. Looking at that plot, it is evident that the maximum amplification of energy of the optimised perturbations increases with the optimisation time. Furthermore, specific optimisation time scales are associated with individual maximal spanwise wavelengths, which is consistent with experimental and numerical results [15–17].

Here, two different numerical experiments are conducted by creating a fully solenoidal and no-slip compatible initial condition. This technique of introducing excitation in the system is explained in more detail in §4. This approach is denominated in this study as a Low Order Model (LOM), for reasons which are explained in section §4.3.

For the current validation test, a streamwise independent version of the adopted formulation was used to perform an optimisation over a single-parameter initial condition, given as

$$w(x, y, z, t = 0) = z^2 \, e^{-\sigma_z z^2} \, e^{\mathbf{i}\beta y}$$

$$u(x, y, z, t = 0) = 0$$

$$v(x, y, z, t = 0) = -\int_y \frac{\partial w}{\partial z} dy = -\frac{1}{\mathbf{i}\,\beta} \frac{\partial w}{\partial z}$$

where optimisation was carried out over parameter σ_z (which has dimensions of L^{-2}). Note that this initial

condition has $\mathbf{u} = (0, v, w)$ independent of x, so

$$\boldsymbol{\omega} = \begin{vmatrix} \mathbf{e_x} & \mathbf{e_y} & \mathbf{e_z} \\ \dfrac{\partial}{\partial x} & \dfrac{\partial}{\partial y} & \dfrac{\partial}{\partial z} \\ 0 & v & w \end{vmatrix} = \left(\frac{\partial w}{\partial y} - \frac{\partial v}{\partial z} \right) \mathbf{e_x} \tag{3.36}$$

with $\mathbf{e_i}$ representing the unit vector in the $i-$th direction; in this manner, the initial condition defined by equation (3.36) represents a pure streamwise vortex. This initial condition also ensures continuity, as can easily be verified. Using this initial condition a similar plot to that obtained by Butler and Farrell [63] is presented in figure 3.15, where amplification of energy is plotted as a function of spanwise wavelength, for the same three optimisation times. Most of the features from the optimal perturbation approach are fully contained in the obtained results, such as the location of maxima and the general form of the plots. Based on the amplification of energy, this low order model was 25-30% "less optimal" than those results of OP [63]; nevertheless, the main features of the perturbation are extremely similar.

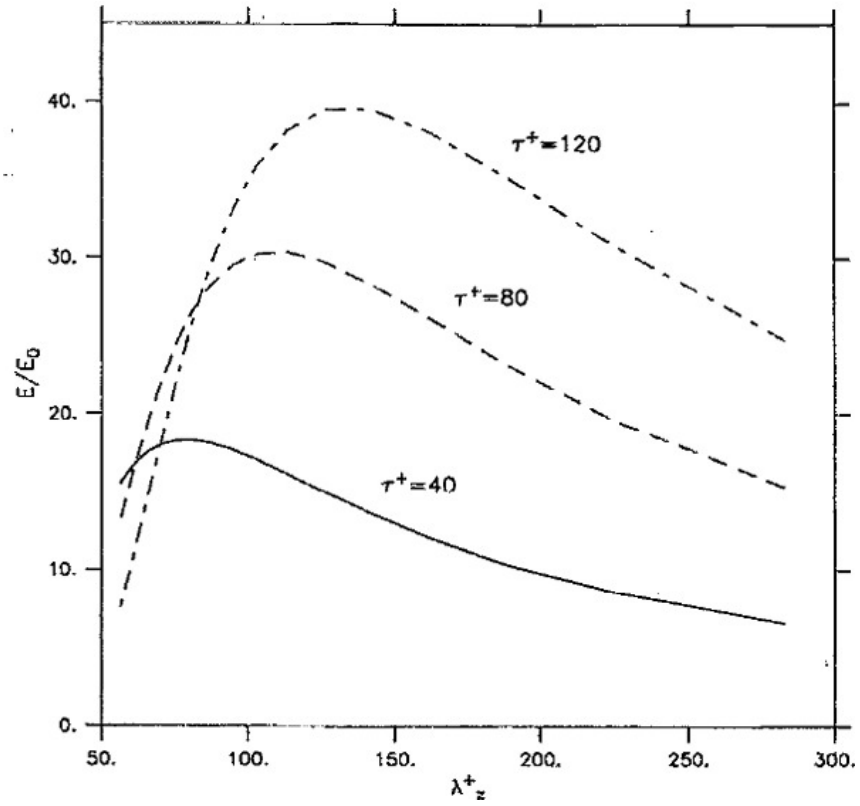

Figure 3.14: Optimal perturbation results. Taken from Butler and Farrell [63]

A second set of tests was carried out over a standard streamwise-dependent version of the code using the same

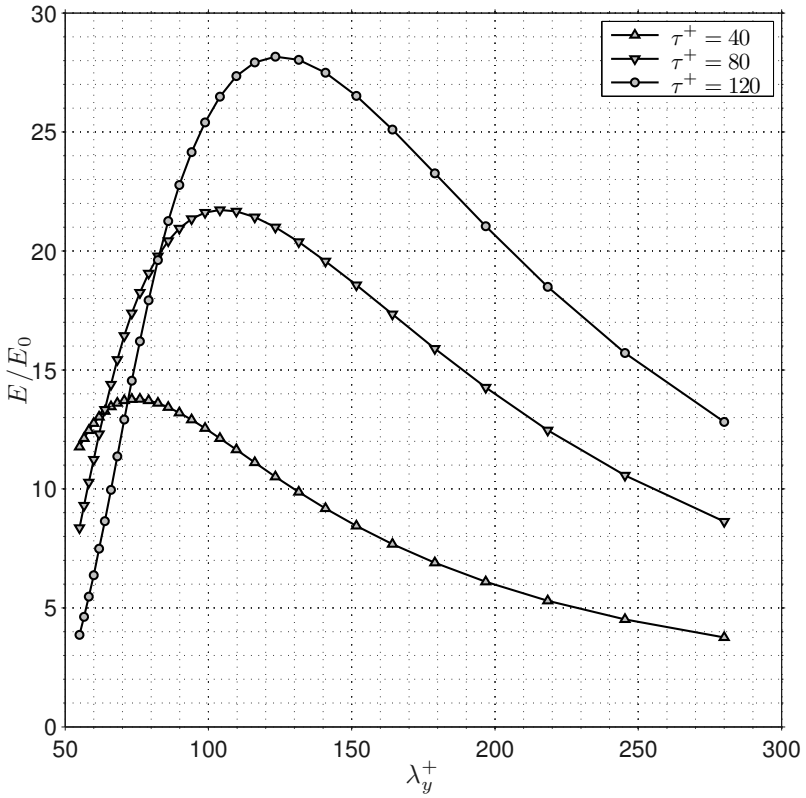

Figure 3.15: Optimal perturbation results. Obtained with a variation of the current code. Streamwise independent formulation.

initial condition as before. In this second test, results were equally satisfactory. As it is shown in fig. 3.16, these results are within the same range as the original OP amplification values, although the location of the maximum of every curve, i.e. at every optimisation time τ^+, lies slightly to the right of the values of spanwise wavelength originally presented by OP results and shown in figure 3.17. In any case, the main features of the OP results are contained in this last plot. Figure 3.17 shows the wall-normal profile of streamwise velocity perturbation for this numerical experiment. As indicated in [63], the optimal perturbation over a period of $\tau^+ = 80$ produces streaks with spanwise wavelength $\lambda_y^+ \approx 110$ with a peak streak velocity at $z^+ \approx 19$. Inspecting the profile produced with the current model, reveals that this feature has also been fully captured by the formulation and numerical implementation adopted here. In particular, for the profile shown in fig. 3.17, the peak of the profile is located at $z^+ = 18.82$, which is within less than 1% of the expected value according to OP. Based on previous results, can be concluded that the adopted formulation and the current code are fully valid and able to reproduce reliably results of similar methodologies, which provide confidence on the validity of the current implementation. It is noteworthy to mention that given that any solution of the model without variation in x should also be a solution of the more general model set up with exactly the same initial condition; this is the case of the validation tests presented in figures 3.15 and 3.16. In the present case, however, the streamwise dependent version of the code was used in conjunction with inflow/outflow

boundary conditions (instead of periodic boundary conditions). This set up could have violate the uniformity of the initial condition, which would explain the difference between such plots. Nevertheless, given the success in reproducing, in a general way, the distribution of energy growth as function of the spanwise spacing as obtained by OP results (figure 3.14, and [63]), it was deemed unnecessary to perform additional validation tests regarding OP results.

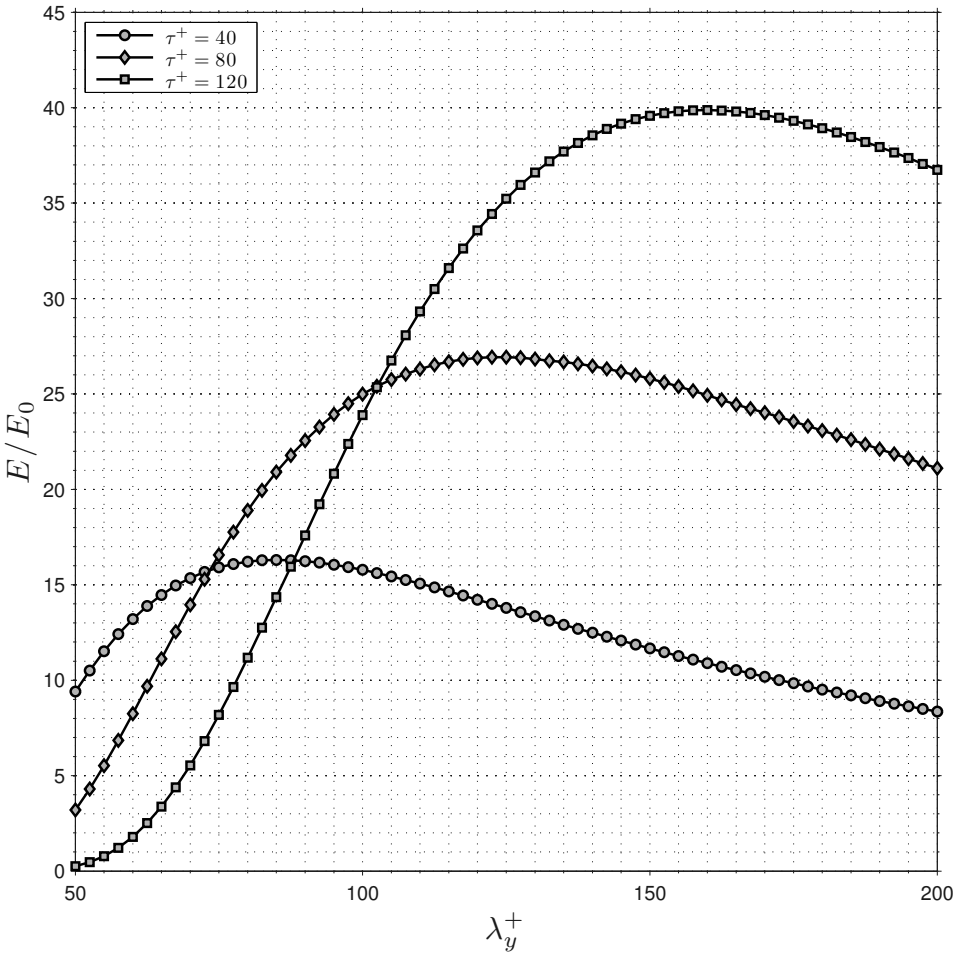

Figure 3.16: Optimal perturbation results. Obtained with the current code using a streamwise-dependent formulation.

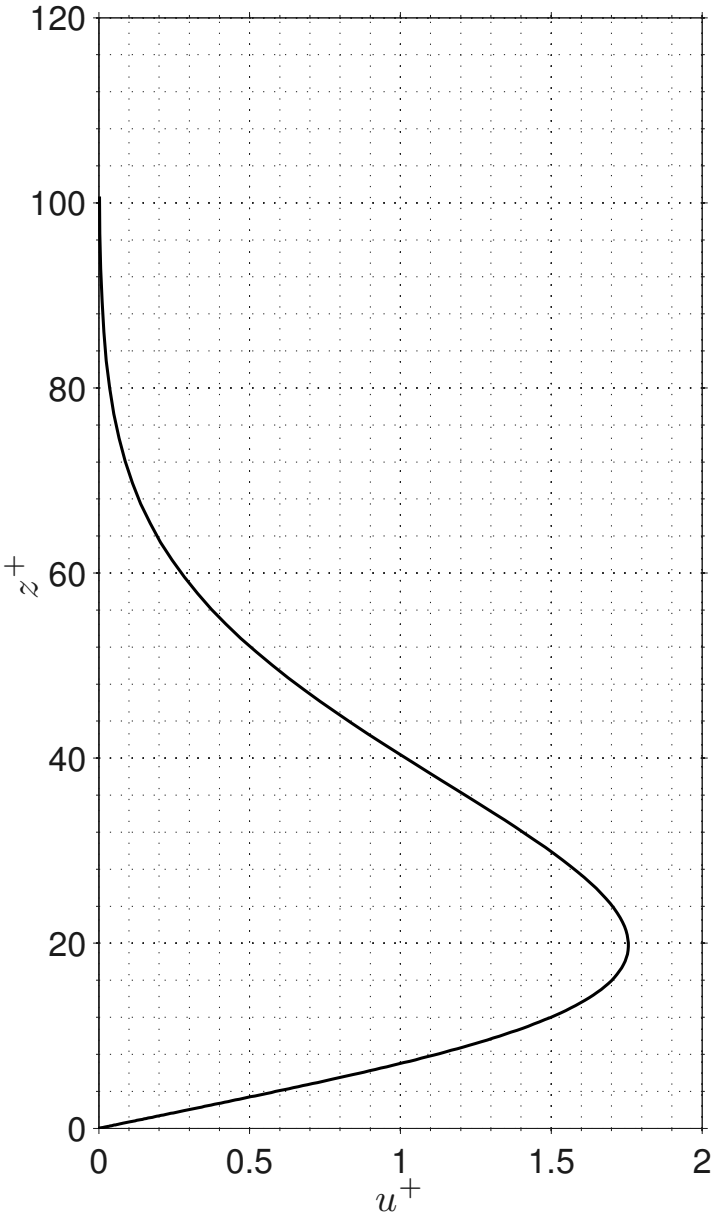

Figure 3.17: LOM results. Profile of streamwise velocity perturbation for $\lambda_y^+ \approx 110$ obtained at $\tau^+ \approx 80$. Peak streak velocity located at $z^+ = 18.82$

3.6 Chapter Summary

In this chapter the numerical aspects of the methodology associated with the Velocity-Vorticity formulation originally proposed by Davies and Carpenter [71] have been discussed. A detailed description of some of the most important aspects of the numerical methods adopted has been presented. Different considerations about spatial and temporal discretization were discussed, as well as some of the implications of the integral boundary conditions associated with this methodology. In order to test the integrity of the numerical implementation and the computational code developed in this thesis, a range of simulations have been compared to results from linear stability theory applied to Tollmien-Schlichting waves and from the Optimal Perturbation method. In both cases, an excellent agreement was found.

Chapter 4

Low-order model and generation of near-wall streaks

One of the targets of the present study is to determine the ability of the linearized formulation to track the generation and development of the so-called near-wall streaks discussed in §1.2. In particular, the approach presented here is to study the behaviour of the Linearized Navier Stokes (LNS) operator is via a viscous initial value problem. In contrast to the classical approach, i.e. to examine and study the eigenvalues of the linearized Navier-Stokes operator, here the analysis concentrates on the perturbation response of the system, linearized around a base profile, to some initial condition or forcing. As it is briefly discussed below, this response is associated with the non-normality of the linearized operator which gives rise to a phenomenon known as transient growth. The approach of this thesis is thus to examine transient growth and its pattern-forming properties as a means to characterise streaks and some of their features.

This chapter is organised as follows: firstly, a brief discussion on concepts associated with transient growth and non-normality of the general LNS operator is presented. Secondly, a short description of the physics of the near-wall streaks, as well as different aspects associated with their measurement, are discussed. In a third section the concept of a low-order numerical model is outlined, and the two methods for generation of streaks studied in this work are introduced. A fourth section presents the results of the exploration of mechanisms to generate streaks along with a discussion of the different measures of streak growth investigated. Finally, conclusions about the suitability of combinations of measures and streaks generation mechanisms in the low-order model are drawn.

4.1 A short overview of turbulent transient growth

Two distinct, though related, approaches to study and analyse the response of linearized perturbed Navier-Stokes equations are eigenmode analysis or via a viscous Initial Value Problem (IVP). As noted by Schmid and Henningson [102], this distinction is not a simple matter of notation, but instead two entirely different ways to examine the behaviour of infinitesimal disturbances and the equations used to study them.

For instance, if the Navier-Stokes (NS) equations for small disturbances are expressed as an evolution operator given by

$$\frac{\partial \mathbf{u}}{\partial t} = \mathcal{L}_{\mathrm{NS}}\left[\mathbf{u}\right] + \mathcal{N}_{\mathrm{NS}}\left[\mathbf{u}\right] + \mathbf{f} \tag{4.1}$$

with $\mathcal{L}_{\mathrm{NS}}$ representing the linear and $\mathcal{N}_{\mathrm{NS}}$ the non-linear part of the NS operator over a small-perturbations vector $\mathbf{u}$, and $\mathbf{f}$ an arbitrary body force term, then linearization is obtained by simply omitting the term $\mathcal{N}_{\mathrm{NS}}$ (as it was presented in §2.2.2).

A classical eigenmode analysis in Linear Stability Theory (LST) would be interested in looking for the eigenvalues of the operator $\mathcal{L}_{\mathrm{NS}}$, from which stability or instability of the system can be judged. In a traditional hydrodynamic stability analysis, the original formulation of the NS equations has to be linearized about a laminar solution and then the most unstable eigenvalues of the resulting operator extracted [109]. For a wide range of cases studied in LST using this approach, the behaviour of the resulting $\mathcal{L}_{\mathrm{NS}}$ can be extracted from the Orr-Sommerfeld and Squire operators[1]. In the laminar case the most unstable eigenvalues could be used to characterise a transition from laminar to turbulent flow. This was precisely the situation presented in the verification test in §3.5.1, where Tollmien-Schlichting waves were associated with eigenmodes of the Orr-Sommerfeld equation. As it has been pointed out by several authors like Trefethen et al. [109], Butler and Farrell [111], Trefethen and Embree [112], Henningson and Reddy [113] and briefly showed in the previous TS-waves verification test, those unstable eigenvalues correspond to eigenmodes of the linearized problem that grow exponentially in time. This feature is known as *exponential growth*.

Although extremely useful in some cases (for instance in Rayleigh-Benard convection or Taylor-Couette flow), the eigenvalue approach fails to accurately predict experimental observations of transition in others types of flows (as in plane Couette flow or plane Poiseuille flow). For instance, in the present case, given that turbulent mean flows are considered linearly stable[2] (see [114]), this approach could be deemed as inappropriate for the current study focused on the evolution and response of small perturbations of turbulent flows. Moreover, this linear stability indicates that in a turbulent flow all eigenvalues of $\mathcal{L}_{\mathrm{NS}}$ have a negative complex part and

[1] Due to the scope of the present work, the definition of the Squire operator has been omitted, but the reader can find such a definition in [102, 110].

[2] It is known that in turbulent flows there is not instability equivalent to the growing Tollmien-Schlichting waves that embody the laminar-turbulent transition.

therefore have no useful additional information. However, as thoroughly discussed by Trefethen et al. [109], it is known that if the eigenfunctions of any linear operator $\mathcal{L}$ are non orthogonal to each other then, even in the case of stable eigenvalues, any input to the system described by $\mathcal{L}$ could be amplified by a large factor. In such case $\mathcal{L}$ is said to be non-normal.

This is precisely the case for $\mathcal{L}_{\mathrm{NS}}$, which has been found to be in some cases extremely non-normal [111, 115–117]. In this way, although every eigenfunction of the linearized NS operator $\mathcal{L}_{\mathrm{NS}}$ may decay exponentially, an amplification of any input forcing or initial perturbation should be expected. In fact, analysing a prototype example Schmid and Henningson [102] show that, for small times, components of the vector $\mathbf{u}$ could experience an *algebraic growth*. The term algebraic growth helps to distinguish this non-normal behaviour from its counterpart, the exponential growth exhibited by normal linear operators. These results clearly indicate that the superposition of two or more exponentially decaying eigenmodes can generate a short-period growth in time, a phenomenon which is entirely caused by the non-orthogonality of the eigenfunctions or eigenvectors. It is thus evident that for the description of the dynamics of $\mathcal{L}_{\mathrm{NS}}$ both eigenfunctions and eigenvalues are equally important, and therefore a simple spectral analysis, i.e. a study of the eigenvalues only, cannot fully capture the evolution of the system described by $\mathcal{L}_{\mathrm{NS}}$.

A number of authors, for instance Hwang and Cossu [20], Butler and Farrell [63], Chernyshenko and Baig [64], Kim and Lim [77], Reddy et al. [118], have associated the non-normality of the $\mathcal{L}_{\mathrm{NS}}$ in turbulent flows with the so-called lift-up effect, a term that links the shear of the mean flow with wall-normal motions of perturbations. This particular component of the linear operator $\mathcal{L}_{\mathrm{NS}}$, termed also as the "linear coupling term" by Butler and Farrell [111] and Kim and Lim [77], has been identified as the main source of non-normality of the eigenmodes of the Linearised NS operator in turbulent wall-bounded flows. This coupling term provides a driving mechanism for the evolution of three-dimensional perturbations. It is known that three-dimensional disturbances in a shear flow can grow algebraically via non-normal linear mechanism, as it has been demonstrated by Ellingsen and Palm [110] and Landahl [119]. For three-dimensional perturbations in an inviscid shear flow, although depending upon the shear profile, one of the relevant mechanisms in the description of their dynamics is the non-normality of the system, as indicated by Trefethen et al. [109]. Furthermore, the three-dimensional flow features associated with this algebraic growth have been recognised to have a distinctive nature, i.e. being streamwise vortices which evolve into streamwise streaks of a higher amplitude [109]. Important as it is for turbulent flows, this type of growth is not exclusive to this class of flows. Algebraic growth has also been recognised to be a key element in laminar viscous shear flows as demonstrated by Butler and Farrell [111], Reddy and Henningson [115], Hultgren and Gustavsson [120].

It is worth highlighting at this point that, as mentioned before, the algebraic growth materialises only for

short periods of time, in the early-stage development of, say, a streamwise velocity perturbation. However, in those cases where instabilities are not observed to develop, the subsequent characteristic element of the small disturbances evolution under linearized operators is a decay or *shut-off* which takes effect at a later stage, after the algebraic growth ceases to dominate and the small perturbation begins to decay exponentially along with the longest-lasting eigenmode. In non-inviscid flows this effect can be directly associated to a viscous effect taking place after the algebraic growth ceases to act. Such a later decay is fully dictated by viscous effects and therefore usually referred to as the *viscous exponential decay* [102, 117]. The coupled action of the algebraic growth plus the viscous-induced damping constitutes what is usually known as *transient algebraic growth* or simply *transient growth*.

In summary, two primary growth mechanisms can thus be defined in the analysis of linear disturbances: firstly, the exponential growth mostly linked to T-S wave instabilities and which can be associated to the normal nature of the eigenvectors of the $\mathcal{L}_{\mathrm{NS}}$ operator; and secondly, the transient growth linked to the lift-up effect and mainly associated to the the non-normal aspect of $\mathcal{L}_{\mathrm{NS}}$. Schmid and Henningson [102] highlights how these mechanisms predominate in different regions of wave number space. Equally, disturbances with a tendency to experience exponential growth will unlikely experience a large transient growth. In general, most of the exponential growth can be associated, though not exclusively, to two-dimensional waves, whereas transient growth is mainly associated with three-dimensional disturbances, as demonstrated by Butler and Farrell [63] and discussed by Trefethen et al. [109].

Arguably, a convenient way of studying such a transient growth and the evolution of small-perturbations is to consider the problem as a viscous Initial Value Problem (IVP), similarly as as in Schmid and Henningson [102], contrary to centering the analysis on the response of the eigenvalues of the $\mathcal{L}_{\mathrm{NS}}$. In this thesis the main attention is, precisely, focused on analysing the linearized NS system using such a viscous IVP approach, primarily because of its potential to make explicit the transient algebraic growth which will allow to introduce tools to detect and quantify short-time response/behaviour of small-perturbations. In this manner, one of the main targets in this work was to characterise the response of the linearized Navier-Stokes operator, through the study of the transient growth, under different flow control conditions.

4.2 Turbulent near-wall streaks and their quantification

Owing to the linearity of the model presented here and its focus on viscous shear flows, particularly on turbulent boundary layers, the short-time perturbations target of this work have an implied connection to the near-wall streaks. These turbulent streaks are characterised by streamwise elongated regions of spanwise alternating

low- and high-speed fluid aligned with the flow direction. Streaks are structures that are universal in the sense that they are always seen in the near-wall region of wall-bounded turbulent flows. Their characteristic dimensions are, in general, always similar if expressed in inner units (see §2.3.3). They are also defined as coherent structures owing to their persistent appearance and regularity in the range of values of their main features. For instance, it is well documented that their length is always about $l_x^+ \approx 1000$ with a spanwise spacing or period of $\lambda_y^+ \approx 100$, although specific values depend on the distance from the wall where they are measured [16] and the method of measurement.

It is clear that in order to evaluate objectively the ability of the model and solver here developed to capture any of the particular features of turbulent streaks it is essential to introduce some gauges or measures. As shown by Butler and Farrell [111], Schmid [117] and Chernyshenko and Baig [64], precisely one of the key elements in any study of short-term disturbances is the adequate selection of a norm to measure the perturbation growth. Although strictly speaking any *norm* is a subclass of a *measure*. In the present work, however, these two terms are used indistinctly to refer to the mathematical tool employed to quantify the size of the disturbance under study. In this way it is possible, by using such a measure, to elicit the quantitative response of the linearized Navier-Stokes operator to a given external forcing or initial condition, and linked this to the generation of near-wall streaks. By investigating the evolution of a given measure, either the amplification or attenuation of the perturbations could be traced as a time–dependent feature. An upshot of this methodology is that it allows us to trace the transient algebraic growth of perturbations and so to evaluate the level of amplification/attenuation[3] in the response of the LNS equations. This proves to be particularly useful in the next study of flow-control techniques, explored and discussed in §5.

It has been common to summarise the response of the LNS equations as an amplification of the perturbations with respect to an initial state [64, 111, 117]. Previous studies using linearized NS systems have employed different definitions to measure the size of the disturbances. Butler and Farrell [111] and Schmid [117] employed a L_2 energy-based norm arguing its physical relevance, albeit Butler and Farrel had to limit the lifetime of the perturbation by the eddy turnover time in order to obtain results comparable to those observed experimentally. This methodology is commonly referred to as the Optimal Perturbation (OP) and describes the amplification with respect to the total initial kinetic energy based on the perturbation velocity fields. Lockerby et al. [38] and Carpenter et al. [1] looked for the strongest response in terms of the streamwise velocity perturbation, and obtained results in good agreement with experiments on streak spacing. Another particularly interesting methodology to measure responses of a linearized NS system is related with amplification of streamwise kinetic energy but, instead of a global evaluation as in [111], focused on a local planar averaging. This type of

[3]For simplicity, from here onwards, the amplification or attenuation of a measure will be referred to just as *amplification* indistinctly.

measure, introduced by Chernyshenko and Baig [64] in their definition of the generalised optimal perturbation (GOP), examines the energy at planes located at specific wall-normal locations. In this case, alternatively, the amplification can be measured against some initial state defined in terms of an empirical normalization using the normal Reynolds stresses, either taken from experiments or direct numerical simulations.

In this thesis a set of different measures have been considered to investigate the transient growth induced by a diverse group of perturbation sources. Main attention has been put on measures based on the amplification of kinetic energy (as in [64]) or streamwise momentum (like in [38]), though other measures involving properties such as vorticity or production of kinetic energy were also considered. In any case, for every measure considered in this work, a standard representation is defined as,

$$\mu(t) = \frac{||A(t)||_{\text{out}}}{||B(t_0)||_{\text{in}}} = \frac{||\cdot||_{\text{out}}}{||\cdot||_{\text{in}}} \tag{4.2}$$

where μ is the specific measure used to track the evolution of the disturbance, A is a property of the system being evaluated at time t and considered as the output or response of the system, and B is a property of the system used as a benchmark or reference value, usually taken at some initial reference time t_0, and therefore considered as the input of the system. In definition (4.2) $||.||$ indicates a norm defined for property A or B. Even though the properties A and B are commonly referred to the same physical quantity, i.e. both energy or both momentum, this is not a special requirement, and therefore in principle different sets of physical quantities are allowed in the definition of μ in (4.2), provided an appropriate normalization is included.

Obviously, in order for a given measure μ to be adequately defined, some additional technical details have to be provided; for instance, a more detailed construction of these measures would require a proper definition of an inner product and additional technical details. Nevertheless, for the scope of the present work, such a definition was deemed unnecessary. As mentioned above, in this work, each measure description requires a definition of a reference property $B(t_0)$ and of a time evolving property $A(t)$. A proper selection of a time-evolving property $A(t)$ is one of the most important elements in the viscous study of linearized systems.

In the present work a wide set of properties A are considered so as to explore the differences, benefits, disadvantages, and the implications of a particular selection of measure. Accordingly, two main categories of measures are defined: a set of *global* measures, defined over a volume domain Ω_V and intended to trace the evolution of structures over the entire domain, in particular the near-wall streaks; and a set of *local* measures directly related with the development of structures at specific planes from the wall, analogous to the generalised optimal perturbation (GOP) norm of [64]. In this study the specific wall-normal locations are called *visualisation planes* and denoted by z_v. Each of these sets includes (mainly, though not exclusively) two groups of physical quantities: maximum streamwise momentum and total kinetic energy, both defined

using perturbation fields. The momentum measures are perhaps more useful for characterising the prompt response or sensitivity of the system; the second group, related to kinetic energy are potentially more useful for characterising larger and more persistent structures. As pointed out by Chernyshenko and Baig [64], owing to the near-wall nature of the streaks, a measure focused on detecting such flow structures in a local region, like in a visualisation plane, in the vicinity of the wall is more likely to capture correctly features like the wall-normal dependency of the spanwise spacing. Equally, it is noteworthy that measures covering globally the domain will favour large-scale structures, even if those are mild compared to the near-wall streaks measured in a given norm. It could be argued that, in this work, the large scale structures are absent owing to the methodology employed to generate the near-wall streaks. Having said this, what is most important to note is that it is only speculation as to which type of measure is most suitable for the characterization of near-wall streaks. In the present work this has been addressed by numerical experimentation, as it is shown in § 4.4.

The selection of a benchmark initial norm $||B(t_0)||_{\text{in}}$ is less critical. In different sources with similar approaches ([20, 64, 102, 111, 117]) it is common to use the simplest initial condition norm, defined as a regular L_2 norm in terms of the total energy for the whole volume under consideration. Here, as in most of the optimal perturbation studies including GOP, the initial flow condition has been commonly associated with streamwise vortices, which does not involve a strong streamwise perturbation velocity. In this way, for instance, one of the measures considered was primarily related to amplification/attenuation of streamwise kinetic energy, analogous to the generalised optimal perturbation (GOP) norm considered by Chernyshenko and Baig [64]. Accordingly, such a definition based on ratio of the streamwise kinetic energy of perturbations at a particular wall-normal distance to initial total kinetic energy of perturbations can be expressed as

$$\mu(t) = \frac{\frac{1}{\Delta z}\int_0^{L_x}\int_{z_v-\Delta z}^{z_v+\Delta z} u^2(t)\, dxdz}{\frac{1}{L_z}\int_0^{L_x}\int_0^{L_z} ke(t_0)\, dxdz} \tag{4.3}$$

where μ is the measure being evaluated at a wall-normal visualisation plane z_v, $u^2(t)$ are perturbations related to the streamwise kinetic energy being evaluated in time and the term ke is the total kinetic energy based on perturbation values $ke(t) = u(t)^2 + v(t)^2 + w(t)^2$, in particular the perturbation energy at time t_0. L_x is the length of the streamwise domain while Δz is the computational thickness at the visualisation plane. Obviously, if the initial kinetic energy lacks any streamwise component, as in some cases considered in this thesis, such a definition of measure would require only the cross-flow components.

Equally, in this study, some norms involving the spatial maximum of perturbation have also been explored; in such cases a different definition of norm $||\cdot||_{\text{in}}$ was required. As a guide for the reader, a selected set of measures explored numerically in the present work and their mathematical definitions are summarised in table 4.1; in this table Ω_1 represents a planar domain for local measures at a given visualisation plane z_v, and

Ω the domain associated to the volumetric or herein so-called global measures.

It is convenient at this point to make a remark on the measures presented in table 4.1 regarding the spanwise periodicity. Given the modal decomposition applied to the representation of the small perturbations in the spanwise direction, each norm actually represents a response per-spanwise wavenumber. In other words, for each λ_y, periodicity would render any measure zero, unless a Fourier reconstruction was made using a given number of different spanwise wavelengths. In the present work, instead, this spanwise modal decomposition is used to decouple the responses of the $\mathcal{L}_{\mathrm{NS}}$ at different spanwise wavelengths, and then to elicit on the responsiveness of the system as a function of the spanwise direction. This is the reason why none of the norms presented in table 4.1 include a functional dependence on the y spatial direction.

Measure	Type	$\|\|\cdot\|\|_{\mathrm{out}}$	$\|\|\cdot\|\|_{\mathrm{in}}$
$\mu_{1,\Omega}$	Volumetric	$\frac{1}{L_x\,L_z}\int_\Omega ke(t)\,d\Omega$	$\frac{1}{L_x\,L_z}\int_\Omega ke(t_0)d\Omega$
$\mu_{2,\Omega}$	Volumetric	$\frac{1}{L_x\,L_z}\int_\Omega \left(u(t)\,w(t)\,\frac{d\,U^B}{d\,z}\right)d\Omega$	$\frac{1}{L_x\,L_z}\int_\Omega \left(ke(t_0)\,\frac{d\,U^B}{d\,z}\right)d\Omega$
$\mu_{3,\Omega}$	Volumetric	$\frac{1}{L_x\,L_z}\int_\Omega \left(ke(t)\,\frac{d\,U^B}{d\,z}\right)d\Omega$	$\frac{1}{L_x\,L_z}\int_\Omega \left(ke(t_0)\,\frac{d\,U^B}{d\,z}\right)d\Omega$
$\mu_{4,\Omega}$	Volumetric	$\max_\Omega \lvert u(t)\rvert$	$\sqrt{\max_\Omega \lvert ke(t_0)\rvert}$
μ_1	Planar	$\frac{1}{L_x\,\Delta z}\int_{\Omega_1} u_{z_v}^2(t)\,d\Omega_1$	$\frac{1}{L_x\,L_z}\int_\Omega ke(t_0)\,d\Omega$
μ_2	Planar	$\frac{1}{L_x}\int_0^{L_x} u_{z_v}^2(t)\,dx$	$\frac{1}{L_x\,L_z}\int_\Omega ke(t_0)\,d\Omega$
μ_3	Planar	$\max_{x\in[0,L_x]} \lvert u_{z_v}(t)\rvert$	$\sqrt{\max_\Omega \lvert ke(t_0)\rvert}$

Table 4.1: Definition of measures to quantify streaks and transient growth.

One main distinctive advantage of the local (planar) measures is that it allows to check patterns of response as functions of the wall-normal position, which is not possible with global / volumetric measures. These patterns proved to be useful in establishing the validity of the current model for streak generation against available experimental data on streak spacing as a function of wall-normal position. On the other hand, the volumetric

measures permit the tracking of the global spatial development of the perturbation as well as of the numerical stability of the system for a particular forcing or initial condition. Irrespective of which particular measure is selected, for cases that are linearly stable, the time evolution always describes a transient, non-normal growth followed by an exponential decay. In figure 4.1, as an example, it is shown this specific behaviour, for a selected initial perturbation.

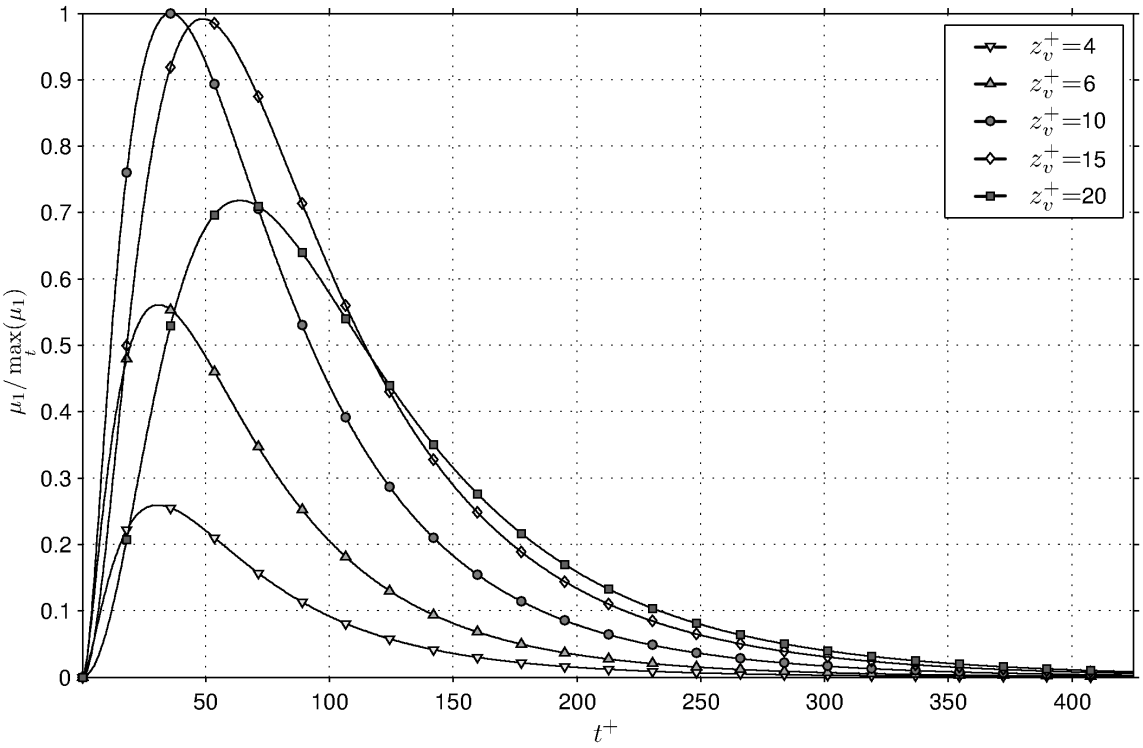

Figure 4.1: Transient growth of energy at different wall-normal locations z_v^+ for a body force at z_f^+ =10 and $\lambda^+ = 100$. Plots have been normalised using the global maximum in time.

Although the use of measures based on the amplification concept is widely extended in studied of small scale perturbations, it is also common to find streak growth studies solely or mainly based on tracking in time a single perturbation property, specifically the spatial maximum of the absolute value of the streamwise perturbation velocity, $\max_\Omega |u(t)|$. This is the case of some previous works exploring flow control by targeting the streamwise streak velocity, such as Lockerby [37] and Togneri [72], to mention just a few. In this approach the measure does not necessarily represent an amplification value. However, this is valid provided there is an appropriate normalization of the initial perturbation (generated by a forcing function or by an initial condition); for completeness, measures alike were also explored in the present work based on some of the definitions $\|\cdot\|$ given in table 4.1. However, to distinguish such measures from the ones strictly defined as amplification measures, these are denoted in the present work simply as μ_i^* or $\mu_{i,\Omega}^*$, for any i-th measure in accordance with the definitions given in table 4.1. Besides, for clarity, any of these is referred to as non-explicit amplification measure i.

4.3 Mechanisms of Streak generation

The LNSE system described by expressions (2.94), (2.97) and (2.99) is mainly focused on capturing the evolution of small scale structures in the near-wall region; i.e., the low-speed streaks. However, since it lacks non-linearity, it is unable to generate, by itself, any excitation required to bring about the initial disturbance to be traced. In other words, any LNSE model will require a 'kick off' or excitation condition that can be then traced as the system evolves in time. The linearized model presented here is not an exception. Thus, in order to study the disturbance evolution, two different methodologies of excitation have been examined. First streak generation using a variety of vorticity forcing sources is considered, including the one used in [1], [38] and [72], for a range of forcing parameters. Secondly, as an alternative, a fully prescribed initial condition (IC) is presented. In some aspects, this IC offers a more flexible mechanism to setup the initial perturbation fields required to generate the streaks. In both cases, the main goal is to examine the impact of the parameters for each type of force or initial condition on the response of the LNSE.

These two techniques to generate streaks in the present LNSE effectively are simple mechanisms to introduce a source or seed term into the system. In the case of the fictitious body force this term effectively acts as a vorticity source, whereas in the initial condition (IC) case it acts as a perturbation velocity source[4]. This source term can be interpreted as a simplified representation of action of the non-linear terms, dropped off during the linearization, as if it was acting over a finite period of time. From this point of view, the role of such a fictitious body force or initial condition is to provide a crude representation of the non-linear terms. However, it is important to highlight that although such analogy can be established, it is not a requirement for this source term to accurately represent a physically feasible vorticity or kinetic energy source in order to "activate" the linearized operator, and therefore in principle it can take any mathematical form. In fact, this analogy can give the misleading impression that tuning of the free parameters is required to generate streaks, and that the non-physical body-force or initial condition is intended to represent some specific physical distribution. However, it is not well known how these parameters and the particular forcing or IC form affect the streaks generated from these models. Nevertheless, for numerical convenience, in this work a minimum requirement for this expression is that it must be analytic in most of the physical region where it is defined. Such representation of a streak generation mechanism is denominated in this thesis as general Excitation Mechanism, and referred to as EM.

For both types of mechanisms of streak generation, as a forcing function and as an initial condition, a set of

[4] In fact, depending upon the specific initial condition, this excitation term could also be considered as a vorticity source, if proper gradients are provided in the definition of the IC.

different functional forms is explored and defined as a product of independent single-variable functions:

$$F_{\mathbf{EM}}(x, y, z, t; \{\Pi\}) = G\, X(x)\, Z(z)\, T(t)\, e^{\mathbf{i}\,\beta\, y} \tag{4.4}$$

where

$F_{\mathbf{EM}}$: Total functional form for the body forcing or initial condition

G : Intensity of total function

$X(x)$: Function in streamwise direction, x

$Z(x)$: Function in wall-normal direction, z

$T(t)$: Function in time, t

$\{\Pi\}$: Set consisting of the total number of parameters defining the functional form

and the function in the spanwise direction corresponds to the modal decomposition adopted in the present work.

4.3.1 The optimization problem: Low-Order Model

By varying the definitions of the functions X, Z and T in (4.4) the behaviour of the linearized Navier-Stokes operator for each of these functional forms can be studied. An upshot of this methodology is that it allows to discern the pattern-forming properties of the LNSE in terms of any selected EM. Every function in (4.4) is composed of a set of parameters that must be specified to define a given LOM. In this regard, one could argue that a single functional form already represents a whole family of functions and that the different combinations of parameters give rise to totally different forcing distributions or initial conditions. Though this rationale is true, in the present work an additional effort has been dedicated to examine several functional forms with different spatial features. In doing so the aim is to ascertain the impact, or lack of it, of a given functional form, either as a forcing function or initial condition, on the LNS equations. In any case, a selection of parameters is required since they are unknown *a priory*. It is common to perform this selection with the basis on some form of optimization of $F_{\mathbf{EM}}$ [102, 111, 117]. As briefly indicated in §3.5.3, this representation involving an optimization, is here denominated as Low-Order Model (LOM) due to the reduced optimization space used in such process, as it is indicated below.

Any formal formulation of an optimization problem requires the definition of a target function and a set of constrains which define a space of feasible solutions. Two distinct types of target functions have usually been

applied in studies dealing with linearized Navier-Stokes systems. Firstly, the most common and widely-used target function employed seeks an initial condition that maximizes the amplification of total kinetic energy as the streaks develop in time. This type of optimization problem has been documented and employed by Butler and Farrell [63], Chernyshenko and Baig [64], Schmid and Henningson [102], Butler and Farrell [111] and Schmid [117]. As mentioned before, Butler and Farrell [111], in their optimal perturbation technique, constrained the space of feasible solutions by introducing an empirical optimization time period in order to obtain the streamwise and spanwise lengths experimentally reported. In this way, appropriate spanwise and streamwise scales were obtained in [111] by defining the optimum as the disturbance that grows the most in energy during a particular period. The choice of this period in such work was the turbulent eddy turnover time ($\tau^+ \approx 80$). However, Kim and Lim [77] suggested that this approximation was arbitrary as the time for optimum growth is actually much shorter. Observing figure 4.1, which was obtained in the present work by maximization of μ_1 over a long evolution time, it is clear that the optimum streak reaches its maximum at around $t^+ \approx 50$, which is considerably shorter than the eddy turnover time, in full agreement with Kim and Lim [77]. Chernyshenko and Baig [64] employed a similar target function, though without a constraint in time, in their Generalised Optimal Perturbation approach. As discussed in §4.2, they proposed to optimize an initial condition to maximize the amplification of kinetic energy over planes parallel to the fluid direction at some predefined distance from the wall. With this methodology they overcame the time constraint artificially imposed in [111]. Another widely employed target function which seeks an optimum perturbation to a turbulent profile was employed by Lockerby [37] and Togneri [72], focusing on streaks with the largest measure of streamwise perturbation velocity at any time during the evolution of the streak (which was previously discussed in § 4.2). In this case a constraint in time was not needed and the measure was expressed just as a relative maximum instead of as an amplification factor, as mentioned above.

Regardless of the type of optimization problem employed to characterize the turbulent streaks, the success of any such optimal formulations is usually evaluated in terms of their ability to reproduce two main particular features of the turbulent streaks: their spanwise spacing and the wall-normal variation of this spacing. As mentioned at the beginning of §4.2, the spanwise spacing is usually assumed to be around $\lambda_y^+ \approx 100$, although different ranges of values have been reported. For instance, Zacksenhouse et al. [18] report experimentally observed values of $\lambda_y^+ = 120 \pm 52$, whereas Hwang and Cossu [20] establish values of $\lambda_y^+ = 80 \pm 1$ by numerical investigation using an energy-based criterion. The work of Smith and Metzler [16] offers a clear insight regarding the wall-normal dependence of the spanwise spacing λ_y^+.

In this way, once a measure is optimized for some specific target function, it is possible to assess the success of the specific methodology by comparing the optimal spanwise wavelength, outcome of the optimization problem, against reported values of λ_y^+. If such an optimal is contained within a range of valid values of

λ_y^+, for the purposes of this work such a combination of measure and parameters is considered as a sound representation of the streaks. In this work, using a parametric optimization, an extensive exploration of values for parameters associated with X, Z and T has been performed. The parameters of a given form $F_{\mathbf{EM}}$ are then ascertained via an optimization performed over the different set of measures presented in table 4.1 for a range of spanwise wavenumbers. Here, four different optimization problems are studied, including optimization of the streak restricted to growth during a period τ^+, as in [111]. A description of the types of optimization problems tackled in the present work, as well as their mathematical formulation, is presented in table 4.2.

In table 4.2, the symbol μ_i represents volumetric or planar measures, τ_t the total simulation time of a given numerical experiment, Ω the total physical domain, $\{\Pi\}$ stands for the set of parameters of a given functional form and F and $F_{\mathbf{EM}}$ indicate the prescribed functional form and the EM after optimization, respectively. The optimization problem Type-I in this work corresponds to the Optimal Perturbation defined by Butler and Farrell [111] if $\tau^+ = 80.0$. Optimization problem Type-II is the most common way to characterise the non-normality of the LNS system, and therefore also explored in the present work. Also, when applied to measures $\mu_1 - \mu_3$, it resembles the Generalized Optimal Perturbation defined by Chernyshenko and Baig [64]. The optimization problem Type-III is essentially the optimization problem defined by Carpenter et al. [1], Lockerby [37] and Togneri [72] if non-explicit amplification measure $\mu^*_{4,\Omega}$ is used. Finally, the optimization problem Type-IV has been introduced to explore the time-averaged behaviour of some of the measures.

The numerical methodology used in this thesis to find these optima consists of a coarse-grained multi-level discrete parametric optimization, where each level is intended to provide a reduced parametric space for the next optimization cycle. The greater the number of levels, the more accurate the values of the parameters defining a specific form $F_{\mathbf{EM}}$ for a given optimization problem.

Optimization problem	**Description**	**Mathematical formulation**
Type-I	To find a $F_{\mathbf{EM}}$ that maximizes μ_i at a point in time, τ	$F_{\mathbf{EM}}(x,y,z,t;\{\Pi\}) = \max_{\Omega, t=\tau} \mu_i(F)$
Type-II	To find a $F_{\mathbf{EM}}$ that maximizes μ_i over a period τ_t	$F_{\mathbf{EM}}(x,y,z,t;\{\Pi\}) = \max_{\Omega, t<\tau_t} \mu_i(F)$
Type-III	To find a $F_{\mathbf{EM}}$ that maximizes μ_i^* over a period τ_t	$F_{\mathbf{EM}}(x,y,z,t;\{\Pi\}) = \max_{\Omega, t<\tau_t} \mu_i^*$
Type-IV	To find a $F_{\mathbf{EM}}$ that maximizes $\int_{\tau_t} \mu_i dt$	$F_{\mathbf{EM}}(x,y,z,t;\{\Pi\}) = \max_{\Omega, t=\tau_t} \int_{\tau_t} \mu_i(F) dt$

Table 4.2: Optimization problems explored for the characterisation of the mechanisms of streak generation

4.3.2 Excitation Mechanism by Forcing

The starting point of the present work, is the LOM employed by Carpenter et al. [1], Lockerby et al. [38] and Togneri [72], whereby the generation of turbulent streaks is produced by introducing a Lorentz-type body force to the LNSE; a coarse-grained optimisation over a small set of forcing parameters is then performed to find a near-optimal streak. This approach to generating streaks is particularly convenient as it is relatively easy, and computationally efficient, to incorporate the streak disturbance into an otherwise conventional computational fluid dynamics simulation. In these previous studies, a Lorentz-type body-force, represented by a double Gaussian function, has been selected as the functional form for F_x.

In this way, a first approach to generate streaks is to introduce a source term F_x in the right-hand side of the streamwise vorticity transport equation (2.95), in place of the original term S_x, acting as a fictitious or synthetic body force,

$$\frac{\partial \omega_x}{\partial t} + \frac{\partial M_z}{\partial y} - \frac{\partial M_y}{\partial z} = \frac{1}{R}\nabla^2 \omega_x + F_x \tag{4.5}$$

with F_x taking a predefined form in accordance with the generalised formulation for $F_{\mathbf{EM}}$ as presented in (4.4). Although this term effectively acts as a simple streamwise vorticity source, due to the solenoidal nature of ω, it also introduces cross-flow components of vorticity, depending upon the specific form of F_x.

In this thesis, aiming to extend the work in [1, 37, 72], a broader set of forcing terms, covering particular domains in space and with different spatial features, were numerically experimented with; for brevity only results for three of them are included[5]. The distributions reported here are, namely: i) a concentrated Gaussian vorticity source (as in [37]); ii) a wall-normal linear and streamwise Gaussian vorticity source; and iii) a wall-normal quadratic, streamwise constant vorticity source. These forces are formulated mathematically in the equations (4.6) to (4.8) in the order aforementioned.

$$F_{1,x} = G\, e^{\left(-\sigma_x\,(x-x_f)^2 - \sigma_z\,(z-z_f)^2\right)}\, T_{t_f}(t)\, e^{\mathbf{i}\beta y}, \qquad \{\forall x, z : x > 0 \wedge z > 0\} \tag{4.6}$$

$$F_{2,x} = G\, \frac{z}{z_f}\, e^{\left(-\sigma_x\,(x-x_f)^2\right)}\, T_{t_f}(t)\, e^{\mathbf{i}\beta y}, \qquad \{\forall x, z : x > 0 \wedge z_{\min} \leq z \leq z_{\max}\} \tag{4.7}$$

$$F_{3,x} = G\, \frac{z^2}{z_f^2}\, T_{t_f}(t)\, e^{\mathbf{i}\beta y}, \qquad \{\forall x, z : x_{\min} \leq x \leq x_{\max} \wedge z_{\min} \leq z \leq z_{\max}\} \tag{4.8}$$

where G is the intensity or strength of the distribution, σ_x and σ_z are parameters defining dispersion of the corresponding Gaussian function, x_f and z_f are the coordinates of the spatial centroid for each distribution

[5] More distributions were actually considered, but the ones presented here are qualitatively representative of the general behaviour elicited.

in the streamwise and wall-normal directions, respectively, and $\{x_{\min}, x_{\max}\}$ and $\{z_{\min}, z_{\max}\}$ define, where appropriate, the extension of the domain for each distribution used, corresponding to the minimum and maximum limits in the streamwise and wall-normal directions, respectively. It is noteworthy that the inclusion of the dependence on the spanwise direction (y) using $e^{\mathbf{i}\beta y}$ was dictated by the modal representation of the perturbations.

Definitions (4.6) to (4.8) were intentionally parametrised in terms of two main concepts, namely: location within the domain and extension over the domain. As mentioned before, such distributions, when applied as a forcing term F_x in eqn. (4.5), allow a streamwise vorticity source to be emulated, and are responsible for generating distinct initial velocity fields of cross-flow perturbations v and w in spanwise (y) and wall-normal (z) directions. In this way, values of σ_x, σ_z, x_f, z_f and regions delimited by $\{x_{\min}, x_{\max}\}$ and $\{z_{\min}, z_{\max}\}$ are used to regulate the range of scales that can be excited and hence the qualities of the streaks generated by the Low-order model (LOM).

The parameter G was assigned to values that guaranteed that the spatial density of each functional form was normalised,

$$G = \left[\frac{1}{L_x L_z} \int_{\Omega} F_x \, d\Omega \right]^{-1} \tag{4.9}$$

which allows the comparison of non-explicit amplification measures μ_i^* for different functional F_x. In previous expression L_x and L_z represent the total lengths of the domain Ω in streamwise and wall-normal directions, respectively. An upshot of this approach is that it allowed to get G prescribed explicitly, instead of being part of the optimization parameter space, and so reducing the number of parameters to be optimized. In any case, owing to the linearity of the current formulation, this value only scales the forcing function which precludes any attempt of inclusion in an optimization problem.

To create a finite duration of the excitation in the model, the function $T_{t_f}(t)$ is set to be a step function:

$$T_{t_f}(t) = \begin{cases} 1 & \text{if } 0 < t \leq t_f, \\ 0 & \text{if } t \leq 0 \vee t > t_f. \end{cases} \tag{4.10}$$

which induces a time-invariant behaviour in the forcing function for a finite period of time t_f. Previous works employing the fictitious body force approach have used this finite period of forcing to tune proper scales of the streaks generated. For instance, it is possible to generate long streak like structures and even to adjust the spanwise scales of the optimal streak by assigning this duration to some different value. A numerical value, somehow common, for this forcing time is $t_f^+ = 15$, a semi-empirical value which was proposed by el Hak and Hussain [121] on the basis that such interval produces the 'best' artificially induced burst: a non-linear

process disrupting the near-wall streaks and which is considered to cause the so-called lift-up effect. This value is used in the LOM model proposed by Lockerby [37] and explored by Togneri [72].

Owing to the seeming arbitrariness of such a selection, in the present work the time function is explored for different periods, including instantaneous forcing. In this last case this function is approximated as $t_f \to 0$ noting that in fact an extended duration is not required to generate streaky structures at all. In this regard, the numerical experiments herein reported were carried out with the forcing term applied for only one time step when instantaneous forcing was intended. By activating this forcing term for a single numerical time step, an approximation to a delta function in time, or more precisely to a discrete-time unit impulse, is produced, and therefore resembling an initial condition, though not fully resolved in time, without abandon of the body-force concept. A more detailed discussion on this equivalence is presented in § 4.3.4.

The majority of results reported here were obtained for values of x_{min} and x_{max} adjusted to ensure that the centroid of each forcing distribution was located at some fixed position. In any case, parameters x_{min}, x_{max} and the location of the centroid parameter x_f do not have material significance, as the response is translationally invariant in the x and y directions. The wall-normal location of this centroid, parameter z_f, was one of the key elements of this numerical study. This parameter does define the location of the centroid, and in some cases the total extension, in wall-normal direction of the distribution, i.e. the values of the limits in the wall-normal direction z_{min} and z_{max}. In this study the range of values for the wall-normal location of the centroid is limited to $z_f^+ = 5.0 - 40.0$; additional details of the numerical simulations are presented in §4.4. A spatial representation of these distributions is shown in figures 4.2a to 4.2c. A summary of values, roles and relations of the parameters for the functional forms of the body-force functions is presented in table 4.3.

Forcing function	x_f^+	σ_x	$x^+_{\min}$	$x^+_{\max}$	z_f^+	σ_z	$z^+_{\min}$	$z^+_{\max}$
$F_{1,x}$	**P.P.**	**P.O.**	0.0	L_x	**P.O.**	**P.O.**	0.0	L_z
$F_{2,x}$	**P.P.**	**P.O.**	0.0	L_x	**P.O.**	N.A.	0.0	$\frac{3.0}{2.0}\, z_f^+$
$F_{3,x}$	**P.P.**	N.A.	**P.P.**	**P.P.**	**P.O.**	N.A.	0.0	$\frac{4.0}{3.0}\, z_f^+$

P.P.: Parameter prescribed; **P.O.**: Parameter to be optimized; **N.A.**: Not applicable;

Table 4.3: Summary of relations and roles in the optimization problem, of the parameters for the forcing functions used as EM to generate streaks.

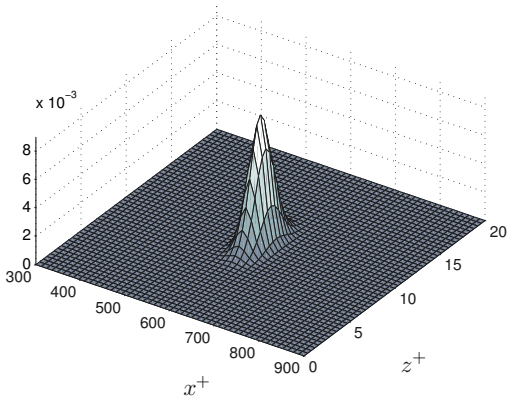

(a) Spatial representation of body-force $F_{1,x}$. Distribution centred at $x_f^+ = 600.0$ and $z_f^+ = 10$

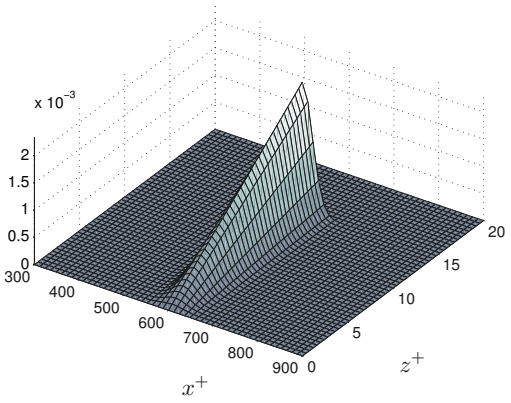

(b) Spatial representation of body-force $F_{2,x}$. Distribution centred at $x_f^+ = 600.0$ and $z_f^+ = 10$

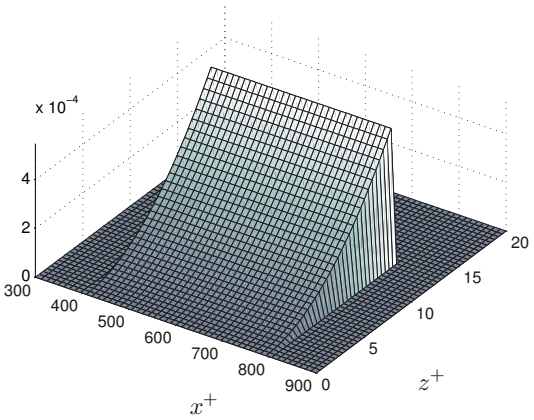

(c) Spatial representation of body-force $F_{3,x}$. Distribution centred at $x_f^+ = 600.0$ and $z_f^+ = 10$

Figure 4.2: Spatial representation of intensity for different vorticity sources. (a) $F_{1,x}$, (b) $F_{2,x}$, (c) $F_{3,x}$. For all the cases $x_f^+ = 600.0$ and $z_f^+ = 10.0$

4.3.3 Excitation Mechanism by Initial Condition

In spite of the convenience and advantages of the body-force approach, there are some obvious drawbacks. As it will be discussed in further detail in § 4.3.4, and briefly exposed in the results section § 4.4, two aspects of this approach which are not fully satisfactory are: the need for an empirical definition of the forcing time t_f^+; and the inconvenience in the prescription of specific perturbation structures. In some way the forcing time can be considered as an adjustment of the spatial-temporal optimization to attain correct scales, as will be discussed further below. This motivated the idea for prescribing initial disturbance velocity fields, rather than an artificial body force on vorticity, which is an alternative and more common methodology to perturb the LNSE. Stipulating explicitly the velocity fields allows a more flexible and coherent means of normalising, plus some other advantages.

Some of the distributions used for setting the fictitious body force were employed as mathematical functions prescribing initial conditions on either spanwise velocity or wall-normal velocity, i.e. the cross-flow components responsible for streak generation. Extra care was taken to guarantee that the initial velocity field was solenoidal, as well as the associated vorticity fields within the primary variables set.

Additionally, where required, the mathematical definition on the domain bounds for each functional distribution was adjusted to also ensure a non-slip condition at the wall. In this manner, most of the previous discussion regarding definition of variables for the functional distributions can apply directly to this EM concept, with the only difference lying on the practical/numerical incorporation of the initial conditions.

Obviously in this new approach the time lapse parameter has been eliminated altogether. Additionally, in order to further speed-up the multilevel optimization process, two new definitions were incorporated to the model, both of them with a reduced set of parameters, for which results are presented here.

In order to generate near-wall streaks in the current LNS simulations with Initial Conditions (IC) as the EM, two functional definitions for the wall-normal velocity are introduced, and particularly with none of them bearing any resemblance to the near-wall streaks. It is shown that these definitions, once a near-optimal set of parameters is found, allow transient growth to act, and thus streaks to develop naturally. This is an additional simplification to the low-order model (LOM) of [38] and to those defined previously.

The first functional IC presented here, introduced in 3.5.3, is referred to as $I_{1,w}$. It consists of a streamwise uniform wall-normal velocity perturbation field defined as,

$$
\begin{aligned}
u(x,y,z,t=0) &= 0 \\
v(x,y,z,t=0) &= -\int_y \frac{\partial w}{\partial z} dy \\
w(x,y,z,t=0) &= G\, z^2\, e^{-\sigma_z\, z^2}\, e^{\mathbf{i}\beta y}
\end{aligned}
\tag{4.11}
$$

where optimisation is performed only over parameter σ_z. Although immaterial to the EM, and just for numerical convenience, the parameter G was adjusted to impose a spatial density of the energy induced by the IC equal to the unit. In this way, and in a similar fashion as to the previous definition of G, this allows to compare non-explicit amplification measures μ_i^* with EM by IC.

A second IC used as EM, herein labelled as $I_{2,w}$, is a variation of the previous one featuring streamwise dependence and defined as

$$
\begin{aligned}
u(x,y,z,t=0) &= 0 \\
v(x,y,z,t=0) &= -\int_y \frac{\partial w}{\partial z} dy \\
w(x,y,z,t=0) &= G\, x^2\, (L_x - x)^2\, e^{-\sigma_x\, (x-x_f)^2}\, z^2\, e^{-\sigma_z\, z^2}\, e^{\mathbf{i}\beta y}
\end{aligned}
\tag{4.12}
$$

with L_x being the total extension of the computational domain under consideration, x_f is the longitudinal location of the centroid for the streamwise Gaussian function and σ_x and σ_z are the dispersion parameters of both Gaussian functions, in a similar manner as for the body-force cases. In this case the optimization is performed over parameters σ_x and σ_z.

Figures 4.3a and 4.3b portrait a physical representation of the distributions for the wall-normal perturbation velocity. As it can be noted, any reference to the centroid location is abandoned, which is why it is absent from the optimization parameters (x_f is prescribed, as with the forcing function case).

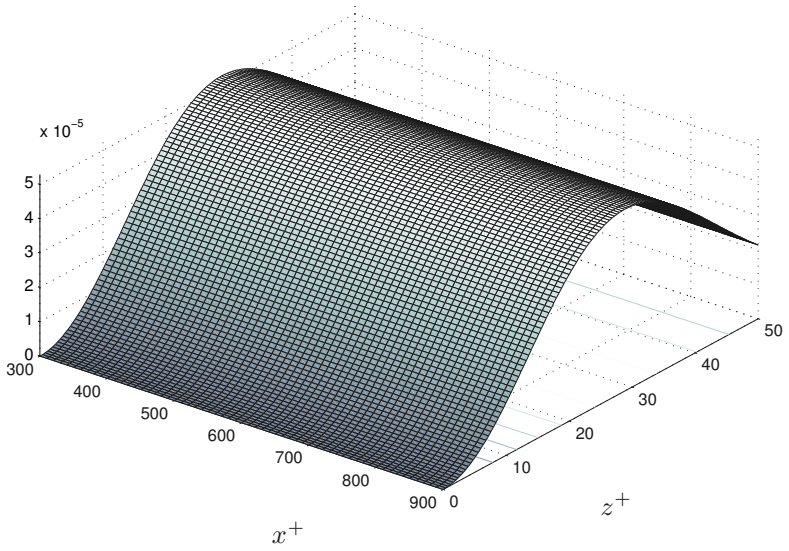

(a) Initial condition $I_{1,w}$

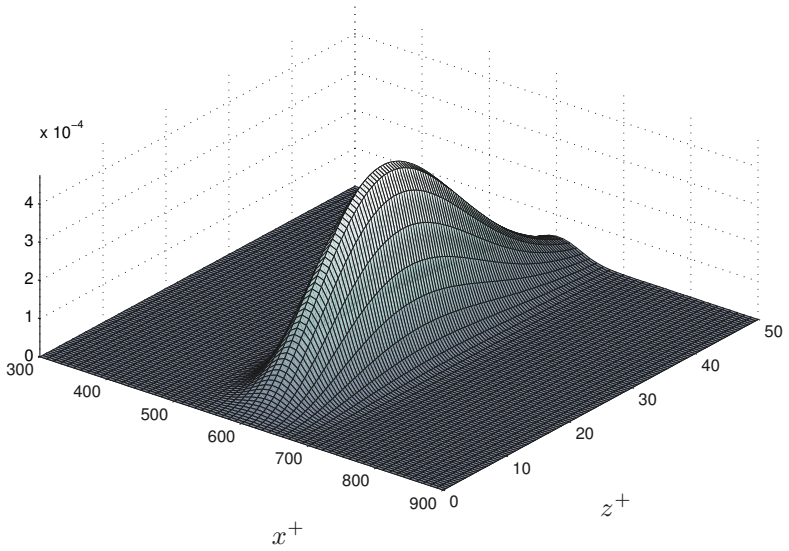

(b) Initial condition $I_{2,w}$

Figure 4.3: Physical representation of distributions employed as LOM for the wall-normal perturbation velocity. (a) Wall-normal perturbation velocity for $I_{w,1}$; (b) Wall-normal perturbation velocity for $I_{2,w}$, located at $x_f^+ = 600.0$

4.3.4 Equivalence between Forcing-EM and Initial-Condition-EM

Although the two EM selected in this thesis may seem, in principle, not fully connected, it has been previously suggested that there is in fact an equivalence between these two types of excitation mechanisms. To elaborate further this idea, let us consider two general examples.

As first example, consider an 'exactly' implicit discretization scheme for the Vorticity Transport Equation (VTE) in x-direction, equation (4.5), as

$$\frac{\omega_x^{n+1}-\omega_x^n}{\Delta t}-\frac{1}{Re}\frac{\partial^2}{\partial z^2}\left(\frac{\omega_x^{n+1}-\omega_x^n}{2}\right)+\frac{M^{n+1}-M^n}{2}=\frac{F_x^{n+1}-F_x^n}{2} \tag{4.13}$$

with n and $n+1$ representing the current and next predicted time step, respectively, M representing the convective terms and F_x the streamwise forcing function, i.e. the EM in the forcing case.

Applying a forcing-EM at $n=0$, and setting a null initial condition for the streamwise vorticity $\omega^0=0$, thus the first time step prediction at $n=1$ can be written, after a simple manipulation, as

$$\frac{\omega_x^1}{\Delta t}-\frac{1}{2\,Re}\frac{\partial^2\omega_x^1}{\partial z^2}+\frac{M^1}{2}=\hat{F_x}^0 \tag{4.14}$$

where a factor of $-1/2$ has been absorbed into the term $\hat{F_x}^0$. By assuming an unforced problem, i.e. prescribing an initial-condition-EM, then $F_x^n=0$ for any n, and equation (4.13), for the first time step, yields

$$\frac{\omega_x^1}{\Delta t}-\frac{1}{2\,Re}\frac{\partial^2\omega_x^1}{\partial z^2}+\frac{M^1}{2}=\frac{1}{2\,Re}\frac{\partial^2\omega_x^0}{\partial z^2}-\frac{\omega_x^0}{\Delta t}-\frac{M^0}{2} \tag{4.15}$$

which is some 'general form' of equation (4.14). So it is clear that provided an initial condition ω^0 can be determined such that

$$\frac{1}{2\,Re}\frac{\partial^2\omega_x^0}{\partial z^2}-\frac{\omega_x^0}{\Delta t}-\frac{M^0}{2}=\hat{F_x}^0 \tag{4.16}$$

then, apart from a sign reversal, the two formulations are fully equivalent. A minor detail must be mentioned: some care must be taken if a direct application of this equivalence is to be applied, since the term M^0 involves convective terms, although this does not alter the degree of difficulty in a conversion between the two types of EM.

As a second example let express the linearization of the general expression equation (4.1) as

$$\dot{\mathbf{u}}=\mathcal{L}_{\mathrm{NS}}\left[\mathbf{u}\right]+\mathbf{f} \tag{4.17}$$

for which it is possible to formulate an explicit discretization scheme as

$$\begin{aligned} u^{n+1} &= u^n + \Delta t\ (\mathrm{L}[u^n] + f^n) \\ &= (u^n + \Delta t f^n) + \Delta t\ \mathrm{L}[u^n] \end{aligned} \tag{4.18}$$

where L stands for any given discrete representation of $\mathcal{L}_{\mathrm{NS}}$. Noting that any initial-condition-EM implies $u^0 = \hat{u}^0$, and $f^n = 0$ for all n time steps, the previous expression in the IC-EM, for the first time step, yields

$$u^1 = \hat{u}^0 + \Delta t\ \mathrm{L}[\hat{u}^0] \tag{4.19}$$

On the other hand, for any forcing-EM $u^0 = 0$, $f^0 = \hat{f}^0$, and $f^n = 0$ for $n = 1$; in this way equation (4.17), for the forcing-EM, can be expressed as

$$u^1 = \Delta t\, \hat{f}^0 \tag{4.20}$$

If these last two expressions are compared then, similarly as in the previous example, an equivalence between both formulations of EM is directly obtained, provided the following relation can be prescribed

$$\Delta t\, \hat{f}^0 = \hat{u}^0 + \Delta t\ \mathrm{L}[\hat{u}^0] \tag{4.21}$$

which would lead exactly to the same subsequent evolution for u as in equation (4.19), with

$$\hat{u}^0 = \left(\frac{I}{\Delta t} + \mathrm{L} \right)^{-1} \hat{f}^0 \tag{4.22}$$

These examples show that, in general, the equivalence between the two EM is easy to elicit for any given initial condition $\hat{u}^0$ (or its representation in terms of vorticity, ω^0), for any given forcing function $\hat{f}^0$. Nevertheless, two additional aspects must be considered for completeness.

In the case of forcing-EM, and examining again the linearized general expression

$$\dot{\mathbf{u}} = \mathcal{L}_{\mathrm{NS}}\left[\mathbf{u}\right] + \mathbf{f}$$

then an immediate question arises when addressing this equivalence: What is the appropriate norm for measuring $\mathbf{f}$? The basic problem is that dimensions of $\mathbf{f}$ and $\mathbf{u}$ are not the same, since $\mathbf{f}$ has same dimensions as $\dot{\mathbf{u}}$, thus care must be taken when selecting an appropriate normalization for $\mathbf{f}$. Regarding this point, let consider the time integration of equation (4.17)

$$u(\mathbf{X},t) - u(\mathbf{X},0) = \int_0^t \mathcal{L}[u(\mathbf{X},t)]\,dt + \int_0^t f(\mathbf{X},t)\,dt \tag{4.23}$$

Now, in accordance with general definitions given by equation (4.4) and equation (4.10), let assume the forcing function to be expressed as

$$f(\mathbf{X},t) \approx f_0(\mathbf{X})\,\delta(t - t_f) \tag{4.24}$$

where t_f stands for the offset in time of the delta function, and $\mathbf{X} = \{x, y, z\}$; thus, using this definition, equation (4.23) can be written as

$$u(\mathbf{X},t) = \hat{u}^0(\mathbf{X}) + \int_0^t \mathcal{L}[u(\mathbf{X},t)]\,dt + f_0(\mathbf{X})\,(2\,\mathrm{H}[t - t_f] - 1) \tag{4.25}$$

or simply as

$$u(\mathbf{X},t) = \hat{u}^0(\mathbf{X}) + \int_0^t \mathcal{L}[u(\mathbf{X},t)]\,dt + f_0(\mathbf{X}) \qquad \text{for } t \geq t_f \tag{4.26}$$

and

$$u(\mathbf{X},t) = \hat{u}^0(\mathbf{X}) + \int_0^t \mathcal{L}[u(\mathbf{X},t)]\,dt \qquad \text{for } t < t_f \tag{4.27}$$

where H is the *Heaviside* function, t_f is the forcing activation time, and $\hat{u}^0$ is any given initial condition. When a forcing-EM is set as excitation mechanism then $\hat{u}^0 = 0$ and previous expression, at instant $t = t_f$, yields

$$u(\mathbf{X},t_f) = f_0(\mathbf{X}) \tag{4.28}$$

which, in the limit $t_f \to 0$ is effectively equivalent to an initial condition, as was discussed before. However, since the forcing function has been assumed to be a product of functionals, the portion of this forcing making the initial condition, after a time integration, is

$$f_0(\mathbf{X}) = G\,X(x)\,Z(z)\,e^{\mathbf{i}\,\beta\,y} \tag{4.29}$$

where all coefficients, except G, represent spatial functionals. A normalization reconciling the temporal and spatial scales must be assumed by G, as it has already been proposed. Additionally, given that the temporal functional is represented by a Heaviside function, it is perfectly valid to express the interval $0 \leq 0 < t_f$, in a discrete representation, as a factor of a time step Δt, as long as this also remains small.

Finally the second noteworthy aspect, although not really a problem, is associated with the technical suitability on the prescription of a specific flow field distribution, for instance, when a specific configuration of velocity or vorticity should be applied but using a forcing-EM. It is clear now that an equivalent forcing functional

form can be relatively easy to obtain by using similar procedures to those exposed in the examples presented above. Nonetheless, such a conversion would require additional steps like calculation of derivatives of the fields and evaluation of the products related to convective terms. This process would eventually render the intended nature of the original distribution into an expression which may not be so easily associated to the original target source, making somehow cumbersome a simple process of prescription of a selected flow field. From this point of view the direct application of the intended initial condition is equivalent and equally fine for the purposes of perturbation of the linearized system.

4.4 Numerical experiments and results

In the present discussion about the numerical experiments, recurring reference will be made to the the Low-Order and Excitation models in conjunction with the LNSE. For brevity, when a mention is to be made in this document about the selection of an EM for the LNSE here implemented, and the set of numerical values obtained by an optimization problem, such set or combination will be sometimes denoted as the LNSE-LOM-system, meaning the full model: selection of a functional EM for the LNSE and the values obtained by the LOM.

A series of simulations have been performed to explore the sensitivity of the streak response to changes in the form of the body-force or the initial condition. The results presented in this section represent a subset of all the forcing types and flow initial conditions considered in this study, but for which results have been broadly similar to those presented; space precludes a full account of these simulations. As base profile for the numerical experiments presented in this work, the turbulent velocity profile presented and discussed in §2.3.3 and §3.4.2 is used as mean base profile. Most of the results were obtained for a zero-pressure-gradient turbulent boundary layer at $Re_{\delta_*} = 5000$. Experiments accounting for variation in Reynolds number did not exhibit significant changes in the streak response when non-dimensionalised with inner units. This Reynolds number independence is discussed below.

For the simulations presented here, a computational domain of size $L_x^+ = 3490$, $L_z^+ = 1360$ was used. The computational domain was resolved using a grid of 350×128 points, i.e. with 128 Chebyshev modes and in accordance with the mapping given in §3.1.2. The resulting effective grid resolution in the streamwise direction is $\Delta x^+ = 10$. For all the numerical simulations the streamwise location of the centroid was set to $x_f^+ = 600.0$ from the origin of the domain. In the spanwise direction a total of 36 Fourier modes were used in the parallel simulations for the optimization. The range of values in the first level of the parametric search was set to $\lambda_y^+ = \{51.25 - 200.0\}$. As indicated before, the wall-normal location of the centroid z_f^+ was set to be part of the optimization parameters space. In this case the first-level optimization was limited to the range of values $z_f^+ = \{5.0 - 40.0\}$. The simulation time was set to a period of $\tau_t^+ = 400.0$, with a time step of $\Delta t^+ \approx 0.20$. For the cases where a streamwise Gaussian function has been employed, the parameter σ_x was constrained to limit either the extension from x_f or the concentration around x_f of the distribution representing a given $F_{\mathbf{EM}}$. A similar procedure was used to constrain values of σ_z, where a Gaussian functional was set in the wall-normal direction. These parameters are associated with the dispersion of the Gaussian function; large values of σ^+ produce highly concentrated distributions, while small values produce widespread distributions. In most of the numerical experiments, except where stated, these parameters were constrained to $\sigma_x^+ = \{0.001 - 1.0\}$ and $\sigma_z^+ = \{0.005 - 1.0\}$, in the streamwise and wall-normal directions, respectively. These constraints helped to

avoid numerical discontinuities of the distributions at the boundaries of the physical domain.

At this point it is convenient to introduce two simple graphic "tools" which are particularly useful for the analysis and presentation of results. The first, hereupon referred to as an *optimization map*, condenses the outcome of the optimal search at every iterative step of the optimization process as a contour map in terms of the parameter pair $\{z_f^+, \lambda_y^+\}$ or $\{\sigma_z^+, \lambda_y^+\}$; any other optimization parameter, required for a given $F_{\mathbf{EM}}$ definition, is hidden. These plots are not intended to expose any tendency in the wall normal direction, in terms of response, owing to the fact that every point in the plot corresponds to different realisations, i.e. to different simulations in terms of forcing or initial condition parameters. The second graphic tool, hereby denominated as a *response map*, helps to envisage, precisely, the wall normal dependence in accordance with measures μ_1 to μ_3 (a contour plot of the measure as a function of the pair $\{z_v^+, \lambda_y^+\}$). This type of plot shows the response of the system for a single form $F_{\mathbf{EM}}$, although includes the complete range of spanwise modes employed in a given simulation, i.e. the optimal spanwise mode is taken. In this work, for simplicity in both types of maps, the values are normalized against the global maximum present in the corresponding plot.

In the forcing-EM case, for the first level of optimization, 10 wall-normal locations of the distribution centroid were prescribed, $z_f^+ = \{5.0, 7.5, 10.0, 12.5, 15.0, 17.5, 20.0, 25.0, 30.0, 40.0\}$. The definitions of the initial-condition-EM do not require of a value for z_f^+, and therefore this was not part of the optimization problem for such EM. The set of values for the spanwise wavelengths, for both cases (using forcing-EM and initial-condition-EM), was set to the range $\lambda_y^+ = \{51.25 - 200.00\}$ using 36 equally spaced modes (as mentioned before). Owing to the coarse-grained parametric method used to search for an optimal, the present LNSE-LOM-system is only able to find a 'near-optimal' streak. However, as it is presented below, once an optimal set of parameters was found for a given optimization problem (Type I to IV), *all* responses exhibited development of streak disturbances in u velocity perturbation (the signature being transient growth: algebraic growth followed by viscous decay). A representative example of this behaviour, was shown in Figure 4.1 (forcing $F_{1,x}$ and measure μ_1) evaluated at five different wall-normal planes. It is clear then that this general behaviour of the generation of streaks is largely insensitive to the form of force or initial condition and measure prescribed; in respect to the validity of LOM it suggests that the exact form and parameters chosen are not particularly important for streak generation phenomena. With the aid of the optimization and response maps, it was possible, in this thesis, to characterize features affecting the structural properties of the 'near-optimal' streaks. However, this study did not focus on a detailed examination of the functional features of each body-force or initial condition; for instance, the variation or trend of a given measure as a function of a single parameter of the selected EM is not presented. Instead, in this work a more global approach is taken, with major interest on the final LOM (i.e. the outcome of the selected optimization problem), regardless what possible implications exist for a single parameter variation.

4.4.1 Results for streaks generation by vorticity forcing-EM

Although it was not included in table 4.3, but due to its importance to the body-force EM, it was necessary to perform an analysis of the impact of the forcing time t_f on the LOM. As starting point for the numerical experiments on t_f^+, the value proposed by el Hak and Hussain [121] of $t_f^+ = 15$ was selected, with LOM given by the optimization problem Type-III using non-explicit amplification measures, particularly $\mu^*_{4,\Omega}$.

Figure 4.4 shows the results of optimization Type-III for the body-force $F_{1,x}$ and non-explicit amplification measure $\mu^*_{4,\Omega}$ using $t_f^+ = 15.0$. This is essentially the optimization problem examined in [1, 37]. From this optimization map it is clear that, for the optimal set of parameters obtained, the LNSE provides a value for the spanwise spacing of $\lambda_y^+ = 89.5$, which is well within the ranges provided in [18] of $\lambda_y^+ = 120 \pm 52$, and close to the range provided in [122] of $\lambda_y^+ = 81.5 \pm 1$.

Figure 4.5 shows results of the optimization Type-III using $F_{1,x}$ and $\mu^*_{4,\Omega}$, although for a forcing time of $t_f^+ = 10.0$. By comparing figures 4.4 and 4.5 it is possible to see a reduction in the optimal spanwise spacing from $\lambda_y^+ = 89.5$ to $\lambda_y^+ = 81.0$, although the optimal wall-normal plane for z_f^+ remains the same. This shows that the empirical value for t_f^+ is in some way a tuning parameter to adjust the output of the LNSE-LOM-system. However, this change is not critical, in this case, as the value of λ_y^+ for $t_f^+ = 10.0$ also remains within the range of $\lambda_y^+ = 120 \pm 52$.

It is worthy of note that for the cases presented in figures 4.4 and 4.5, the optimal values for σ_x^+ and σ_z^+ remain unvaried, both equal to 1.0; suggesting that they are unaffected by changes of forcing time. However, this is in fact just an artifact of the coarse-grained optimization. Additional levels of optimization reveal that these parameters also change, but the variation is so small that in a first-level loop of the optimization cycle they appear insensitive to changes in t_f^+. The relatively large values of σ_x^+ and σ_z^+, which implies a higher concentration around $\{x_f^+, z_f^+\}$, indicate that this optimization problem ($\{$Type-III, $\mu_4^*\}$) favours functional forms or distributions producing high spatial gradients, which in turn helps to generate streaks with a high streamwise momentum, in comparison to the other forcing conditions, i.e., to other sets of parameters, in accordance to figures 4.4 and 4.5. For the moment these results indicate that if the spatial density of the forcing function is kept constant, a concentrated source is required to generate high values of streamwise momentum.

In order to tackle the question regarding generality of previous results, the optimal response of the forcing functions $F_{2,x}$ and $F_{3,x}$, for exactly the same conditions as above, are examined. Results for these two functional forces for a forcing time of $t_f^+ = 15.0$ are presented in figures 4.6 and 4.7. It is clear that $F_{2,x}$ shares some features with $F_{1,x}$, as both involve a Gaussian function in the streamwise direction x. This is

in fact reflected in the results obtained for $F_{2,x}$, which for the case {Type-III, $\mu^*_{4,\Omega}$} are strikingly similar to those obtained for $F_{1,x}$ for the same problem. The set of optimal values in this case are also consistent with previous results: $z_f^+ = 10.0, \lambda_y^+ = 85.25, \sigma_x^+ \approx 1.0$. This seems to indicate that, from the point of view of the linearized operator studied in this thesis, the wall-normal variation of the vorticity source is not so critical for the selectivity of the adequate spanwise scales. Some caution must be taken at this moment, however, as this is only true for the problem {Type-III, μ^*_4} and forces $F_{1,x}$ and $F_{2,x}$.

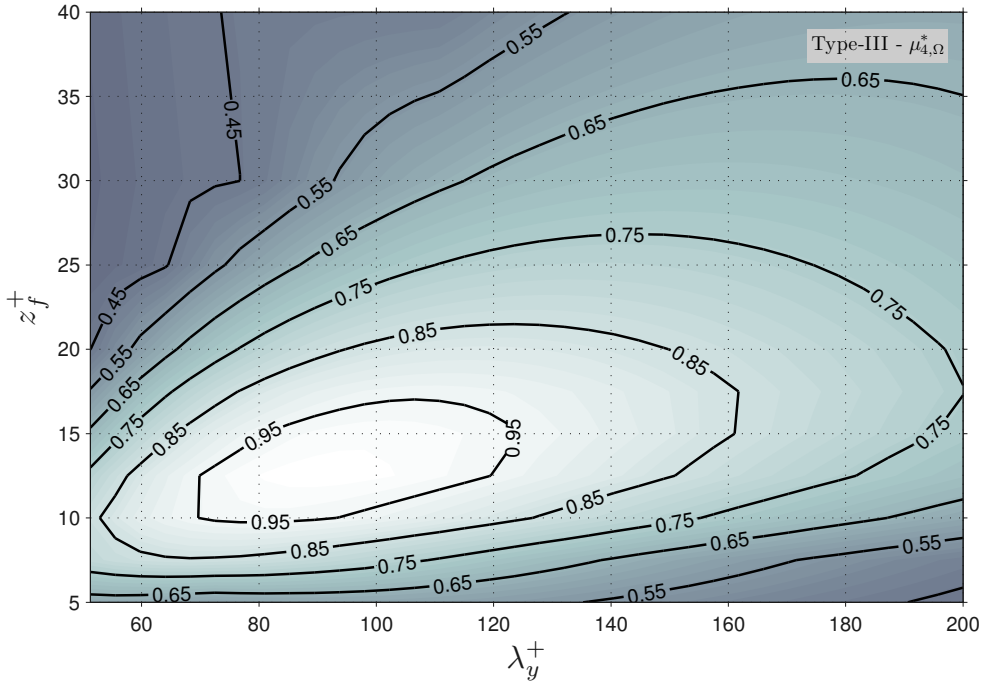

Figure 4.4: Optimization map showing results of a 1-level optimal solution for problem Type-III using $F_{1,x}$ and $\mu^*_{4,\Omega}$. Optimal set $\{z_f^+ = 12.5, \lambda_y^+ = 89.5, \sigma_x^+ \approx 1.0, \sigma_z^+ \approx 1.0\}$. Values have been normalized against global maximum, so contour lines indicate % w.r.t. that global. Simulation parameters: $Re_{\delta_*} = 5000$, $\tau_t^+ = 400$, $t_f^+ = 15$

Results of $F_{3,x}$ for the same problem {Type-III,μ^*_4} show a totally different picture. In this case the optimal set is $z_f^+ = 25.0, \lambda_y^+ = 174.5$, which is totally off the range of theoretical and experimental expected values for λ_y^+. Distribution $F_{3,x}$ features, in a finite region, a streamwise independent vorticity source. However, it seems that due to the lack of streamwise variation, the operator favours large spanwise scales and high values of z_f^+, in order to generate high values of streamwise momentum per spatial density unit of the body-force. In such conditions a trade-off between the viscous diffusion and the small spatial gradients seems to take place, which might explain the large values of streamwise perturbation velocity only at high values of λ_y^+. It is clear then that universality for this type of problem ({Type-III,μ^*_4}) does not exist, and an adequate selection of the expression for forcing-EM must be carried out along with the optimization problem, if a sensible range of optimal spanwise scales λ_y^+ is to be obtained.

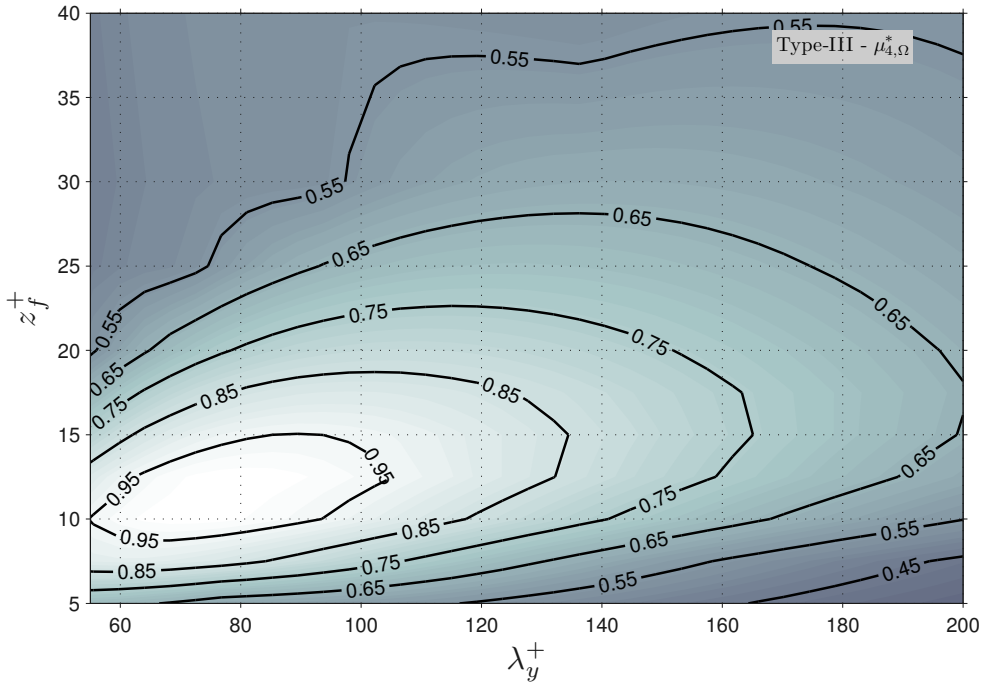

Figure 4.5: Optimization map showing results of a 1-level optimal solution for problem Type-III using $F_{1,x}$ and $\mu^*_{4,\Omega}$. Optimal set $\{z_f^+ = 12.5, \lambda_y^+ = 81.0, \sigma_x^+ \approx 1.0, \sigma_z^+ \approx 1.0\}$. Values have been normalized against global maximum value; contour lines denote percentage of measure with respect the maximum. Simulation parameters: $Re_{\delta_*} = 5000$, $\tau_t^+ = 400$, $t_f^+ = 10$

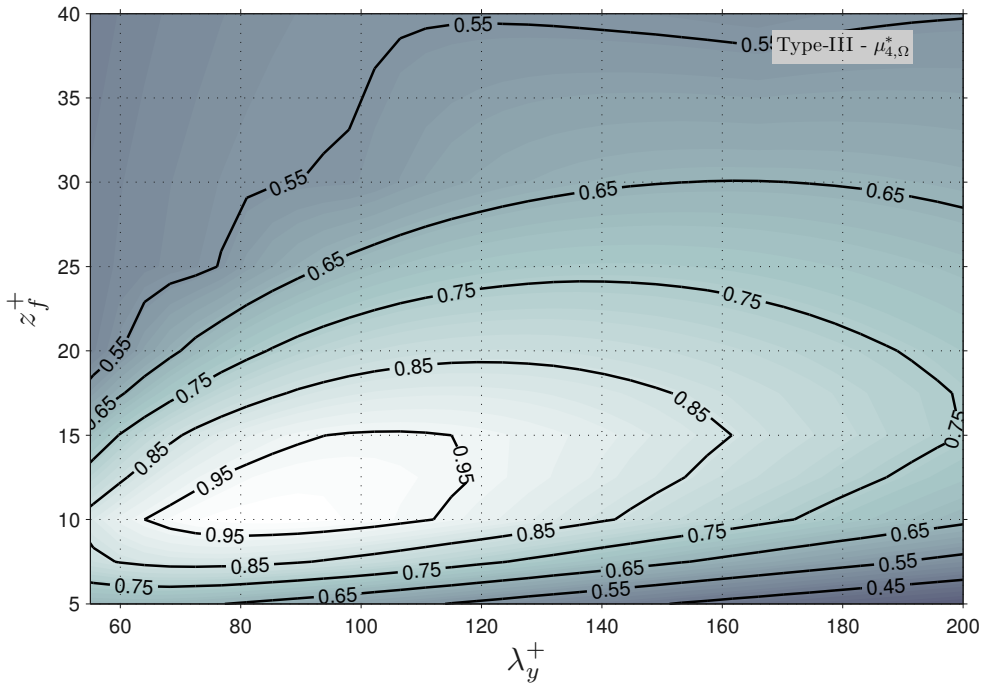

Figure 4.6: Optimization map showing results of a 1-level optimal solution for problem Type-III using $F_{2,x}$ and $\mu^*_{4,\Omega}$. Optimal set $\{z_f^+ = 10.0, \lambda_y^+ = 85.25, \sigma_x^+ \approx 1.0\}$. Values have been normalized against global maximum value; contour lines denote percentage of measure with respect the maximum. Simulation parameters: $Re_{\delta_*} = 5000$, $\tau_t^+ = 400$, $t_f^+ = 15$

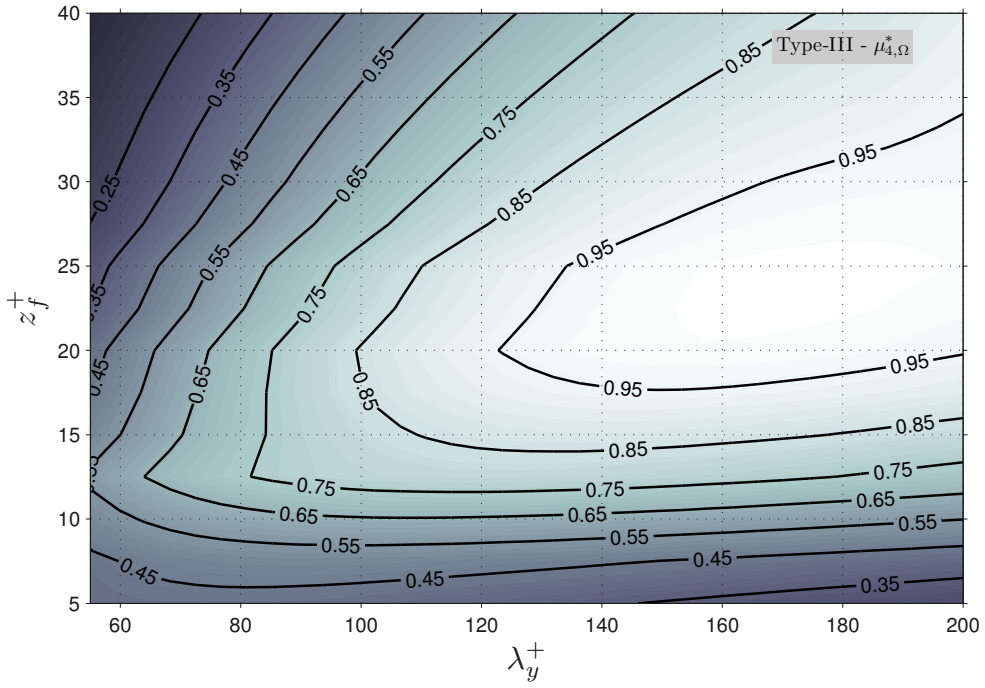

Figure 4.7: Optimization map showing results of a 1-level optimal solution for problem Type-III using $F_{3,x}$ and $\mu^*_{4,\Omega}$. Optimal set $\{z_f^+ = 25.0, \lambda_y^+ = 174.5\}$. Values have been normalized against global maximum value; contour lines denote percentage of measure with respect the maximum. Simulation parameters: $Re_{\delta_*} = 5000$, $\tau_t^+ = 400$, $t_f^+ = 15$

What about the structure itself of the streaks generated? In figures 4.8 to 4.10 a side view of the evolution is shown, at five different time instants, of the streamwise perturbation velocity for the optimal perturbations obtained with problem {Type-III, μ_4^*} for forces $F_{1,x}$, $F_{2,x}$ and $F_{3,x}$, respectively.

A well known and distinctive feature of the streamwise streaks is their streamwise elongation and upwards tilting of the downstream portion of the streak. This effect can be seen in figures 4.8 to 4.10, indicating that the LNSE can capture this behaviour, independently of the type of EM/LOM employed to generate the perturbations. It can also be seen that, from the generation of streaks point of view, there is no a radical distinction between these three situations ($F_{1,x}$, $F_{2,x}$ and $F_{3,x}$); i.e. all of them produce optimal perturbations that evolve in time in a similar fashion. It could be argued that, because these three forcing distributions generate a source of vorticity (in this case streamwise vorticity), a similarity should be expected, irrespective of their precise forcing features. However, it is clear that the attainment of experimentally observed spanwise scales relies on a more subtle combination of forcing type, measure and the optimization problem used.

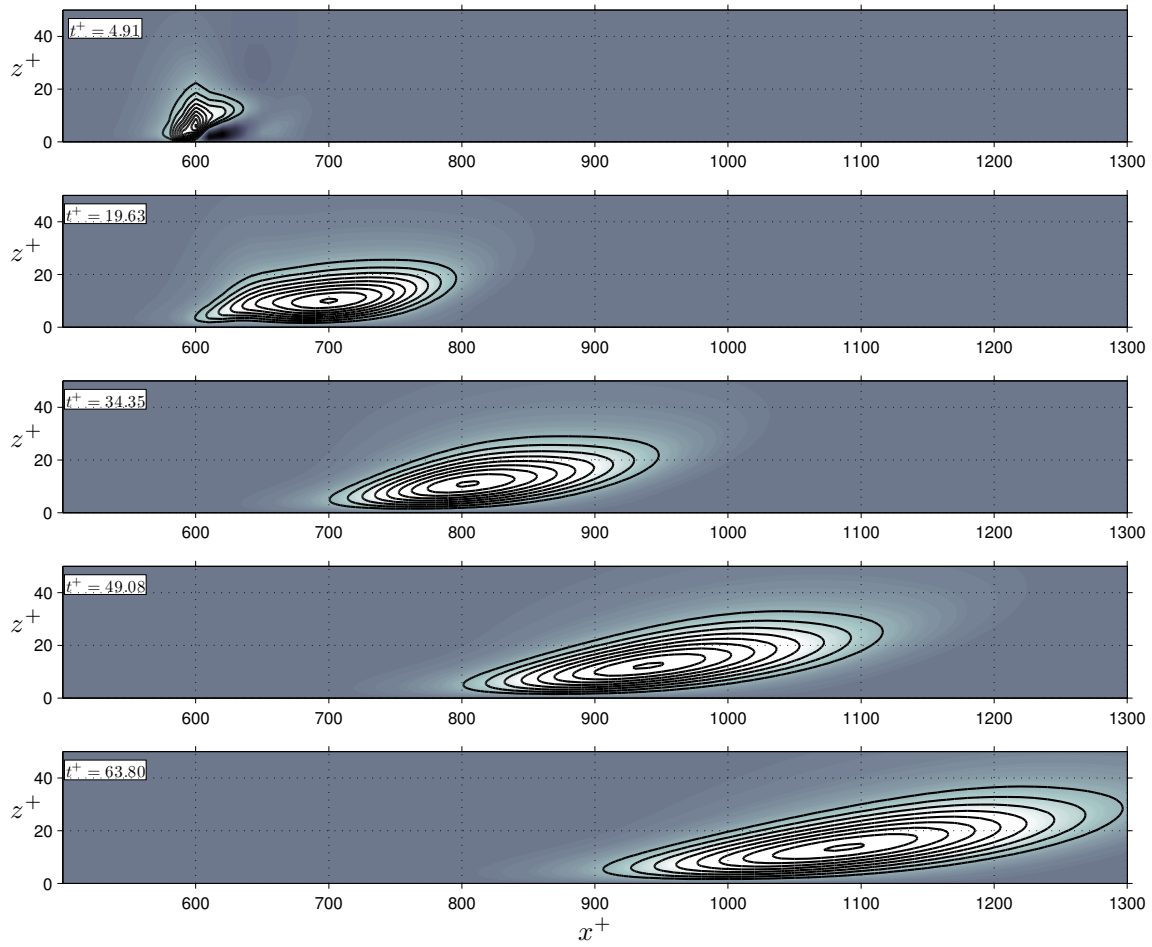

Figure 4.8: Development of streak for optimal values of problem Type-III using $F_{1,x}$ and $\mu^*_{4,\Omega}$; optimal set $\{z_f^+ = 12.5, \lambda_y^+ = 89.5, \sigma_x^+ \approx 1.0, \sigma_z^+ \approx 1.0\}$. Side view contours of streamwise velocity at $t^+ \approx 5, 20, 34, 49, 64$. Contours denote positive fraction of maximum streamwise perturbation velocity with increment of 0.1 from 0.19 to 0.99. Simulation parameters: $Re_{\delta_*} = 5000$, $\tau_t^+ = 400$, $t_f^+ = 15$

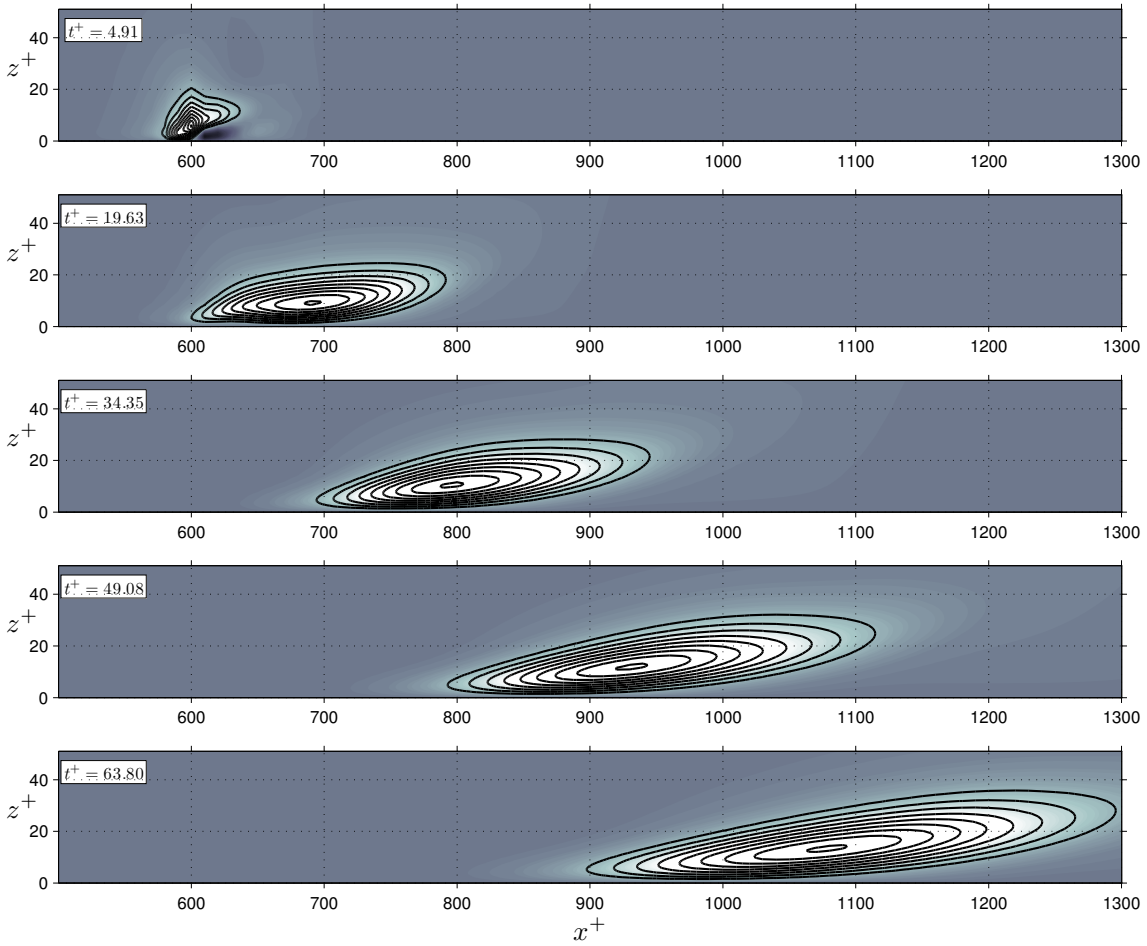

Figure 4.9: Development of streak for optimal values of problem Type-III using $F_{2,x}$ and $\mu^*_{4,\Omega}$; optimal set $\{z_f^+ = 10.0, \lambda_y^+ = 82.25, \sigma_x^+ = 1.0\}$. Side view contours of streamwise velocity at $t^+ \approx 5, 20, 34, 49, 64$. Contours denote positive fraction of maximum streamwise perturbation velocity with increment of 0.1 from 0.19 to 0.99. Simulation parameters: $Re_{\delta_*} = 5000$, $\tau_t^+ = 400$, $t_f^+ = 15$

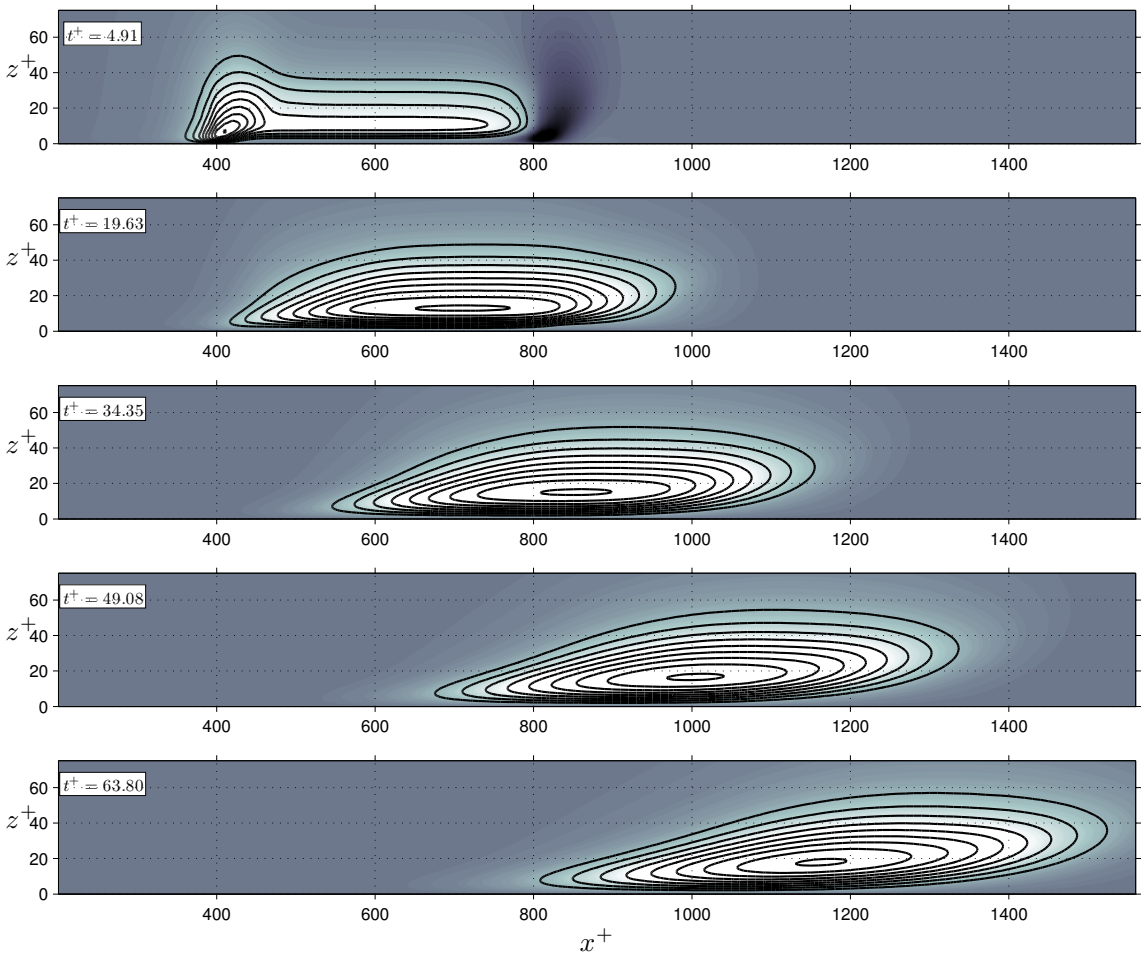

Figure 4.10: Development of streak for optimal values of problem Type-III using $F_{3,x}$ and $\mu^*_{4,\Omega}$; optimal set $\{z_f^+ = 25.0, \lambda_y^+ = 174.5\}$. Side view contours of streamwise velocity at $t^+ \approx 5, 20, 34, 49, 64$. Contours denote positive fraction of maximum streamwise perturbation velocity with increment of 0.1 from 0.19 to 0.99. Simulation parameters: $Re_{\delta_*} = 5000$, $\tau_t^+ = 400$, $t_f^+ = 15$

It is important to point out that the agreement with experimental data that has been found so far has been obtained thanks, maybe in a large part, to the normalization chosen. In other words, although the measure $\mu^*_{4,\Omega}$ is a non-explicit amplification measure, results of different simulations can be compared with each other because of the normalization in terms of the density of forcing (definition G in (4.9)). If another definition is chosen to perform the normalization, the optimal perturbations obtained from problem Type-III with μ^*_4 would be different. However, it is convenient to highly that, for the explicit amplification measures, the essential feature of our approach is to determine

$$\frac{\|A_{out}\|_{\text{out}}}{\|B_{in}\|_{\text{in}}}$$

where A_{out} and B_{in}, in general, can possibly be different properties. In this case, contrary to the non-explicit measures (like μ^*_4), changing

$$B_{in} \to G\, B_{in}$$

for any G makes no difference since then

$$A_{out} \to G\, A_{out}$$

Therefore, as it has been done, it is clear that it is easiest to restrict attention, for instance, to

$$\|B_{in}\|_{\text{in}} = 1$$

This rationale seems evident when the EM is an initial condition, but its implications are more subtle when there is a forcing present, as is the case for the currently studied EM. This type of EM needs a normalization in such a way that different forcing functions can be compared as if they were 'the same' (see § 4.3.4). In the present work, instead of exploring possible options for defining G, it was decided to explore different amplification measures, given a reference state $B(t_0)$, fixing the value of G as the density of the forcing function by using equation (4.9). It is obvious that the definition of measures μ_i requires the reference state to be non zero. When an initial condition is defined, amplification measures do not pose any problem. However, in the forcing-function case, strictly speaking, the initial state is zero so any reference to it will produce an ill-posed definition of μ_i. In order to overcome this apparent inconvenient two different scenarios are possible: to use the flow field at some number of computational steps after the imposition of the forcing; or to use the forcing time itself, t^+_f, to extract a reference state (as proposed before in § 4.3.4). In any of these cases, it is necessary to normalise the forcing-EM to produce, independent of any functional form, a fixed reference input; in this work, such normalization is always fixed using the definition of G.

In figures 4.11 and 4.12 are shown the results for the optimization problem {Type-II, $\mu_{4,\Omega}$} for $F_{1,x}$ using as a reference state the conditions at $t^+ = t^+_f$ and $t^+ = 2\Delta t^+$, respectively. Figures 4.13 and 4.14 present

simulation with the same conditions, but for $F_{3,x}$. As it can be seen, the use of different reference states bring about a change in the maximum spanwise mode observed. Although not presented here, this outcome was recurrent for the different measures and forces studied in this work. From these maps is evident that the time instant to extract the reference state to produce any amplification normalization is extremely critical.

It is interesting that the selection of the reference-state time can heavily influence whether an LOM is deemed accurate or not. In these figures is possible to see that for $F_{1,x}$, if $t_0 = t_f^+$, the optimal perturbation obtained reproduces adequately the expected streak scales, but using $t_0 = 2\Delta t^+$ renders the optimal off the appropriate ranges. For $F_{3,x}$, this situation is the exact opposite. In other words, even the distribution $F_{3,x}$, which previously seemed to not be able to produce appropriate spanwise scales of streaks, now looks like a more preferable candidate to LOM over $F_{1,x}$ (depending upon the reference state chosen).

An additional, and obviously, favourable upshot of using amplification measures is connected to the parameter G. Once an amplification measure was selected, the results of the optimization became fully independent of G, as had previously argued. In this way, whether or not G was used in the normalization of the EM, the results of all optimization problems using an explicit amplification measure were the same. This offers confidence in the explicit amplification measures (labelled from this point on just as the amplification measures) as a valid and robust way to find the optimal solution to any LOM.

Even though it is commonly accepted to consider amplification of energy as a standard measure for the study of transient growth, other measures were also considered (as defined in table 4.1), whose results are presented in the optimization maps 4.11 to 4.14.

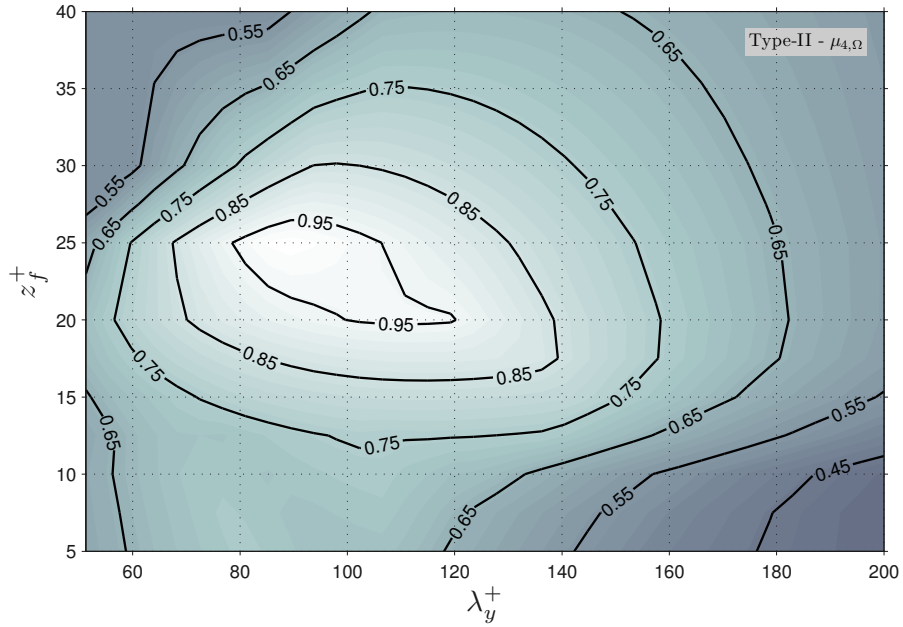

Figure 4.11: Optimization map showing results of a 1-level optimal solution for problem Type-II using $F_{1,x}$ and $\mu_{4,\Omega}$; reference state for amplification $B(t_0 = t_f^+)$. Optimal set $\{z_f^+ = 25.0, \lambda_y^+ = 89.5, \sigma_x^+ = 0.005, \sigma_z^+ = 0.5\}$. Values have been normalized against global maximum value; contour lines denote percentage of measure with respect the maximum. Simulation parameters: $Re_{\delta_*} = 5000$, $\tau_t^+ = 400$, $t_f^+ = 15$

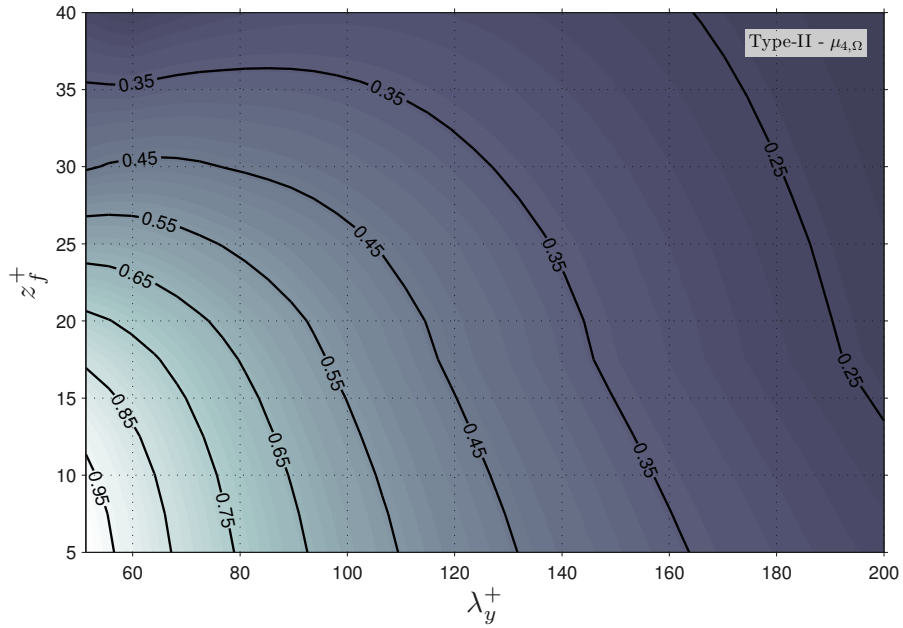

Figure 4.12: Optimization map showing results of a 1-level optimal solution for problem Type-II using $F_{1,x}$ and $\mu_{4,\Omega}$; reference state for amplification $B(t_0 = 2\Delta t^+)$. Optimal set $\{z_f^+ = 5.0, \lambda_y^+ = 51.25, \sigma_x^+ = 0.001, \kappa_x^+ = 0.005\}$. Values have been normalized against global maximum value; contour lines denote percentage of measure with respect the maximum. Simulation parameters: $Re_{\delta_*} = 5000$, $\tau_t^+ = 400$, $t_f^+ = 15$

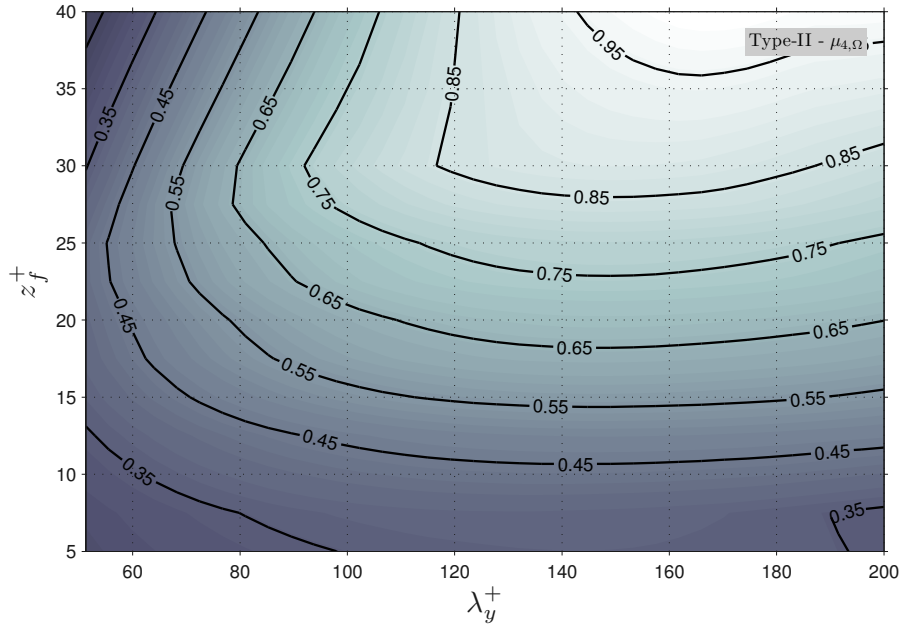

Figure 4.13: Optimization map showing results of a 1-level optimal solution for problem Type-II using $F_{3,x}$ and $\mu_{4,\Omega}$; reference state for amplification $B(t_0 = t_f^+)$. Optimal set $\{z_f^+ = 40.0, \lambda_y^+ = 166.0\}$. Values have been normalized against global maximum value; contour lines denote percentage of measure with respect the maximum. Simulation parameters: $Re_{\delta_*} = 5000$, $\tau_t^+ = 400$, $t_f^+ = 15$

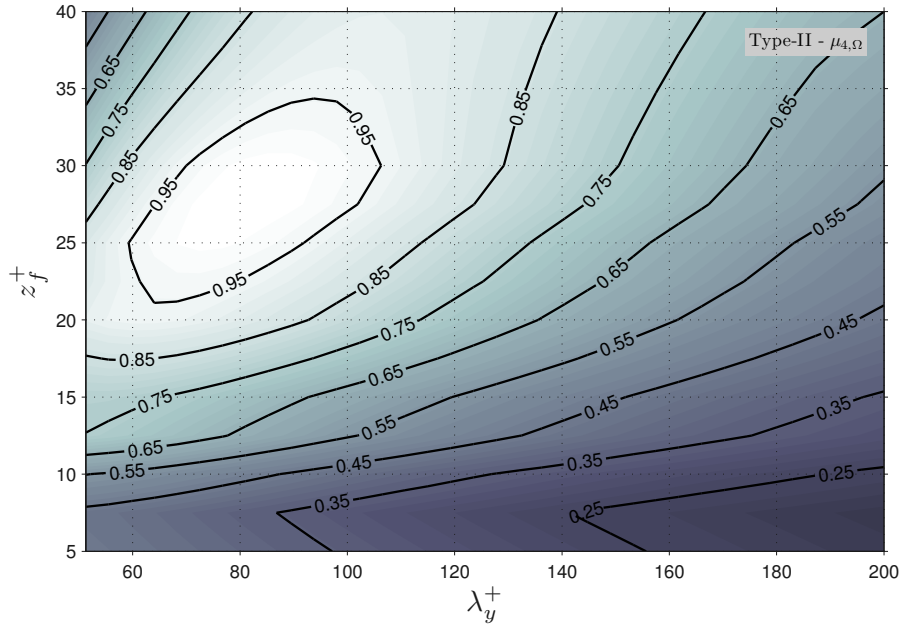

Figure 4.14: Optimization map showing results of a 1-level optimal solution for problem Type-II using $F_{3,x}$ and $\mu_{4,\Omega}$; reference state for amplification $B(t_0 = 2\Delta t^+)$. Optimal set $\{z_f^+ = 27.55, \lambda_y^+ = 81.0\}$. Values have been normalized against global maximum value; contour lines denote percentage of measure with respect the maximum. Simulation parameters: $Re_{\delta_*} = 5000$, $\tau_t^+ = 400$, $t_f^+ = 15$

At this point a decision has to be made in terms of what reference state to use in the solution of any of the optimization problems previously defined. To circumvent this issue the forcing time is made to approach zero, $t_f^+ \to 0$. In other words, in accordance with the ideas presented in § 4.3.4, this was equivalent to setting an initial condition, although using a forcing-EM. The system is then forced only for 1 or 2 time steps, which allows the same time instant to be used as a reference point in both cases: i.e., $t_0 = t_f^+ = 2\Delta t^+$. In this way it is still possible to estimate measures with their basis on an initial instant, without abandoning the concept of forcing-EM. By adopting such a methodology in the present work, some of the arbitrariness and empiric nature of LOM forcing was removed.

In all of the remaining simulations presented, the forcing term is applied for no more than two time steps, as an approximation to a delta function in time. However, The question is: is it possible for the forcing term to produce transient growth if applied for only one or two time steps? Actually, the answer is already provided by the amount of data available which relies only on initial conditions to produce transient growth [102].

A sample of different optimization maps, containing a variety of results obtained using a delta forcing in time, for the different optimization problems in table 4.2, is presented in figures 4.15 to 4.18; for simplicity the values of the optimal set of parameters has been intentionally omitted.

Figures 4.15a, 4.15c and 4.15e present the results of the optimization problem {Type-I, $\mu_{1,\Omega}$ } for forcing functions $F_{1,x}, F_{2,x}$ and $F_{3,x}$, respectively. This specific case corresponds to the maximization of the perturbation over $\tau^+ = 80.0$, which is analogous to the optimal perturbation case presented in [63]. In figures 4.15b, 4.15d and 4.15f are presented the results for a similar type of problem, Type-I with $\tau^+ = 80.0$ using $\mu_{5,\Omega}$. In all these cases the maximum perturbation has been found to be within a range of values for λ_y^+ that is consistent with experimental findings.

Optimization maps for the problem Type-IV, i.e. using integration in time for the period of simulation τ_t^+, are presented in figures 4.16a, 4.16c and 4.16e for the measure $\mu_{4,\Omega}$, and in the figures 4.16b, 4.16d and 4.16f for the measure μ_3. In this last case, which corresponds to optimization over a visualization plane, the optimal was found for $z_v^+ = 15.0$.

Figures 4.17a to 4.17c and figures 4.18a to 4.18c show the results for the optimization problems Type-II and Type-IV, respectively, using planar measure μ_1 for the three forcing functions. In the first case, optimization problem presented in figure 4.17, the visualization plane used was $z_v^+ = 10.0$, whereas in figure 4.18 the optimization was performed over $z_v^+ = 17.5$. From these plots, it is clear that measures μ_1, μ_2 and μ_3 have an excellent disposition to provide an optimal perturbation with scales similar to those observed experimentally.

The majority of the results presented so far have been centered in the spanwise scales of the streaks generated.

What about the wall-normal dependence on the streaks scales? Figures 4.19 and 4.20 show the response maps (described earlier) for the optimal perturbation obtained with problem {Type-IV, μ_1 at $z_v^+ = 10.0$ }, for forces $F_{1,x}$ and $F_{2,x}$ respectively. These show the dependence in the wall-normal direction of the response of the LNSE employed here. As it can be seen, there is some resemblance of these maps with their optimization counterparts, but both emerge from different concepts.

In the response map cases the vertical axis can be thought of as probes at fixed, vertical positions from the the wall. These response maps are constructed with a single simulation, even so, it is clear that the experimental streak scales are being picked-up, as it is a simulation of the optimal, selected by an LOM. It can be seen in these plots an increase of the strongest spanwise streak scale with the wall-normal direction, in agreement with experimental findings. Additionally, in both cases presented in figures 4.19 and 4.20, the range of most responsive spanwise scales, for the given set of parameters of each body-force, is in excellent agreement with those reported in literature, and discussed previously.

Considering the great variety of the selected forcing functions and the different optimization specifications considered, it is evident that, in general, the selectivity of the LNSE operator is dominant. The qualitative similarity between all of the response maps is surprising, considering the diversity of functional forms employed for the forcing form.

Different interpretations can be argued to justify a given selection of body-force, measure and type of optimization problem (selection of a LNSE-LOM-system); however, what is immediately striking from all these results is the remarkable persistence of range $75 - 120$ to appear in the optimization maps, which is in consonance with the experimentally observed values of streak spacing (e.g. [16, 18, 123]). Furthermore, the location in the wall-normal direction where this maximum response occurs, with the LNSE-LOM-system employed in this thesis, lies at $z_f^+ \approx 10 - 17$; this is affected, but not completely determined, by the wall-normal forcing location. These values are in broad agreement with the experimental findings on streaks ([16, 20, 122]).

Finally, in every response map the optimal spanwise wavelength, for a given wall-normal visualization plane, increases with distance away from the wall, which is also a well-known characteristic of the near-wall streaks. This suggests that also this specific region has a special link to the LNSE in terms of near-wall structures generation, in this case the streaks.

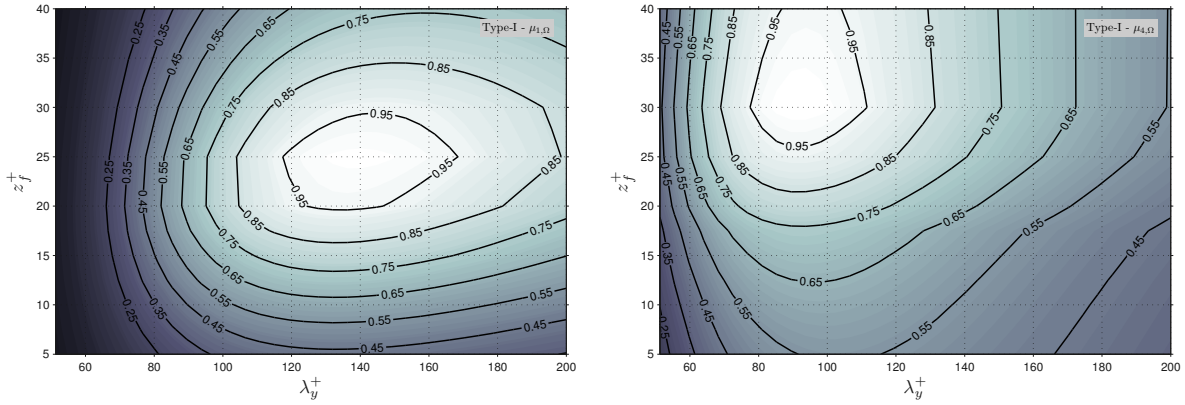

(a) Results for force $F_{1,x}$, $\mu_{1,\Omega}$

(b) Results for force $F_{2,x}$, $\mu_{1,\Omega}$

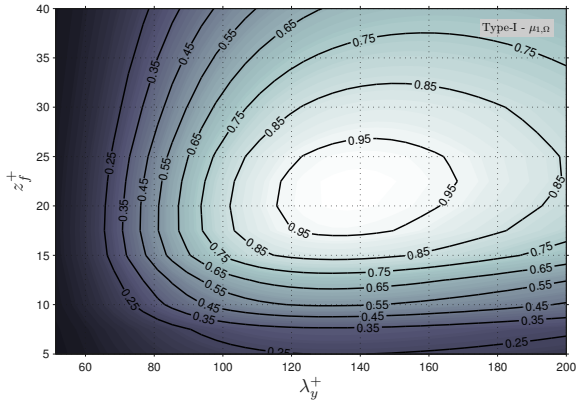

(c) Results for force $F_{3,x}$, $\mu_{1,\Omega}$

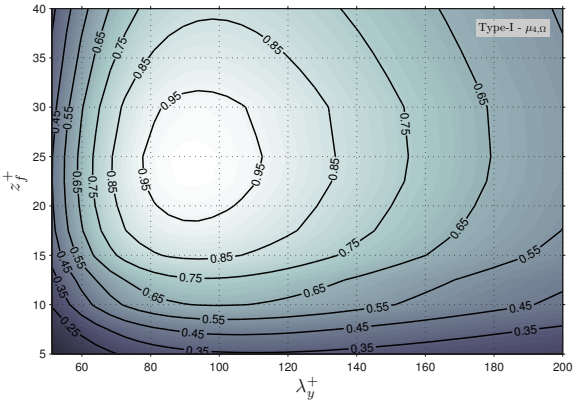

(d) Results for force $F_{1,x}$, $\mu_{4,\Omega}$

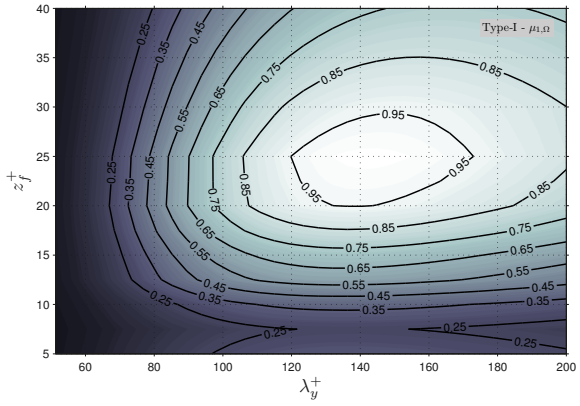

(e) Results for force $F_{2,x}$, $\mu_{4,\Omega}$

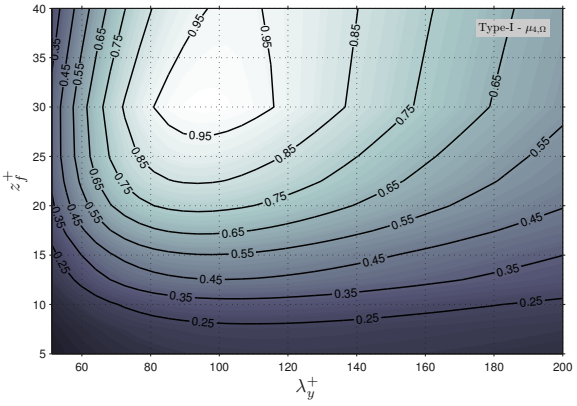

(f) Results for force $F_{3,x}$, $\mu_{4,\Omega}$

Figure 4.15: Optimization maps for problem Type-I with $\tau^+ = 80.0$ and with measures $\mu_{1,\Omega}$ and $\mu_{4,\Omega}$. (a) Results for force $F_{1,x}$, $\mu_{1,\Omega}$; (b) Results for force $F_{2,x}$, $\mu_{1,\Omega}$; (c) Results for force $F_{3,x}$, $\mu_{1,\Omega}$; (d) Results for force $F_{1,x}$, $\mu_{4,\Omega}$; (e) Results for force $F_{2,x}$, $\mu_{4,\Omega}$; (f) Results for force $F_{3,x}$, $\mu_{4,\Omega}$. Values have been normalized against global maximum value; contour lines denote percentage of measure with respect the maximum. Simulation parameters: $Re_{\delta_*} = 5000$, $\tau_t^+ = 400$, $t_f^+ = 2\Delta t^+$

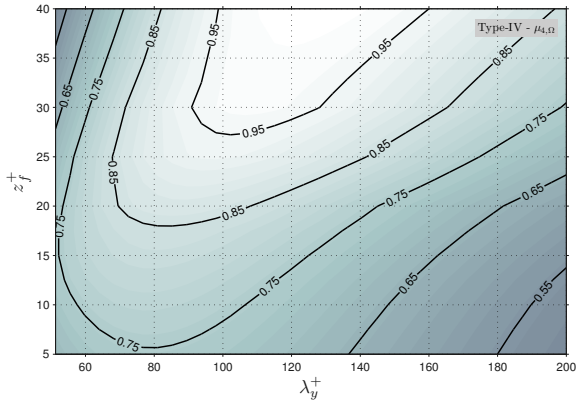

(a) Results for force $F_{1,x}$, $\mu_{4,\Omega}$;

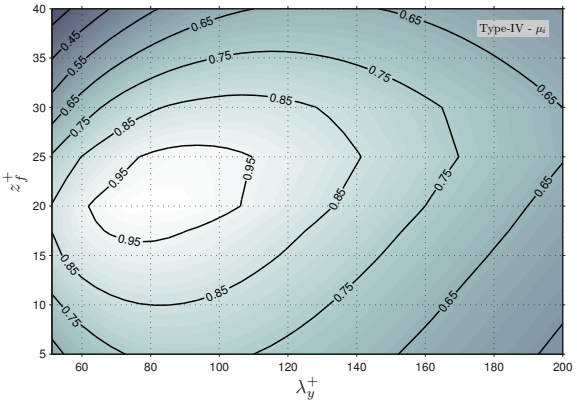

(b) Results for force $F_{2,x}$, $\mu_{4,\Omega}$;

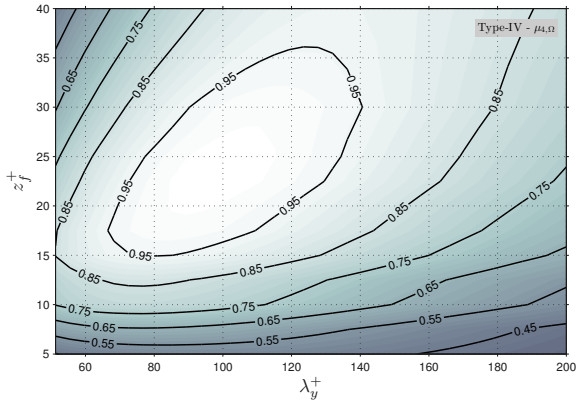

(c) Results for force $F_{3,x}$, $\mu_{4,\Omega}$;

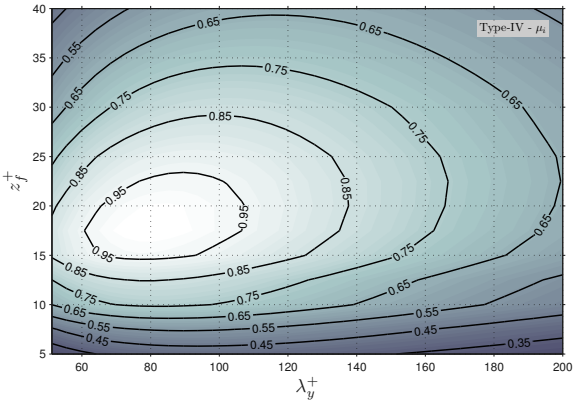

(d) Results for force $F_{1,x}$, $\mu_{3,\Omega}$;

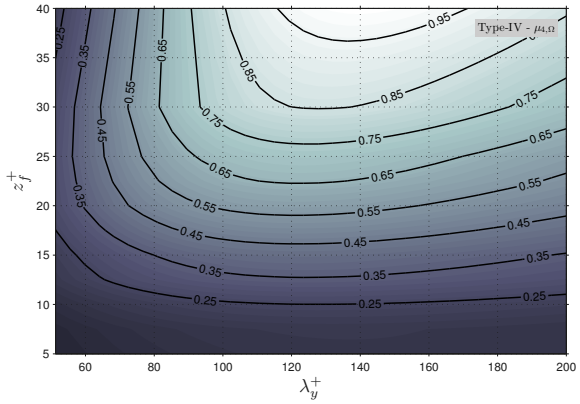

(e) Results for force $F_{2,x}$, $\mu_{3,\Omega}$;

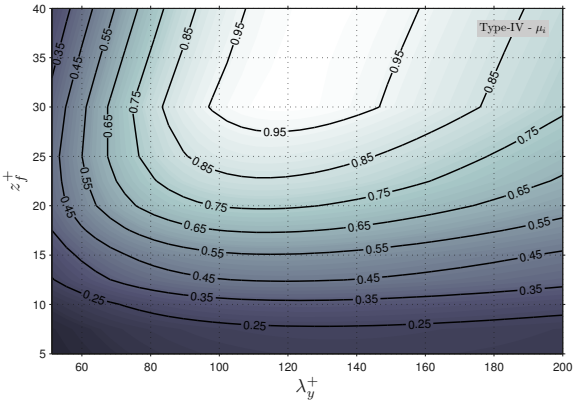

(f) Results for force $F_{3,x}$, $\mu_{3,\Omega}$;

Figure 4.16: Optimization maps for problem Type-IV with measures $\mu_{4,\Omega}$ and μ_3 using $z_v^+ = 15.0$. (a) Results for force $F_{1,x}$, $\mu_{4,\Omega}$; (b) Results for force $F_{2,x}$, $\mu_{4,\Omega}$; (c) Results for force $F_{3,x}$, $\mu_{4,\Omega}$; (d) Results for force $F_{1,x}$, μ_3; (e) Results for force $F_{2,x}$, μ_3; (f) Results for force $F_{3,x}$, μ_3. Values have been normalized against global maximum value; contour lines denote percentage of measure with respect the maximum. Simulation parameters: $Re_{\delta_*} = 5000$, $\tau_t^+ = 400$, $t_f^+ = 2\Delta t^+$

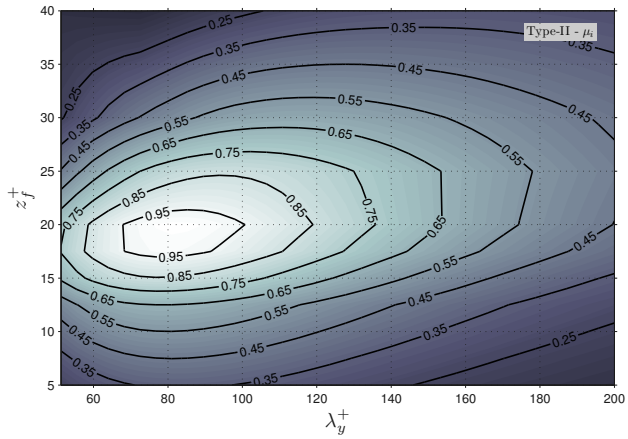

(a) Results for force $F_{1,x}$, μ_1

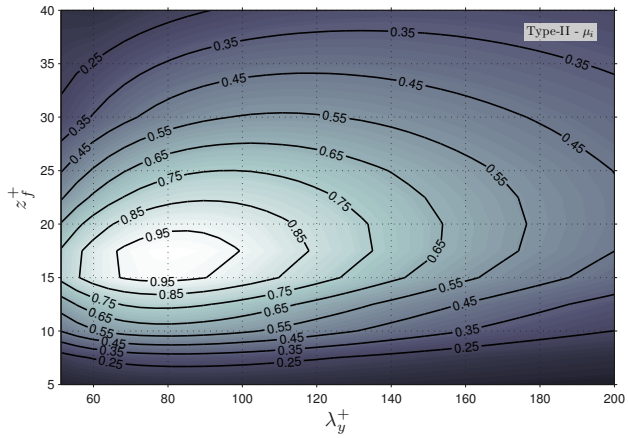

(b) Results for force $F_{2,x}$, μ_1

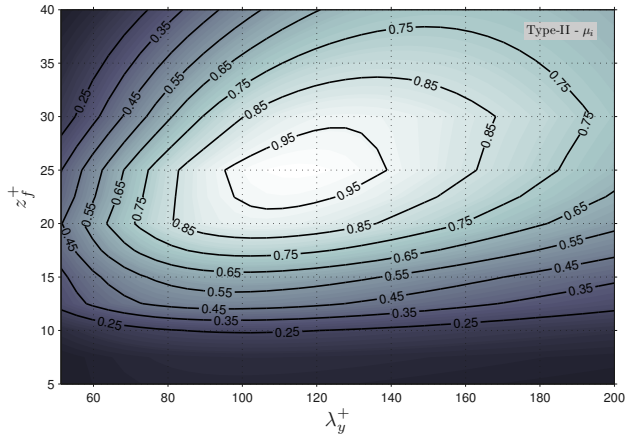

(c) Results for force $F_{3,x}$, μ_1

Figure 4.17: Optimization maps for problem Type-II with measure μ_1 using $z_v^+ = 17.5$. (a) Results for force $F_{1,x}$, μ_1; (b) Results for force $F_{2,x}$, μ_1; (c) Results for force $F_{3,x}$, μ_1. Values have been normalized against global maximum value; contour lines denote percentage of measure with respect the maximum. Simulation parameters: $Re_{\delta_*} = 5000$, $\tau_t^+ = 400$, $t_f^+ = 2\Delta t^+$

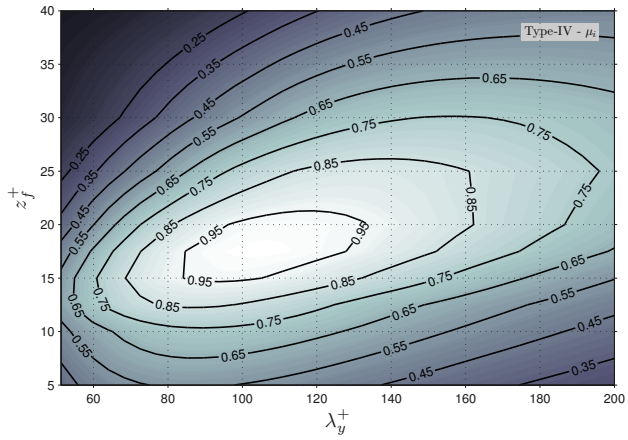

(a) Results for force $F_{1,x}$, μ_1

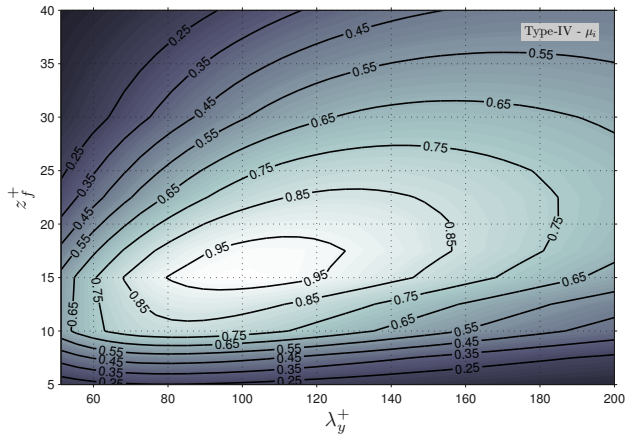

(b) Results for force $F_{2,x}$, μ_1

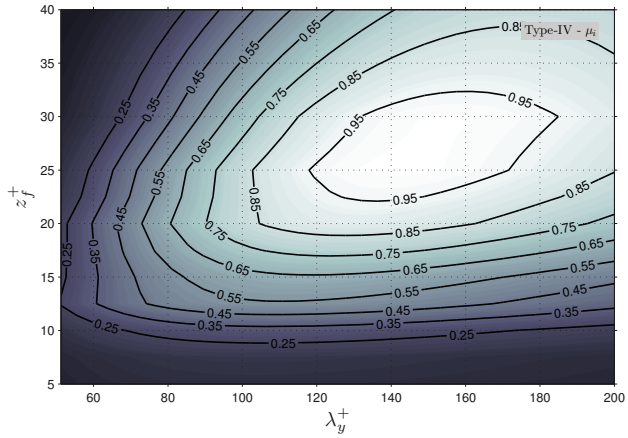

(c) Results for force $F_{3,x}$, μ_1

Figure 4.18: Optimization maps for problem Type-IV with measure μ_1 using $z_v^+ = 10.0$. (a) Results for force $F_{1,x}$, μ_1; (b) Results for force $F_{2,x}$, μ_1; (c) Results for force $F_{3,x}$, μ_1. Values have been normalized against global maximum value; contour lines denote percentage of measure with respect the maximum. Simulation parameters: $Re_{\delta_*} = 5000$, $\tau_t^+ = 400$, $t_f^+ = 2\Delta t^+$

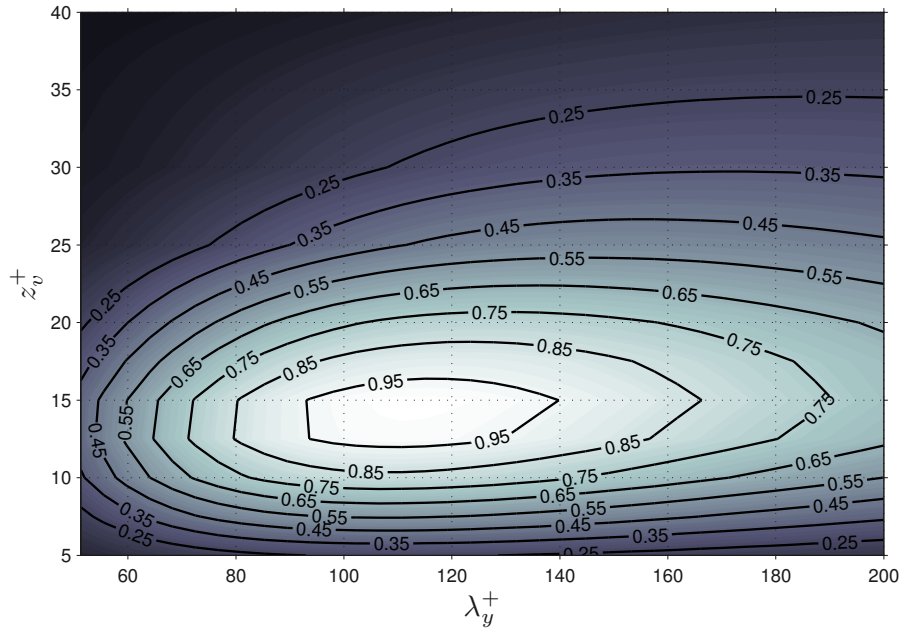

Figure 4.19: Response map of optimal perturbation for problem Type-IV using $F_{1,x}$ and μ_1; Values have been normalized against global maximum value; contour lines denote percentage of μ_1 with respect the maximum. Simulation parameters: $Re_{\delta_*} = 5000$, $\tau_t^+ = 400$, $t_f^+ = 2\Delta t^+$

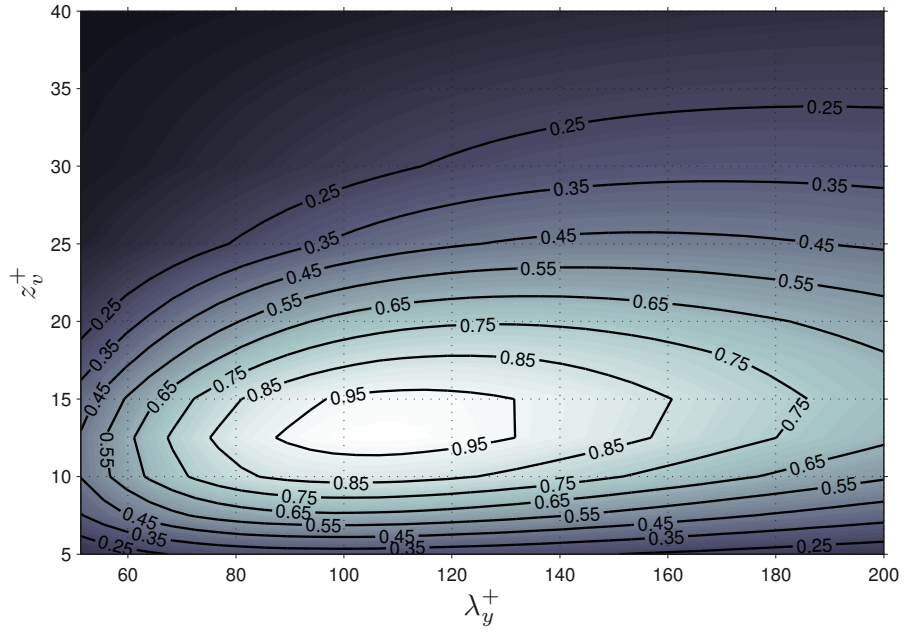

Figure 4.20: Response map of optimal perturbation for problem Type-IV using $F_{2,x}$ and μ_1; Values have been normalized against global maximum value; contour lines denote percentage of measure with respect the maximum. Simulation parameters: $Re_{\delta_*} = 5000$, $\tau_t^+ = 400$, $t_f^+ = 2\Delta t^+$

4.4.2 Results for streaks generation by initial condition

Using the initial conditions introduced in § 4.3.3 and labelled as $I_{1,w}$ and $I_{2,w}$ (equations (4.11) and (4.12)), parametric optimizations were performed following the same methodology as previously discussed. In this case, however, since there is not z_f^+ to optimize, the optimization maps have been redefined using $\{\sigma_z^+, \lambda_y^+\}$. The dispersion variable σ_x^+ was constrained to $\{5.0 \times 10^{-5} - 1.0\}$ for the IC $I_{2,w}$, whereas the parameter σ_z^+ was set to be within the range $5 \times 10^{-5} - 1.0 \times 10^{-2}$ for $I_{1,w}$ and $5 \times 10^{-4} - 2.5 \times 10^{-2}$ for $I_{2,w}$.

Regarding initial condition $I_{1,w}$: in the optimization map of the figure 4.21 are presented the results of the optimization for the problem Type-II with μ_2 at $z_v^+ = 15.0$; and figure 4.22 presents the response map for the optimal perturbation. As previously mentioned, the optimization problem was constrained, which meant that the maximum could lie on the border of the parametric space. Nevertheless, with such values the response map shows good agreement with the expected spanwise wavelength, λ_y^+, as presented in figure 4.22. In this case the difference between the optimization and response maps is even more noticeable. In the second map for this initial condition, an increase of the (local) optimum spanwise wavelength can be seen at farther visualization planes from the wall, as it has been observed experimentally. Figure 4.23 presents the results of the same optimization problem as in the previous case, i.e. {Type-II, μ_2} at $z_v^+ = 15.0$, but for initial condition $I_{2,w}$, whereas figure 4.24 presents the response map for this condition. In this case the optimum is not on the border of the feasible parametric space, and it can then be considered as a maximum global. Equally, as in the previous case, the trend obtained in the response map shows an excellent agreement with the expected tendency for the spanwise wavelength, λ_y^+. In figures 4.25 and 4.26 the development of the streaks generated using the corresponding initial conditions is presented. A top view for the evolution of the optimal streak obtained with IC $I_{2,w}$ is presented in figure 4.27. These plots of the streamwise perturbation velocity reveals that, in fact, using an initial condition which is streamwise homogeneous (or independent) generates a more elongated streak, as is expected.

In the initial condition case these optimal perturbations were found using only two optimization levels; the conditions then are clearly sub-optimal. Even so, the spanwise scales for these perturbations are near to those experimentally observed. In figure 4.27 a top view of the evolution in time of the streamwise perturbation velocity is presented. In this figure it is explicit the spanwise spacing and periodicity attained by the near-optimal perturbation. The initial condition featuring streamwise variation develops a much shorter structure, but nevertheless elongates as it develops. It is clear that, with basis on these results, it is not necessary to have the condition acting for some finite period to generate streaks, as in the forcing case. What is most important is that the complete streak-generation phenomenon is properly captured, and transient growth can be seen to dominate the evolution of the streaks modelled by the current LNSE-LOM-system.

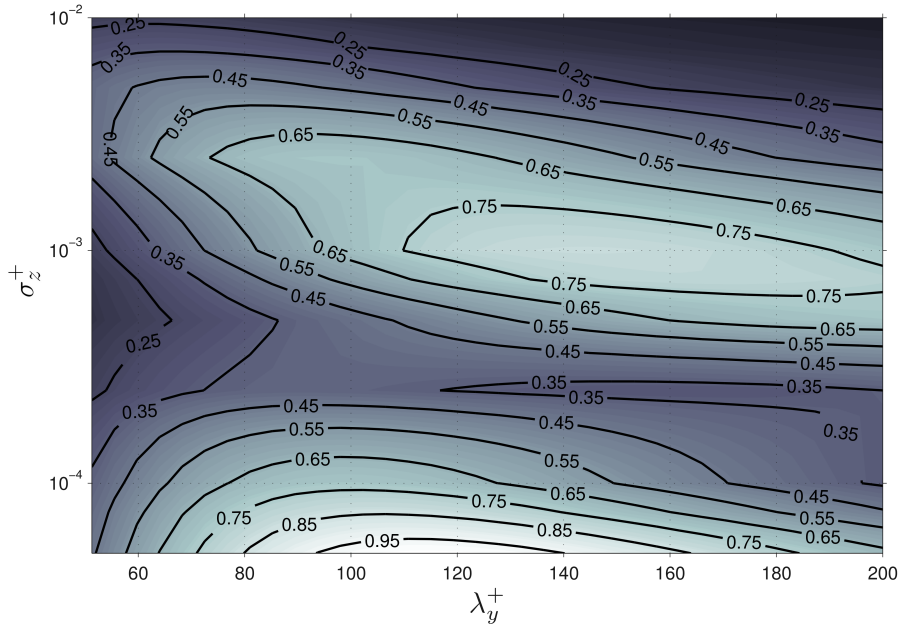

Figure 4.21: Optimization map for problem Type-II with μ_2 at $z_v^+ = 15.0$ using as LOM $I_{1,w}$; values have been normalized against global maximum value; contour lines denote percentage of μ_2 with respect to the maximum. Optimal set values: $\sigma_z^+ = 5.0 \times 10^{-5}, \lambda_y^+ = 115.0$. Simulation parameters: $Re_{\delta_*} = 5000$, $\tau_t^+ = 400$

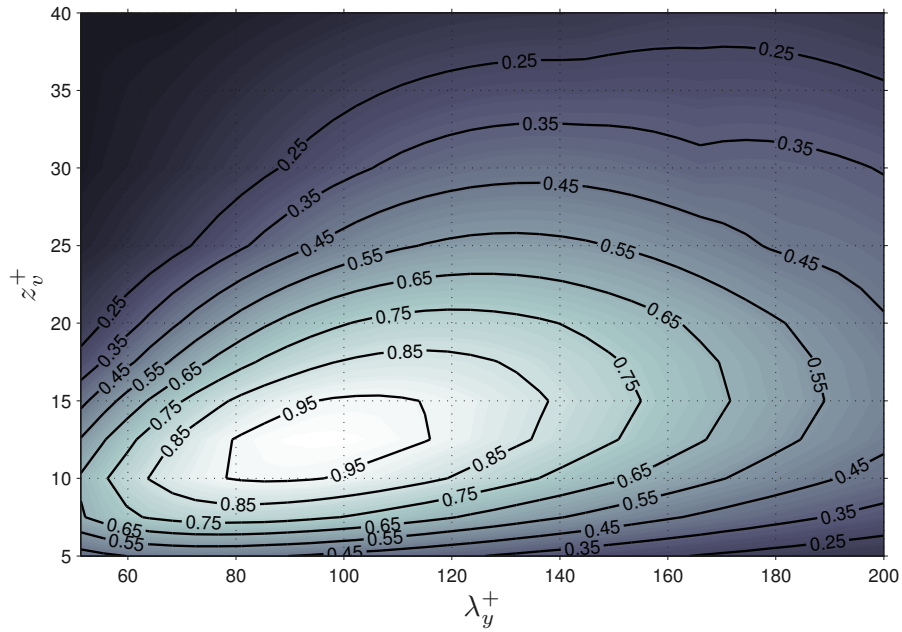

Figure 4.22: Response map of optimal perturbation for problem Type-II with μ_2 at $z_v^+ = 15.0$ using as LOM $I_{1,w}$; values have been normalized against global maximum value; contour lines denote percentage of measure with respect the maximum. Simulation parameters: $Re_{\delta_*} = 5000$, $\tau_t^+ = 400$

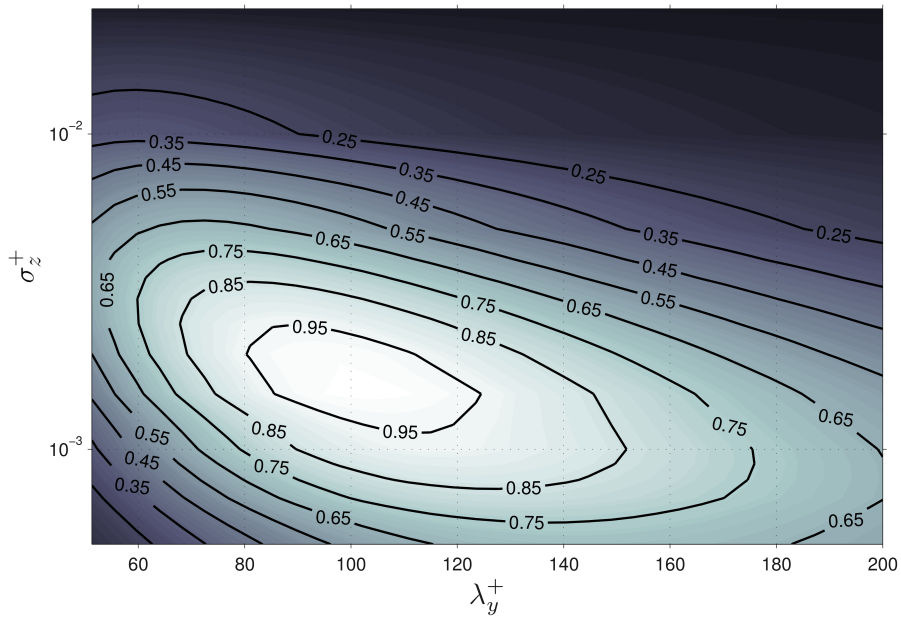

Figure 4.23: Optimization map for problem Type-II with μ_2 at $z_v^+ = 15.0$ using as LOM $I_{2,w}$; values have been normalized against global maximum value; contour lines denote percentage of μ_2 with respect to the maximum. Optimal set values: $\sigma_x^+ = 5.0 \times 10^{-5}, \sigma_z^+ = 1.5 \times 10^{-3}, \lambda_y^+ = 102.25$. Simulation parameters: $Re_{\delta_*} = 5000$, $\tau_t^+ = 400$

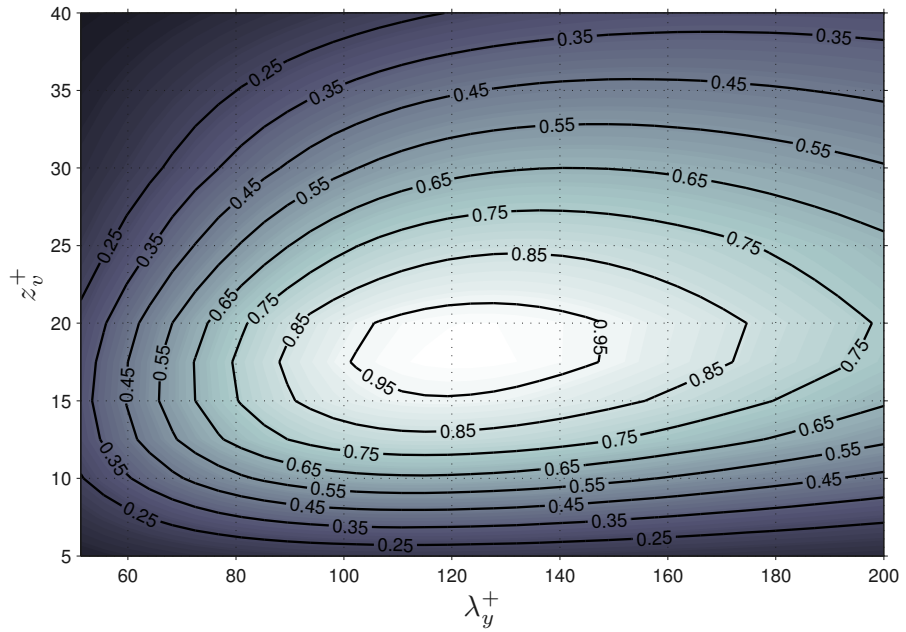

Figure 4.24: Response map of optimal perturbation for problem Type-II with μ_2 at $z_v^+ = 15.0$ using as LOM $I_{2,w}$; values have been normalized against global maximum value; contour lines denote percentage of measure with respect the maximum. Simulation parameters: $Re_{\delta_*} = 5000$, $\tau_t^+ = 400$

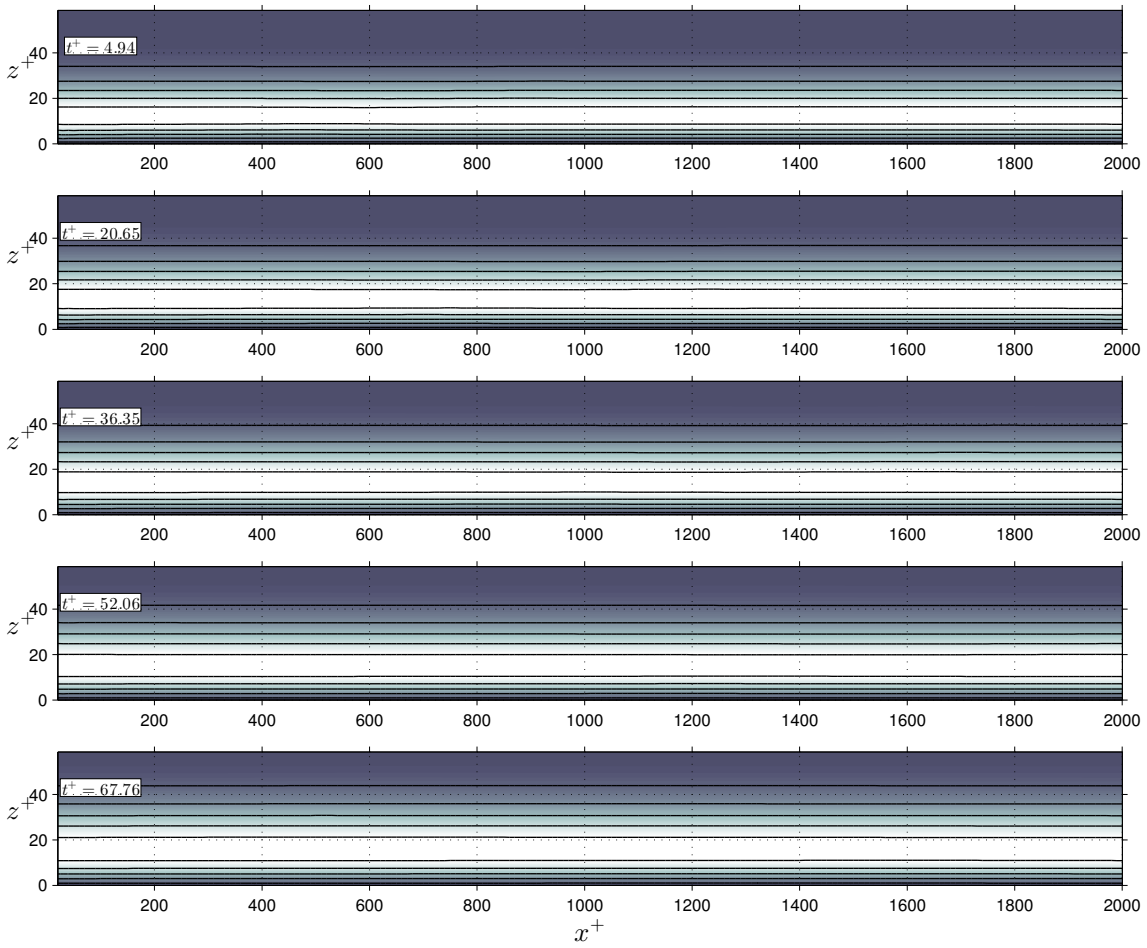

Figure 4.25: Development of streak for optimal perturbation with values from problem Type-II using $I_{1,w}$ and μ_2; optimal set $\sigma_z^+ = 5.0 \times 10^{-5}, \lambda_y^+ = 115.0$. Side view contours of streamwise velocity at $t^+ \approx 5, 20, 36, 52, 67$. Contours denote positive fraction of maximum streamwise perturbation velocity with increment of 0.1 from 0.19 to 0.99. Simulation parameters: $Re_{\delta_*} = 5000$, $\tau_t^+ = 400$

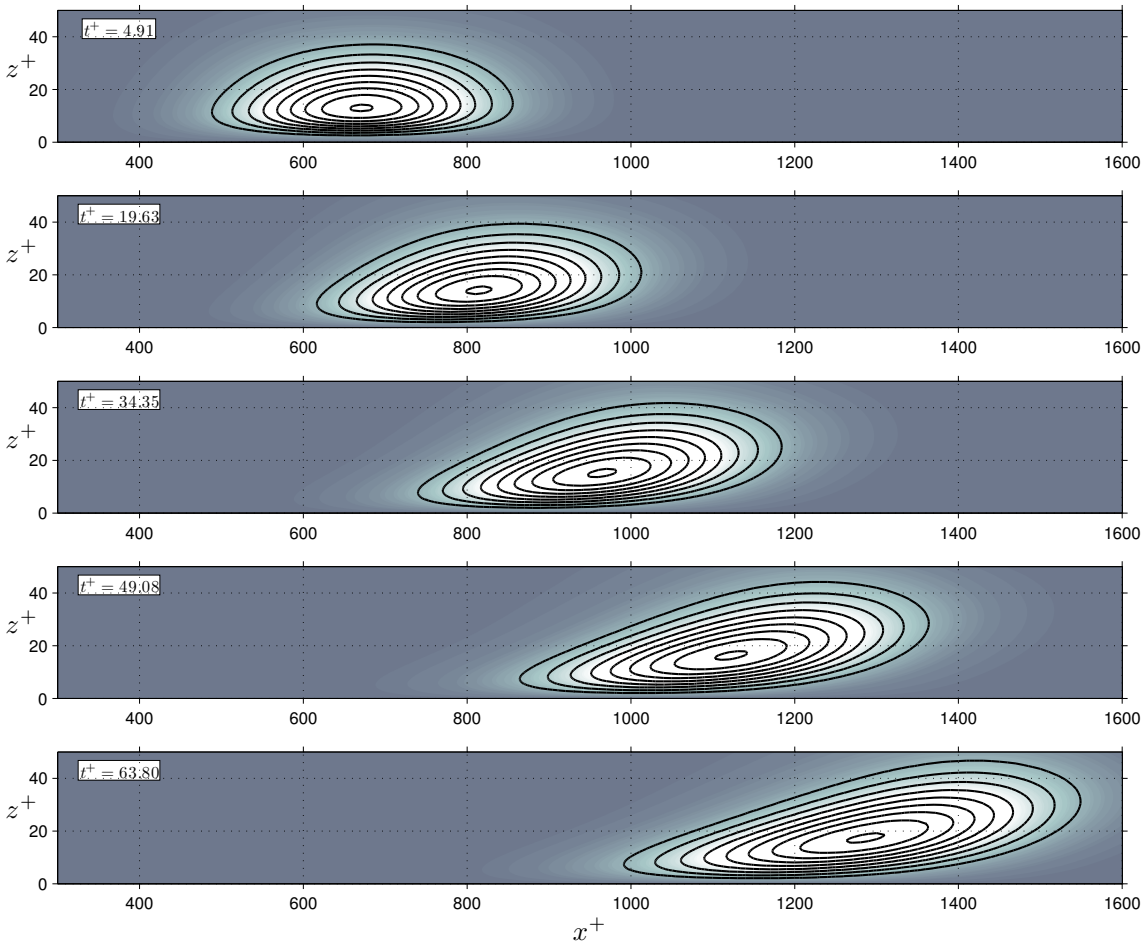

Figure 4.26: Development of streak for optimal perturbation with values from problem Type-II using $I_{2,w}$ and μ_2; optimal set $\sigma_x^+ = 5.0 \times 10^{-5}, \sigma_z^+ = 1.5 \times 10^{-3}, \lambda_y^+ = 102.25$. Side view contours of streamwise velocity at $t^+ \approx 5, 20, 34, 49, 64$. Contours denote positive fraction of maximum streamwise perturbation velocity with increment of 0.1 from 0.19 to 0.99. Simulation parameters: $Re_{\delta_*} = 5000$, $\tau_t^+ = 400$

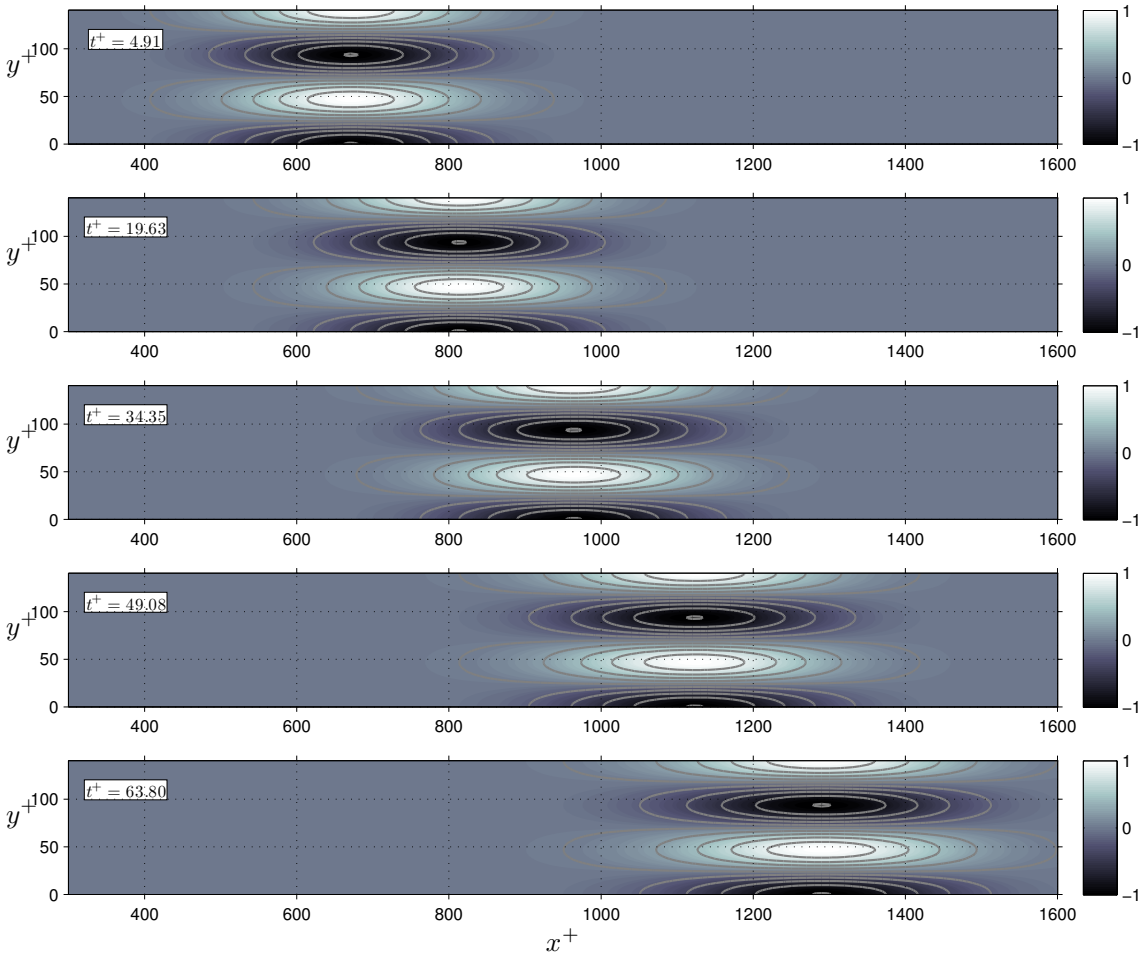

Figure 4.27: Development of streak for optimal perturbation with values from problem Type-II using $I_{2,w}$ and μ_2; optimal set $\sigma_x^+ = 5.0 \times 10^{-5}, \sigma_z^+ = 1.5 \times 10^{-3}, \lambda_y^+ = 102.25$. Top view contours of streamwise velocity at $t^+ \approx 5, 20, 34, 49, 64$. Contours denote positive fraction of maximum streamwise perturbation velocity with increment of 0.1 from 0.19 to 0.99. Simulation parameters: $Re_{\delta_*} = 5000$, $\tau_t^+ = 400$

4.4.3 The Reynolds number dependency

A final analysis is required in order to elicit about the Reynolds number dependency. The current model has been focused on the near-wall region of turbulent flows, and therefore it would be expected that the structures modelled with the LNSE-LOM-system, and also their evolution, scale in viscous or inner units.

In figures 4.28a and 4.28b the results for the optimization problem Type-II using $I_{2,w}$ and μ_2 are presented for $Re_{\delta_*} = 5000$ and $Re_{\delta_*} = 10000$, respectively; in this case the optimal set is defined by $\sigma_x^+ = 5.0\times10^{-5}, \sigma_z^+ = 1.5 \times 10^{-3}, \lambda_y^+ = 102.25$, in both cases. These flow regimes correspond to $Re_\tau = 1365$ and $Re_\tau = 2741$, with the boundary layer thickness taken as characteristic dimension, correspondingly.

Equally, in figure 4.29 it is seen the transient growth developed by the optimal perturbation resulting from this optimization problem, for the two different flow regimes. As it can be seen in these plots, there is not significant difference between the outcome of the optimization problem for these two regimes. The structures developed with the current model are almost identical, hence producing plots that are hardly discernible of each other. Such difference is minimum and a close-up, in the transient plot for instance, is required to appreciate the distinction between these two different situations. Such a detailed view is shown in 4.30.

It is clear from this set of plots that the optimal perturbations scale in inner units, as there are, practically, not differences between either the optimization plots or the transient growth plots for the two cases. These findings are in good agreement with previous works ([1, 122]) where the influence of the Reynolds number on the spanwise scale of optimum streaks has been found to be really small, and in some cases almost negligible, as in the present case. It is noteworthy that, although not exposed in the present document, similar results, showing Reynolds number independence, were obtained for the different EM (as body-force or as initial condition) employed in this work.

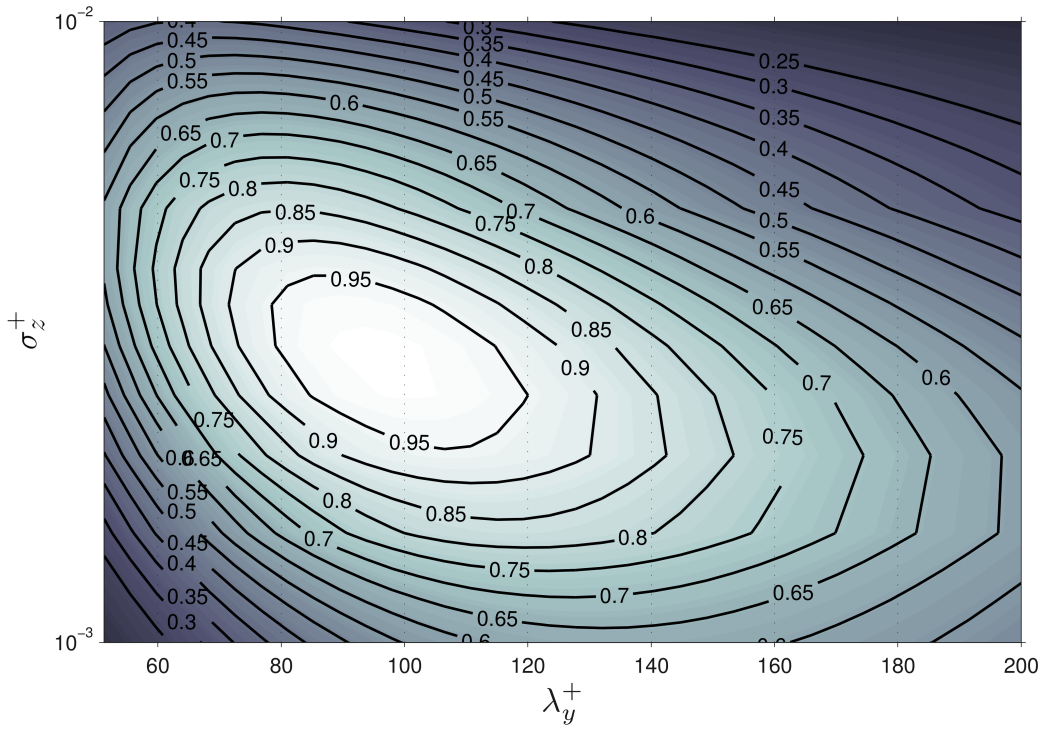

(a) TBL at $Re_{\delta_*} = 5000$

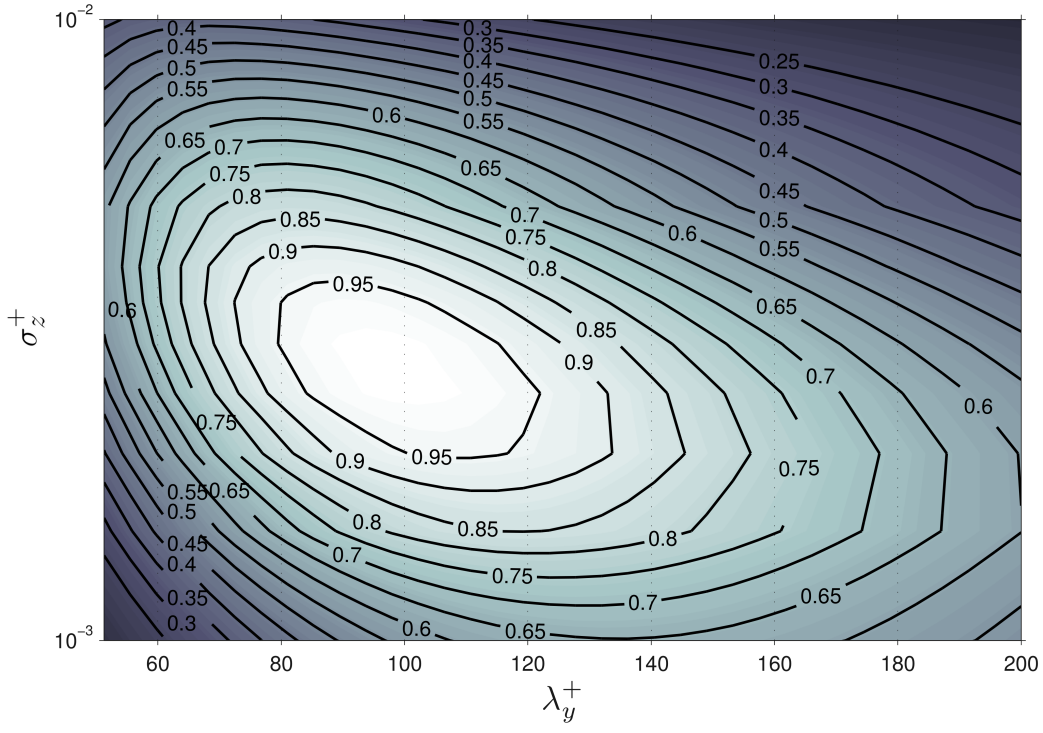

(b) TBL at $Re_{\delta_*} = 10000$

Figure 4.28: Optimization plots obtained from problem {Type-II, μ_2} at $z_v^+ = 15.0$, using $I_{2,w}$ as EM and for (a) TBL at $Re_{\delta_*} = 5000$; and (b) TBL at $Re_{\delta_*} = 10000$.

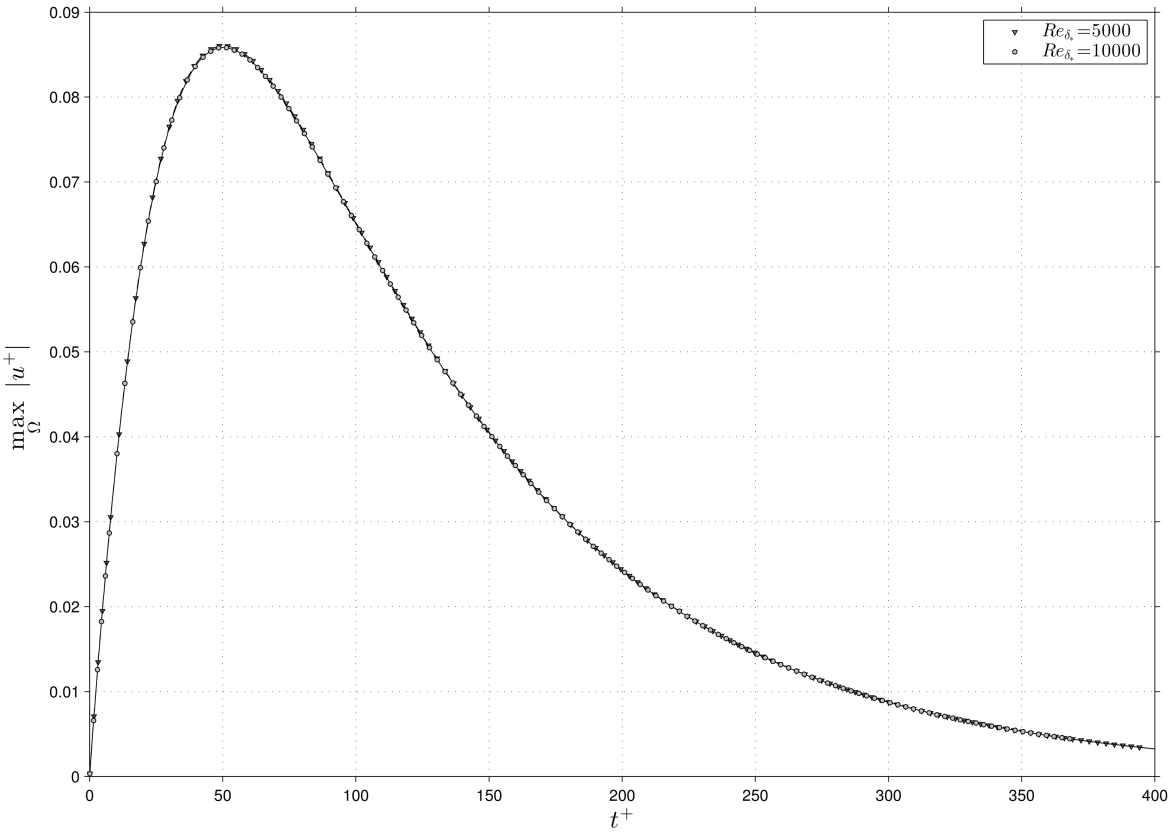

Figure 4.29: Transient growth and decay of the maximum streamwise perturbation velocity $\max_\Omega ||u^+||$, for two different regimes. Evolution of optimal perturbations obtained from problem {Type-II, μ_2} for $I_{2,w}$ for a TBL at $Re_{\delta_*} = 5000$ ($\triangledown$), and for a TBL at $Re_{\delta_*} = 10000$ ($\circ$). Optimal set $\sigma_x^+ = 5.0 \times 10^{-5}, \sigma_z^+ = 1.5 \times 10^{-3}, \lambda_y^+ = 102.25$

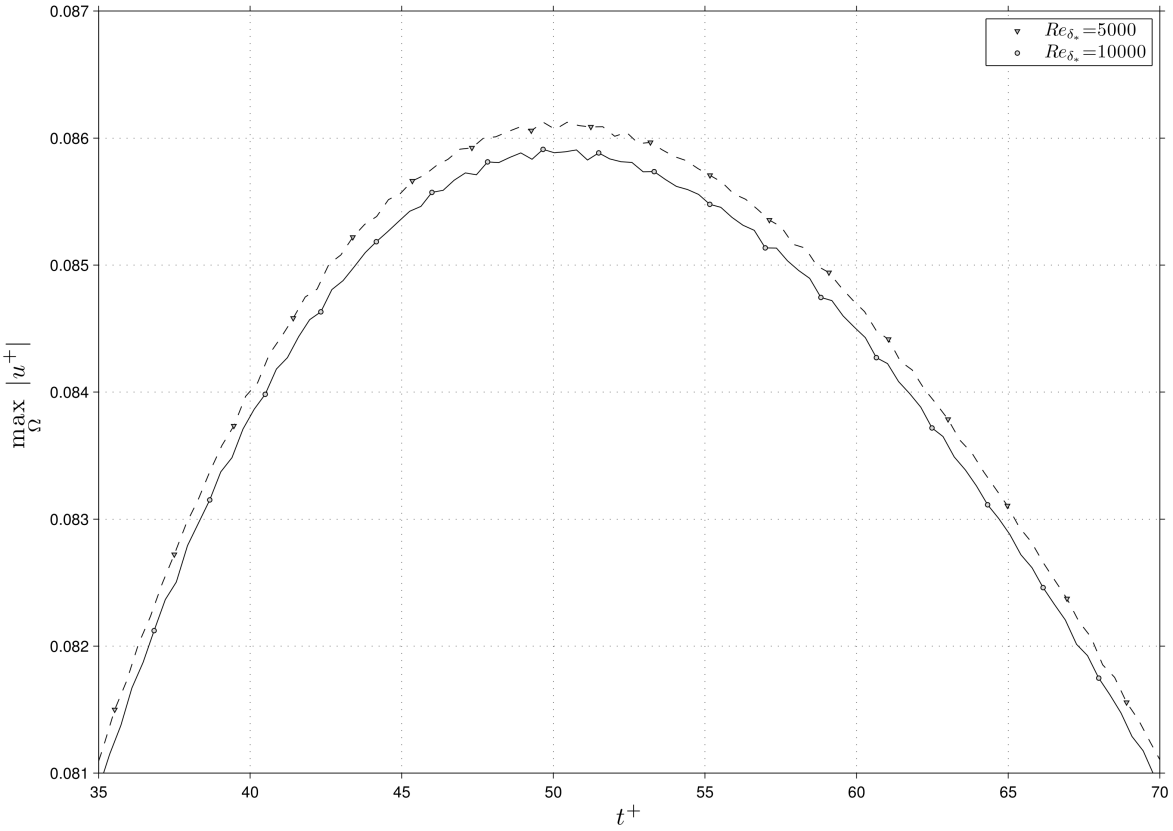

Figure 4.30: Detailed view of the evolution in time of the optimal perturbations obtained from problem {Type-II, μ_2} for $I_{2,w}$ for a TBL at $Re_{\delta_*} = 5000$ ($\triangledown$), and for a TBL at $Re_{\delta_*} = 10000$ ($\circ$). Optimal set $\sigma_x^+ = 5.0 \times 10^{-5}, \sigma_z^+ = 1.5 \times 10^{-3}, \lambda_y^+ = 102.25$

4.5 Conclusions

Observing the different optimization and response maps and the plots portraying the evolution of streaks, it is clear that there exists a certain selectivity of the LNSE operator, although not one that will bring about experimentally observed streak scales without tuning. This might be the dominant process in the generation of streaks in the near-wall region.

It is apparent that the key features of the mechanism of generation of streaks are linear, since the LNSE-LOM-system studied here was successful capturing some spatial features experimentally observed of the streaks: the spanwise periodicity and its wall-normal dependency. In any case, an optimization process was always required for the LNSE to produce results comparable to those reported in literature.

It was found that the LNSE-LOM-system must include the selection of a functional excitation mechanism (EM), a selection of a measure, and an optimization problem (LOM in this case), as it is made in this work.

Independently of the type of EM employed (by body-force or an initial condition), the LNSE-LOM-system responds by creating streamwise elongated perturbations, harmonic in the spanwise direction, resembling the alternating high- and low- speed streaks usually observed in experiments on wall-bounded flows.

Equally, it was always possible to find parameters that make the response of the different forces or initial conditions exhibit an optimum at around $\lambda_y^+ = 100 \pm 30$, and within the region defined by $z^+ = 17 \pm 5$. In this sense, the selection of almost any type of LOM will provide accurate results, but only if empirically tuned via the definition of the optimization problem. This includes the selection of a measure, of the LOM or optimization problem itself, and of the EM to be used as the streak generation mechanism, set which has been here denominated as the LNSE-LOM-system.

It was also showed and discussed that the LOM was improved by using initial conditions, as this EM required less parameters to calibrate (the forcing time being one such parameter eliminated). Based on the results obtained, EM based on initial conditions $I_{1,w}$ and $I_{2,w}$ have been chosen to perform the numerical experiments on flow control, presented and discussed in the next chapter.

The optimal condition selected to perform the flow control study is being defined using optimization over visualization planes, as with measures μ_1 or μ_2 defined at visualization planes within the range $z_v^+ = 12.5 \pm 5$. These measures (and the range for z_v^+) showed consistency and regularity defining the LOM, and their results provide good optimal conditions for a wide variety of optimization problems.

4.6 Chapter summary

In the present chapter a fairly extensive review on turbulent streak generation was presented. The concepts of exponential growth, algebraic growth and viscous dissipation of the small scale perturbations studied in this work, were linked to the concept of transient growth. A discussion about the necessity of defining an optimization problem to prescribe an appropriate LOM was presented. Results using an ample set of options as candidate for LOM were discussed and presented, for the forcing-EM, as well as for the initial-condition-EM. In both cases satisfactory results were obtained in terms of streak generation, with optimal perturbations evolving in a transient growth, and exhibiting values of spanwise periodicity (λ_y^+) largely in agreement with those obtained by other experimental and numerical works.

Chapter 5

Flow control by wall displacement

Recent studies of wall-bounded turbulence have shown that spanwise oscillations of the surface (perpendicular to the flow) and streamwise-travelling waves of spanwise wall velocity can bring about a substantial reduction in skin-friction drag. It has been found that these wall-oscillation control approaches have a strongly disruptive/inhibitive effect on the near-wall streak structures (Jung et al. [60], Karniadakis and Choi [61], Ricco and Quadrio [58]). For instance, this flow control concept has been investigated numerically by Quadrio et al. [57], who performed DNS of a plane channel turbulent flow, and also experimentally by Auteri et al. [124], who corroborated some of the previous findings on the impact of this control technique on skin-friction drag.

Given that it is commonly accepted that near-wall streak structures play a major role in the turbulent regeneration mechanism (Kline et al. [15]), it might be expected that an explanation for the efficacy of such control methods would be readily forthcoming. However, there is still a lack of clarity in the understanding of the physical mechanism(s) underpinning this type of control strategy, which stands in the way of efficient prediction and engineering application. In section §4 it was shown that the linearized Navier-Stokes operator along with the low-order model and the excitation mechanisms (set here referred to as the LNSE-LOM-system), is a satisfactory basic model for the streak generation phenomenon. Now the aim is to numerically model flow control techniques generated by spanwise wall motions, using this LNSE-LOM-system.

The majority of the numerical studies on drag reduction (DR) using spanwise wall motion have been performed using direct numerical simulations (DNS). As such, computational limitations have restricted the studies to relatively low- and mid-range Reynolds numbers. In this chapter the behaviour of near-wall streaks using linearized Navier-Stokes equations is investigated, which in turn allows to consider extremely high Re regimes (far beyond the current capabilities of DNS). The idea of using linearized Navier-Stokes equations to predict

aspects of nonlinear turbulent flows stems from the work of Landahl [7], who argued that near-wall turbulence could be effectively modelled as a linear system driven by spatially and temporally intermittent vorticity bursts originating in the viscous sublayer.

Trying to keep the simplicity of the current model, these spanwise oscillatory motions are introduced in the linearized system as part of the background or base flow over which the perturbations generated by the LNSE-LOM-system will develop. From here onwards it is assumed, then, that these spanwise oscillations have a direct impact on the base flow profile in the spanwise direction, and this alone; the oscillatory base flow is superposed on the streamwise component already present. Further details about this assumption are discussed later. In this chapter the results of the numerical investigation on the impact of these spanwise oscillations of wall velocity, on the structure and development of the streaks generated, are presented and discussed. Two variants of this control concept are examined: control by an unsteady spanwise oscillating wall, and control by a stationary wave of streamwise-modulated spanwise wall displacement. These flow conditions are integrated into a single generalised control: the Streamwise-Travelling Wave of Spanwise Velocity (STWSV).

The boundary wall generates a thin boundary layer resembling, to a degree, the laminar Stokes layer. Due precisely to this similarity, this spanwise oscillatory flow can be viewed as a Generalized Stokes Layer (GSL) (Quadrio and Ricco [55]). By incorporating the GSL profile as part of the LNSE-LOM-system, an open-loop control of the turbulent flow has been assumed; i.e., the control actuation is decoupled from the response of the LNSE-LOM-system. In any case, for the purposes of this study, the response of the system under the influence of a modified base flow, referred to as the controlled case, is compared against the response of the LNSE-LOM-system for the uncontrolled case, i.e. without any spanwise oscillation, in terms of streak growth, strength and development.

This chapter is organised as follows: firstly, a modified version of the mathematical model for the LNSE is introduced in order to account for the spanwise component introduced by the GSL profile. Secondly, a short description of the GSL profile and the types of analytical and mathematical models considered here to calculate such a profile are presented and discussed. In a third section the results of the numerical experiments of this thesis, using both types of initial conditions discussed in §4.3.3 and for different Reynolds numbers flows, are presented and compared against values obtained for drag-reduction by Quadrio et al. [57]. Finally, conclusions about the effects of this type of flow control on the streak development in our low-order model are drawn and discussed.

5.1 Modified Linearized Navier-Stokes Equations

As it has been previously indicated (see §2.3) the prescribed base flow determines the nature and stability of the operators comprising the LNSE-LOM-system. The methodology here adopted was thus to modify the mean base profile to include the Stokes-like layer induced by spanwise wall oscillations. In the current implementation, the GSL profile is superposed over the turbulent streamwise velocity profile $U(z)$. It is assumed that this composite base profile is not altered by the response of the LNSE-LOM-system. Another way of looking at this is that by incorporating such a spanwise velocity profile as part of the base flow, the stability of a new LNSE-LOM-system, including a spanwise component, is examined and the impact of inflectional points, for instance, evaluated. Nevertheless, in both type of analysis, as a control case or as a new stability analysis, the outcome and methodology are exactly the same: we will rely on the streak development to elicit the effect of the spanwise component by comparing the streak development under these new conditions against the original behaviour in a homogeneous parallel flow.

In this section we present the modifications required in the mathematical model introduced earlier in order to incorporate this additional spanwise component. It should be noted that the use of such superposition is only strictly correct if the streamwise turbulent profile $U(z)$ is obtained from an exact parallel flow solution of the Navier-Stokes equations. In this way, since the streamwise base profile adopted bears a semi-empirical nature, it is clear that an approximation has implicitly been made when the generalised Stokes layer is simply added along the spanwise direction, orthogonal to the turbulent mean flow. This assumption is discussed in more detail in the next section §5.2.

The original mathematical model consists of two vorticity transport equations and a Poisson equation, (§2.2.1), and which are replicated again here,

$$\frac{\partial \omega_x}{\partial t} + \frac{\partial M_z}{\partial y} - \frac{\partial M_y}{\partial z} = \frac{1}{Re_{\delta_*}} \nabla^2 \omega_x + S_x \tag{5.1}$$

$$\frac{\partial \omega_y}{\partial t} + \frac{\partial M_x}{\partial z} - \frac{\partial M_z}{\partial x} = \frac{1}{Re_{\delta_*}} \nabla^2 \omega_y + S_y \tag{5.2}$$

$$\nabla^2 w = \frac{\partial \omega_x}{\partial y} - \frac{\partial \omega_y}{\partial x} \tag{5.3}$$

The mean base profile now includes the spanwise velocity component induced by the GSL profile, which can be represented in general as

$$\mathbf{U^B} = [U(z), V(x,z,t), 0] \tag{5.4}$$

$$\mathbf{\Omega^B} = [\Omega_x(x,z,t), \Omega_y(x,z,t), \Omega_z(x,z,t)] \tag{5.5}$$

with $V(x,z,t)$ being the unsteady, streamwise-modulated, spanwise velocity component. Following a methodology similar to that presented in §2.4, we can write down the components of the operator $\mathbf{M}$ in equations (5.1) and (5.2), with the mean flow vorticity replaced by its definition in terms of velocity, as

$$\mathbf{M_x} = \left(\frac{\partial U^B}{\partial z} - \frac{\partial W^B}{\partial x}\right) w - \left(\frac{\partial V^B}{\partial x} - \frac{\partial U^B}{\partial y}\right) v + \left(\omega_y W^B - \omega_z V^B + \omega_y w - \omega_z v\right) \tag{5.6}$$

$$\mathbf{M_y} = \left(\frac{\partial V^B}{\partial x} - \frac{\partial U^B}{\partial y}\right) u - \left(\frac{\partial W^B}{\partial y} - \frac{\partial V^B}{\partial z}\right) w + \left(\omega_z U^B - \omega_x W^B + \omega_z u - \omega_x w\right) \tag{5.7}$$

$$\mathbf{M_z} = \left(\frac{\partial W^B}{\partial y} - \frac{\partial V^B}{\partial z}\right) v - \left(\frac{\partial U^B}{\partial z} - \frac{\partial W^B}{\partial x}\right) u + \left(\omega_x V^B - \omega_y U^B + \omega_x v - \omega_y u\right) \tag{5.8}$$

Let us consider that the wall motion induces an alternating spanwise flow described by an unsteady GSL profile, although as function only of the streamwise (x) and wall-normal (z) directions (which is discussed in more detail in the next section). In this manner, the corresponding modified two-dimensional flow assumptions for the mean flow velocity components can be written, in abbreviated form, as

$$\begin{array}{lll} U^B = U(z) & V^B = V(x,z,t) & W^B = 0 \\ \dfrac{\partial U^B}{\partial x} = 0 & \dfrac{\partial V^B}{\partial x} = V_x & \dfrac{\partial W^B}{\partial x} = 0 \\ \dfrac{\partial U^B}{\partial y} = 0 & \dfrac{\partial V^B}{\partial y} = 0 & \dfrac{\partial W^B}{\partial y} = 0 \\ \dfrac{\partial U^B}{\partial z} = U_z & \dfrac{\partial V^B}{\partial z} = V_z & \dfrac{\partial W^B}{\partial z} = 0 \end{array} \tag{5.9}$$

and the components of $\mathbf{M}$ can be re-written as

$$\begin{aligned} \mathbf{M_x} &= U_z\, w - V_x\, v - V^B\, \omega_z + \omega_y\, w - \omega_z\, v \\ \mathbf{M_y} &= V_x\, u + V_z\, w + U^B\, \omega_z + \omega_z\, u - \omega_x\, w \\ \mathbf{M_z} &= -V_z\, v - U_z\, u - U^B\, \omega_y + V^B\, \omega_x + \omega_x\, v - \omega_y\, u \end{aligned} \tag{5.10}$$

If the expressions in (5.10) are substituted in the streamwise Vorticity Transport Equation (VTE) (5.1), the following expression is obtained

$$\begin{aligned} \frac{\partial \omega_x}{\partial t} = {} & V_{xz}\, u + V_{zz}\, w + U_z\, \omega_z + V_x \frac{\partial u}{\partial z} + V_z \frac{\partial w}{\partial z} + U \frac{\partial \omega_z}{\partial z} - \frac{\partial\left(\omega_x v - \omega_y u\right)}{\partial y} + \cdots \\ & + \frac{\partial\left(\omega_z u - \omega_x w\right)}{\partial z} + V_z \frac{\partial v}{\partial y} + U_z \frac{\partial u}{\partial y} - V \frac{\partial \omega_x}{\partial y} + U \frac{\partial \omega_y}{\partial y} + \frac{1}{Re_{\delta_*}} \nabla^2 \omega_x + S_x \end{aligned}$$

where, for instance, $V_{\xi\zeta}$ indicates a double derivative of V^B along generic directions ξ and ζ, respectively. In the present case, it is assumed that the GSL profile is, in general, analytical, so the order of such double differentiation is irrelevant. By incorporating the definitions of secondary variables in the last expression, and

after some trivial rearrangement, the modified streamwise vorticity transport equation can be finally rewritten as

$$\frac{\partial \omega_x}{\partial t} = -V_{xz} \int_z^\infty \left(\omega_y + \frac{\partial w}{\partial x} \right) dz + V_x \left(\omega_y + \frac{\partial w}{\partial x} \right) + V_z \int_z^\infty \left(\frac{\partial \omega_y}{\partial x} + \frac{\partial^2 w}{\partial x^2} \right) dz + \cdots$$
$$+ V_{zz}\, w - \mathbf{i}\beta\, V\, \omega_x + U_z \int_z^\infty \left(\frac{\partial \omega_x}{\partial x} - \mathbf{i}\beta \frac{\partial w}{\partial x} \right) dz - U \frac{\partial \omega_x}{\partial x} + \frac{1}{Re_{\delta_*}} \nabla^2 \omega_x + f_x \tag{5.11}$$

where, as in §2.4, f_x represents the non-linear and source terms and constitutes the core of the EM (at least for the body-force type).

Proceeding in a similar manner, the spanwise Vorticity Transport Equation (VTE) can be rewritten as

$$\frac{\partial \omega_y}{\partial t} = -U_{zz}\, w + U_z \int_z^\infty \left(\mathbf{i}\beta \omega_x + \beta^2\, w \right) dz - U \frac{\partial \omega_y}{\partial x} + \cdots$$
$$+ V_z \int_z^\infty \left(\mathbf{i}\beta \omega_y + \mathbf{i}\beta \frac{\partial w}{\partial x} \right) dz - \mathbf{i}\beta\, V_x\, w + \frac{1}{Re_{\delta_*}} \nabla^2 \omega_y + f_y \tag{5.12}$$

where f_y stands for the non-linear and source terms appearing in the original formulation.

The perturbations have been assumed to be spanwise homogeneous and therefore conveniently expressed as $\phi = \hat{\phi}\, e^{\mathbf{i}\beta y}$ with β being a particular spanwise wave-mode, following same Fourier decomposition presented in equation (2.42).

As mentioned above, there is no need to modify the third equation composing the LNSE system (the Poisson equation for the wall-normal velocity), as it involves perturbation terms only, and no reference to the mean base profile is present. The numerical methodology applied for solving the modified VTE's is essentially the same as that one employed to solve the original LNSE-LOM-system, i.e. the uncontrolled case, for which a detailed description was presented in chapter § 3.

With this modified LNSE-LOM-system, an appropriate profile of spanwise velocity needs to be generated, as well as proper first and second order partial derivatives along the streamwise and wall-normal coordinates; such a profile must be evaluated at prescribed locations in the computational grid. In the next section the details of the GSL profile and the methodologies to generate it, including required derivatives, are presented and discussed.

5.2 The generalised Stokes layer

In skin-friction flow control by spanwise wall motions the aim is to create a thin boundary layer, perpendicular to the flow direction, which should induce drag reduction (DR) (although drag increase (DI) is possible depending upon the conditions of the oscillating flow). Such a thin layer, as in the common Stokes layer, is induced by the motion of an oscillating wall which, owing to the no-slip condition, transfers momentum to the adjacent fluid. By imposing this boundary condition on the fluid, the wall motion creates a velocity distribution in the fluid that oscillates with an amplitude, at the wall, equal to the oscillation amplitude imparted by the motion of the wall. In the wall normal direction this amplitude decays as one moves into the fluid. Therefore, the envelope[1] of this velocity distribution, and therefore the velocity profile itself, decreases with the distance from the wall, in such a way that at some point in the wall-normal direction this spanwise boundary layer is fully subdued. It is noteworthy that, for the cases here examined, this oscillatory Stokes boundary layer needs to be laminar (low Reynolds number).

The main difference between the Stokes layer and the type of flow control here adopted, the generalised Stokes layer, lies in the prescription of the boundary condition at the wall. Specifically, in the generalised Stokes layer the wall boundary condition is an unsteady, streamwise-modulated wave of spanwise wall velocity, which in the present case has been prescribed as

$$V_{wall} = A_w \, \Re \left[e^{\mathbf{i}(\kappa_x x - \omega t)} \right] \tag{5.13}$$

where A_w is the velocity amplitude, κ_x is a streamwise wavenumber and ω is the temporal oscillation frequency of the wave. This form of control generates waves of spanwise velocity moving (backward or forward) in the streamwise direction with a phase speed $c = \omega/\kappa_x$, which represents a generalised form of spanwise-wall actuation including the two extreme cases: pure spanwise oscillation (κ_x=0), and stationary or standing streamwise waves of spanwise velocity (ω=0). In figure 5.1 is presented a schematic representation of the boundary condition applied for a GSL.

Both numerical and experimental research on this type of flow control, and its variants, have been recently performed. For instance, Choi et al. [59] demonstrated, experimentally, drag reduction of up to 45% using pure wall oscillations in the spanwise direction ($\kappa_x = 0$) with an optimum period of around $T^+ = 100 - 125$, which was shown to be independent of the wall-oscillation amplitude. On the other hand, Viotti et al. [125] investigated numerically the standing wave case ($\omega = 0$), and found energetic performance improvement with

[1] An imaginary curve connecting the maxima of the absolute value of this profile along the wall-normal direction.

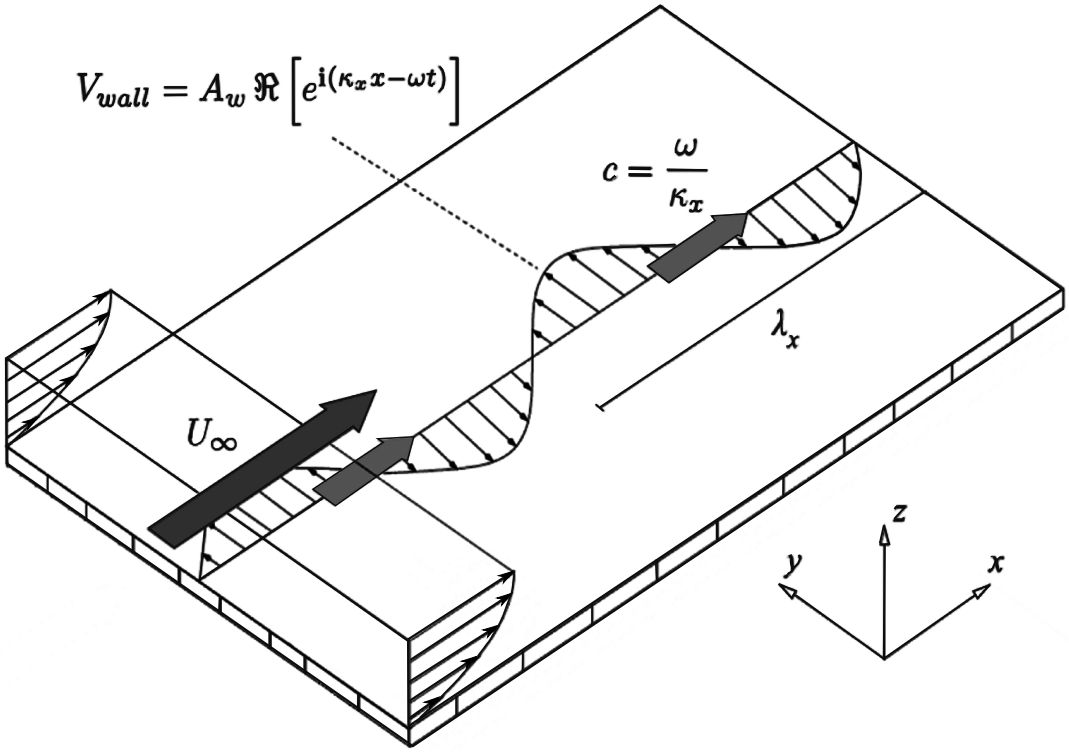

Figure 5.1: Schematic representation of the actuation as spanwise motion of the wall bounding a TBL (adapted from [57])

.

more than 40% of reduction on the maximum friction at large intensities of the spanwise oscillations. Quadrio et al. [57] investigated numerically the effect of the GSL with a wall-forcing of the form $V = A\sin(\kappa_x x - \omega t)$ with κ_x being the streamwise wavenumber and ω the oscillation frequency of the wave, just as in our formulation. They found that a wide-range of $(\kappa_x - \omega)$ exist for which DR is of the order of 47-48%, which is greater than maximum drag reduction obtained by spanwise oscillations and standing steady waves, separately. Their numerical experiments were focused on turbulent channel flow. However, they also found that in the $(\kappa_x - \omega)$ map there exists a region where DI occurs, associated with a constant phase speed $c = 0.5$ or in inner units of $c^+ \approx 10$. These values of drag reduction and drag increase were obtained for a set of simulations performed at $Re = 4760$ and $A = 0.5U_c$ where U_c is the centre-line channel velocity. The present numerical experiments on DR/DI by spanwise oscillations, using the LNSE-LOM-system, have been mainly focused on this last set of results involving an exploration over the $(\kappa_x - \omega)$ control map studied by Quadrio et al. [57].

In order to get the spanwise base profile, a similar analysis to that in Quadrio and Ricco [55] is followed: the flow induced in a laminar Poiseuille channel flow by the wall motion given by equation (5.13) is used. However, due to the expected symmetry around the center-line of the channel (if synchronised bounding walls are generating the GSL), and because of the proximity of present formulation to TBL flows, only the fluid flow contained within the boundary layer thickness of a streamwise TBL is studied: an incompressible flow driven

in the spanwise direction by the motion of the wall at laminar regime, and immersed within a homogeneous streamwise turbulent boundary layer.

As it is noted in [55], and in the previous discussion of the present formulation, the governing Navier-Stokes equations are simplified substantially if the terms involving derivatives in the spanwise direction are assumed to be null; in fact, examining equation (5.13), it is clear that there is no spanwise variation in the driving oscillatory motion. In accordance with the previous assumptions and with the definitions in equation (5.9), let the base flow be described, by

$$\mathbf{U}^B = [U^B, V^B, W^B] \tag{5.14a}$$

$$U^B = U(z) \tag{5.14b}$$

$$V^B = V(x, z, t) \tag{5.14c}$$

$$W^B = 0 \tag{5.14d}$$

where U^B,V^B and W^B stand for the streamwise (x-direction), spanwise (y-direction) and wall-normal (z-direction) velocity components of a mean base flow containing the GSL, respectively. It is easy to verify that for this flow the wall-normal pressure-gradient should be zero. Additionally, for simplicity, let assume that the streamwise pressure gradient term is negligible. Therefore, after these simplifications are substituted into the governing Navier-Stokes equations, and dropping the upper index B for simplicity, such a system reduces to the form:

$$\frac{\partial V}{\partial t} + U\frac{\partial V}{\partial x} = \frac{1}{Re}\left(\frac{\partial^2 V}{\partial x^2} + \frac{\partial^2 V}{\partial z^2}\right) \tag{5.15}$$

where Re is the appropriate Reynolds number. It is clear that if it is assumed that the streamwise velocity component ($U(z)$) is a solution of the momentum equations, then the flow field given by $\mathbf{U}^B = [U(z), V(x, z, t), 0]$ will also be a solution if equation (5.15) is satisfied. Equation (5.15) shows that a one-way coupling between the streamwise profile U^B and the spanwise profile V^B exists, provided by the convective term.

In the present work the set of parameters ($\kappa_x - \omega$) is chosen such that the thickness of this generalised Stokes layer is very thin and mostly concentrated in the sub-viscous and buffer regions of the TBL, as it will be shown in next sections. Although the current Stokes formulation is based on a laminar flow assumption, it can be argued that this is acceptable for turbulent flows because the dominant viscous terms are expected to be much larger in magnitude compared to the Reynolds stress terms, at least, within the region containing the Stokes layer, as explained in Ricco and Quadrio [58]. Additional evidence on the validity of the idea that

a superposition of the GSL profile V^B over the streamwise profile $U^B(z)$ is an appropriate assumption can be found in [58].

Given the amount of numerical tests required for the current DR/DI experiments, a methodology able to produce valid GSL profiles in an accurate and fast way is needed. Three different approaches to obtain such a numerical profile from equation (5.15) were explored in this work, although the drag reduction/drag increase (DR/DI) tests were accomplished using only that methodology showing best accuracy and computational performance. Such approaches are presented and briefly discussed in the next sections; a comparison is presented to justify the final selection of the numerical methodology employed to produce the GSL profile V^B to be used in the flow control tests of this thesis.

5.2.1 Analytical solution

A first attempt towards obtaining a valid spanwise profile is by employing an analytical solution of the generalised Stokes layer with the imposed condition at the wall: $V_{wall} = A_w \, \Re\left(e^{\mathbf{i}(\kappa_x x - \omega t)}\right)$. An analytical expression for this flow has been derived by Quadrio and Ricco [126]. However, the published expression contained errors/problems associated with the conditions at the wall. A corrected version of the analytical expression is presented here.

Following the dimensional analysis presented in Quadrio and Ricco [126] [2] , and assuming that in the proximity of the wall the streamwise velocity U^B can be expressed as a linear expansion in z, then the $y-$momentum equation (5.15) can be rewritten, in dimensional form, as

$$\left(z - \frac{c}{\delta_S \, \tau}\right) \frac{\partial V}{\partial \zeta} = \frac{\nu}{\delta_S \tau \lambda_x} \frac{\partial^2 V}{\partial \zeta^2} + \frac{\lambda_x \nu}{\delta_S^3 \tau} \frac{\partial^2 V}{\partial z^2} \tag{5.16}$$

where $\tau = (dU/dz)_{z=0}$ is the streamwise velocity-gradient at the wall, δ_S is a measure of the Stokes boundary-layer thickness, $c = \omega/\kappa_x$ is the wave speed, $\lambda_x = 2\,\pi/\kappa_x$ is the streamwise wavelength of the wave, and a variable $\zeta = x - t$ is used in replacement of x, so that $\partial\,/\partial x = \partial\,/\partial\zeta$ and $\partial\,/\partial t = -\partial\,/\partial\zeta$. As in Quadrio and Ricco [126], the GSL profile is considered to be appropriately expressed as

$$V = \Re\left[F(z) e^{\mathbf{i}2\pi\zeta}\right]$$

[2] Although some of the aspects of their discussion are presented here, for the sake of brevity the reader is referred to [126] for a more detailed explanation of this analysis.

and then equation (5.16) can be rewritten as

$$\mathbf{i}\frac{2\,\pi\,\delta_S^3\,\tau}{\nu\,\lambda_x}\left(z-\frac{c}{\delta_S\,\tau}-\mathbf{i}\frac{2\,\pi\,\nu}{\delta_S\,\lambda_x\,\tau}\right)F(z)=\frac{d^2\,F(z)}{d\,z^2} \tag{5.17}$$

with boundary conditions given by

$$F(0)=1 \qquad \text{and} \qquad \lim_{z\to\infty}F(z)=0$$

Using the (non-trivial) transformations proposed by Quadrio and Ricco [126], equation (5.17) can be recast as,

$$\tilde{F}''(\tilde{z})=\tilde{z}\,\tilde{F}(\tilde{z})$$

which in turn has analytical solution given by an Airy function of the first kind $\tilde{F}=\theta Ai(\tilde{z})+\gamma Ai(\tilde{z}e^{2/3\pi\mathbf{i}})$. After applying the boundary conditions defined previously and substituting back the original set of variables, an expression for the GSL profile is obtained in dimensional form, as

$$V(x,z,t)=A_w\,\Re\left\{K_1\,e^{\mathbf{i}(\kappa_x x-\omega t)}\,Ai\left[e^{\mathbf{i}\pi/6}\left(\frac{\kappa_x\tau}{\nu}\right)^{\frac{1}{3}}\left(z-\frac{\omega}{\kappa_x\tau}-\frac{\mathbf{i}\,\kappa_x\nu}{\tau}\right)\right]\right\} \tag{5.18}$$

where K_1 is a constant defined by the parameters of the travelling wave given by

$$K_1=\left(Ai\left[-e^{\mathbf{i}\pi/6}\left(\frac{\kappa_x\tau}{\nu}\right)^{\frac{1}{3}}\left(\frac{\omega}{\kappa_x\tau}+\frac{\mathbf{i}\kappa_x\nu}{\tau}\right)\right]\right)^{-1}$$

This expression for K_1 is a corrected version of the one published in [126] in order to fit properly the boundary condition at $z=0$ (this has been tested in the present code). It is important to highlight that this expression is only valid for restricted values of z^+, where the assumption of linear streamwise base velocity profile is reasonable.

This formulation simplifies to the steady Stokes layer proposed by Viotti et al. [125] when $\omega=0$ and $\mathbf{i}\,\kappa_x\nu/\tau=0$, although it is not defined for oscillating-wall flow when $\kappa_x=0$. In this last case, the correct formulation is the traditional analytic formula for the second Stokes problem.

For use in the computational code, a non-dimensionalization in outer units is required. A dimensionless variant of the analytical GSL profile can thus be obtained as follows. First, let us introduce a variable η_1, defined by the travelling wave parameters and the flow regime, as

$$\eta_1=\frac{\omega}{\kappa_x\,\tau^*}-\mathbf{i}\,\frac{\kappa_x}{Re_{\delta_*}\,\tau^*} \tag{5.19}$$

with τ^* being the dimensionless wall-shear stress. Using η_1, we can reformulate equation (5.18) as

$$V(x,z,t) = A_w^* \, \Re\left\{ K_1 \, e^{\mathbf{i}(\kappa_x x - \omega t)} \, Ai\left[e^{\mathbf{i}\pi/6} \, (\kappa_x \, \tau^* \, Re_{\delta_*})^{\frac{1}{3}} \, (z - \eta_1) \right] \right\} \tag{5.20}$$

with

$$K_1 = \left(Ai\left[-e^{\mathbf{i}\pi/6} \, (\kappa_x \, \tau^* Re_{\delta_*})^{\frac{1}{3}} \, \eta_1 \right] \right)^{-1}$$

and A_w^* being the non-dimensional amplitude of the travelling wave considered.

Figures 5.2 and 5.3 show contours for the GSL profiles in the TBL at $Re_{\delta_*} = 1 \times 10^4$. In the first figure 5.2 a snapshot of the GSL profile is shown, taken at $t^+ = 120$, for a STWSV with wave speed $c^+ = 0.5$ and prescribed by $A^+ = 12.0$, $\kappa_x^+ = 0.06$, $\omega^+ = 0.03$.

Figure 5.3 illustrates the contour of a GSL profile for a STWSV with wave speed $c^+ = 2.0$ prescribed by $A^+ = 12.0$, $\kappa_x^+ = 0.06$, $\omega^+ = 0.12$. In both cases the GSL profile is calculated for a computational domain of $L_x^+ = 400.0$.

Although the availability of an analytic expression offers numerical advantages in obtaining a valid spanwise base profile, this analytical formulation initially only allows to get the velocity profile V^B. The LNSE-LOM model in this work, presented in equations (5.11) and (5.12), features derivatives of V^B including the wall-normal direction, which would require then to obtain derivatives of the Airy function with complex arguments. Instead of trying to obtain further analytical expressions for such derivatives, and aiming to keep simplicity in the formulation, all derivatives of V^B are estimated numerically, and no further relations are derived.

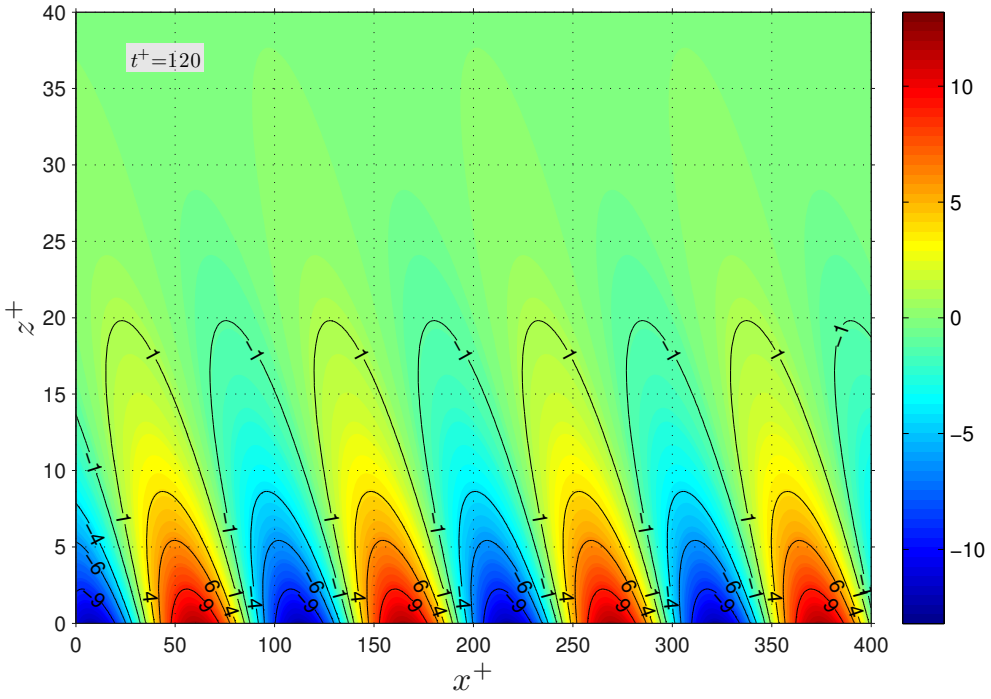

Figure 5.2: Side view of a generalised Stokes layer obtained by analytical expression for a STWSV with $c^+ = 0.5$. GSL distribution for $Re_{\delta_*} = 1 \times 10^4$, $A^+ = 12.0$, $\kappa_x^+ = 0.06$, $\omega^+ = 0.03$, $t^+ = 120$.

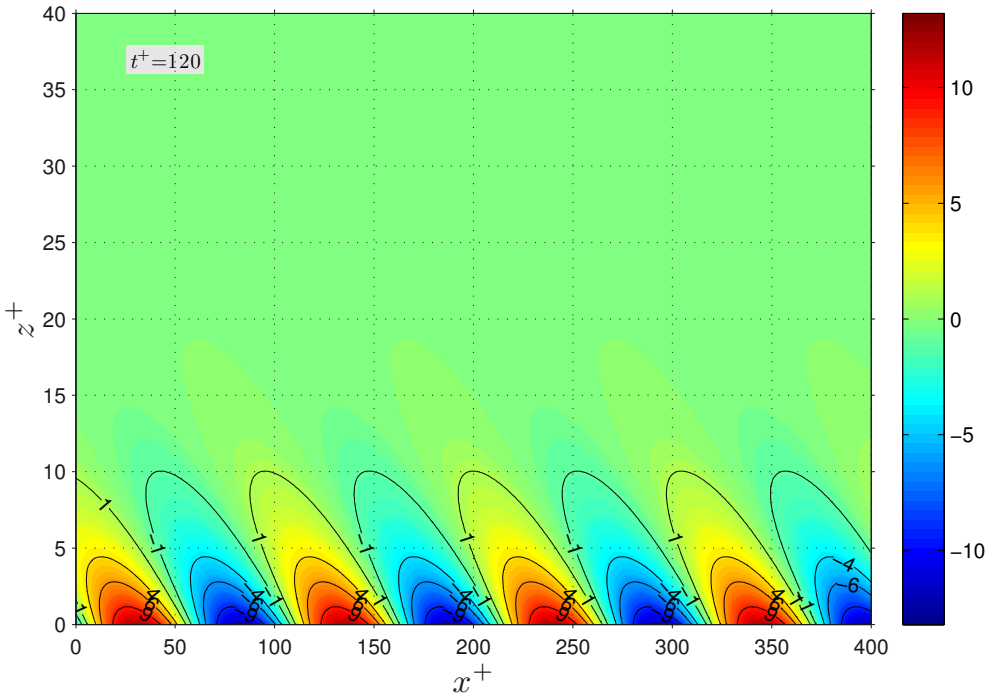

Figure 5.3: Side view of a generalised Stokes layer obtained by analytical expression for a STWSV with $c^+ = 2.0$. GSL distribution for $Re_{\delta_*} = 1 \times 10^4$, $A^+ = 12.0$, $\kappa_x^+ = 0.06$, $\omega^+ = 0.12$, $t^+ = 120$.

5.2.2 Solution by hybrid solver: Spectral - Finite Differences

A big disadvantage of the analytic GSL profile is that it assumes $u^+ = z^+$. As mentioned before, this is only valid for a small finite region close to the wall, restricting the use of the analytical solver. Therefore, a second methodology explored to produce GSL profiles is based on the Chebyshev-Finite Differences (spectral-FD) numerical solver already adopted in this work and described in chapters 2 and 3. In this case, for the GSL profiles defined by the momentum equation (5.15), the application of the current solver is straightforward. Owing to the one-way coupling, only a streamwise profile $U(z)$ and the selected STWSV boundary condition ($\kappa_x - \omega$) need to be prescribed. Additionally, a simple examination of the original formulation reveals that the GSL profile can be obtained from a modified version of the spanwise VTE. A modified version of the current mathematical formulation to obtain V^B can be stated as

$$\frac{\partial V}{\partial t} = -U\,\frac{\partial V}{\partial x} + \frac{1}{Re_{\delta_*}}\underset{\sim}{\Delta}\,V \tag{5.21}$$

with $\underset{\sim}{\Delta} = \dfrac{\partial^2}{\partial x^2} + \dfrac{\partial^2}{\partial z^2}$.

Equally, by adopting the numerical considerations discussed in chapter § 3, for this simplified case the final numerical operator also involves double integration in the wall-normal direction, and the previous expression can be rewritten as

$$\mathbf{I}\left[\frac{\partial V}{\partial t}\right] = \mathbf{I}\left[-U\,\frac{\partial V}{\partial x} + \frac{1}{Re_{\delta_*}}\left(\frac{\partial^2 V}{\partial x^2}\right)\right] + \mathbf{K}\left[\frac{V}{Re_{\delta_*}}\right] \tag{5.22}$$

with $\mathbf{I}$ and $\mathbf{K}$ representing the integral operators presented in § 3.1.2. The streamwise direction is discretized using an equi-spaced grid with the finite differences scheme previously discussed in § 3.1.1; the time integration method has also been adopted from the core numerical solver. Additionally, owing to the decoupling of the GSL governing equation from other relations for this flow, only the predictor and corrector steps are required, and just once per time iteration.

In figures 5.4 and 5.5 are presented the contours of the GSL profiles obtained for STWSV with wave speed of $c^+ = 0.5$ and $c^+ = 2.0$, respectively. The cases presented in these figures were obtained for a computational grid of size $L_x^+ = 400.0$, with a grid spacing of $\Delta x^+ = 0.8$ and using 128 Chebyshev nodes. Observing these figures is clear that the numerical solution produced here captures the same general features as the analytical expression presented previously. From close visual comparison it is apparent that there is good quantitative agreement between these two solutions.

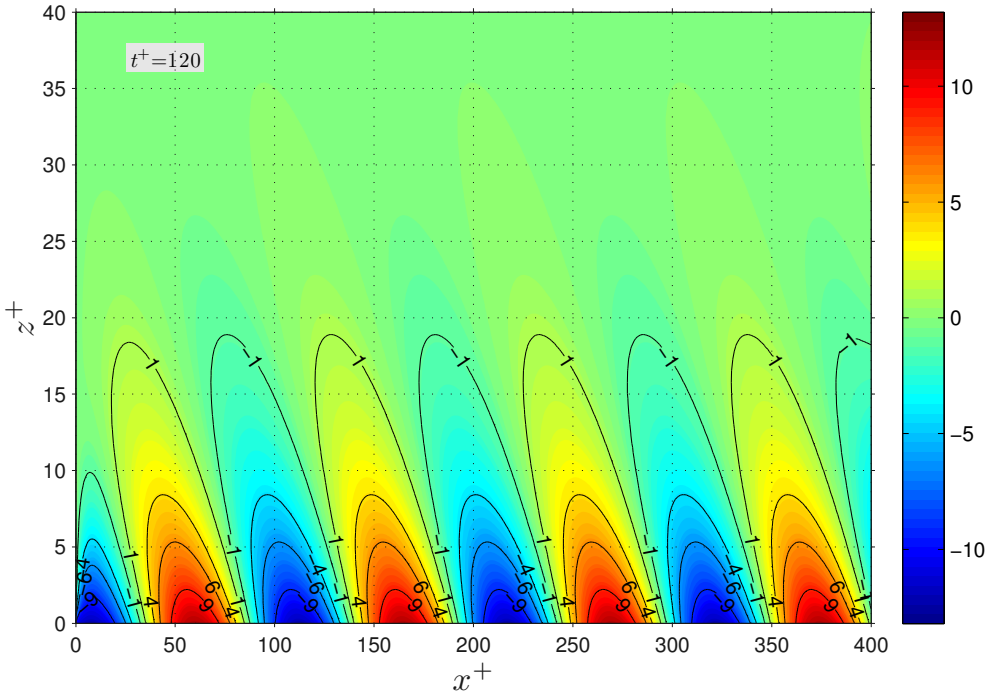

Figure 5.4: Side view of a generalised Stokes layer obtained by spectral-FD solver for a STWSV with $c^+ = 0.5$. GSL distribution for $Re_{\delta_*} = 1 \times 10^4$, $A^+ = 12.0$, $\kappa_x^+ = 0.06$, $\omega^+ = 0.03$, $t^+ = 120$.

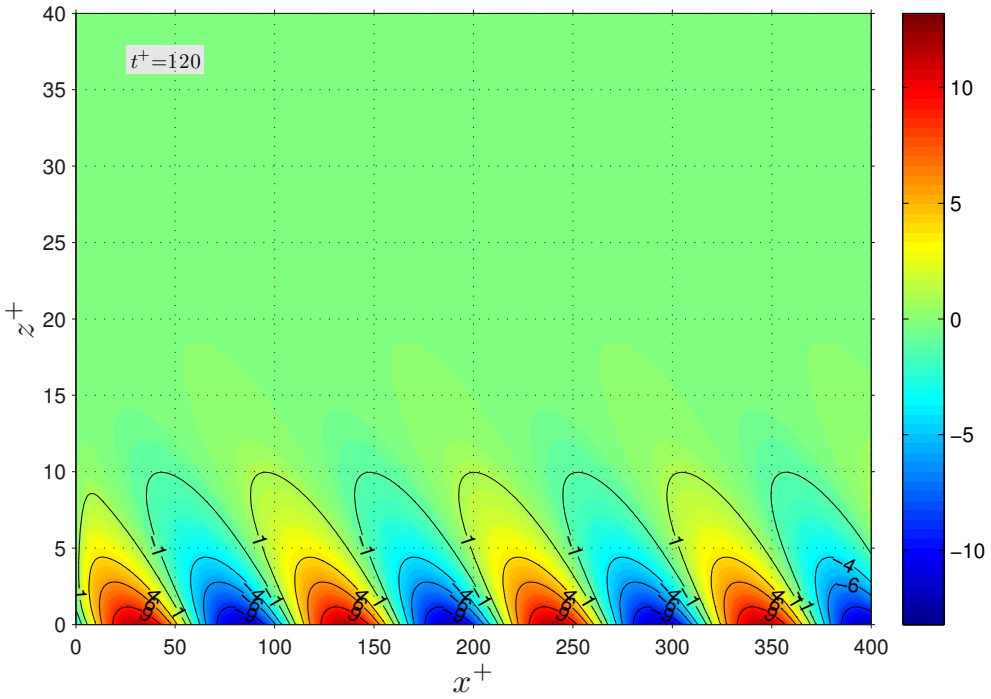

Figure 5.5: Side view of a generalised Stokes layer obtained by spectral-FD solver for a STWSV with $c^+ = 2.0$. GSL distribution for $Re_{\delta_*} = 1 \times 10^4$, $A^+ = 12.0$, $\kappa_x^+ = 0.06$, $\omega^+ = 0.12$, $t^+ = 120$.

It is noteworthy that using the numerical solver, a computational GSL profile can be produced in "real time", i.e. by solving two problems in parallel: the LNSE-LOM-system plus the GSL profile, though evidently decoupled. This does not pose a problem computationally, as long as the temporal step used for both cases can be of roughly equal size. The computational penalty added to the main LNSE-LOM-system due to the additional steps to estimate a GSL profile is minimal. Nevertheless, for most of the numerical experiments, the GSL profile solution using the spectral-FD solver consumed a similar order of computational time spent by the estimation of the analytical formulation.

Although depending on the computational details, it is clear that the computational grid can be adjusted to produce valid GSL profiles without increasing excessively the computational cost over the analytical formulation. This numerical solver has the advantage of being valid throughout the boundary layer thickness of the TBL. However, as it will be shown later, the numerical solution, as in any computational solution advancing in time, produces results which, though barely noticeable, degrade in accuracy as time advances, due precisely to the time integration. In any case, since such trend was minimal in all the numerical tests performed, it is argued that this would not affect the results for the DR/DI tests.

5.2.3 Semi-analytical solution

A third methodology explored to produce the required GSL profiles for the DR/DI tests consisted of a semi-analytical expression. Although the differences in computational time and accuracy of the GSL profiles obtained previously were not dramatically different, with this third approach a 'best-of-the-two' methodologies was pursued; i.e. to produce consistently valid GSL profiles, without degradation of accuracy in time, in a quick manner and without any interlocking of the time step size between the LNSE-LOM-system and the GSL solver.

In this case a functional form is assumed (as best guess of the shape of the GSL profile), and therefore, in this document and for reference purposes, such an approach is also referred to as the *Ansatz* solution, or simply the GSL *Ansatz*. To produce a semi-analytical (Ansatz) solution, a methodology similar to that exposed in §5.2.1 is followed. By introducing a new variable $\zeta = x - ct$, with $c = \omega/\kappa_x$ being the wave speed, the spanwise momentum equation (5.15) can be rewritten as

$$(U - c)\,\frac{\partial V}{\partial \zeta} = \frac{1}{Re}\left(\frac{\partial^2 V}{\partial \zeta^2} + \frac{\partial^2 V}{\partial z^2}\right) \tag{5.23}$$

If it is assumed that, in a similar way as in §5.2.1, the spanwise velocity can be expressed as

$$V = A\,\Re\left(e^{\mathbf{i}\kappa_x\zeta}\,f(z)\right) \tag{5.24}$$

and introducing the non-dimensional relations used in this work, the above equation reduces to the dimensionless expression

$$f''(z) - \left((U-c)\,\mathbf{i}\kappa_x Re_{\delta_*} + \kappa_x^2\right) f(z) = 0 \tag{5.25}$$

with $f(z)$ defined as a complex-valued function. This equation, along with the boundary conditions

$$f(0) = 1 \qquad \text{and} \qquad \lim_{z\to\infty} f(z) = 0$$

can be cast as a boundary-value problem and solved numerically using, for instance, finite-difference discretization of the second derivative. Although it would have been possible to solve the equation (5.25) by using the spectral integral operators defined previously, in a similar manner as in § 5.2.2, a non-uniform mesh finite difference scheme was adopted to solve equation (5.25). The scheme adopted is a centered finite difference scheme, given by

$$f''_k = \frac{2\,h_1\,f_{i+1} - 2\,f_i(h_1+h_2) + 2\,h_2\,f_{i-1}}{h_1\,h_2\,(h_1+h_2)} \tag{5.26}$$

for any wall-normal grid point i, and where $h_1 = z_{i+1} - z_i$ and $h_2 = z_{i+2} - z_{i+1}$ are two consecutive grid spacings. This scheme, as discussed by Khodier [127], eliminates numerical diffusion. This approach provided additional versatility in terms of calculation of the second derivative of the GSL profile directly from the numerical scheme, as well as the possibility to change the distribution of the grid points.

In this work, a LU decomposition of the complex matrix resulting form the centered finite difference scheme is used to get the solution of $f(z)$; in conjunction with the equation (5.24) defined above, this scheme allows to calculate the spanwise velocity profile $V(x,z,t)$, at each position in space and time for any combination of ω and κ_x. Equally, even though in this formulation the derivatives could also be generated by semi-analytical expressions (except in the wall-normal direction), most of the numerical tests on DR/DI were produced with derivatives obtained numerically from the grid values of the GSL profile.

Once more, GSL profiles for the same type of STWSV with wave speeds of $c^+ = 0.5$ and $c^+ = 2.0$ are presented in figures 5.6 and 5.7, respectively, but employing the ansatz solution proposed above. These

travelling waves were obtained for the same set of parameters as in the two previous cases (analytical and numerical solutions). Performing an initial visual assessment against previous results, it is possible to see that there are no changes, and an apparently equally valid profile has been obtained, just as in the previous cases. In this sense the ansatz solution is successful.

It is important to mention that owing to the fact that the ansatz solution is prescribed, an immediate upshot is attained: the calculation of the GSL profile is considerably speeded up. Since there is no solving of any additional problem in the simulations, any computational penalty of the GSL profile estimation, with respect to the original LNSE-LOM-system solution, is essentially negligible. If a further computational improvement is desired, derivatives in streamwise direction can be estimated using also semi-analytical expressions obtained straightforward from the equation (5.24).

In summary, by using the finite differences scheme to solve the ODE (5.25), a considerable computational speed-up is expected since the solution of the linear system posed by the FD must be solved just once: at the beginning of the simulation. Obtaining the GSL profile V at each time step thus becomes just a matrix multiplication with $N_z \times N_x$ operations per time step. In any case, a more precise assessment of the performance, required to select any of the three methodologies proposed, is presented in next section.

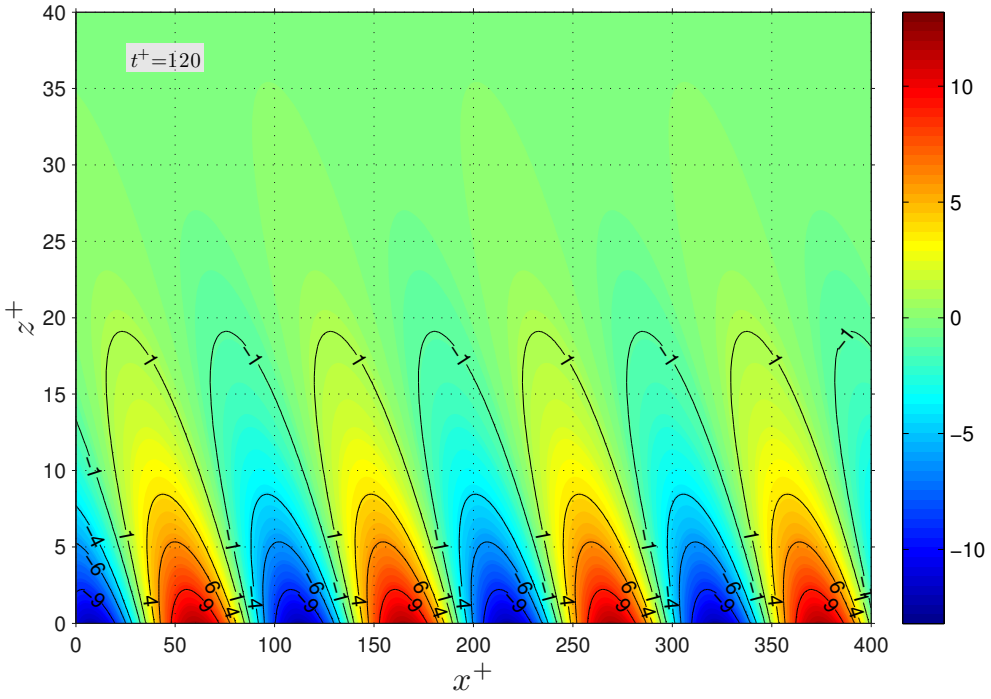

Figure 5.6: Side view of a generalised Stokes layer obtained by numerical ansatz for a STWSV with $c^+ = 0.5$. GSL distribution for $Re_{\delta_*} = 1 \times 10^4$, $A^+ = 12.0$, $\kappa_x^+ = 0.06$, $\omega^+ = 0.03$, $t^+ = 120$.

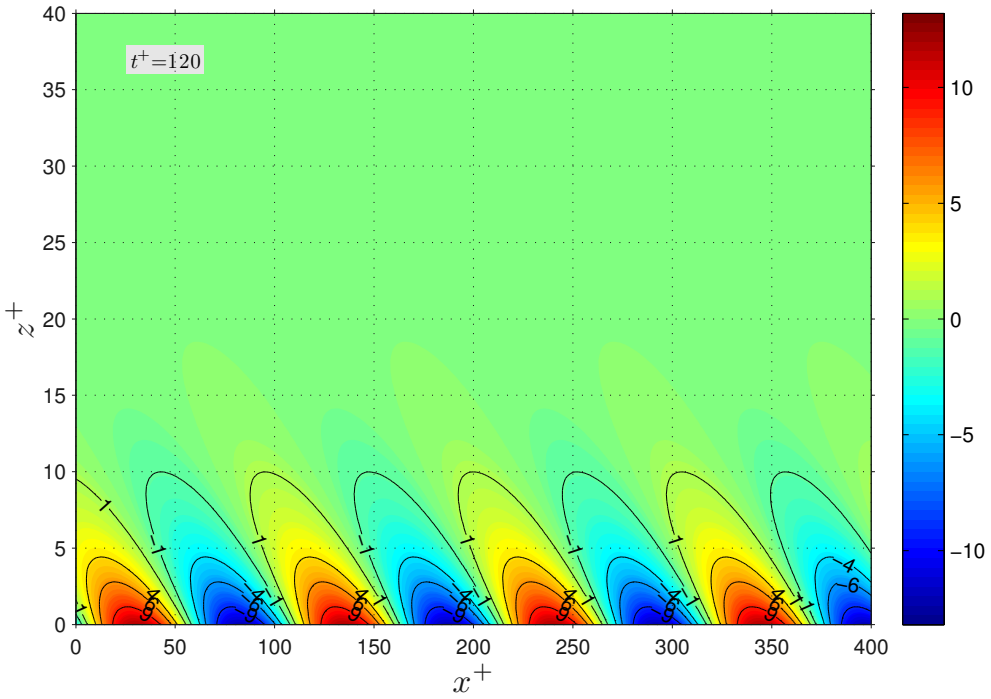

Figure 5.7: Side view of a generalised Stokes layer obtained by numerical ansatz for a STWSV with $c^+ = 2.0$. GSL distribution for $Re_{\delta_*} = 1 \times 10^4$, $A^+ = 12.0$, $\kappa_x^+ = 0.06$, $\omega^+ = 0.12$, $t^+ = 120$.

5.2.4 Comparison of solution approaches

The GSL profiles obtained with the three different methodologies previously presented are essentially similar to each other. Figure 5.8 shows a comparison of the profiles obtained with the three methodologies, for a GSL of a STWSV defined by the parameters $Re_{\delta_*} = 10^4$, $A^+ = 12.0$, $\kappa_x^+ = 0.06$, and $\omega^+ = 0.12$. The profiles presented were extracted at $t^+ = 120.0$, at six different phases (streamwise locations) of the travelling wave. There is not apparent distinction between the profiles obtained with the three types of GSL solvers. In figures 5.9 and 5.10 are portrayed the profiles, obtained with the semi-analytical approach, of the spanwise velocity and its first two derivatives, also for a GSL of a STWSV defined by the parameters $Re_{\delta_*} = 10^4$, $A^+ = 12.0$, $\kappa_x^+ = 0.06$, and $\omega^+ = 0.12$. These profiles have been taken at $t^+ = 120.0$, although at two different streamwise locations (or, equivalently, at two different points in the cycle): figure 5.9 portraits the velocity and its derivatives at a point with maximum spanwise velocity at the wall; figure 5.10 presents the velocity and its derivatives at a point with minimum spanwise velocity at the wall (nearly null). These profiles (velocity and its derivatives) are included given their importance in the stability behaviour. These plots make evident that, since the GSL profile is almost fully contained within the near-wall region ($z^+ < 30$), its inflection points will always be present in this region. Although a deep exploration of the GSL profile stability was not performed in this work, it can be anticipated that the presence of these inflexion points in this region of high streamwise shear will play a crucial role in the stability of the LNSE-LOM-system.

Focusing the attention again in the comparison between the different approaches to get a GSL profile, the detailed examination presented in figure 5.11 reveals that there are actually minor differences, which are more pronounced in the point of maximum curvature in the profile. This tendency is preserved even at different reynolds numbers, as it can be seen in figure 5.12 where a STWSV with the same parameters is presented, although for $Re_{\delta_*} = 5000$. As a side note, in this figure it is possible to appreciate that, as it would be expected, the spanwise profile scales in inner units, so it is Reynolds number independent if represented in inner units. In terms of GSL profiles assessment, it seems that all methodologies are equally valid as a mechanism to obtain a GSL profile for any given STWSV.

In order to get a clearer indication of which methodology fits the current linearized formulation it is necessary to do a more in-depth evaluation of the GSL profiles. This selection was made using: quality of the profile in terms of accuracy, and speed of the GSL solver chosen, as previously mentioned. The accuracy and speed analyses for the numerical approximations are presented in appendix A. With basis on this evaluation, the GSL profile obtained by employing the semi-analytical (Ansatz) approximation has been selected as model for the spanwise velocity profile to be used in the STWSV flow control study, along with the LNSE-LOM-system previously selected.

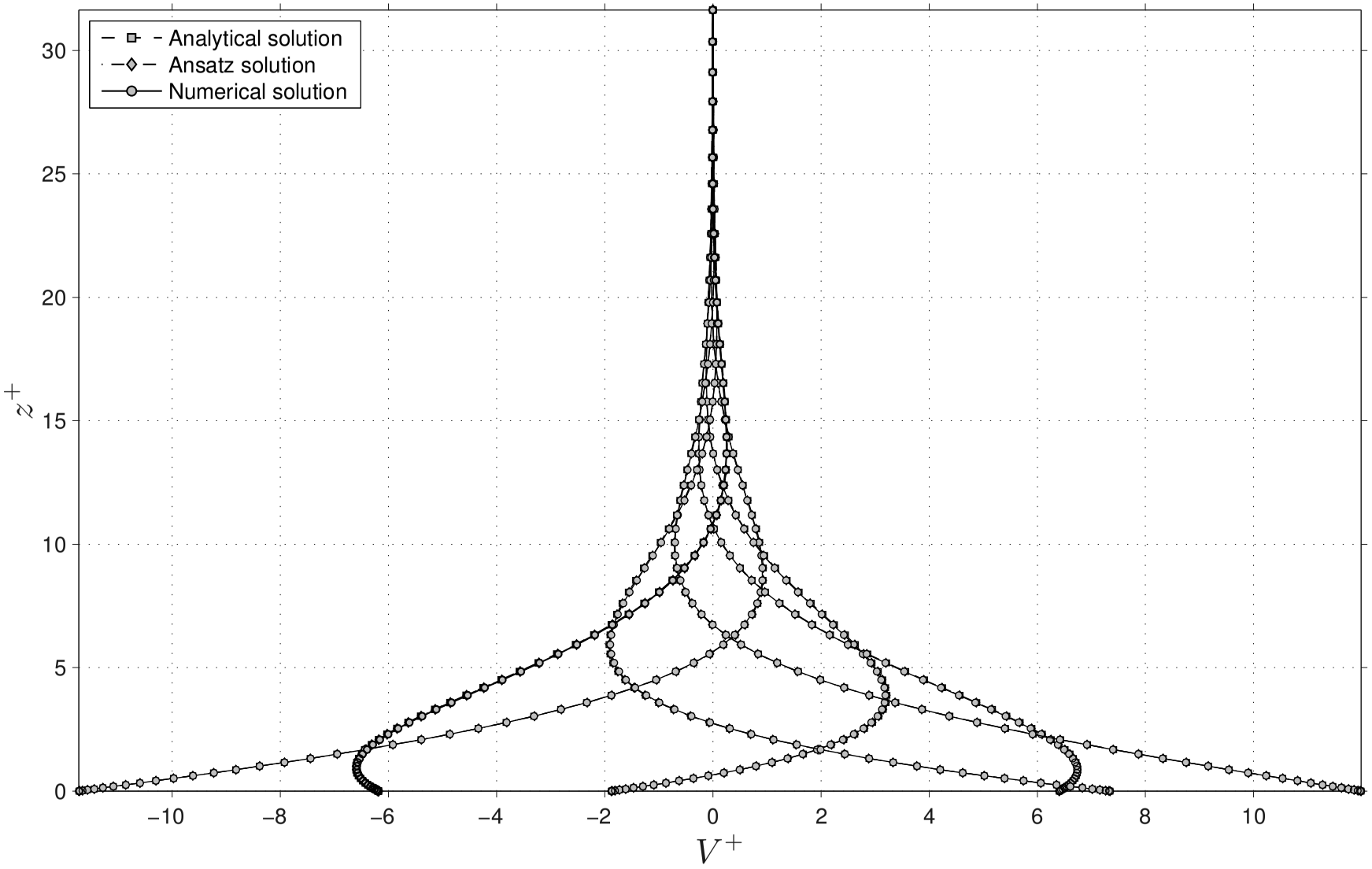

Figure 5.8: Comparison at six different phases of the cycle, between the GSL velocity profile computed via (i) Analytical solution, (ii) Ansatz solution, and (iii) Numerical solution, for a STWSV with $c^+ = 2.0$. GSL at $Re_{\delta_*} = 10^4$, $A^+ = 12.0$, $\kappa_x^+ = 0.06$, $\omega^+ = 0.12$, $t^+ = 120$.

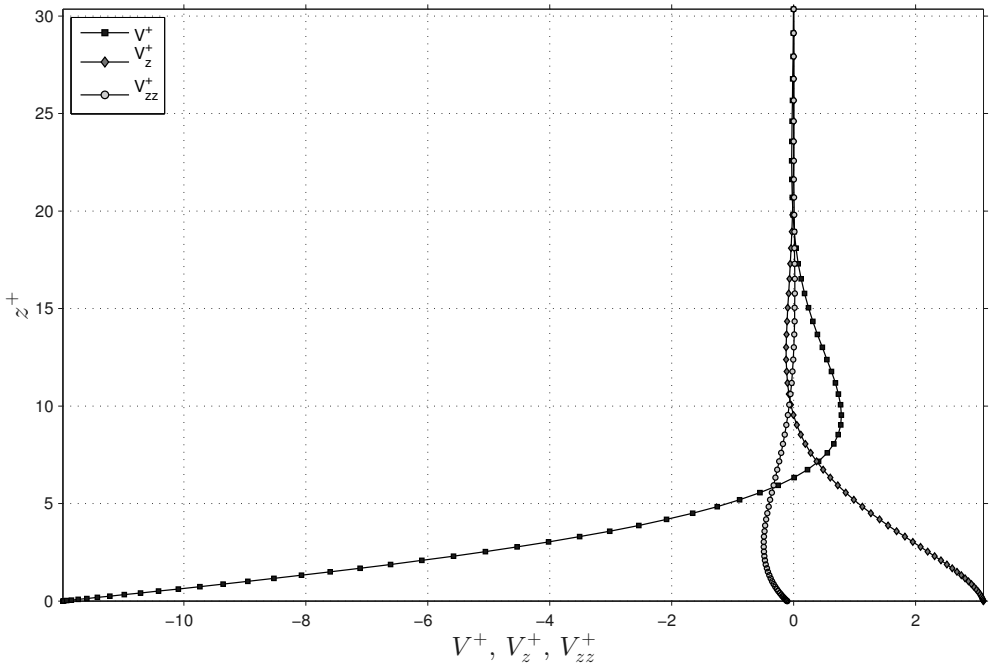

Figure 5.9: Comparison of the spanwise velocity profile (V^+) obtained by semi-analytical solution of the GSL, against its first (V_z^+) and second (V_{zz}^+) derivatives in wall-normal direction. Profile of GSL phase with maximum amplitude at the wall at $t^+ = 120$ and STWSV with $c^+ = 2.0$. GSL defined at $Re_{\delta_*} = 10^4$, $A^+ = 12.0$, $\kappa_x^+ = 0.06$, $\omega^+ = 0.12$, $t^+ = 120$.

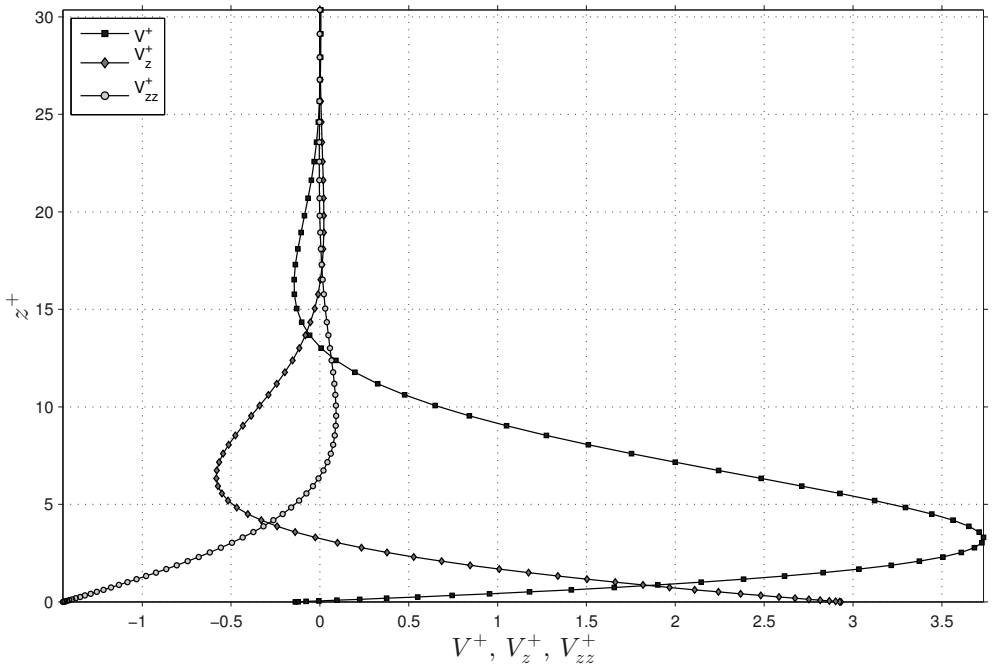

Figure 5.10: Comparison of the spanwise velocity profile (V^+) obtained by semi-analytical solution of the GSL, against its first (V_z^+) and second (V_{zz}^+) derivatives in wall-normal direction. Profile of GSL phase with (approximate) null amplitude at the wall at $t^+ = 120$ and STWSV with $c^+ = 2.0$. GSL defined at $Re_{\delta_*} = 10^4$, $A^+ = 12.0$, $\kappa_x^+ = 0.06$, $\omega^+ = 0.12$, $t^+ = 120$.

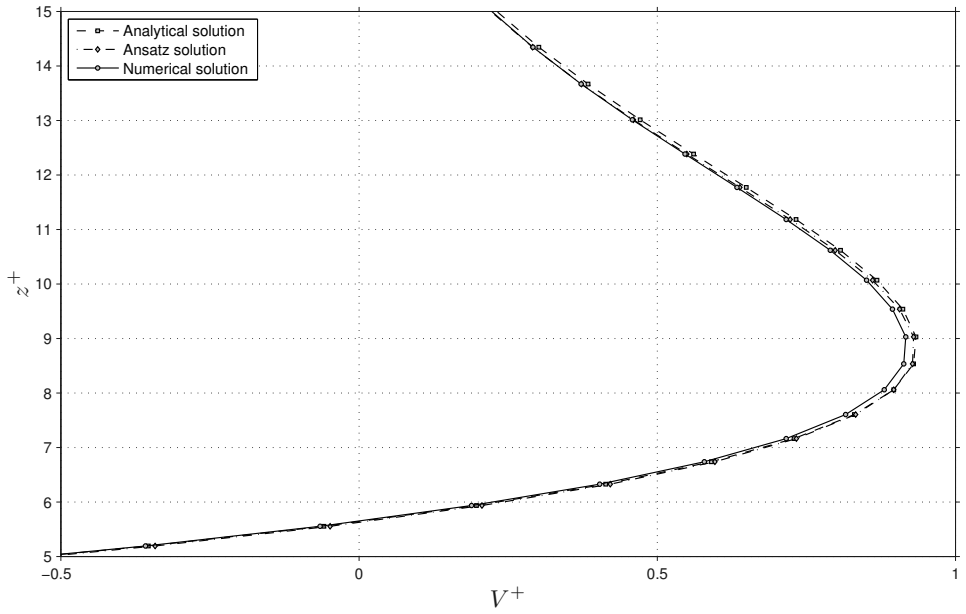

Figure 5.11: Detailed comparison, for a single phase of the cycle, between the GSL velocity profile, at $Re_{\delta_*} = 1 \times 10^4$, computed via (i) Analytical solution, (ii) Ansatz solution, and (iii) Numerical solution using spectral-FD code, for a STWSV with $c^+ = 2.0$. GSL distribution for $Re_{\delta_*} = 10^4$, $A^+ = 12.0$, $\kappa_x^+ = 0.06$, $\omega^+ = 0.12$, $t^+ = 120.0$.

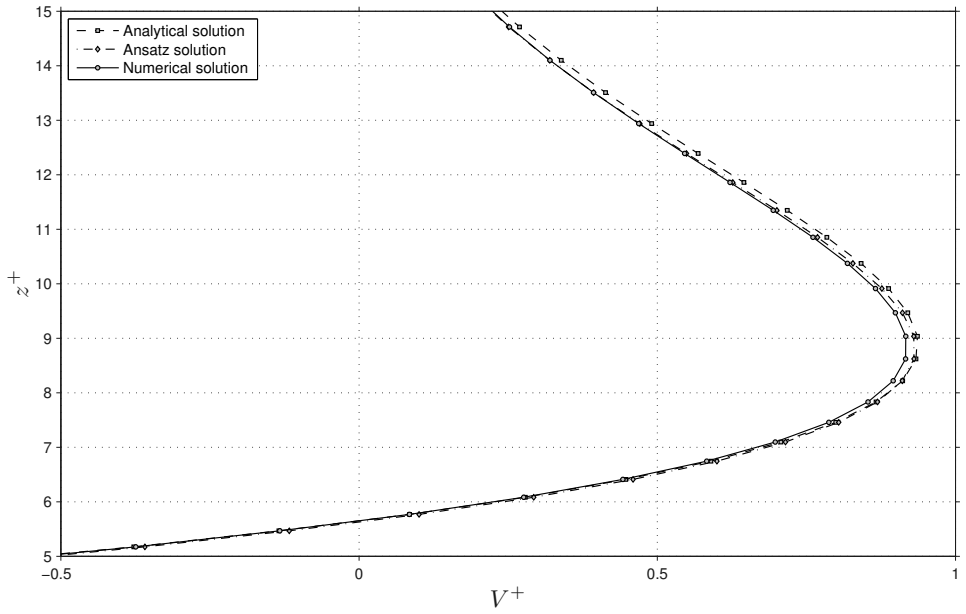

Figure 5.12: Detailed comparison, for a single phase of the cycle, between the GSL velocity profile, at $Re_{\delta_*} = 5 \times 10^3$, computed via (i) Analytical solution, (ii) Ansatz solution, and (iii) Numerical solution using spectral-FD, for a STWSV with $c^+ = 2.0$. GSL distribution for $Re_{\delta_*} = 5 \times 10^3$, $A^+ = 12.0$, $\kappa_x^+ = 0.06$, $\omega^+ = 0.12$, $t^+ = 120.0$

5.3 Numerical Simulations

The main aim of this part is to investigate if there is any correlation between the response of the linearized system and the results on skin-friction drag reduction obtained experimentally and numerically for flow control techniques of the same nature as in [57, 58, 125]. In such works results have been obtained for turbulent channel flows and for a range of parameter values of the STWSV given by $0 \leq \kappa_x^+ \leq 0.025$ and $-0.3 \leq \omega^+ \leq 0.3$, approximately.

In the present thesis, a number of numerical simulations are performed on turbulent boundary layer flows, initially at $Re_\tau = 200$, with control using streamwise-travelling waves (STWSV) over the same range of κ_x^+ and ω^+ as those mentioned above, with wave velocity amplitude $A_w^+ = 12$ (as in the DNS of Quadrio et al. [57]).

A noteworthy remark is that the flow control techniques described in this thesis will, in reality, affect the mean streamwise velocity profile, and therefore the wall-shear stress. It is not possible to predict or quantify this effect with the current linear model. As such, there is no impact on the definition of viscous units as a result of control. For this reason it is also not possible to say that a *direct* estimation of drag reduction or drag increase can be obtained using the model here developed. Instead, changes in the measures, previously introduced, are compared to published DNS results in terms of drag reduction or drag increase (DR/DI). Therefore, in order to examine the effect of the flow control by spanwise wall oscillations on the generation of streaks generated with a selected LNSE-LOM-system, it is necessary to devise a mechanism to quantify the change of growth intensity of the near-wall structures undergoing controlled transient growth. This is discussed in further detail below, in section § 5.3.1.

Although most of the results obtained and reported here correspond to a turbulent boundary layer, it was possible to model the development of near-wall streaks for the channel flow case using the same code and methodology developed here by modifying the streamwise base flow profile and taking the boundary layer edge as equivalent to the channel centre-line. In this way, in those cases where the turbulent channel base flow profile is used, the profile $U(z)$ is generated with the parameters defined for channel flows in table 2.1, and with the values presented in table 3.1. The numerical methodology to obtain such a profile is, in essence, the same as in the TBL case. Nevertheless, by using this approach, in the great majority of the simulations, the numerical results gave very similar outcomes. This was arguably expected, owing to the fact that neither the streaks nor the oscillatory flow had any significant protrusion into the outermost part of the boundary layer.

For the different numerical experiments presented in this section, a streamwise periodic computational domain

was set to $L_x^+ = 3141.6$, with simulations extending over a period of $\tau_t^+ = 300.0$. In all the cases the streamwise domain was discretized using a grid spacing of $\Delta x^+ = 10.472$. In the wall-normal direction a total of $N_z = 128$ collocation points were prescribed. The periodicity in streamwise direction was enforced by setting

$$\phi(x = 0, y, z, t) = \phi(x = L_x, y, z, t) \tag{5.27}$$

for all the perturbation variables, as indicated in § 2.2.3, and equation (2.33).

5.3.1 Transient growth change quantification and instability definition

Regarding the numerical tests presented here, two methods are used for the quantification of the change of transient growth as compared to an uncontrolled case, i.e. with no STWSV present. This value, also referred to as the measure increase or measure reduction (MI/MR), is the resulting change obtained when the flow control actuation is activated. Using the values of amplification measure, at a given time instant t, an estimation of percentage change (ϵ) for every point in the control parameter space (pair $\omega - \kappa_x$) is calculated as

$$\epsilon = \frac{\mu_{i,c}(t) - \mu_{i,u}(t)}{\mu_{i,u}(t)} \times 100 \tag{5.28}$$

with $\mu_{i,c}$ representing the $i-$th measure for the controlled case, $\mu_{i,u}$ the same $i-$th measure for the uncontrolled case and t is the time instant at which the change is calculated.

In addition to the ϵ control measure, it is possible to obtain a controlled transient growth change measure independent of the time scale, for every point in the parametric control space (pair $\kappa_x - \omega$), by using the maximum values in time. In this way, first the maximum in time of an amplification measure given by the LNSE-LOM-system is taken, and then this value is compared to the maximum in time of the same amplification measure obtained without flow control; then a percentage change, $\epsilon_{\max\, t}$, is calculated as

$$\epsilon_{\max\, t} = \frac{\max\limits_{\tau_t} \mu_{i,c} - \max\limits_{\tau_t} \mu_{i,u}}{\max\limits_{\tau_t} \mu_{i,u}} \times 100 \tag{5.29}$$

with $\mu_{i,c}$ and $\mu_{i,u}$ being the $i-$th measure for the controlled case and uncontrolled cases, respectively, and τ_t being the total simulation time. The use of one or another of these definitions is explicitly declared when they are used later in the control experiments.

The term 'instability' will be constantly employed later on in the different subsequent discussions. Thus, it is imperative to define what it will be considered as instability for the purposes of the present work. Once a percentage change has been calculated, for a given control operational point ($\kappa_x - \omega$), the term instability will characterize the phenomenon in which a perturbation undergoing transient growth, under the effect of the spanwise oscillations control, exhibits a percentage change of growth, of a selected measure, higher than a given percentage of the maximum obtained for the uncontrolled case. As it will be mentioned later again, in the present work such threshold was chosen to be 50%; i.e. once the percentage change of maximum streak growth of a given measure ($\epsilon_{\max\, t}$) is above 50%, then such a near-wall structure (being this a streamwise streak or not) will be considered as an instability. Additionally, just to clarify in the present context, an instability will not necessarily imply unbounded growth; nevertheless, in some of the control cases studied, this has been the final outcome. For this reason, on a few occasions of the remainder part of this thesis, any instability will also be referred to as a potential unbounded growth case.

5.3.2 The spanwise oscillation wave phase

The influence of the phase angle between the streamwise travelling wave of the spanwise wall oscillations and, either the initial spatial location of the centre of excitation, or the initial excitation time, was explored in a number of numerical tests. It is obvious that due to the periodicity of the STWSV, a wave phase angle ϕ (or simply the wave phase) can be incorporated into the original STWSV prescription as

$$V_{wall} = A_w \, \Re \left[e^{\mathbf{i}(\kappa_x x - \omega t + \phi)} \right] \tag{5.30}$$

with a periodicity between $[0, 2\pi]$. The main aim of this phase study is to determine if there exists any influence of the relative position between the different points of the wave and the streak perturbation on the evolution of the perturbation.

Regarding the spatial locality, in all the numerical tests the spatial location of the IC-EM used to generate the initial perturbation, and therefore the initial spatial location of the near-wall streak generated, has been fixed. In this way, once variables x_f and z_f (if required) are chosen for a given initial condition, then all numerical experiments are performed keeping the spatial location of the EM fixed. For the initial condition $I_{1,w}$ there is not an explicit location x_f and z_f, but instead a single parameter σ_z determines the spatial distribution of the initial condition.

In all the streak control numerical experiments presented in this work, the STWSV is initiated in the simulation at the same time instant as the simulation starts, i.e. the spanwise oscillation control is constantly present

during the evolution of the perturbation under study. However, as a *'Thought Experiment'*, the effect of a delay between the perturbation onset and the start-up time of the STWSV (labelled as t_c) was performed, and its results are discussed in § 5.3.3. To this end, and since the effect of such a delay will be only to change the wave phase between the STWSV and the perturbation evolving in time, a control start-up time t_c is also introduced in the definition of the wave phase angle. The details and results of such a *'Thought Experiment'* are explained in further detail in § 5.3.3.

It is possible to consider both types of phase angle (either defined by the initial spatial location or by the control activation time) by defining a wave phase ϕ_i of the STWSV as

$$\phi_i = \omega\, t_c \, - \, \kappa_x \, x_f \, + \, \rho_i \, \pi \tag{5.31}$$

for any i-th fraction of π. In this expression ω is the temporal frequency of the STWSV, κ_x its streamwise wavenumber, t_c the start-up time instant at which the STWSV is effectively initiated, and ρ_i is a fraction factor for π, which in turn produced a different offset between initial EM location and travelling wave for every ϕ_i. It is easy to see that, due to the periodicity of the STWSV, only half of a complete wave cycle is required in a phase-effect study, and therefore phases are restricted to $[0, \pi]$.

Firstly, though, how important is a given wave phase in the development of the streaks? In figures 5.13a to 5.13c the development of streaks, in terms of streamwise perturbation velocity, is shown for a low-order optimal perturbation generated with $I_{2,w}$, developing in a TBL at $Re_\tau = 200$ and for a number of control wave phases. A similar situation, although for a TBL at $Re_\tau = 5000$, is presented in figures 5.14a to 5.14c. In all these cases (figures 5.13a to 5.13c and 5.14a to 5.14c) the control activation time is effectively set to zero, $t_c = 0$. As it can be seen, the choice of specific wave phase, i.e. a value of ρ_i, has a dramatic impact on the streak development.

As the intention in this work is to explore an ample set of waves for given combinations of κ_x and ω, it would be unpractical, and certainly a bit unrealistic, to ascertain the impact of single specific wave phases, without consideration of other points in the wave cycle. For this reason, in the numerical experiments involving spanwise wall oscillations, a series of parallel simulations at discrete values of ρ_i have been performed, and then an average over the phases has been taken using the temporal evolution of the different measures μ_i introduced in §4.

In figures 5.15 and 5.16 the evolution of the uncontrolled case is compared against the phase-average of the flow control cases presented before in figures 5.13a to 5.13c and figures 5.14a to 5.14c, respectively. In all these cases the initial condition $I_{2,w}$ has been used as excitation mechanism (EM), and its parameters

obtained by optimization of the problem {Type-II, μ_1} defined at $z_v^+ = 12.5$; i.e. the optimal parameter combination of this uncontrolled case is being considered here for all the different simulations (controlled and uncontrolled).

It is expected that the number of phases to be included in the averaging process might have a sensitive impact on the outcome for a particular control case. In this work the numerical experiments included 12, 24 or 36 phases (the specific number of phases ρ_i is explicitly indicated for every case discussed). However, although not explicitly described here, it was found that averaging above 12 different phases did not produce significant changes in the final result, and for this reason all numerical experiments here reported employed at least 12 phases.

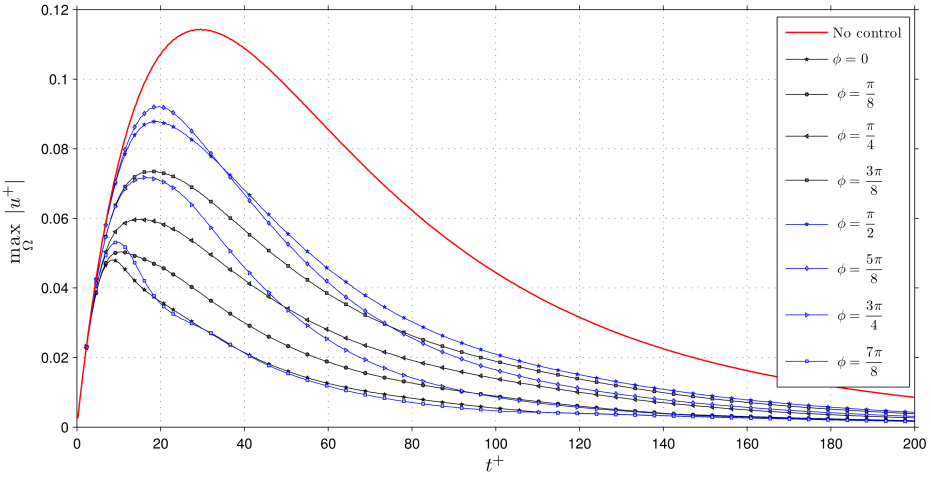

(a) Transient evolution of streak within a STWSV defined by $\kappa_x^+ = 0.000$ and $\omega^+ = 0.060$

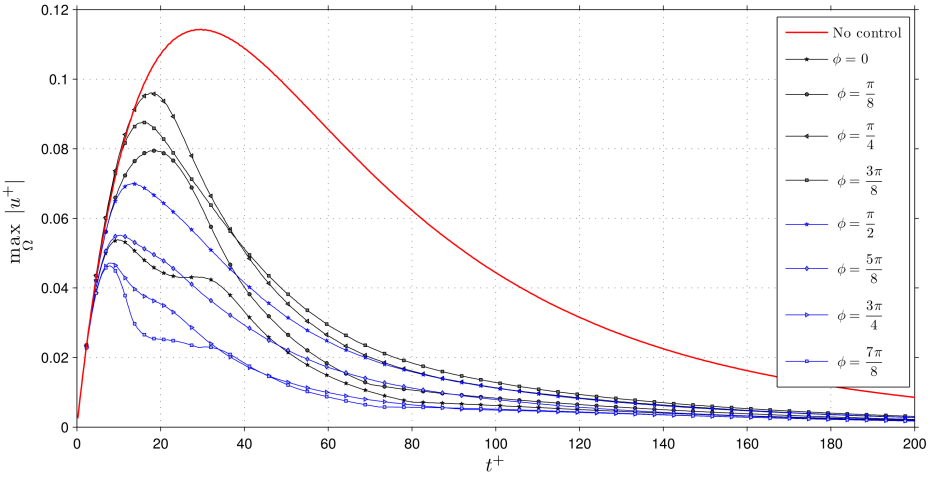

(b) Transient evolution of streak within a STWSV defined by $\kappa_x^+ = 0.006$ and $\omega^+ = 0.000$

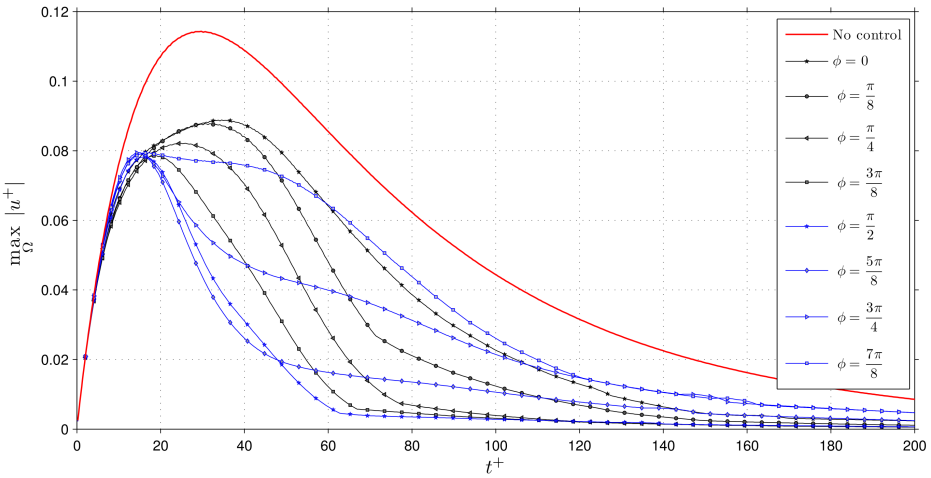

(c) Transient evolution of streak within a STWSV defined by $\kappa_x^+ = 0.006$ and $\omega^+ = 0.060$

Figure 5.13: Comparison of the effect of 8 different phases over the transient growth of a low-order optimal perturbation under action of different STWSV. Optimal perturbation obtained from LNSE-LOM-system defined by {Type-II, μ_1} for $I_{2,w}$ as EM, and for a TBL at $Re_\tau = 200$. Optimal perturbation parameters: $\sigma_{x,EM}^+ = 1.0 \times 10^{-4}, \sigma_{z,EM}^+ = 3.9 \times 10^{-3}, \lambda_y^+ = 86$.

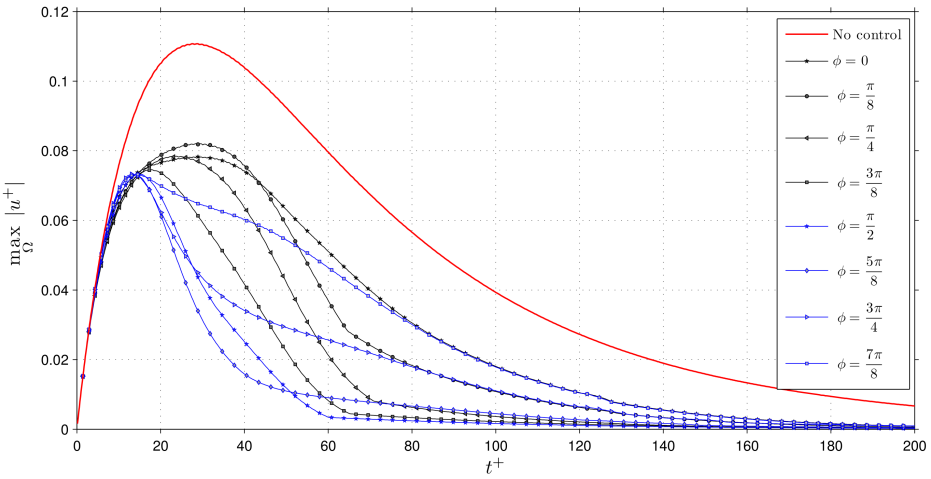

(a) Transient evolution of streak within a STWSV defined by $\kappa_x^+ = 0.006$ and $\omega^+ = 0.060$

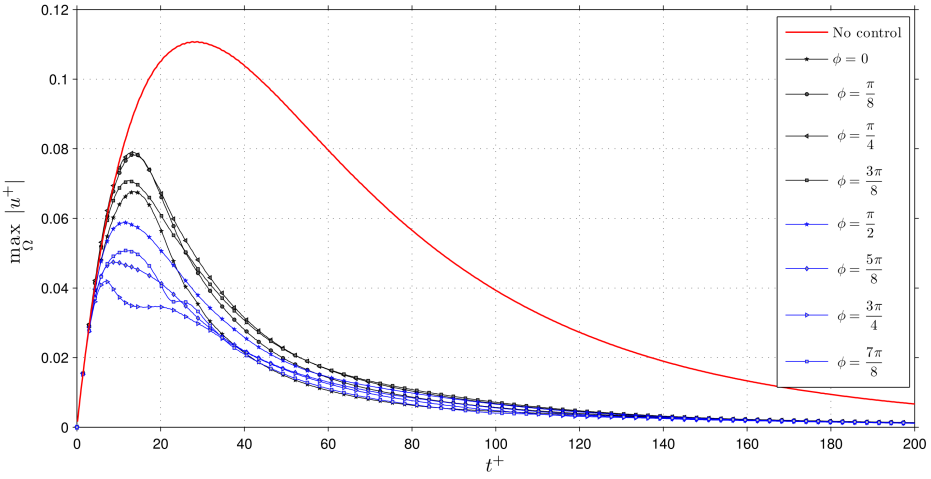

(b) Transient evolution of streak within a STWSV defined by $\kappa_x^+ = 0.012$ and $\omega^+ = 0.030$

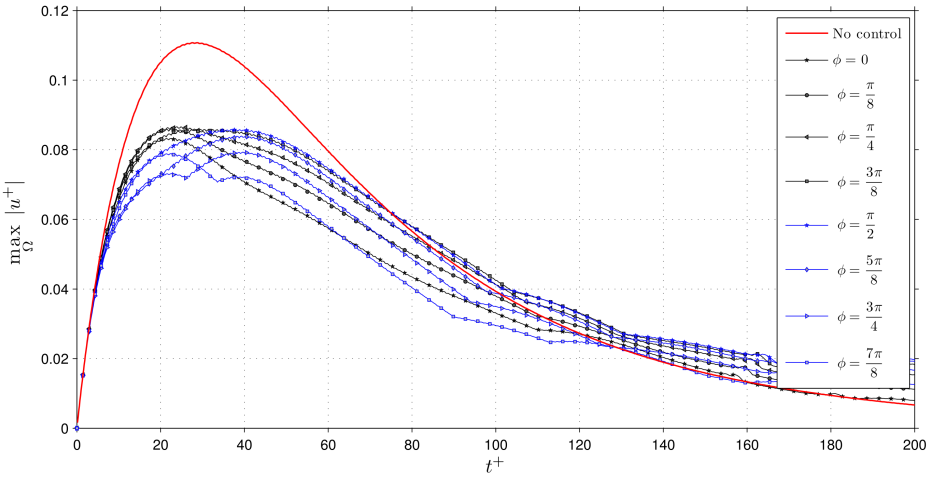

(c) Transient evolution of streak within a STWSV defined by $\kappa_x^+ = 0.024$ and $\omega^+ = 0.270$

Figure 5.14: Comparison of the effect of 8 different phases over the transient growth of a low-order optimal perturbation under action of different STWSV. Optimal perturbation obtained from LNSE-LOM-system defined by {Type-II, μ_1} at $z_v^+ = 12.5$ for $I_{2,w}$ as EM, and for a TBL at $Re_\tau = 5000$. Optimal perturbation parameters: $\sigma_{x,EM}^+ = 1.0 \times 10^{-4}, \sigma_{z,EM}^+ = 3.9 \times 10^{-3}, \lambda_y^+ = 86$.

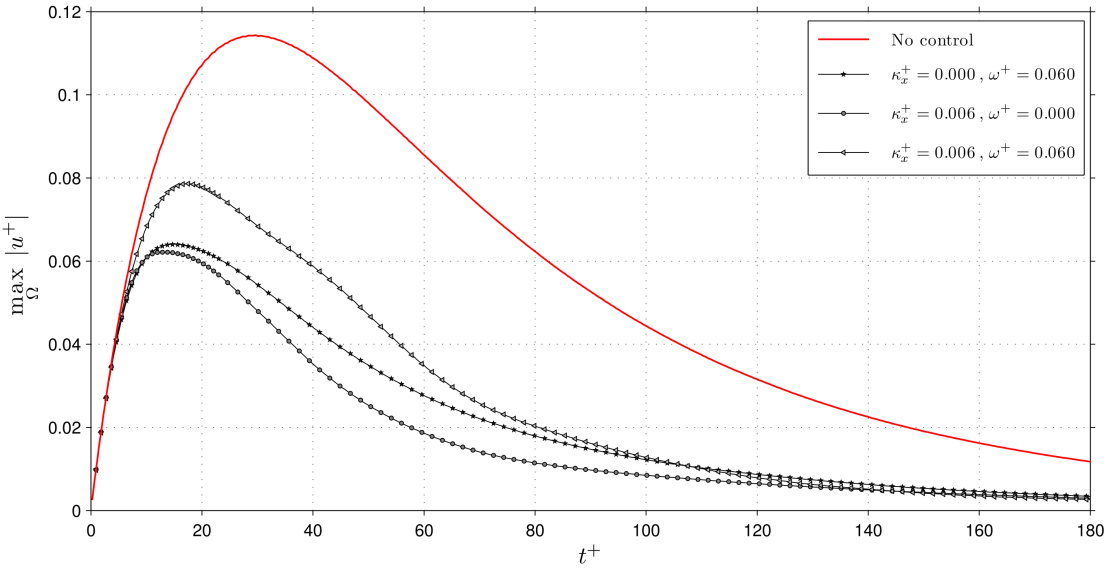

Figure 5.15: Comparison of streak transient growth between uncontrolled case and phase-averaged STWSV for a TBL at $Re_\tau = 200$; average streamwise perturbation velocity using 12 phases. Optimal perturbation defined by {Type-II, μ_1} at $z_v^+ = 12.5$ for $I_{2,w}$; perturbation parameters: $\sigma_{x,EM}^+ = 1.0 \times 10^{-4}, \sigma_{z,EM}^+ = 3.9 \times 10^{-3}, \lambda_y^+ = 86.0$

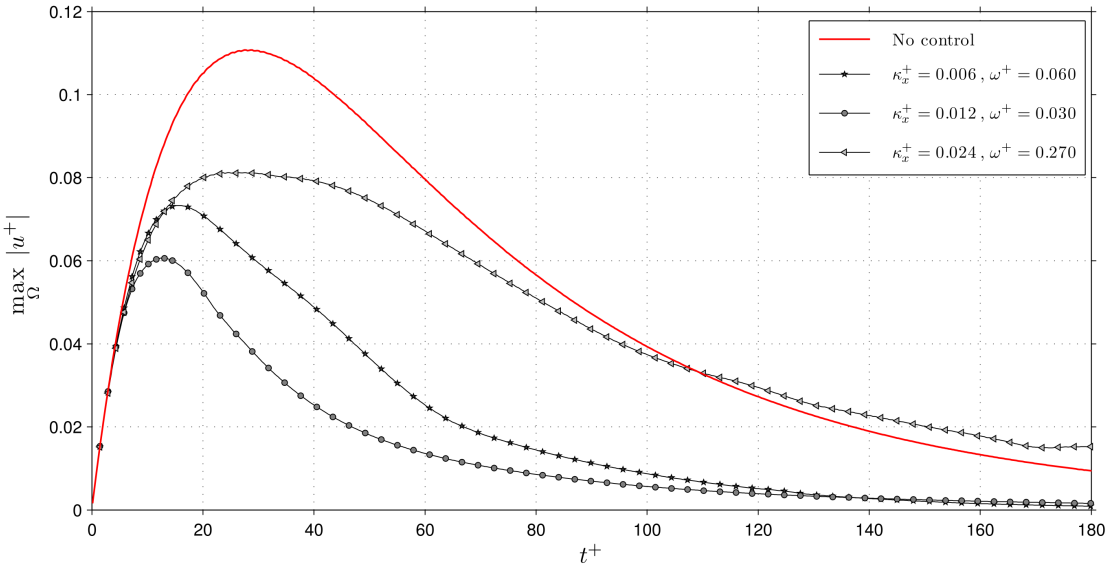

Figure 5.16: Comparison of streak transient growth between uncontrolled case and phase-averaged STWSV for a TBL at $Re_\tau = 5000$; average streamwise perturbation velocity using 12 phases. Optimal perturbation defined by {Type-II, μ_1} at $z_v^+ = 12.5$ for $I_{2,w}$; perturbation parameters: $\sigma_{x,EM}^+ = 1.0 \times 10^{-4}, \sigma_{z,EM}^+ = 3.9 \times 10^{-3}, \lambda_y^+ = 86.0$

At this point another comparison is useful. In figure 5.17 is presented the transient growth for uncontrolled and controlled cases, for the same wave speeds and cases as in figure 5.15, but this time using a turbulent channel profile as the mean streamwise base flow. The same low-order optimal perturbation used in the turbulent Boundary layer case (figure 5.15) has been employed as the streak EM. It is possible to observe a close correlation of transient evolutions between the uncontrolled cases for both type of profiles, turbulent channel and turbulent boundary layer; equally, a high similarity in the evolution of the control cases is present between these two base flows.

These results confirm the previous conjecture regarding the similarity in the responses for these two types of flows, from the point of view of the present LNSE-LOM-system. This fact supports the premise of using the linearized system here adopted, along with a TBL base profile, to perform comparisons against the DNS results of DR/DI in channel flow presented by Quadrio et al. [57].

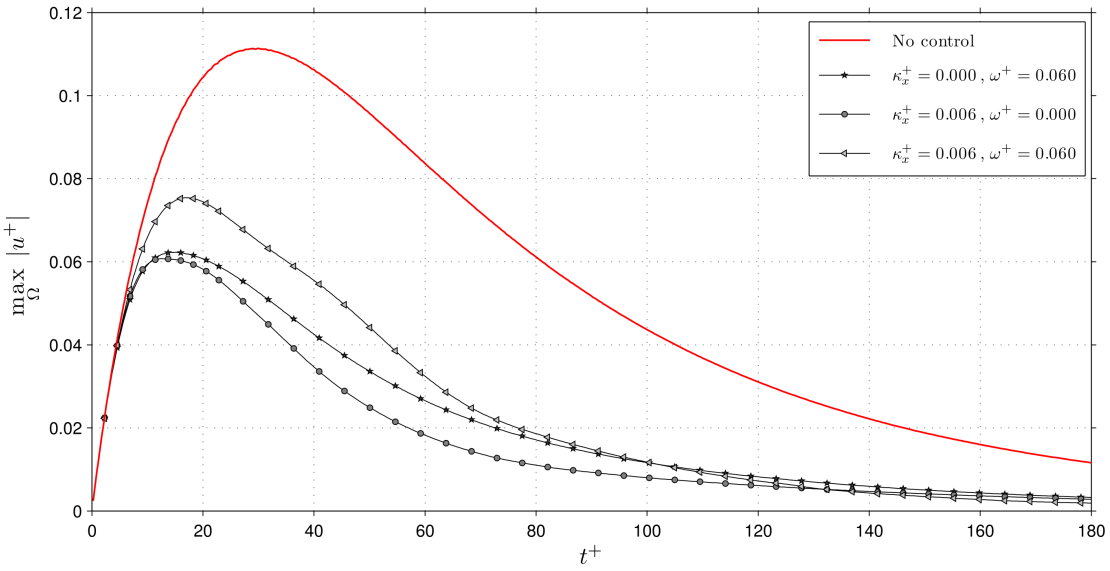

Figure 5.17: Comparison of streak transient growth between uncontrolled case and phase-averaged STWSV for a turbulent Channel flow at $Re_\tau = 200$; average streamwise perturbation velocity using 12 phases. Optimal perturbation defined by {Type-II, μ_1} at $z_v^+ = 12.5$ for $I_{2,w}$; perturbation parameters: $\sigma_{x,EM}^+ = 1.0 \times 10^{-4}, \sigma_{z,EM}^+ = 4.0 \times 10^{-3}, \lambda_y^+ = 86$.

5.3.3 Effect of the control activation time

In the definition of the wave phase angle presented in equation (5.31), a control start-up time was introduced. A *'Thought Experiment'* in which any transient development of the generalised Stokes layer (GSL) is simply ignored, is then implemented by setting the parameter $t_c > 0$. As briefly explained in § 5.3.2, this control activation time is assumed to be an artificial delay between the onset of the perturbation evolution and the activation of the spanwise GSL profile. It is important to note that this is a pure 'theoretical' exercise, as such phenomena does not have any physical relevance since, in this 'thought experiment', the GSL is considered effectively null initially and then instantaneously switched on, which is not possible to be true in a real control case scenario. The main aim of this exercise is to evaluate if the absence of the transient build-up period of the GSL has any influence on the response of the LNSE-LOM-system.

In order to assess the impact of this control-activation or starting-up time, a series of numerical simulations were performed with the spanwise wall oscillation becoming active at different time instants t_c. A sample of these results is presented in figures 5.18 to 5.20, where a comparison of the effect of flow control becoming active at $t_c^+ = 0, 20 \text{ and } 50$ is shown for a TBL at $Re_\tau = 200$. Although the cases presented in these plots are for a STWSV with $\kappa_x^+ = 0.006$ and $\omega_t^+ = 0.060$ as control operational point, similar results were obtained for another ample set of operational points. In figures 5.18 and 5.20 the control is applied on a perturbation generated with $I_{2,w}$ as EM, whereas in figure 5.19 the EM used is the streamwise independent condition $I_{1,w}$. In these three cases the initial perturbation is defined with the LNSE-LOM-system {Type-II, μ_1} at $z_v^+ = 12.5$.

From these results it can be seen that, as probably expected, the effect of the spanwise oscillation is felt immediately after the flow control becomes active. The transient growth for streaks under the influence of control reveals two general tendencies. For instance, in cases like those shown in figures 5.18 and 5.19, there is a reduction of the intensity of the streak generated in comparison to the uncontrolled case, soon afterwards the activation of the control. In these simulations this inhibitive effect remains unaltered, which makes the controlled streak becoming strongly subdued and therefore to vanish at a much earlier stage in comparison with the uncontrolled case. On the other hand, in situations like the one portrayed by figure 5.20, although an initial reduction can appear, a later enhancement of the intensity of the streak by the influence of the control can be observed. This tendency was obtained especially in control cases of perturbations at spanwise scales greater than the optimal spanwise spacing. For instance, in figure 5.20 the evolution shown is for a perturbation developing at $\lambda_y^+ = 258$, i.e. approximately three times the optimal spanwise spacing for the same initial perturbation $I_{2,w}$. This particular observation is discussed later.

In any case, what is important to note is that, from the tendency depicted in these plots, it seems clear that if an inhibitory action exists, it occurs at early stages in the development of the streak, i.e. at the algebraic growth stage. On the other hand, if a streak enhancement occurs, it occurs at the later dissipative stage. It is interesting to note that in some cases this growth was seemingly unbounded. Some examples of control producing streak enhancement, although no unbounded, are shown in figure 5.20.

Since this particular numerical experiment was a pure artifact, and for practical relevance, the remaining numerical tests on streak control were performed with this control activation time of the oscillation effectively null ($t_c = 0$). For instance, if it is conjectured that the streak development is an element of a turbulence cycle, it would be extremely difficult to synchronise a control activation time of the order of $t^+ \approx 10$, for any kind of practical control application. Instead, it is arguably more realistic to assume that, given the sort of time scales involved, to consider the starting-up time equal to zero (in combination with the phase averaging earlier discussed) is equivalent to assume that the flow control is always activated, independent of the existence or not of the streak.

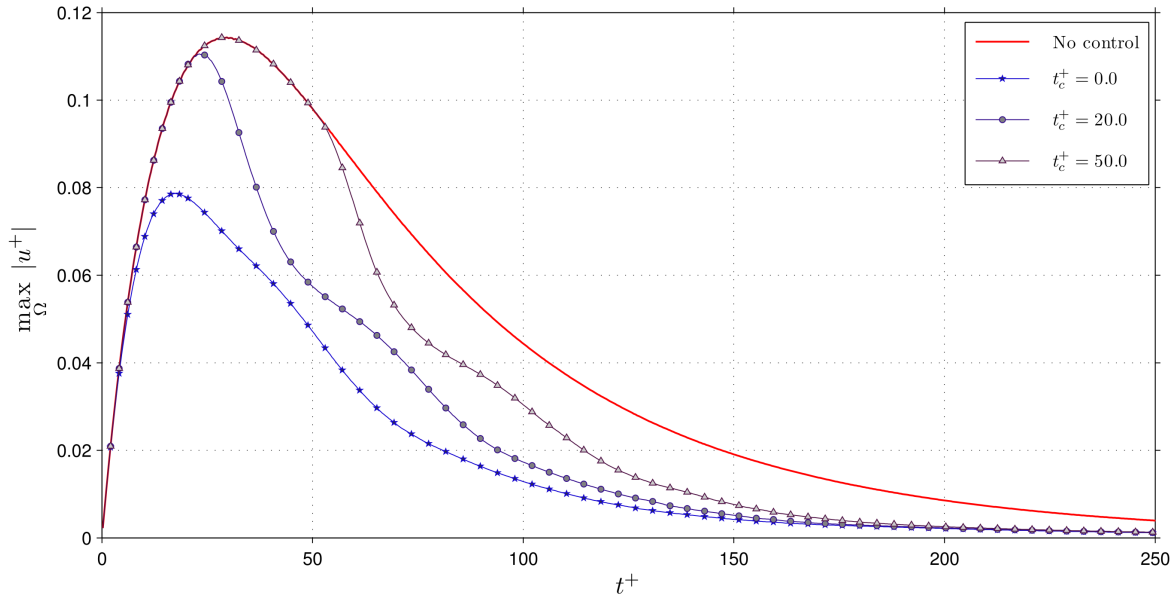

Figure 5.18: Comparison of the effect of change in the control activation time t_c^+ on the streamwise perturbation velocity. Results for a STWSV with $\kappa_x^+ = 0.006$, $\omega^+ = 0.060$. Streak generated with LNSE-LOM-system {Type-II, μ_1} at $z_v^+ = 12.5$, using $I_{2,w}$ as EM and for a TBL at $Re_\tau = 200$. Optimal perturbation parameters: $\sigma_{x,EM}^+ = 1.0 \times 10^{-4}, \sigma_{z,EM}^+ = 3.9 \times 10^{-3}, \lambda_y^+ = 86.0$

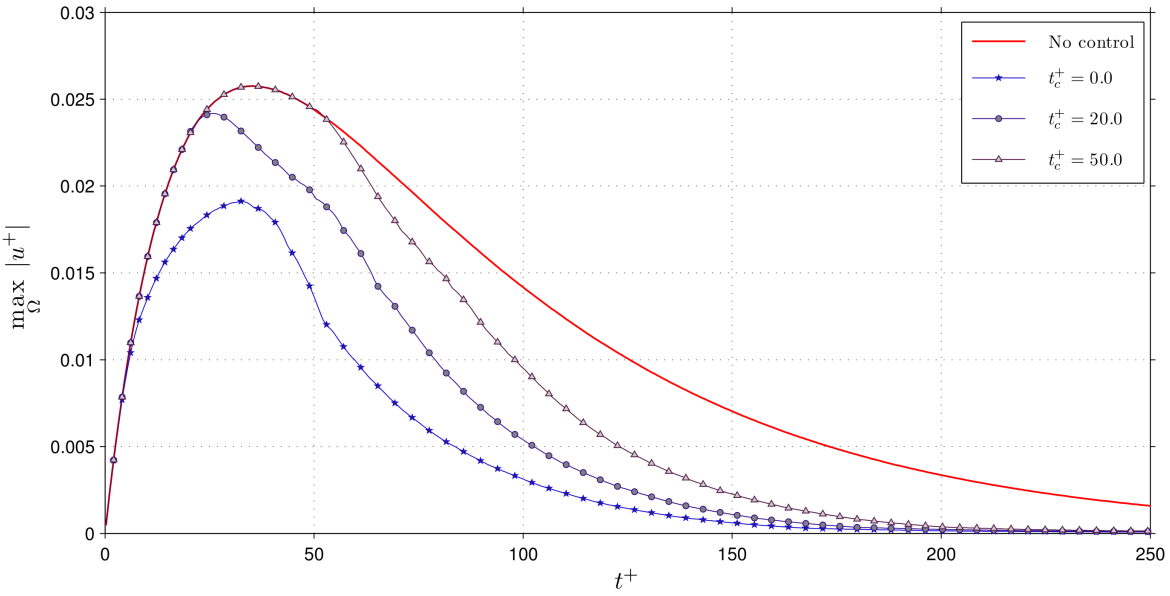

Figure 5.19: Comparison of the effect of change of the control activation time t_c^+ on the streamwise perturbation velocity. Results for a STWSV with $\kappa_x^+ = 0.006$, $\omega^+ = 0.060$. Streak generated with LNSE-LOM-system {Type-II, μ_1} at $z_v^+ = 12.5$, using streamwise independent $I_{1,w}$ as EM and for a TBL at $Re_\tau = 200$. Optimal perturbation parameters: $\sigma_{z,EM}^+ = 3.25 \times 10^{-3}, \lambda_y^+ = 74.5$

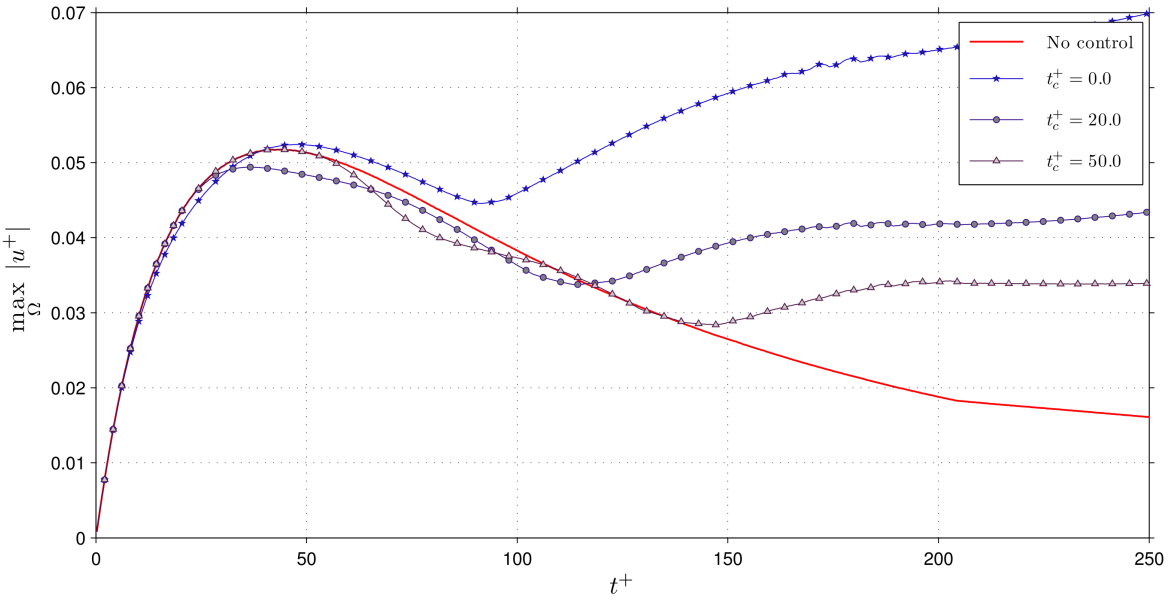

Figure 5.20: Comparison of the effect of change in the control activation time t_c^+ on the streamwise perturbation velocity evolution. Results for a STWSV with $\kappa_x^+ = 0.006$, $\omega^+ = 0.060$. Sub-optimal streak derived from LNSE-LOM-system {Type-II, μ_1} at $z_v^+ = 12.5$, using $I_{2,w}$ as EM and for a TBL at $Re_\tau = 200$. Sub-optimal perturbation parameters: $\sigma_{x,EM}^+ = 1.0 \times 10^{-4}, \sigma_{z,EM}^+ = 3.9 \times 10^{-3}, \lambda_y^+ = 258.0$

5.3.4 Controlled streak growth response

Using the LNSE-LOM-system adopted in this work and the considerations previously presented, the effect of STWSV was assessed for a number of combinations of $(\omega^+ - \kappa_x^+)$. The parameter-space map of drag-reduction/drag-increase (DR/DI) obtained using DNS by Quadrio et al. [57] is used as main benchmark result and presented in figure 5.21.

In this plot of skin-friction change the red regions indicate a drag reduction (a maximum decrease being $\approx$ 48%, which occurs near ω^+=0.018, κ_x^+=0.0075); additionally, a clear feature is the presence of a blue corridor/region indicating a drag increase (a maximum increase being $\approx$ 20%), associated with a wave speed of $c^+ \approx 10.0$

Numerical tests were performed in this work to assess the ability of the LNSE-LOM-system adopted on reproducing features of the DNS control map. Two main sets of tests were performed: firstly using as excitation mechanism (EM) the streamwise independent initial condition $I_{1,w}$; secondly using three-dimensional condition $I_{2,w}$.

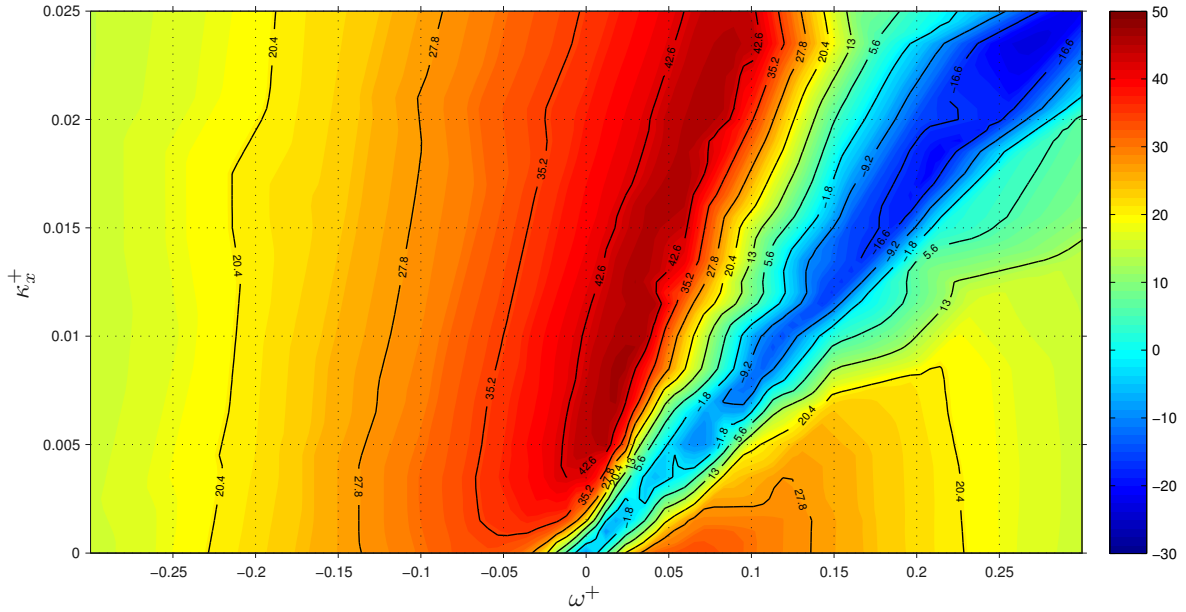

Figure 5.21: Contour plot over the actuation parameter space (ω^+, κ_x^+) of drag reduction as calculated by DNS, [57] for a channel at $Re_\tau = 200$. Plot reproduced using data provided by authors.

Controlled streak growth response. Streamwise independent EM

Numerical tests were performed over a number of STWSV using the streamwise-independent EM $I_{1,w}$ with parameters obtained using the LNSE-LOM-system optimized for {Type-II,μ_1} at $z_v^+ = 12.5$ for a TBL at $Re_\tau = 200$. The optimal perturbation was so defined using the following values: $\sigma^+_{z,EM} = 3.25 \times 10^{-3}$ and $\lambda_y^+ = 74.5$. The phase-averaging process was performed using 36 phases. The computational domain was set periodic in the streamwise direction covering a length of $L_x^+ = 3141.6$ discretized using a spacing of $\Delta x^+ = 10.47$. As in the previous tests, a total of $N_z = 128$ collocation points were employed in the wall-normal direction. The total simulation time was set to $\tau^+ = 300$.

A parameter-space map of Measure-Increase/Measure-Reduction (MI/MR) ϵ for μ_1 at $z_v^+ = 12.5$ is plotted in figure 5.22 for a perturbation developing in a TBL at $Re_\tau = 200$. In particular, this plot is produced by evaluating ϵ at $t^+ = 10$; the influence of the selection of a specific instant will be discussed later. There are a number of striking similarities between this plot and the DR/DI control map presented above. The red regions in figure 5.22, indicating maximum streak-amplification reduction, correlate relatively well to regions of maximum drag reduction (the red regions in figure 5.21). This similarity is both in terms of approximate position as well as relative magnitude between different regions. The maximum percentage change in streak growth amplification in figure 5.21 is approximately 56%; which is again comparable to that found in DNS for drag reduction. However, it is noteworthy that an optimum control parameter combination for the maximum suppression of streak growth is not found within the ranges plotted in figure 5.22, whereas an optimum drag reduction can be identified for the DNS simulation results shown in figure 5.21.

It is important to remind that the map portrayed in figure 5.22 has been obtained by calculating ϵ using the values of amplification measure μ_1 at $t^+ = 10$, which is clearly a very early stage in the streak development. By constructing the contour plot in figure 5.22 at such an early time, full incorporation of large (and potentially unbounded) growth was avoided. In this way, this time interval was chosen to be long enough to categorise the suppression of streak growth where instability was absent, but sufficiently short to make it possible to disregard the large amplifications that would otherwise have been found in parameter ranges where instability was known to develop[3]. As a result, all of the contour values that are plotted in figure 5.22 represent streak growth suppression (i.e., there is no region of streak growth increase), with a minimum change being approximately 10%. Nevertheless, even though the unstable development does not become apparent within the curtailed timeframe, it is still possible to see an initial glimmer of the instability in the plotted contours. This occurs along an upward diagonal, where there is relatively weak streak suppression (low ϵ); the slope angle of this diagonal is similar to the angles that bound the drag increase corridor region in figure 5.22.

[3]However, this situation of unbounded growth was only observed for parameter values where there was highly unstable behaviour, but most importantly, only at spanwise modes different from the optimal value. This is discussed later.

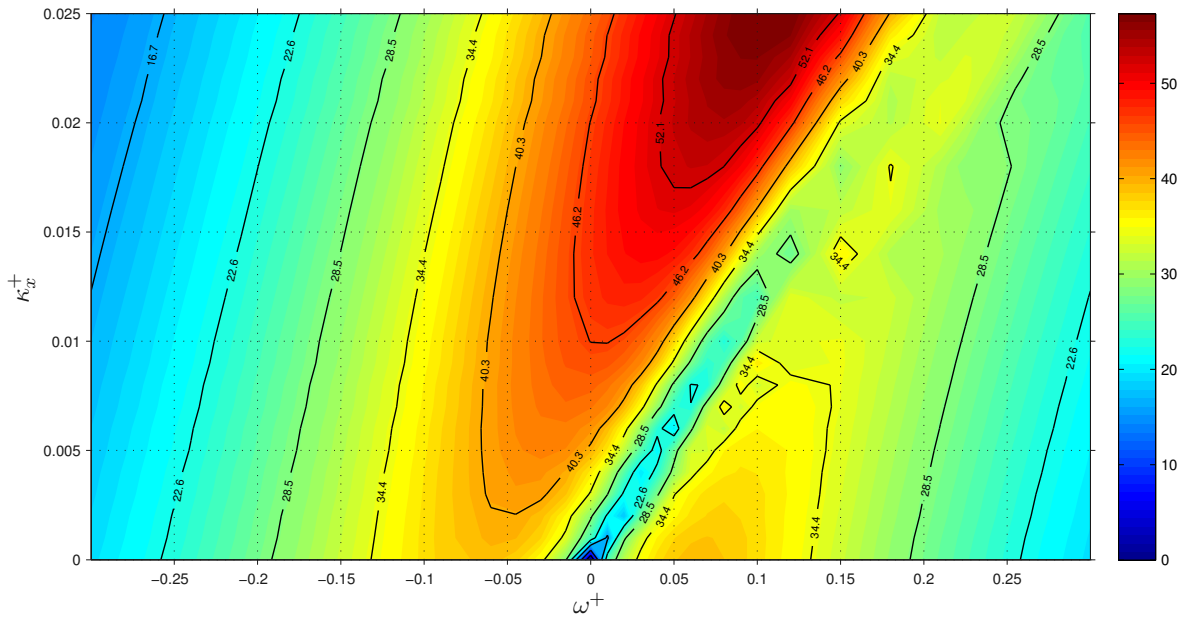

Figure 5.22: Contour plot over the actuation parameter space (ω^+, κ_x^+) of percentage change in streak amplification (ϵ) at $t^+ = 10$ as calculated by the LNSE-LOM-system. Results for an optimal perturbation generated with LNSE-LOM-system {Type-II, μ_1} at $z_v^+ = 12.5$, using streamwise independent $I_{1,w}$ as EM and developing in a TBL at $Re_\tau = 200$. Optimal perturbation parameters: $\sigma_{z,EM}^+ = 3.25 \times 10^{-3}, \lambda_y^+ = 74.5$

Considering a further evolution of the optimal perturbation, control maps were obtained at different elapsed simulation times. In figures 5.23a and 5.23b are presented the control maps for ϵ obtained with values of μ_1 taken at $t^+ = 20$ and $t^+ = 80$, respectively. Observing these plots is clear that a strong reduction in the amplification measure continues developing as the streak evolves and decays in time. In this way, at $t^+ = 80$ any resemblance to the main features presented in figure 5.21 has been lost. Particularly, for this optimal perturbation ($I_{1,w}$ with LNSE-LOM defined by {Type-II,μ_1}), any vestige of measure increase (MI), which could be correlated to the blue region of DI in figure 5.21, is completely absent. In the case of the control map for ϵ at $t^+ = 80$ (figure 5.23b), the main portion of the map presents a huge reduction in the intensity of the stream amplification measure μ_1, with values of measure reduction (MR) up to $\approx 95\%$. As mentioned, even the region where DI occurs in figure 5.21 has been fully substituted for a region of almost complete reduction. This also seems to imply that the spanwise oscillation accelerates the decay stage of the transient growth process, subduing the streak at much early stages, at least for the perturbation developing at optimal λ_y^+.

The control maps considered up until now have been constructed using the percentage change ϵ, which is solely based on measures of streak growth at the end of a fixed time period, for instance $t^+ = \{10, 20, 80\}$, rather than considering the maximum over a chosen time interval. In order to consider the general effect of the control, independent of the time scales involved, an alternative calculation, labelled as $\epsilon_{\max\, t}$, was performed

using the maximum values of the amplification measure, as defined by equation (5.29). In figure 5.24 is shown the control map obtained using the definition of $\epsilon_{\max\, t}$ with μ_1 as the amplification measure. Again, as in the previous plots, some of the general characteristics of the DR map are contained, but the values of percentage of MR are again off the scale, producing values up to $\approx 80\%$ for the maximum reduction available in the control map. Something worth to highlight is that for the pure oscillating wall (STWSV with $\kappa_x^+ = 0.0$), the control map presented in figure 5.24 is able to reproduce the scales of maximum MR at around $\omega^+ \approx 0.06$, i.e. for the oscillation period $T^+ \approx 100$. This result corresponds, extremely well, to the value also obtained in DNS results and verified experimentally by other works ([57, 58, 124])

Control maps up until this point have been obtained for an optimal perturbation developing at the optimal spanwise scale $\lambda_y^+ = 74.5$, for the streamwise independent EM $I_{1,w}$. The question remains: do the spanwise scales λ_y^+ of the chosen streak affect the control map significantly? Numerical experiments aimed at addressing this question were performed at different spanwise scales, although using otherwise the same optimal parameters of $I_{1,w}$. Interestingly, at spanwise scales above the optimal λ_y^+ a region of measure increase (MI) was found. In these cases, there is a diagonal corridor in the actuation parameter space, for sub-optimal spanwise scales, where instabilities (or very large increases in the disturbance amplification, as the transient growth illustrated in figure 5.20) were discovered in the numerical simulations with the LNSE-LOM-system; this is illustrated, for a reduced parameter space, in figure 5.25. Examining each of the plots contained in this figure (figures 5.25a to 5.25d), it is clear the presence of lumpiness in the control maps. This feature seems to be evidence of a discretization of the unstable response, although additional exploration in this direction was not performed.

The regions of high growth in the disturbance energy were found to correlate closely with the (blue) region of drag increase seen in figure 5.21. It was observed that instabilities developed more readily from initial conditions that were localised in x (as $I_{2,w}$, discussed later), but even with the initial conditions that are considered here (which are taken to be the streamwise invariant EM $I_{1,w}$), instabilities still became manifest after a sufficient period of time. In order to identify these regions of instability, a threshold value of 50% increase is defined as an instability criterion for $\epsilon_{\max\, t}$, using maximum values over the total simulation time (see § 5.3.1). Using this criterion the regions of instability present in figures 5.25a to 5.25d are identified and presented in figures 5.26a to 5.26d for perturbations developing at $\lambda_y^+ = 298.0, 223.5, 175.8$ and 149.0, respectively. This type of response, with presence in the control map of regions of growth above 50%, was observed for streaks developing, approximately, at spanwise scales in the range $120 < \lambda_y^+ < 320$. although with different intensity at each spanwise mode studied. The instability regions portrayed in figures 5.26a to 5.26d are a subset of such a range. It is important to mention that for some of the cases where instability was obtained, i.e. cases where the controlled perturbations exhibited growth above 50%, the perturbations

developed, eventually, unbounded growth. However, this was not always observed and therefore a detailed examination of this phenomenon is not reported in this document[4].

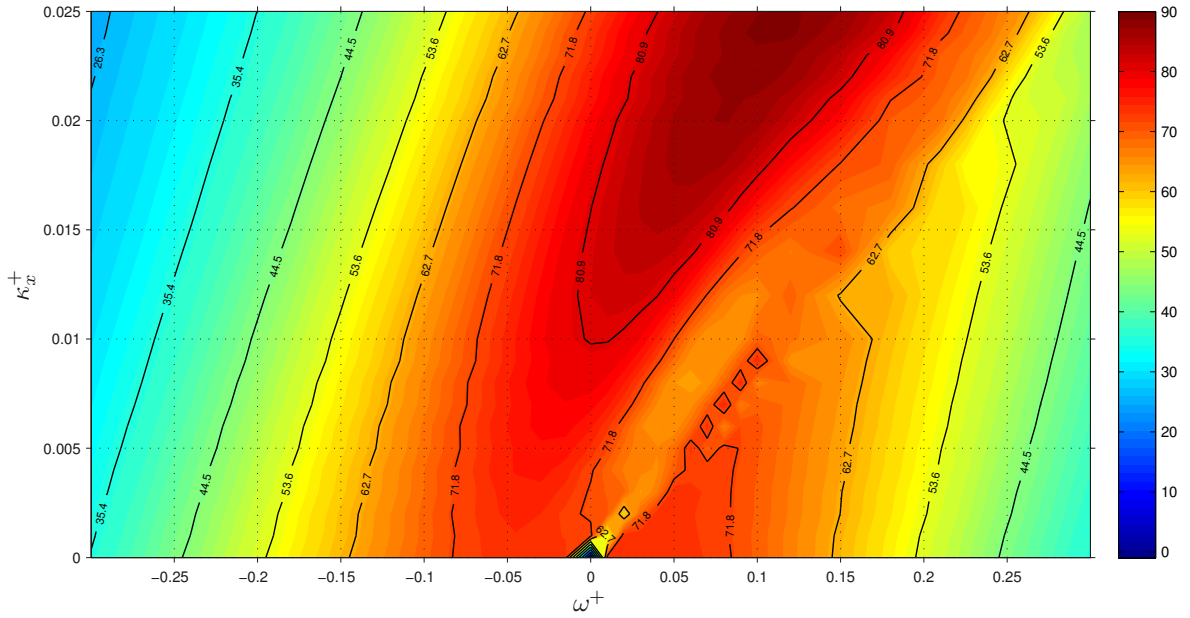

(a) Control map for ϵ taken at $t^+ = 20$

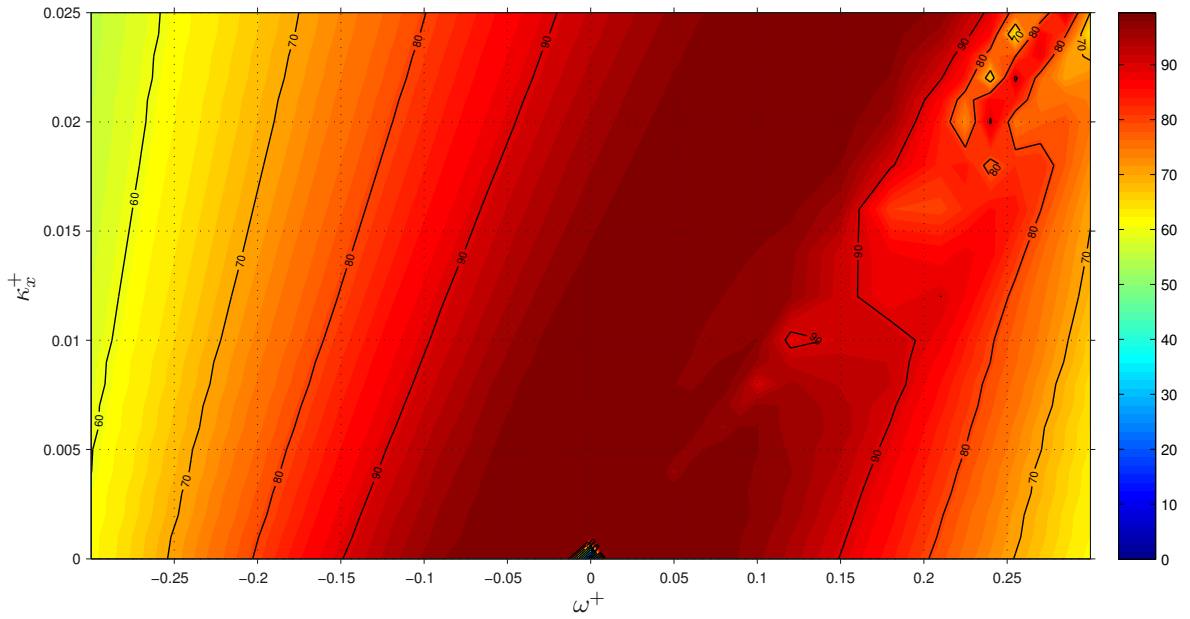

(b) Control map for ϵ taken at $t^+ = 80$

Figure 5.23: Contour plots over the actuation parameter space (ω^+, κ_x^+) of percentage change in streak amplification (ϵ) evaluated at (a) $t^+ = 20$, and (b) $t^+ = 80$, as calculated by the LNSE-LOM-system. Results for perturbation developing in a TBL at $Re_\tau = 200$.

[4]Equally, the extension and scope of the present work preclude a much more in-deep examination of those cases which would be, otherwise, extremely valuable for the stability analysis of this flow condition.

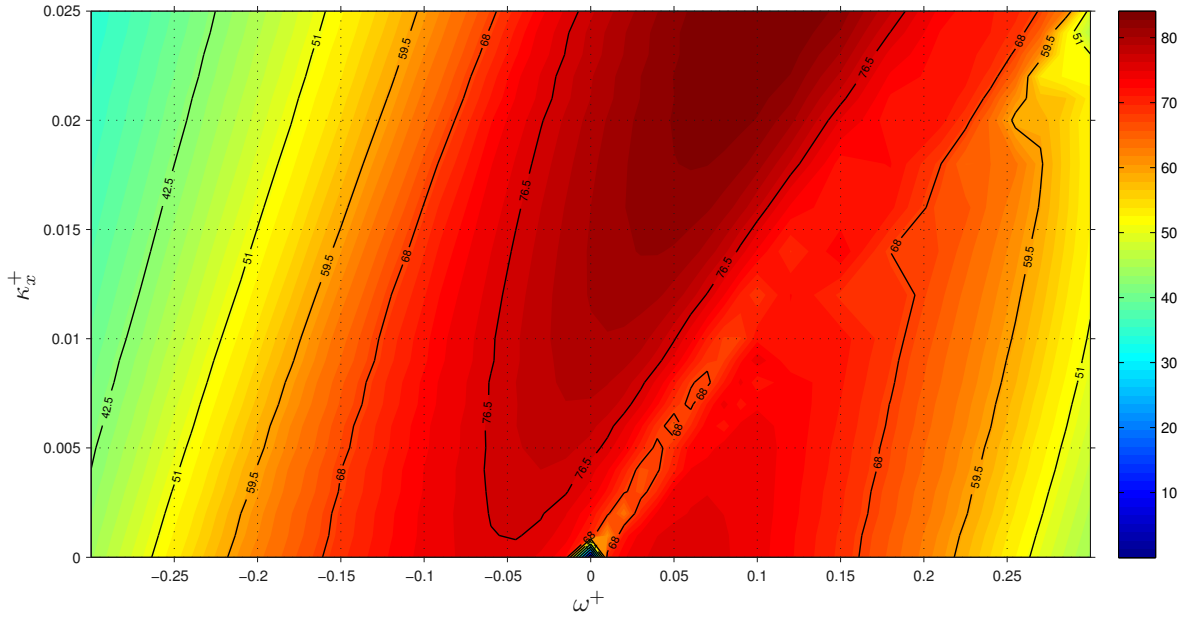

Figure 5.24: Contour plot over the actuation parameter space (ω^+, κ_x^+) of percentage change in streak amplification ($\epsilon_{\max\, t}$) using $\max_{\tau_t}\, \mu_1$ as calculated by the LNSE-LOM-system. Results for perturbation developing in a TBL at $Re_\tau = 200$ with $I_{1,w}$ as EM.

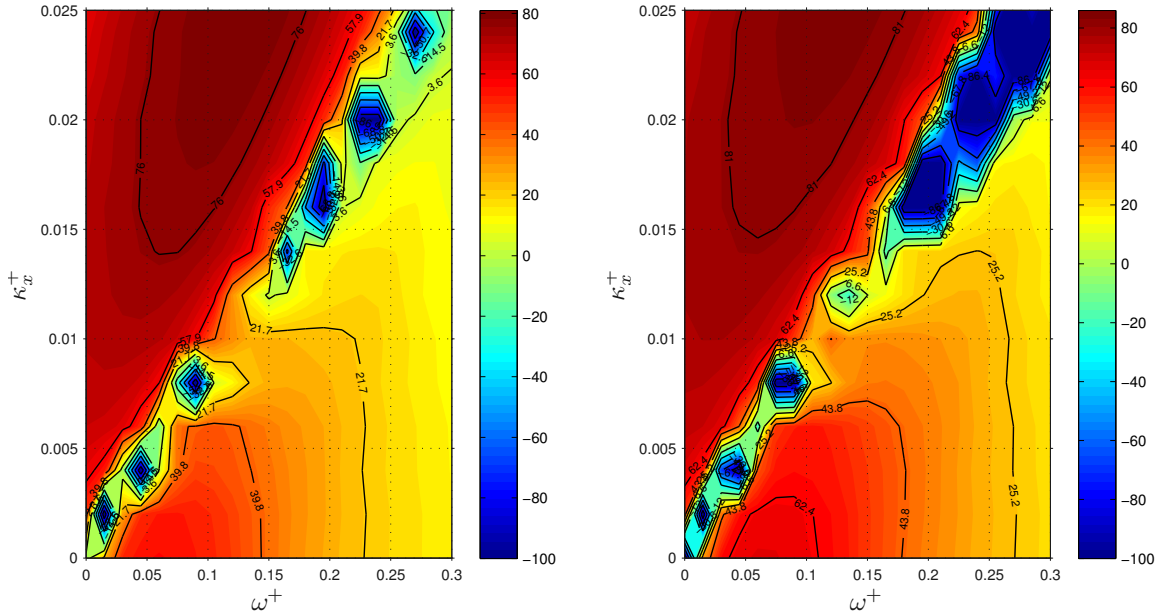

(a) Control map obtained at $\lambda_y^+ = 298.0$

(b) Control map obtained at $\lambda_y^+ = 223.5$

(c) Control map obtained at $\lambda_y^+ = 178.8$

(d) Control map obtained at $\lambda_y^+ = 149.0$

Figure 5.25: Contour plots over a reduced actuation parameter space (ω^+, κ_x^+) of percentage change in maximum streak amplification ($\epsilon_{\max\, t}$) using $\max_{\tau_t}\, \mu_1$ for perturbations developing at (a) $\lambda_y^+ = 298.0$, (b) $\lambda_y^+ = 223.5$, (c) $\lambda_y^+ = 178.8$, and (d) $\lambda_y^+ = 149.0$, as calculated by the LNSE-LOM-system. Results for a TBL at $Re_\tau = 200$ with $I_{1,w}$ as EM.

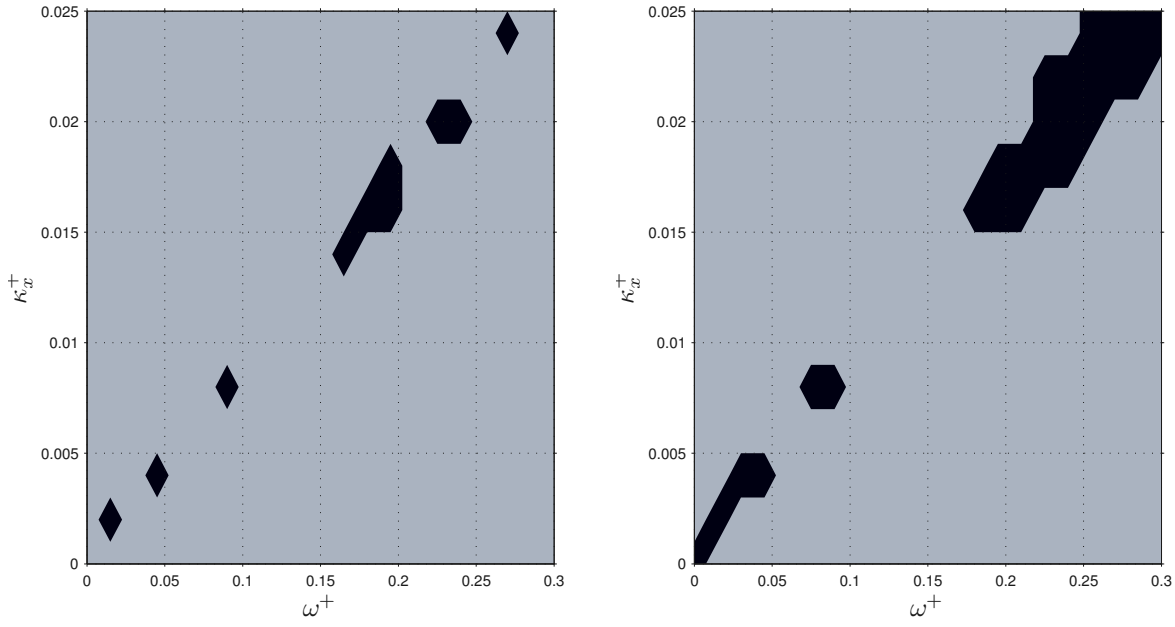

(a) Control map obtained at $\lambda_y^+ = 298.0$

(b) Control map obtained at $\lambda_y^+ = 223.5$

(c) Control map obtained at $\lambda_y^+ = 178.8$

(d) Control map obtained at $\lambda_y^+ = 149.0$

Figure 5.26: Regions of significant streak amplification increase ($> 50\%$) occurring over long time scales ($\tau_t^+ = 300$) due to streamwise-travelling wave actuation. Results generated for streamwise independent initial condition $I_{1,w}$ as EM. Contour plots produced over a reduced actuation parameter space (ω^+, κ_x^+) of percentage change in maximum streak amplification ($\epsilon_{\max t}$) using $\max_{\tau_t} \mu_1$ for perturbations developing at (a) $\lambda_y^+ = 298.0$, (b) $\lambda_y^+ = 223.5$, (c) $\lambda_y^+ = 178.8$, and (d) $\lambda_y^+ = 149.0$, as calculated by the LNSE-LOM-system. Results for a TBL at $Re_\tau = 200$.

5.3.5 Controlled streak growth response. Streamwise dependent EM

In order to assess the impact of the streamwise variation of the perturbation model, numerical tests of flow control with spanwise oscillating waves were also conducted employing the streamwise dependent condition $I_{2,w}$ (introduced in § 4.3.3) as excitation mechanism for the LNSE-LOM-system. The optimal perturbation was prescribed using the parameters obtained by the problem {Type-II,μ_1} optimized at $z_v^+ = 12.5$ for a TBL at $Re_\tau = 200$. The optimal perturbation parameters resulting from such a LOM are: $\sigma^+_{z,EM} = 3.9 \times 10^{-3}, \sigma^+_{x,EM} = 1.0^{-4}$ and $\lambda_y^+ = 81.1$. The phase-averaging process was performed using 24 phases. As in the previous case, the computational domain was set periodic in the streamwise direction extending for a length of $L_x^+ = 3141.6$ and discretized using a spacing of $\Delta x^+ = 10.47$. Equally, a total of $N_z = 128$ collocation points were employed in the wall-normal direction, with a total simulation time set to $\tau_t^+ = 300$.

Control maps of ϵ for μ_1 at $z_v^+ = 12.5$ are shown in figures 5.27a and 5.27b obtained with ϵ evaluated at $t^+ = 10$ and 80, respectively. In figure 5.27c is presented the control map obtained using the maximum values in time for the evaluation of $\epsilon_{\max\, t}$. In all these cases the perturbation evolves in a TBL at $Re_\tau = 200$. The most important observation brought by these results is that, except for some differences in the values of ϵ, as in the case of control applied to a streamwise independent perturbation, there are a number of similarities between the control maps of the linear case and the DR/DI control map presented in figure 5.21. For instance, it is clear that the red regions of the maps presented in figure 5.27, indicating maximum streak-amplification reduction, correlate relatively well to regions of maximum drag reduction. As with the previous condition, such a similarity is particularly good at initial stages in the streak development, both in terms of approximate position as well as relative magnitude between different regions.

Equally, for this perturbation $I_{2,w}$, an optimum control parameter combination for the maximum suppression of streak growth is not found within the ranges plotted in figure 5.27. As the perturbation evolves in time, there is a significant reduction in the streak amplification, which is reflected in the vast reduction zone present in the control map obtained at $t^+ = 80$. This feature was also clearly seen in the case of the streamwise invariant condition.

In summary, all major features observed in the case of the of $I_{1,w}$ as EM, were obtained for the condition $I_{2,w}$. This shows that there is not a difference in the response of the LNSE-LOM-system to control by STWSV by streamwise variations in the condition used as an excitation mechanism (EM).

Regarding the appearance of instabilities for perturbations evolving at different values of λ_y^+, figure 5.28 shows that, as is the case for the streamwise invariant condition, a strong zone of instabilities appears for spanwise scales greater than the optimal spanwise scale λ_y^+. Figure 5.28 presents a full parameter space

control map for the same perturbation $I_{2,w}$, but this time for a spanwise scale of $\lambda_y^+ = 243.3$, three times the original optimal spanwise scale. It is noteworthy that, in all the numerical tests performed, the appearance of instabilities in a corridor around $c^+ \approx 10$ was observed for streaks developing at spanwise scales in the range given by $1.5\,\lambda_{y,opt}^+ < \lambda_y^+ < 4\,\lambda_{y,opt}^+$, approximately, with $\lambda_{y,opt}^+$ being the optimal spanwise scale. In this case, specifically, this range corresponds to values between $120 < \lambda_y^+ < 330$; instabilities were not observed for streaks developing at $\lambda_y^+ > 330$. This range of spanwise scales, for which the streaks exhibited some degree of instability under the effect of spanwise control, coincides with that observed in the streamwise-independent EM, $I_{1,w}$. Again, for the purposes of the present work, an instability has been defined as the phenomenon in which a perturbation undergoing transient growth, under the effect of the spanwise oscillations control, exhibits a growth of the selected measure above 50% of the maximum obtained for an uncontrolled case. For this three-dimensional EM $I_{2,w}$, such a zone is even more continuous, and evidently in greater agreement with the drag-increase region portrayed in the blue corridor of figure 5.21. This seems to indicate that, in fact, the appearance of instabilities is somehow insensitive to the three-dimensionality of the initial condition, although for condition $I_{2,w}$ this MI region is clearly more pronounced. Looking specifically for the instabilities as defined by the potential 'unbounded' growth criterion (growth $>$ 50%), figure 5.29 exhibits a continuous corridor, along the line of wave speed $c^+ \approx 10.0$. This particular finding reinforces the idea of a strong correlation between the appearance of instabilities and the increase of skin-friction drag produced by this type of flow control, and exposed by the DNS results.

In any case, given the results obtained for the EMs $I_{1,w}$ and $I_{2,w}$, what is really important to conclude is that the main features of the response of the LNSE-LOM-system to the control by STWSV seem to be inherent to the linearized system, independent of the excitation mechanism. It thus appears evident that, as long as the EM used to initially excite the system is obtained by an optimization methodology (even a low order one, as in the present work), the STWSV-control map obtained for the evolution of the perturbation under the effect of the spanwise oscillations will preserve the same main characteristics. In the same manner, this also seems to imply that the similarities between the drag-reduction map obtained by DNS in [57] (figure 5.21) and the control map obtained by the current LNSE-LOM-system is preserved independently of the three-dimensionality of the initial condition generating the near-wall streaks.

It should be emphasised that, as it can be concluded from the control maps obtained for specific time intervals (e.g. the control maps of ϵ for $t^+ = 10, 20, 80$), when the control map is taken at early t^+ $(= 10)$, it captures well the effect of the control on the algebraic growth of the near-wall structure, before any viscous effect inhibits it. By comparing the control maps obtained at different time periods, it is also clear that the quantitative agreement does depend on a chosen timescale, at least from the LNSE-LOM-system perspective.

Even though until this point nothing has been mentioned about the streamwise structure of the near-wall perturbations evolving under the influence of the STWSV-control, it is convenient to say that one of the immediate effects of the spanwise oscillation was to destroy any resemblance to a streamwise streak. All near-wall structures undergoing a controlled transient growth evolved in structures with distinctive features depending on the combination of control parameters applied. This facet of the present work is discussed in more detail in § 5.3.7.

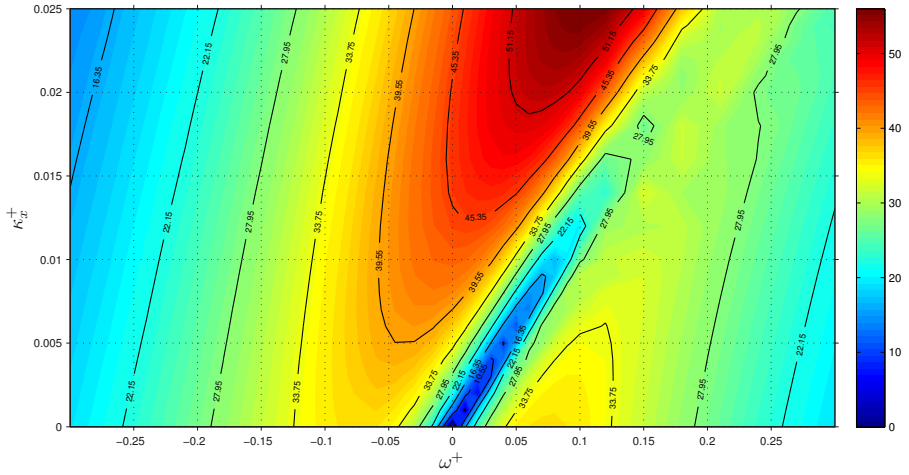

(a) Control map for ϵ taken at $t^+ = 10$

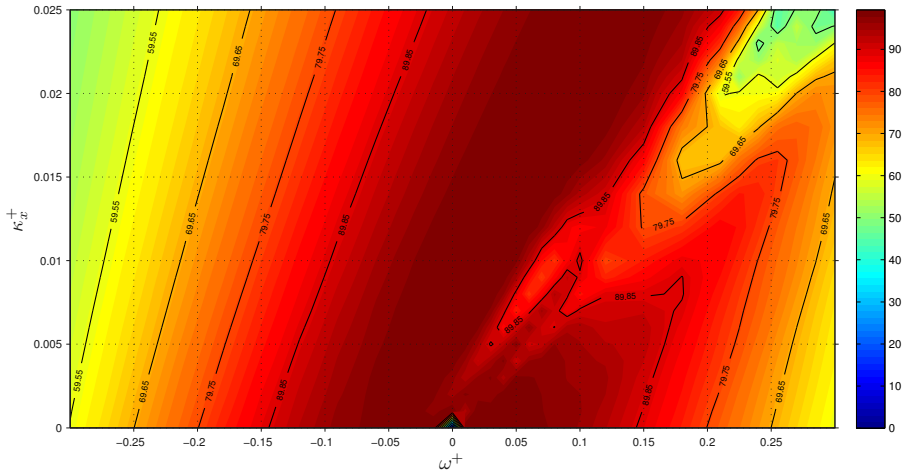

(b) Control map for ϵ taken at $t^+ = 80$

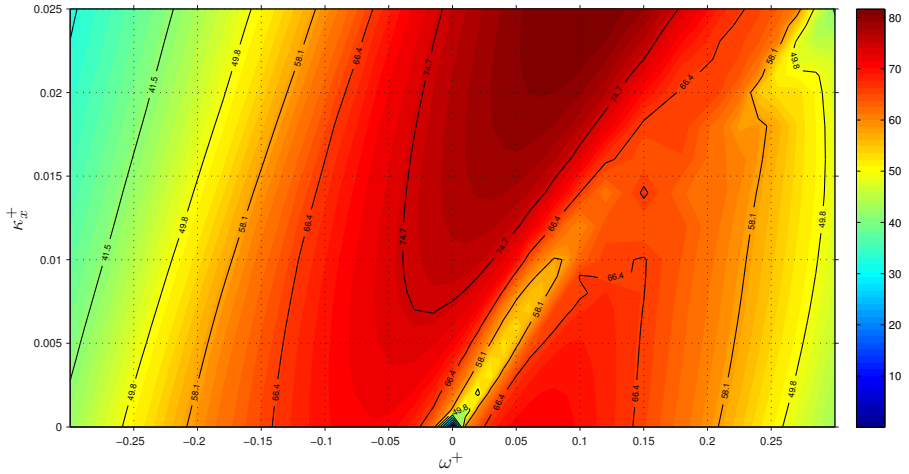

(c) Control map for $\epsilon_{\max\ t}$ estimated using $\max_{\tau_t}\ \mu_1$

Figure 5.27: Contour plots over parameter space (ω^+, κ_x^+) of percentage change in streak amplification (ϵ) evaluated at (a) $t^+ = 10$, (b) $t^+ = 80$, and (c) for $\max_{\tau_t}\ \mu_1$, as calculated by the LNSE-LOM-system. Perturbation generated with $I_{2,w}$ in a TBL at $Re_\tau = 200$.

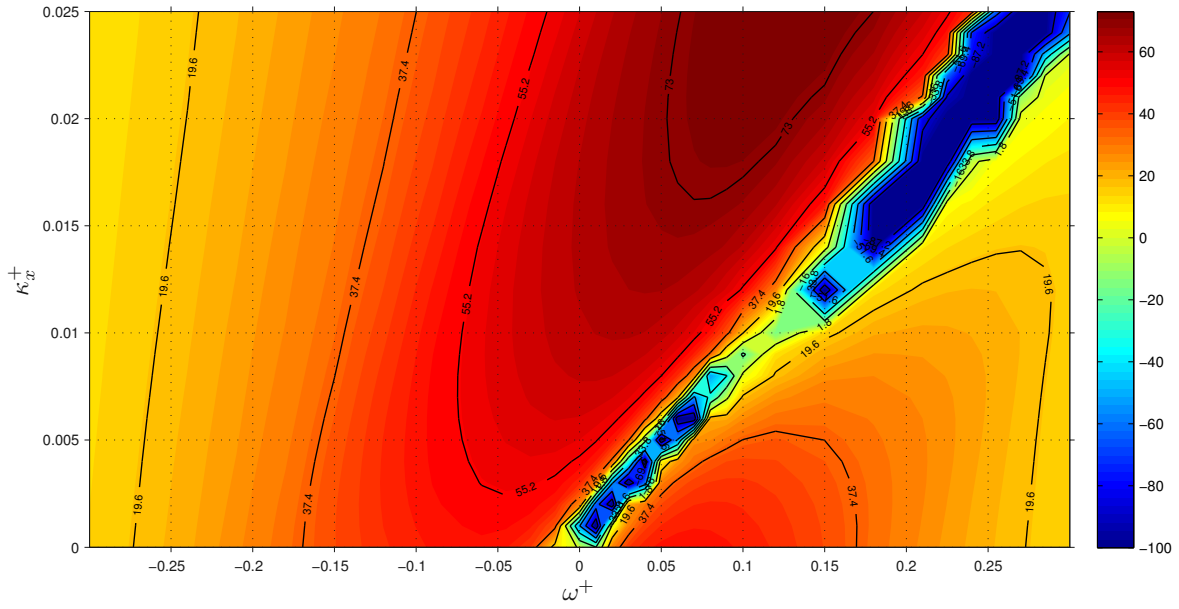

Figure 5.28: Contour plot over the actuation parameter space (ω^+, κ_x^+) of percentage change of maximum streak amplification ($\epsilon_{\max\, t}$) using $\max_{\tau_t}\ \mu_1$ as calculated by the LNSE-LOM-system. Results for perturbation developing in a TBL at $Re_\tau = 200$ with EM $I_{2,w}$ and for a spanwise scale of $\lambda_y^+ = 243$.

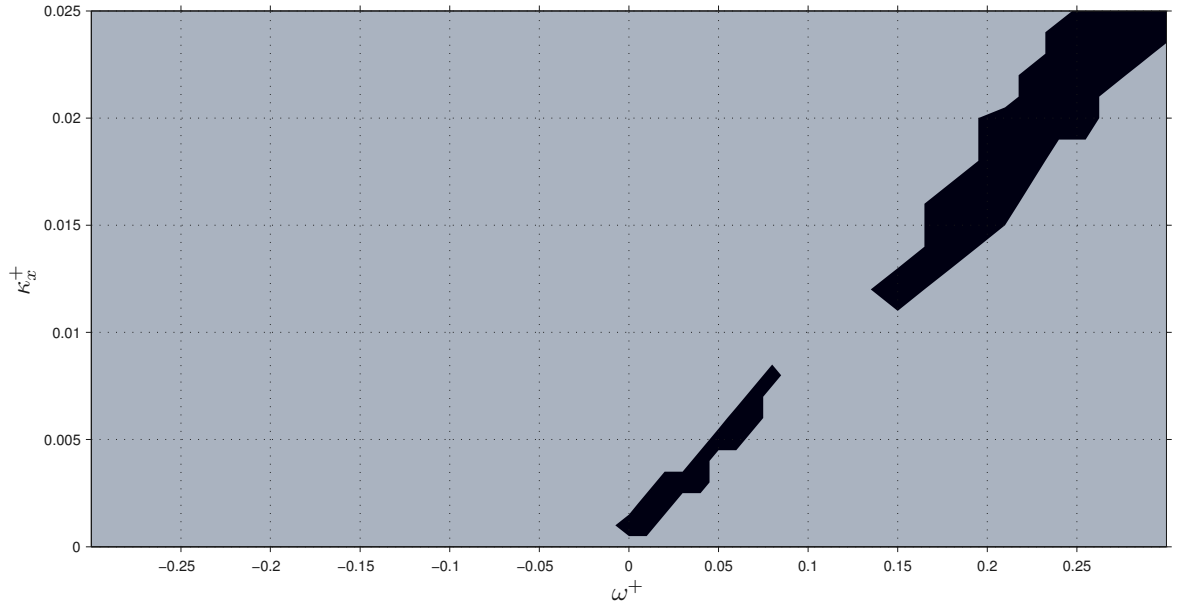

Figure 5.29: Regions of significant streak amplification ($> 50\%$) occurring over long time scales ($\tau_t^+ = 300$) due to streamwise-travelling wave actuation. Results generated for streamwise dependent condition $I_{2,w}$. Contour plot produced over a actuation parameter space (ω^+, κ_x^+) of percentage change in streak amplification (ϵ) using maximum values of μ_1 for perturbation evolving at $\lambda_y^+ = 243.0$, as calculated by the LNSE-LOM-system. Results for a TBL at $Re_\tau = 200$.

5.3.6 Additional observations on controlled streak growth response

Results obtained so far seem to indicate that a linear phenomenon is present, to a certain degree, in the process of DR/DI for flow control by spanwise oscillation of the walls bounding the flow. Conjecturing that this phenomenon might be reflected on other properties (measures) of the near-wall streaks simulated, an additional exploration was performed on a different set of measures, although space precludes a full inclusion of the results. Nevertheless, owing to the apparent good quality of agreement with the DNS results provided by two of these new measures, it was deemed appropriate to shortly include such results here. The tentative justification in doing this is that the important streak properties for drag production may not be the same as those for identifying optimal streak response. In this way, for these new measures, re-optimization is not performed – The original EM is kept constant.

A problem with previous ways of calculating ϵ, and therefore of constructing the control maps, is the necessity of defining a time instant at which the percentage change ϵ is calculated. An approach to avoid requiring a specific time instant was to calculate $\epsilon_{\max\, t}$ using the maxima values in time. This, however, could be argued to be not sensible owing to the maxima occurring at different time instants depending upon the particular control case ($\omega^+ - \kappa_x^+$). Another methodology to calculate ϵ, avoiding the time-instant issue, can be based on a time-averaged measure. In the previous simulations special attention was given to the streamwise perturbation velocity and streamwise perturbation energy at specific planes. Now, using the definition of $\mu_{2,\Omega}$ introduced in table 4.1, a new time-integrated measure μ_{N1} can be defined as

$$\mu_{N1} = \int_{\tau_t} \mu_{2,\Omega}\, dt = \frac{1}{L_x\, L_z} \int_{\tau_t} \int_{\Omega} u\, w\, \frac{d\, U^B}{d\, z}\, dt \tag{5.32}$$

with τ_t being the total simulation time, L_x and L_z the streamwise and wall-normal lengths, Ω representing the complete computational domain, u and w representing the streamwise and wall-normal perturbation velocities and U^B the mean streamwise base profile. This measure can be linked to the so-called lift-up effect discussed in §4. Equally, using the wall-normal perturbation velocity, a second time-integrated measure μ_{N2} can be defined as

$$\mu_{N2} = \int_{\tau_t} \max_{\Omega} |w(t)|\, dt \tag{5.33}$$

which, although evidently not capturing the expected physics, demonstrated to be a better predictor or estimator of the correlation between DR/DI and MR/MI, as shown by the results presented later in this section. By using these new measures the percentage of measure change (ϵ) can be simply defined as

$$\epsilon = \frac{\mu_{i,c} - \mu_{i,u}}{\mu_{i,u}} \times 100 \tag{5.34}$$

with $i = N1, N2$ and where evaluation at a particular time instant has been replaced by the time integration.

Using the new measures μ_{N1} and μ_{N2}, control maps were obtained for the optimal perturbation generated with $I_{2,w}$ and as defined by the problem {Type-II,μ_1} optimized at $z_v^+ = 12.5$ for a TBL at $Re_\tau = 200$. In this manner, the optimal perturbation parameters are given as: $\sigma^+_{z,EM} = 3.9 \times 10^{-3}, \sigma^+_{x,EM} = 1.0^{-4}$ and $\lambda_y^+ = 81.1$. The phase-averaging process was performed using 24 phases.

Observing the plots in figures 5.30a and 5.30b it is completely clear that, as initially conjectured, there exist other properties that are closely correlated with the DNS data. In the case of μ_{N1} there is a better agreement in the general shape of the contour map, although the levels of MR are somehow enhanced compared with those for DR/DI. The blue DI corridor present in the DNS results is more clearly observed in this plot, although still being mostly a MR region and not a MI region. However, the control map using the measure μ_{N2} offers the strongest resemblance of the main characteristics of the figure 5.21. In this case even the levels of reduction and increase are closely correlated to those present in the DR/DI map. The general scales and locations of maxima and minimum regions are also in good agreement with those portrayed by the DNS results.

It has been shown that most of the reduction phenomenon occurs at very early stages in the streak development, whereas the streak intensity increase (and the unbounded growth, if present), occurs essentially at later stages in the transient growth. Considering these two types of response of the LNSE-LOM-system as independent processes, and in order to facilitate identification of similarities between the drag-reduction map obtained by DNS and the control map obtained by the LNSE-LOM-system, a double linear mapping (i.e. the positive values are scaled independently of the negative values) was performed to scale the values of MR/MI ϵ into figures comparable to those of DR/DI present in figure 5.21. It should be noted that the only intention of such a mapping or scaling is simply to visually identify specific similarities between maps. Evidently, such a linear scaling is just an artifact and therefore it should not be interpreted as an attempt to formulate a conversion method, of any kind, between the MR/MI results and the DR/DI predictions.

In figure 5.31 the linearly scaled control map obtained using μ_{N2} is compared to the DR/DI map obtained by Quadrio et al. [57] (reproduced again in figure 5.31a for comparison purposes). The degree of agreement for the general location and shape between regions of MR/MI and zones of DR/DI is excellent. Although conclusions cannot be made in terms of percentage change scales, this control map reflects almost exactly that obtained for changes in skin-friction drag. In order to avoid repetition, no additional maps for μ_{N2} are included at this point. Nevertheless, it is very important to mention that, even more surprisingly, almost exactly equal control maps (in terms of shape, location of zones, existence of a MI corridor, locations of maximum MR for $\kappa_x^+ = 0.0$, etc) were obtained in simulations with sub-optimal spanwise scales (i.e. λ_y^+ different from the

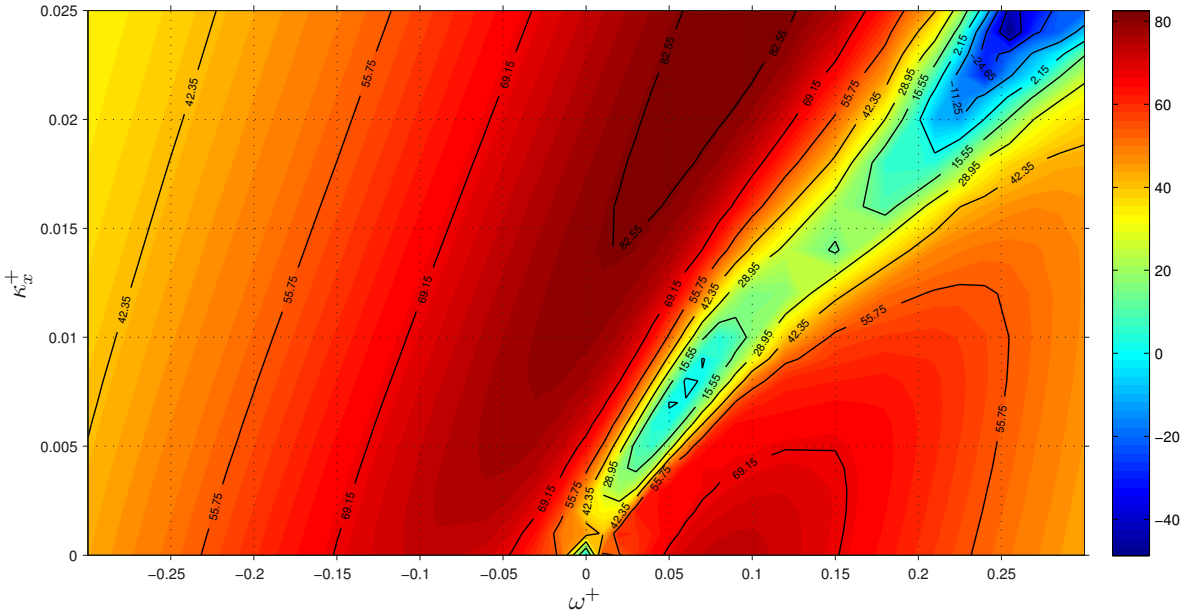

(a) Control map for ϵ estimated using μ_{N1}

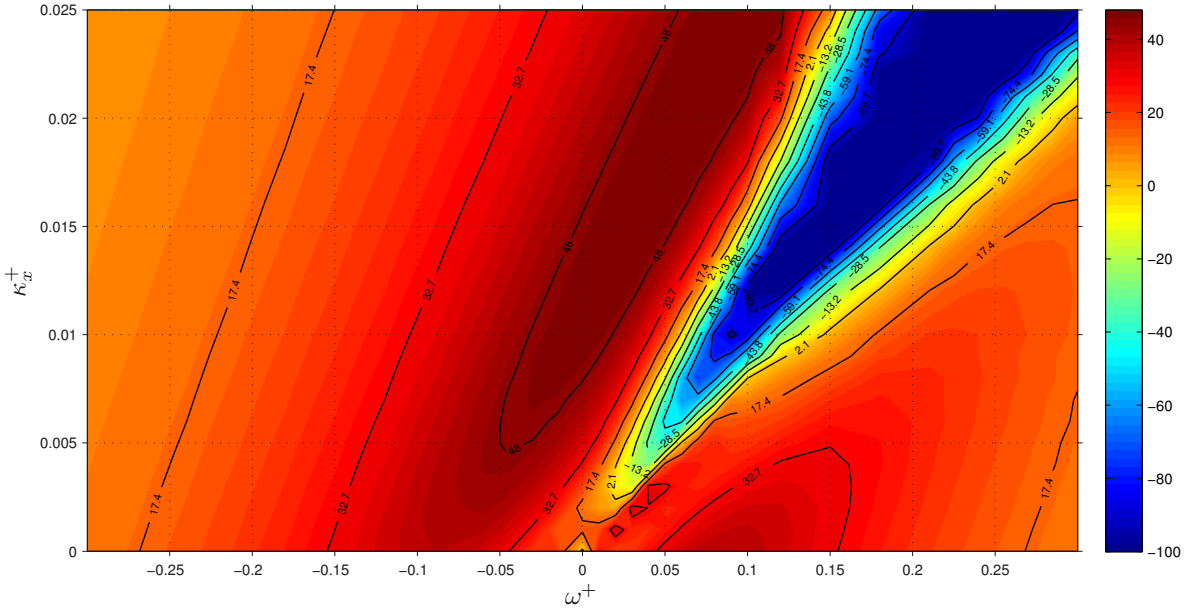

(b) Control map for ϵ estimated using μ_{N2}

Figure 5.30: Contour plots over parameter space (ω^+, κ_x^+) of percentage change in streak amplification (ϵ) evaluated using (a) μ_{N1}, and (b) μ_{N2}, as calculated by the LNSE-LOM-system. Perturbation generated with $I_{2,w}$ in a TBL at $Re_\tau = 200$.

optimal $\lambda_y^+ = 81.1$), and for streaks generated by using the streamwise independent EM $I_{1,w}$. These later results suggest that measure μ_{N2} correlates to the skin-friction changes in a direct way, without any regard to the EM used or the spanwise scale selected, which makes such correlation much stronger than that obtained with the streak amplification based on streamwise perturbation energy or velocity. Motivated by this apparent good correlation between the time integration of $|w|$ and the results of drag-reduction considered, and in order

to get a possible clearer picture of the impact of the spanwise oscillation control, an additional exploration was carried out on the spatial evolution of the near-wall streaks.

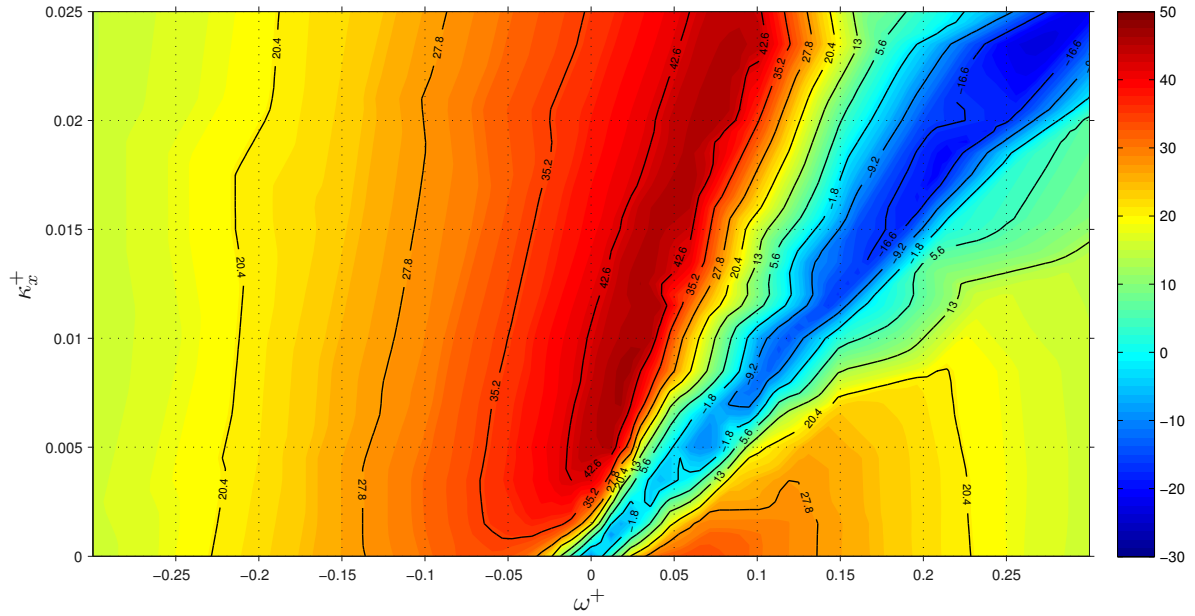

(a) Drag-reduction/drag-increase map obtained by DNS in [57]

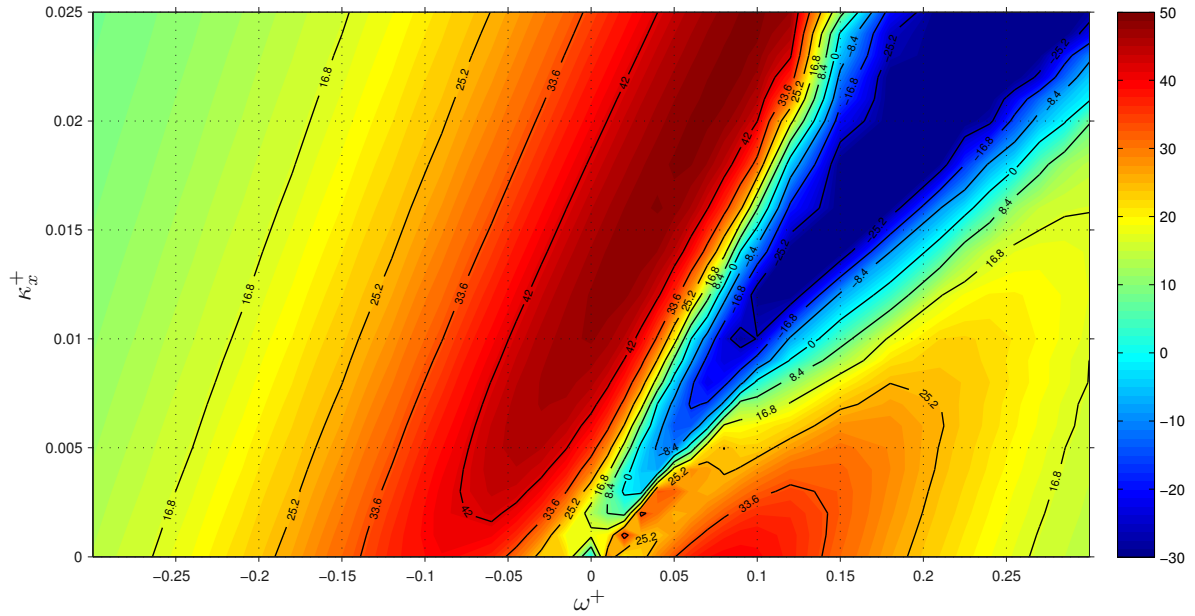

(b) Control map linearly scaled for ϵ estimated using μ_{N2}

Figure 5.31: Comparison of contour plots over parameter space (ω^+, κ_x^+) between (a) DNS results for DR/DI as obtained by [57], and (b) linearly scaled percentage change in streak amplification (ϵ) evaluated using μ_{N2}, as calculated by the LNSE-LOM-system. Perturbation generated with $I_{2,w}$ in a TBL at $Re_\tau = 200$.

Figures 5.32a and 5.32b show comparisons of the spatio-temporal evolution of the location of the maxima for the streamwise and wall-normal perturbation velocities, respectively, for perturbations evolving uncontrolled and under the effect of the spanwise oscillation for specific control cases (as indicated in such plots). It should

be noted that these plots have been obtained for perturbations generated using $I_{2,w}$, although evolving at a spanwise wavelength of $\lambda_y^+ = 243$, roughly three times the optimal spanwise wavelength for the same EM ($\lambda_{y,opt}^+ = 81.1$). The purpose of focusing the attention on such a spanwise scale is to examine in some detail the extreme response of the near-wall structures to the STWSV-control observed at this range of spanwise scales in some of the control maps, for instance in the control maps portrayed in figures 5.25 and 5.28. The main justification relies on that, as previously shown, at this range of spanwise scales the perturbations exhibited strong measure reduction (MR) in regions of the control map where drag reduction (DR) is expected, and strong measure increase (MI) in those regions where drag increase (DI) is expected.

It is necessary to highlight that, at this range of spanwise scales (above the optimal spanwise scale), it was observed the development of additional coherent structures above the inner sub-viscous region, not related with the standard near-wall streaks. This was observed even for uncontrolled perturbations, i.e. perturbations evolving in an underlying mean flow with null spanwise velocity. Since these additional coherent structures are not related to the near-wall streaks thoroughly discussed up until now in this work, and for clarity in the discussion, they have been labelled simply as 'secondary' structures. Equally, in order to bring some clarity on the type of structures observed, the near-wall structures (which in the uncontrolled case are the near-wall streaks) have been labelled 'primary' near-wall structures. Using this categorisation, it is clear that in figures 5.32a and 5.32b two clearly distinctive regions can be appreciated: firstly, a lower layer where the so-called primary structures evolve in the region below $z^+ \approx 30$; secondly, an upper layer, in the region $z^+ > 30$, where the secondary perturbations seem to evolve and remain.

Although not explicitly presented, it is possible to see that in the early stages of the structures development the most important structures are those located near the wall (region $z^+ < 30$). This however can be inferred by observing that, in the early stages of the perturbation evolution for the uncontrolled case, the spatio-temporal evolution of the maxima streamwise velocity is always located in the viscous layer. For reference purposes only, this region is here denominated as the 'Region of primary near-wall structures dominance', as indicated in the plots. On the other hand, the region above this layer is here labelled as the 'Region of secondary structures dominance'. At later stages, nevertheless, the secondary structures present in the upper layer above $z^+ \approx 30$ are the most predominant structures, at least in terms of the maximum streamwise velocity. This behaviour explains the apparent jumps observed in the figures 5.32a and 5.32b. Therefore, in order to clarify this distinction between primary and secondary structures and their independent evolution, and to avoid any distraction caused by these apparent jumps of the location of the maxima, a dashed line is used as indication of the instant where the maxima are exchanged from the primary to the secondary structures.

A detailed examination of the figures 5.32a and 5.32b reveals that: one of the main effects of the STWSV

in those cases producing streak (or near-wall structures) intensity amplification is to keep the regions of maximum streamwise and wall-normal perturbation momentum closer to the wall. As established previously, a term deemed to be of high relevance in the formation of streaks is the lift-up term, which using the notation employed here is given by $w\, dU^B/dz$, involving the wall-normal perturbation velocity w and the mean base flow shear or gradient dU^B/dz, which is usually larger in the proximity of the wall than in those regions far within the boundary layer. It seems clear that by maintaining regions of high wall-normal perturbation velocity close to the wall, the lift-up effect is enhanced. If it is assumed that this phenomenon of prolonged existence of regions of larger w close to the wall is related to the lift-up effect, in fact the result of the flow control in those cases with instabilities, which correlate to those regions of drag increase, is to intensify the lift-up effect, keeping the production of streamwise perturbation velocity within the buffer region of the boundary layer ($z^+ < 30$), and then possibly maintaining a conversion of energy from the mean streamwise base flow into coherent streamwise perturbation structures. A quantification of this phenomena can be obtained, precisely, through the study of the transient growth for those control cases. For instance, an indication of this phenomenon of increase of the intensity of the streamwise perturbation velocity can be appreciated in figure 5.20, where the STWSV-control induces an increase in the streamwise momentum in comparison to the uncontrolled case.

With basis on all the previous evidence and results, then it seems plausible to suggest that there exists a correlation between lifespan of the near-wall primary structures and the increase of the skin-friction drag. If this is assumed to be true, even partially, then the spatio-temporal evolutions shown in figure 5.32 could, at least partially, phenomenologically explain the increase in skin-friction drag: owing to the relation between perturbations near the wall and the wall-shear stress, a strong production of streamwise velocity close to the wall would translate into stronger gradients of streamwise velocity in the vicinity of the wall, and thus into increase of the wall-shear stress. Examining the cases where there is a measure reduction then this argument could also help to explain those situations when the wall oscillation produces an inhibition of drag. For instance, in figure 5.32b it can be seen an earlier separation of the maximum wall-normal perturbation velocities from the wall, compared with the uncontrolled case. In this situation, it seems plausible to suggest that the spanwise oscillation control helps to anticipate the upwards advection of the wall-normal velocity structures and therefore provoking a reduced activity in the vicinity of the wall. By reducing the near-wall activity in comparison with the uncontrolled case (i.e. provoking a short lifespan of the structures within the near-wall region), the STWSV-control seems to reduce the lift-up effect, which would eventually be translated into a reduced formation of streamwise momentum structures, i.e. a reduced gradient of the streamwise velocity. Although the findings of the numerical experiments performed in this work appear, initially, to support the mechanism just outlined, it is necessary to explore with much more care and detail this seeming

mutual correlation between drag increase/decrease and the evolution of the wall-normal perturbation velocity along with the production/inhibition of streamwise perturbation momentum.

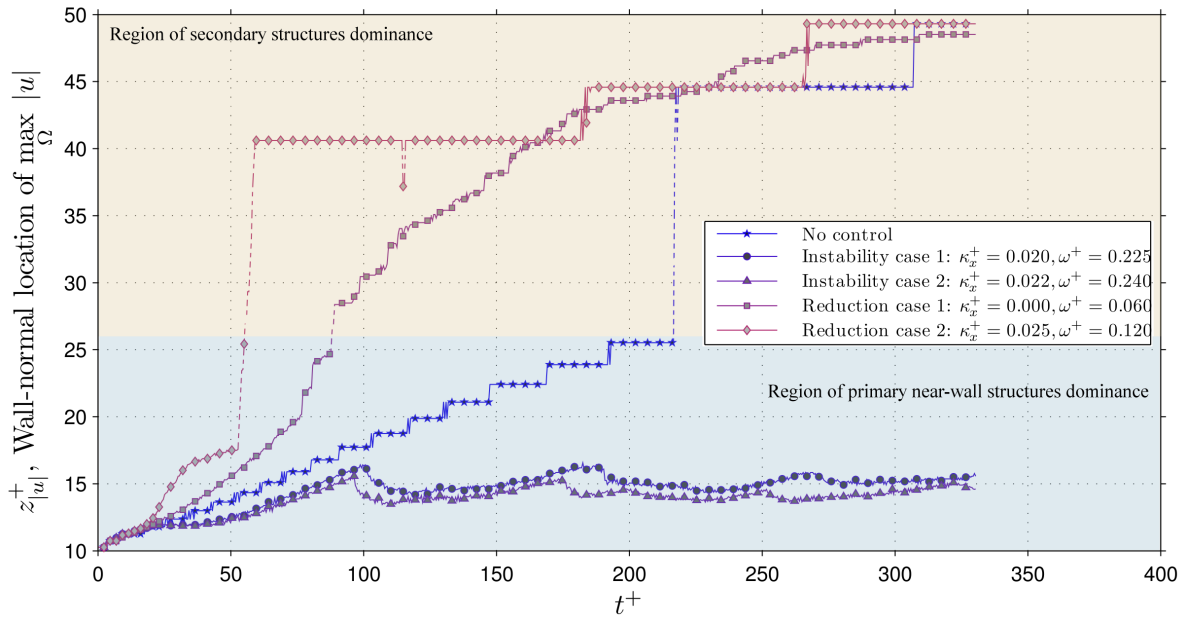

(a) Spatio-temporal evolution in wall-normal direction of $\max_\Omega |u|$

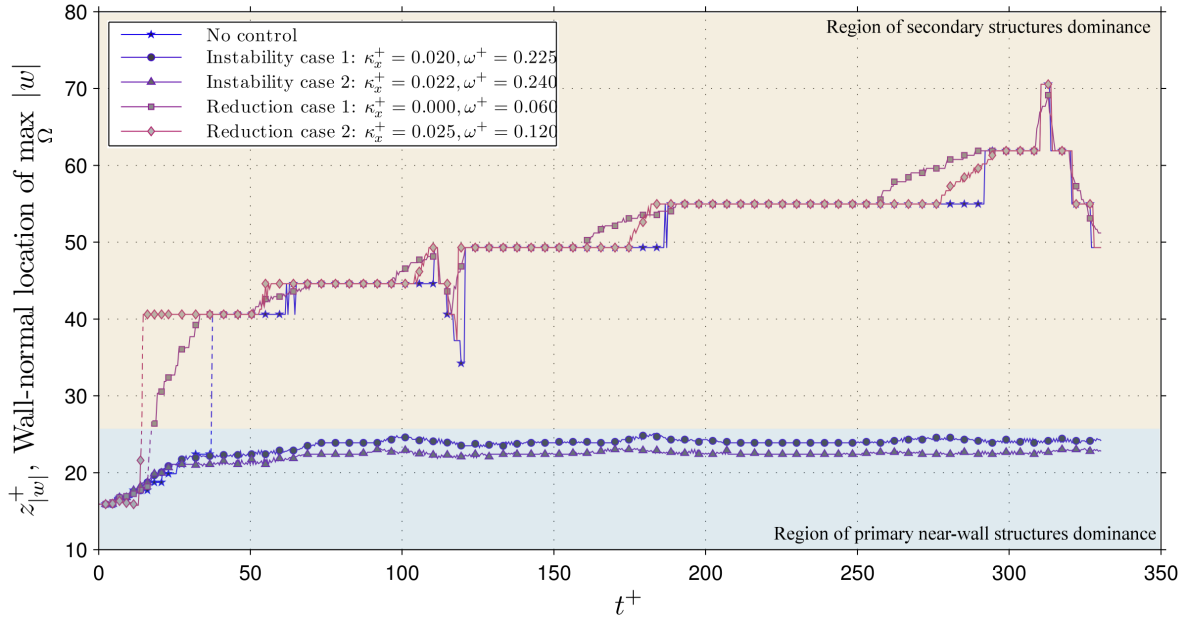

(b) Spatio-temporal evolution in wall-normal direction of $\max_\Omega |w|$

Figure 5.32: Comparison of spatio-temporal evolution of near-wall streak, in wall-normal direction, between uncontrolled and controlled cases for (a) global maximum of streamwise perturbation velocity ($\max_\Omega |u|$), and (b) global maximum of wall-normal perturbation velocity ($\max_\Omega |w|$), as calculated by the LNSE-LOM-system. Perturbation generated with $I_{2,w}$ in a TBL at $Re_\tau = 200$, at sub-optimal spanwise scale $\lambda_y^+ = 243$. Instability cases refer to those control cases producing unbounded growth, as seen in figures 5.28 and 5.29

5.3.7 Temporal evolution and perturbation coherent structures

In the previous section, based on the trends exhibited by the temporal-spatial evolution of the maxima of the perturbation velocities, it was argued that one of the main effects of the spanwise control is to affect the wall-normal perturbation structures, therefore affecting the lift-up effect (in comparison with the uncontrolled case), and consequently generating changes in the streamwise perturbation structures. Nevertheless, it is still unclear what is the resulting structure, or how has the streak been modified by the presence of the spanwise oscillating wave. Again, different questions remain: are the controlled streamwise structures still near-wall streaks?; do the controlled wall-normal perturbation structures, as in the uncontrolled case, decay monotonically in time? In other words, although a correlation has been shown between LNSE-based control maps and the DNS-based drag reduction/increase maps, no hint of the type of structure resulting from controlling the small scale perturbations has been presented.

However, before any discussion aiming to address the previous questions is elaborated, it is necessary to make some comments on the spanwise representation followed in this work. In summary, although not mentioned before, the single-spanwise-mode perturbation variables in the present model are complex-valued, with their real part assumed to represent a dominant-centred structure around the y-axis, and the imaginary part assumed to represent a dominant-off-centred structure. In order to clarify this, let the spanwise modal decomposition be expressed as (see equation (2.42)),

$$\phi_\beta = \hat{\phi}_\beta \, e^{\mathbf{i}\beta y} \tag{5.35}$$

with

$$\hat{\phi}_\beta = \phi_\mathsf{r} + \mathbf{i}\phi_\mathsf{i}$$

representing the complex-valued variable (in the Fourier space) and β being the specific spanwise mode studied. This modal decomposition allows us to distinguish and to decouple two different evolutions of the perturbations. Firstly, for the purposes of this work, a dominant-centred variable or structure[5] is a flow field variable which holds a symmetry around the y-axis, at all time during its evolution (transient growth), which can be expressed as

$$\phi(-y) = \phi(y)$$

for any y position; this kind of variables, depending upon the context, are usually referred to as even variables. Secondly, an off-centred structure or variable is a flow field variable for which there is not y-axis reflection,

[5]For simplicity in this discussion, the terms 'variable' and 'structure' are employed indistinctively. In both cases meaning a small perturbation flow field, usually velocity or vorticity.

but its evolution holds at any time instant the relation

$$\phi(-y) = -\phi(y)$$

for any y position; this kind of variables are commonly referred to as odd variables. Thus, using the modal decomposition given by equation (5.35), any even field variable can be expressed as

$$\begin{aligned} \phi_{\beta\,\mathrm{even}} &= \frac{\phi_\beta(y) + \phi_\beta(-y)}{2} \\ &= \hat{\phi}_\beta \, \frac{e^{\mathbf{i}\beta y} + e^{-\mathbf{i}\beta y}}{2} \\ &= \hat{\phi}_\beta \, \cos(\beta y) \end{aligned} \tag{5.36}$$

and any odd field variable as

$$\begin{aligned} \phi_{\beta\,\mathrm{odd}} &= \frac{\phi_\beta(y) - \phi_\beta(-y)}{2} \\ &= \hat{\phi}_\beta \, \frac{e^{\mathbf{i}\beta y} - e^{-\mathbf{i}\beta y}}{2} \\ &= -\mathbf{i}\hat{\phi}_\beta \, \sin(\beta y) \end{aligned} \tag{5.37}$$

which is equivalent to say that the odd fields are associated to a cosine expansion and the even fields to a sine expansion (when they are assumed to be part of a Fourier decomposition, as it is the case in this work, see equation (2.42)). In these definitions both $\phi_{\beta\,\mathrm{even}}$ and $\phi_{\beta\,\mathrm{odd}}$ are also complex-valued variables. It is normally assumed that the relevant physical information is contained in the real part of these variables. Thus, using previous expressions, a dominant-centred structure or variable can be properly defined as

$$\mathrm{Re}[\phi_{\beta\,\mathrm{even}}] = \mathrm{Re}[\hat{\phi}_\beta] \, \cos(\beta\, y) = \phi_{\mathsf{r}} \cos(\beta\, y) \tag{5.38}$$

and a dominant-off-centred structure or variable as

$$\mathrm{Re}[\phi_{\beta\,\mathrm{odd}}] = -\,\mathrm{Im}[\hat{\phi}_\beta] \, \sin(\beta\, y) = -\phi_{\mathsf{i}} \sin(\beta\, y) \tag{5.39}$$

with Re and Im being the real part and imaginary part operators, respectively. This clearly indicates that, in the representation adopted, the evolution of a given even flow field $\phi_{\beta\,\mathrm{even}}$ is fully captured by the real part of $\hat{\phi}_\beta$, whereas the evolution of an odd field $\phi_{\beta\,\mathrm{odd}}$ is fully represented by the imaginary part of $\hat{\phi}_\beta$; it should be recalled that $\hat{\phi}_\beta$ stands for the Fourier expansion coefficient of a given spanwise β mode in the decomposition expressed by equation (2.42).

In order to discriminate between these two types of behaviour it is common to refer to the centred-dominant structures as the varicose instability mode, and to the off-centred-dominant structure as the sinusoidal instability mode [128–130]. Nevertheless, although in the remainder of this document these terms are adopted, in this work there was not attempt to study the varicose and sinusoidal instability modes, and therefore the usage of the terms 'varicose' mode and 'sinusoidal' mode will refer to the previously discussed dominant-centred (even) and dominant off-centred (odd) fields, respectively. Finally, regarding this centred and off-centred perturbations distinction, it should be kept in mind that isolating the varicose mode, i.e. studying only the real part of a perturbation field, is equivalent to examine the perturbation at the plane given by $\beta y = 0$. Equally, by isolating the sinusoidal mode (imaginary part of the complex-valued perturbation variable) is equivalent to examine the perturbation at the plane given by $\beta y = \pi/2$.

The main feature of the mathematical model of this work is that assumes that the mean base flow is spanwise homogeneous, even in the controlled-cases (e.g. when the STWSV is present), whereas the perturbations are assumed to be spanwise periodic. In particular, the initial flow field has always been normalised so as to have a real amplitude for the wall-normal component of the perturbation velocity ($w = w_{\mathsf{r}} e^{\mathbf{i}\beta y}$), and for the streamwise component of the perturbation velocity ($u = u_{\mathsf{r}} e^{\mathbf{i}\beta y}$). In this manner u and w are assumed to be described by a symmetric (even or varicose-mode) behaviour, when perturbations evolve uncontrolled, i.e. with no spanwise oscillation present. On the other hand, with this normalisation in place, the spanwise perturbation velocity can be fully described by an off-centred (odd or sinusoidal-mode) behaviour ($v = v_{\mathsf{i}} e^{\mathbf{i}\beta y}$) in an uncontrolled transient growth. The main outcome of this is that the evolution of the perturbation velocity components in the transversal plane, with respect to the flow direction, is decoupled of each other.

In the absence of the spanwise mean velocity profile, i.e. during the uncontrolled transient growth of streamwise streaks, thus the varicose mode is the dominant or exclusive behaviour of the streamwise and wall-normal perturbation velocities, whereas the off-centred mode (sinusoidal mode) is the dominant behaviour of the spanwise perturbation velocity. In order words, in the absence of any spanwise oscillation, the symmetry for the varicose modes is preserved. Precisely for this reason in the results presented up until this point, and in order to keep simplicity, such clarification between varicose and sinusoidal modes has been deemed unnecessary and therefore omitted[6]. The imposition of spanwise oscillations in the base flow completely changes the situation of the uncontrolled case. In general, the incorporation of the spanwise profile V^B in the mean flow breaks the symmetry between y and $-y$ directions at any given time instant. Therefore, under this rationale, eventually the varicose mode could become the most dominant behaviour in the evolution of the spanwise velocity, or the sinusoidal mode the most dominant one of the streamwise perturbation velocity.

[6] Nevertheless, in the calculation of all the energy and momentum measures presented throughout this document, both modes have been considered.

A number of additional numerical simulations were performed to visualise the effect of the spanwise oscillations on the odd/even behaviour previously described. These numerical simulations were focused on the control cases presented above as examples of the two main different responses (MR/MI) of the LNSE-LOM-system; these results allowed us to extract details of the structures obtained under the effect of the STWSV-control. Following the legend of figure 5.32, the example control cases have been labelled as: control-MR case 1 ($\kappa_x^+ = 0.00, \lambda_{x,\mathrm{GSL}}^+ = \infty, \omega^+ = 0.06$); control-MR case 2 ($\kappa_x^+ = 0.025, \lambda_{x,\mathrm{GSL}}^+ = 251.3, \omega^+ = 0.120$); control-MI case 1 ($\kappa_x^+ = 0.020, \lambda_{x,\mathrm{GSL}}^+ = 314.2, \omega^+ = 0.225$); and control-MI case 2 ($\kappa_x^+ = 0.022, \lambda_{x,\mathrm{GSL}}^+ = 285.6, \omega^+ = 0.240$). To facilitate comparisons between the structures obtained and the waviness of the given STWSV-control imposed, it has also been included in the labels the corresponding GSL wavelength, which is denoted as $\lambda_{x,\mathrm{GSL}}^+$. In all these cases the initial perturbation has been generated with $I_{2,w}$ as EM, within a TBL at $Re_\tau = 200$ ($Re_{\delta_*} = 770$), and modelled at a spanwise spacing $\lambda_y^+ = 243$, corresponding to $3\lambda_{y,opt}^+$ of the selected LNSE-LOM-system. The computational simulation parameters used are: $L_x^+ = 3141.6$, $\Delta x^+ = 7.85$ ($N_x = 401$), and $N_z = 128$. In these simulations the domain was also set to be periodic in the streamwise direction, exactly as in the simulations presented previously.

One of the main conclusions drawn from the results presented in § 5.3.6 is that the wall-normal perturbation velocity seems to be an excellent estimator for the sought correlation between MR/MI and DR/DI. For this reason the attention here is focused mainly on the evolution of the perturbation component. In figures 5.33 to 5.37 are presented the plots of the temporal evolution of the uncontrolled and controlled cases, for the varicose mode w_r. Normalization has been performed using the maximum or global temporal value, although independently for each sequence; in all the contour plots the color-scale has been adjusted to help the examination of details throughout the time snapshots presented. Such an adjustment has been carried out simply by limiting the maximum and minimum values of the color scale, but keeping the original values.

Examining in detail these plots, two distinct trends are recognisable: i) a monotonic decay, with structures undergoing convection away from the wall, being drifted upwards (figures 5.33 to 5.35); and ii) a nearly constant development of structures close to the wall with a much reduced level of wall-normal convection, i.e. with drifting almost null (figures 5.36 and 5.37).

The first trend observed (monotonic decay with strong upwards convection) is observed in the development of the wall-normal perturbation velocity in the uncontrolled case and the control cases associated previously to reduction of measure (MR), which correlate to the DR phenomenon. The main difference between the uncontrolled and the controlled cases is the speed at which such phenomenon occurs. In the control cases it seems that the degree of wall-normal convection, and the corresponding decay, is faster than in the uncontrolled case, anticipating the subduing of wall-normal velocity structures in the region close to the wall.

On the other hand, for those control cases corresponding to a measure increase (MI), which have been showed to correlate to the drag increase regions in the DNS-based map, the situation is dramatically different. As it can be seen in figures 5.34 and 5.35, during the development of the simulation there is a permanent formation of structures, which are also convected upwards (from the wall), but at a much reduced pace. In this new scenario, there is also a nearly constant formation of strong negative and positive regions of wall-normal velocity, even at the later stages of the perturbation evolution.

In figures 5.38 to 5.41 are presented the plots of temporal evolution of the uncontrolled and controlled cases, for the sinusoidal w_{i}. As in the previous cases, in these plots the wall-normal velocity has been normalized using the maximum or global value in time for each independent sequence, and the color-scale has been adjusted for detail enhancement (as described above). Given that in the uncontrolled case the wall-normal velocity only develops a dominant-centred mode, thanks to the decoupling discussed earlier, in this set of plots the uncontrolled response has been omitted. As in the varicose cases, two different tendencies can be seen, each associated to specific operational points of the spanwise oscillation control. For instance, in those cases where a reduction of measure was observed in the control maps (see figures 5.30 and 5.31), the evolution of the wall-normal velocity describes a monotonic decay, as it can be seen in figures 5.38 and 5.39. However, as seen for the varicose mode, in those control cases where an increase of measure was observed, the sinusoidal mode also exhibits the formation of coherent structures, which appear to form a train of positive and negative packets (figures 5.40 and 5.41). Equally, as in the varicose mode response, there is no decay of the structures being formed which also remain for longer periods of time within the region below $z^+ < 60$.

However, maybe the most important aspect to note is that, as anticipated at the beginning of this discussion, under the effect of the STWSV-control the symmetry of the wall-normal perturbation velocity is broken by the spanwise oscillations, and therefore such perturbation component cannot any longer be described only by an even (varicose) mode behaviour; in fact, the introduction of the spanwise oscillation control has brought about a much more 'interesting' picture where the evolution of the coherent structures varies in accordance with the control case, and clearly features a degree of waviness in coherence with the underlying spanwise oscillation state. This last aspect can be appreciated by comparing the streamwise periodicity of the 'new' structures, i.e. under the effect of STWSV-control, with the streamwise wavelength of each corresponding generalised Stokes layer imposed. It is clear that the imposition of the GSL, describing a given streamwise modulated wave of spanwise oscillations, dictates the subsequent evolution of the structures, inducing an interchange between the real and imaginary parts of the perturbations, i.e. interchange of the role of the varicose and sinusoidal modes during the near-wall perturbation evolution.

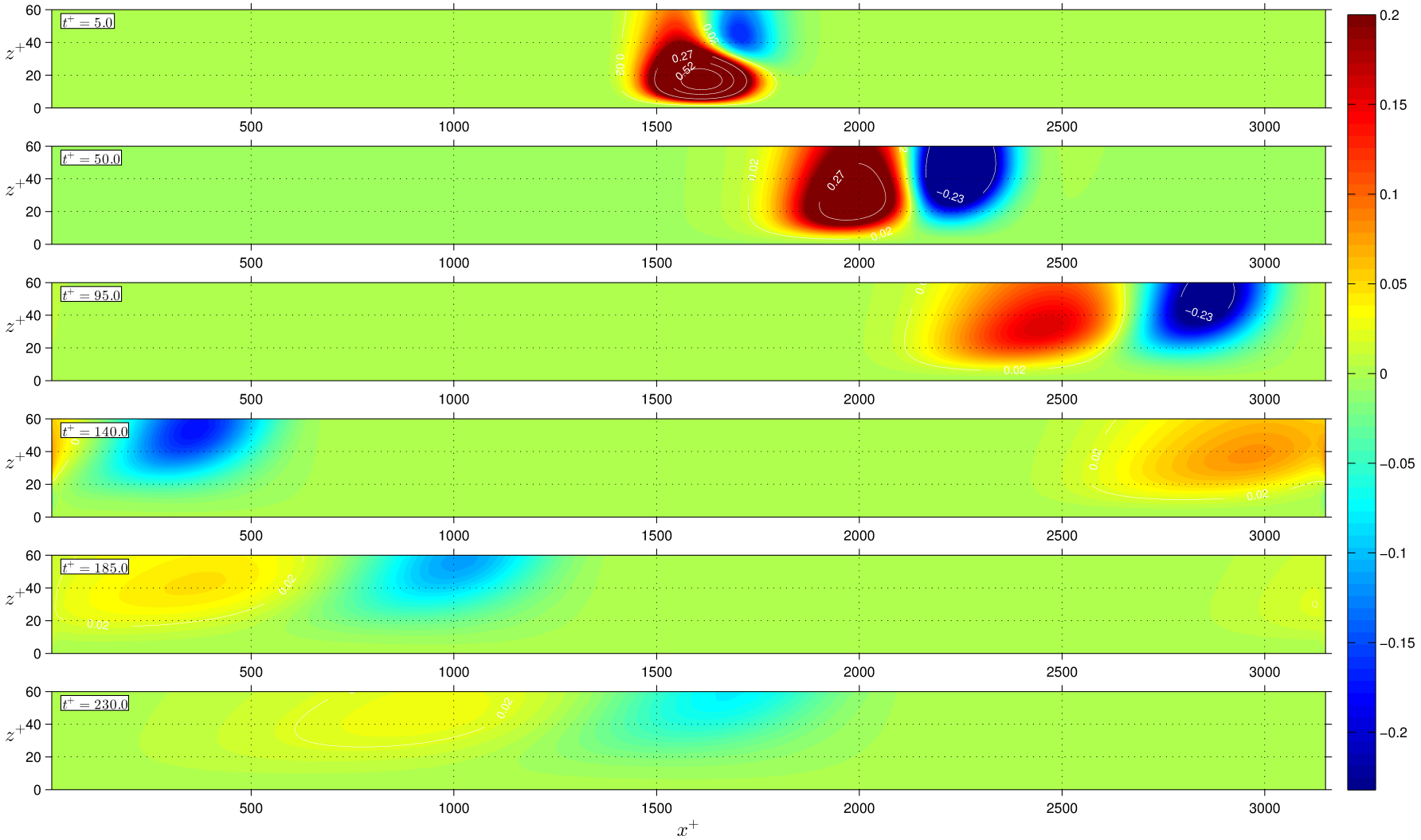

Figure 5.33: Side view of the temporal evolution of the wall-normal perturbation varicose mode w_r (at $\beta y = 0$); uncontrolled case. Time snapshots taken at $t^+ = 5,\ 50,\ 95,\ 140,\ 185,\ 230$. Perturbation generated with $I_{2,w}$ as EM in a TBL at $Re_\tau = 200$ with a spacing $\lambda_y^+ = 243$. Normalization has been performed using $\max_t |w_\mathsf{r}|$, and the color-scale adjusted for detail enhancement.

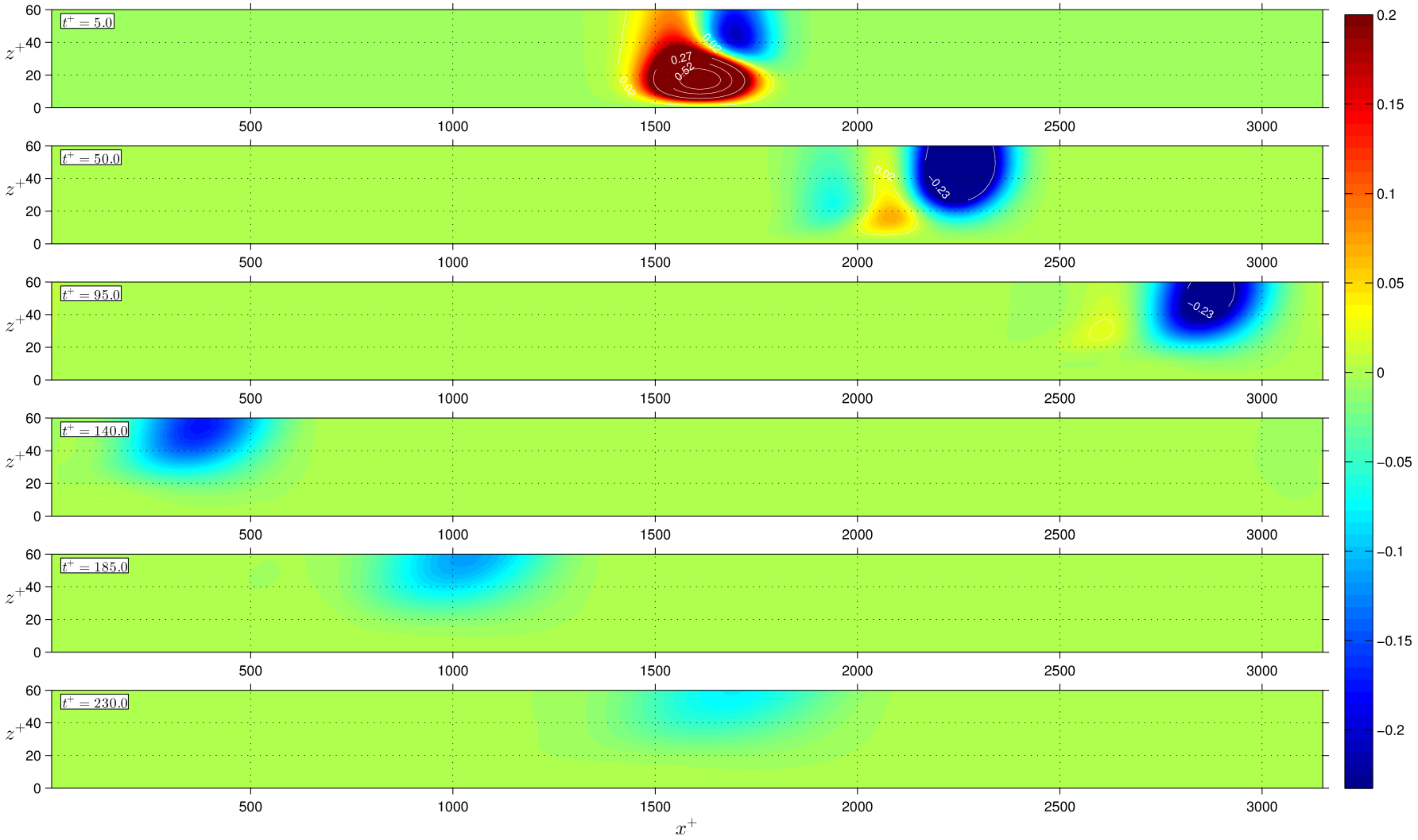

Figure 5.34: Side view of the temporal evolution of the wall-normal perturbation varicose mode w_r (at $\beta y = 0$); controlled perturbation, reduction case 1: $\kappa_x^+ = 0.00$, $\lambda_{x,\mathrm{GSL}}^+ \approx \infty$, $\omega^+ = 0.06$. Time snapshots taken at $t^+ = 5, 50, 95, 140, 185, 230$. Perturbation generated with $I_{2,w}$ as EM in a TBL at $Re_\tau = 200$ with a spacing $\lambda_y^+ = 243$. Normalization has been performed using $\max_t |w_\mathsf{r}|$, and the color-scale adjusted for detail enhancement.

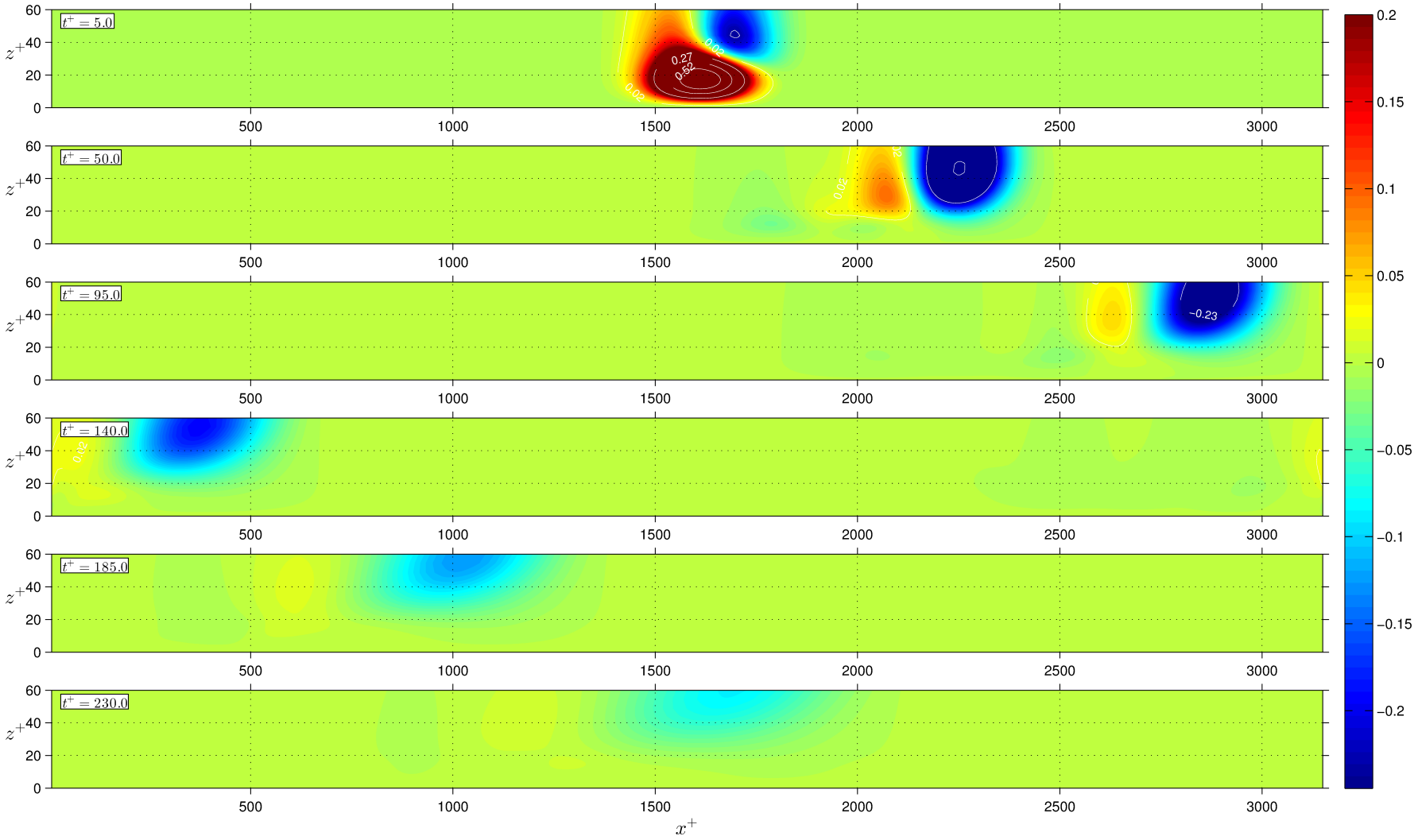

Figure 5.35: Side view of the temporal evolution of the wall-normal perturbation varicose mode w_{r} (at $\beta y = 0$); controlled perturbation, reduction case 2: $\kappa_x^+ = 0.025$, $\lambda_{x,\mathrm{GSL}}^+ \approx 251.3$, $\omega^+ = 0.120$. Time snapshots, of a side view at $\beta\, y = 0$, taken at $t^+ = 5,\ 50,\ 95,\ 140,\ 185,\ 230$. Perturbation generated with $I_{2,w}$ as EM in a TBL at $Re_\tau = 200$ with a spacing $\lambda_y^+ = 243$. Normalization has been performed using $\max_t |w_{\mathsf{r}}|$, and the color-scale adjusted for detail enhancement.

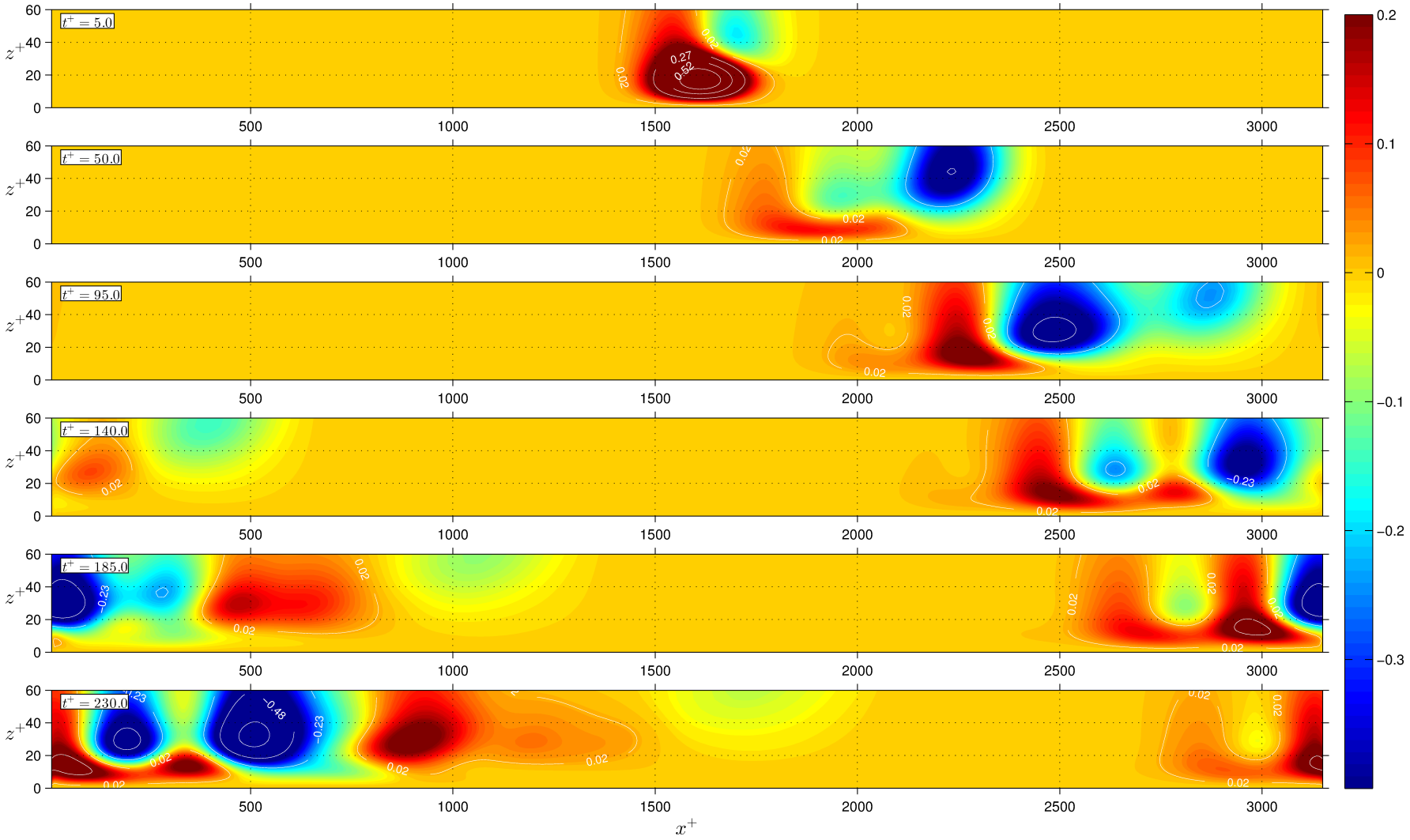

Figure 5.36: Side view of the temporal evolution of the wall-normal perturbation varicose mode w_r (at $\beta y = 0$); controlled perturbation, increase case 1: $\kappa_x^+ = 0.020$, $\lambda_{x,\mathrm{GSL}}^+ \approx 314.2$, $\omega^+ = 0.225$. Time snapshots taken at $t^+ = 5, 50, 95, 140, 185, 230$. Perturbation generated with $I_{2,w}$ as EM in a TBL at $Re_\tau = 200$ with a spacing $\lambda_y^+ = 243$. Normalization has been performed using $\max_t |w_\mathsf{r}|$, and the color-scale adjusted for detail enhancement.

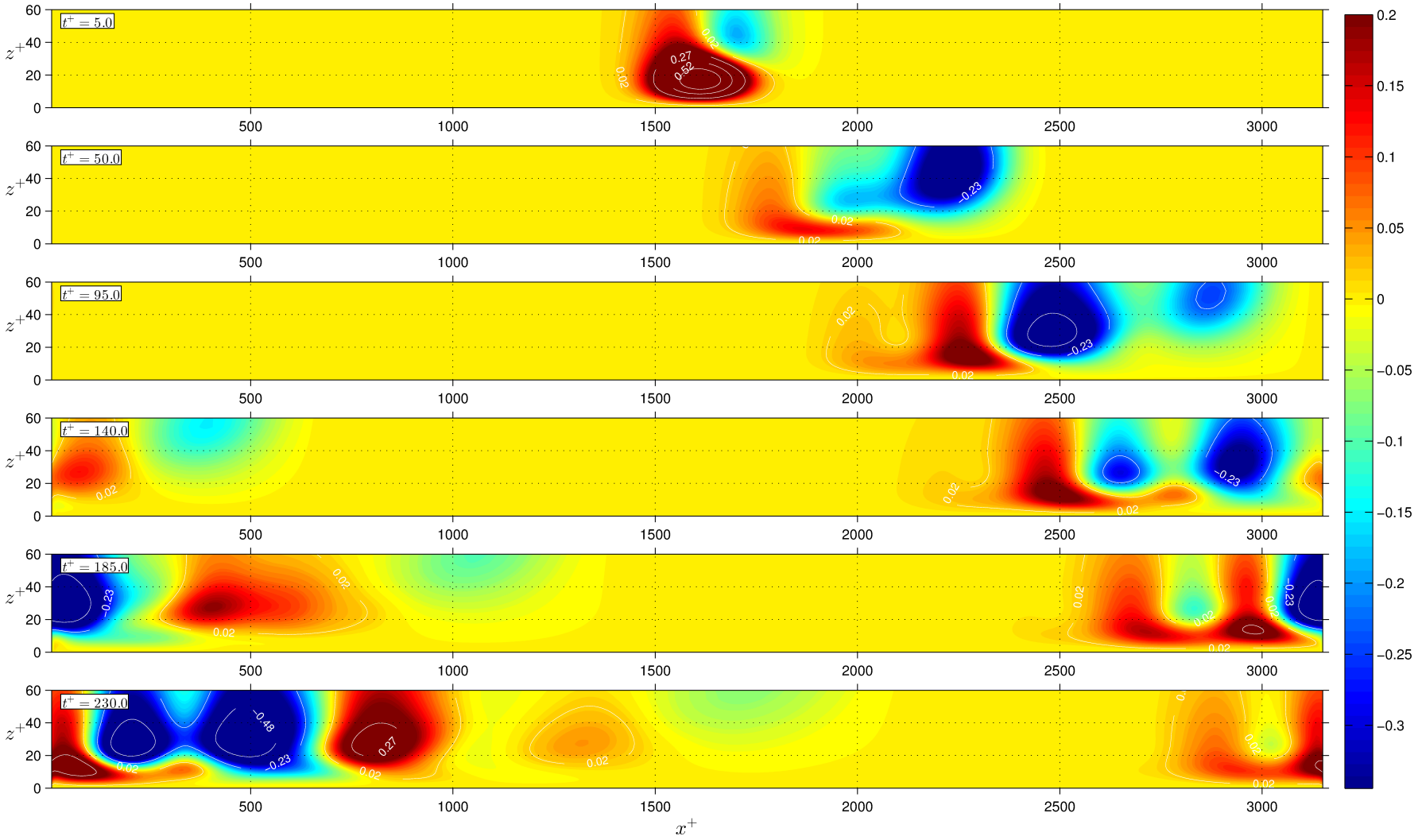

Figure 5.37: Side view of the temporal evolution of the wall-normal perturbation varicose mode w_r (at $\beta y = 0$); controlled perturbation, increase case 2: $\kappa_x^+ = 0.022$, $\lambda_{x,\mathrm{GSL}}^+ \approx 285.6$, $\omega^+ = 0.240$. Time snapshots taken at $t^+ = 5, 50, 95, 140, 185, 230$. Perturbation generated with $I_{2,w}$ as EM in a TBL at $Re_\tau = 200$ with a spacing $\lambda_y^+ = 243$. Normalization has been performed using $\max_t |w_\mathsf{r}|$, and the color-scale adjusted for detail enhancement.

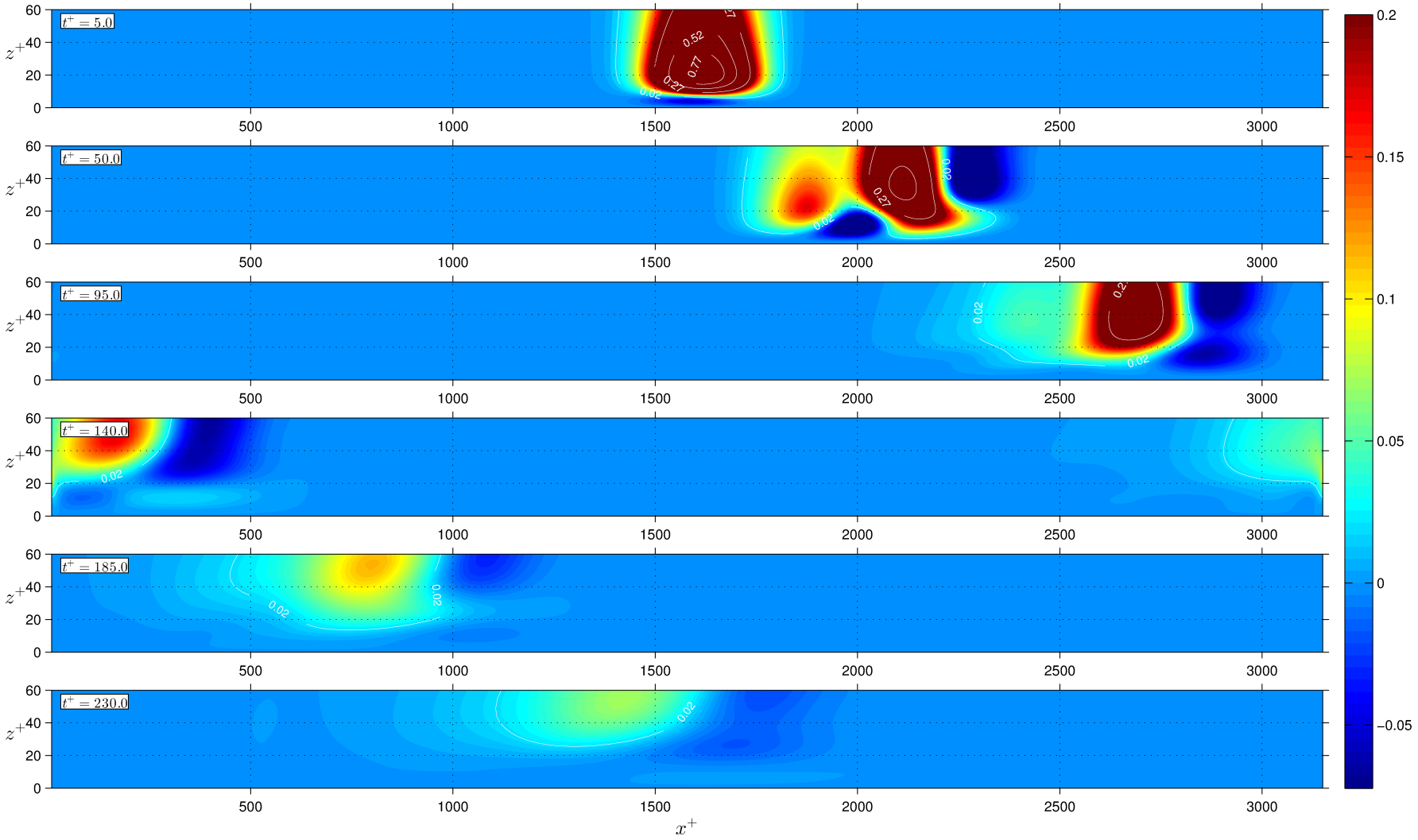

Figure 5.38: Side view of the temporal evolution of the wall-normal perturbation sinusoidal mode w_{i} (at $\beta y = \pi/2$); controlled perturbation, reduction case 1: $\kappa_x^+ = 0.00$, $\lambda_{x,\mathrm{GSL}}^+ \approx \infty$, $\omega^+ = 0.06$. Time snapshots taken at $t^+ = 5,\ 50,\ 95,\ 140,\ 185,\ 230$. Perturbation generated with $I_{2,w}$ as EM in a TBL at $Re_\tau = 200$ with a spacing $\lambda_y^+ = 243$. Normalization has been performed using $\max_t |w_{\mathrm{i}}|$, and the color-scale adjusted for detail enhancement.

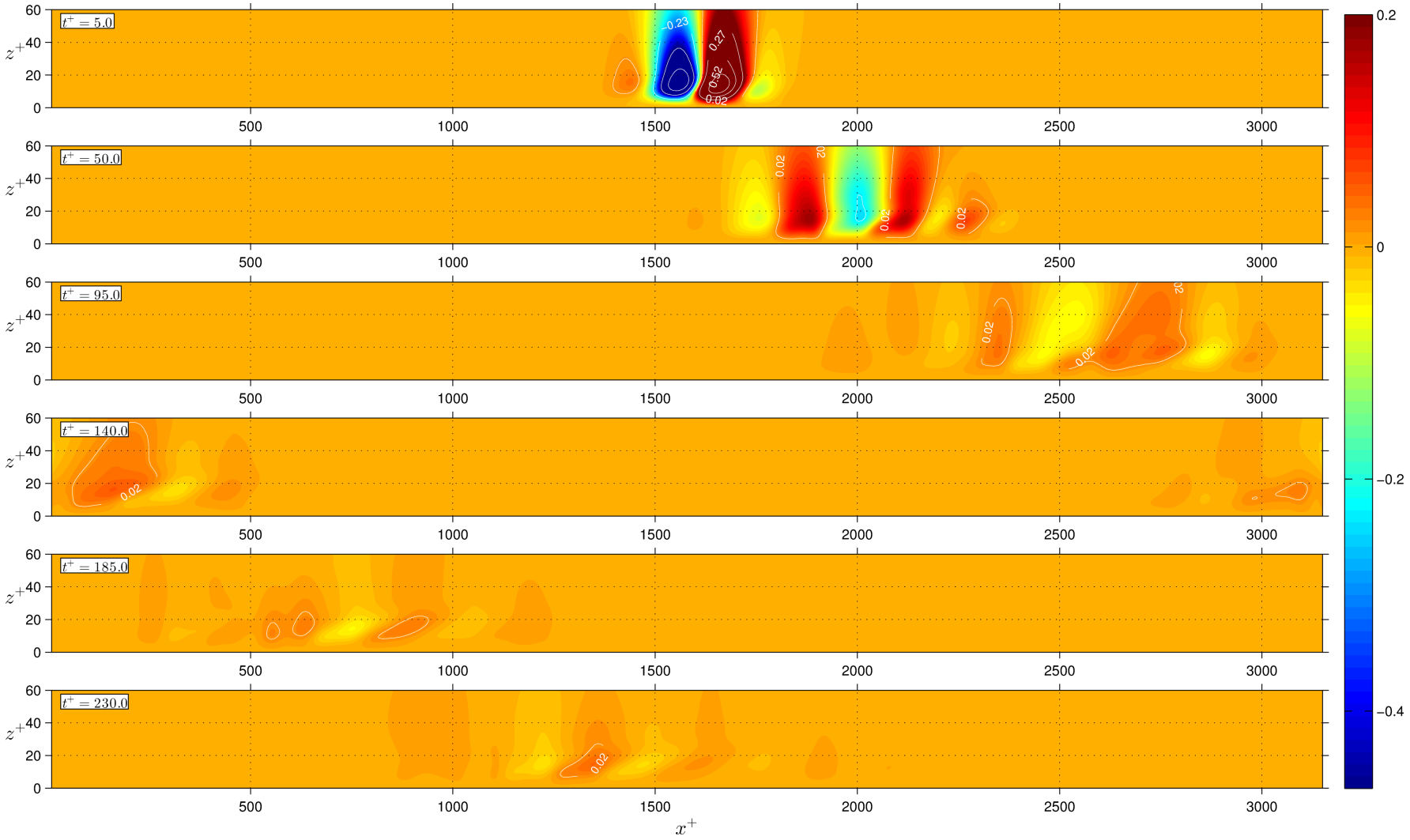

Figure 5.39: Side view of the temporal evolution of the wall-normal perturbation sinusoidal mode w_{i} (at $\beta y = \pi/2$); controlled perturbation, reduction case 2: $\kappa_x^+ = 0.025$, $\lambda_{x,\mathrm{GSL}}^+ \approx 251.3$, $\omega^+ = 0.120$. Time snapshots, of a side view at $\beta\, y = 0$, taken at $t^+ = 5,\ 50,\ 95,\ 140,\ 185,\ 230$. Perturbation generated with $I_{2,w}$ as EM in a TBL at $Re_\tau = 200$ with a spacing $\lambda_y^+ = 243$. Normalization has been performed using $\max_t |w_{\mathrm{i}}|$, and the color-scale adjusted for detail enhancement.

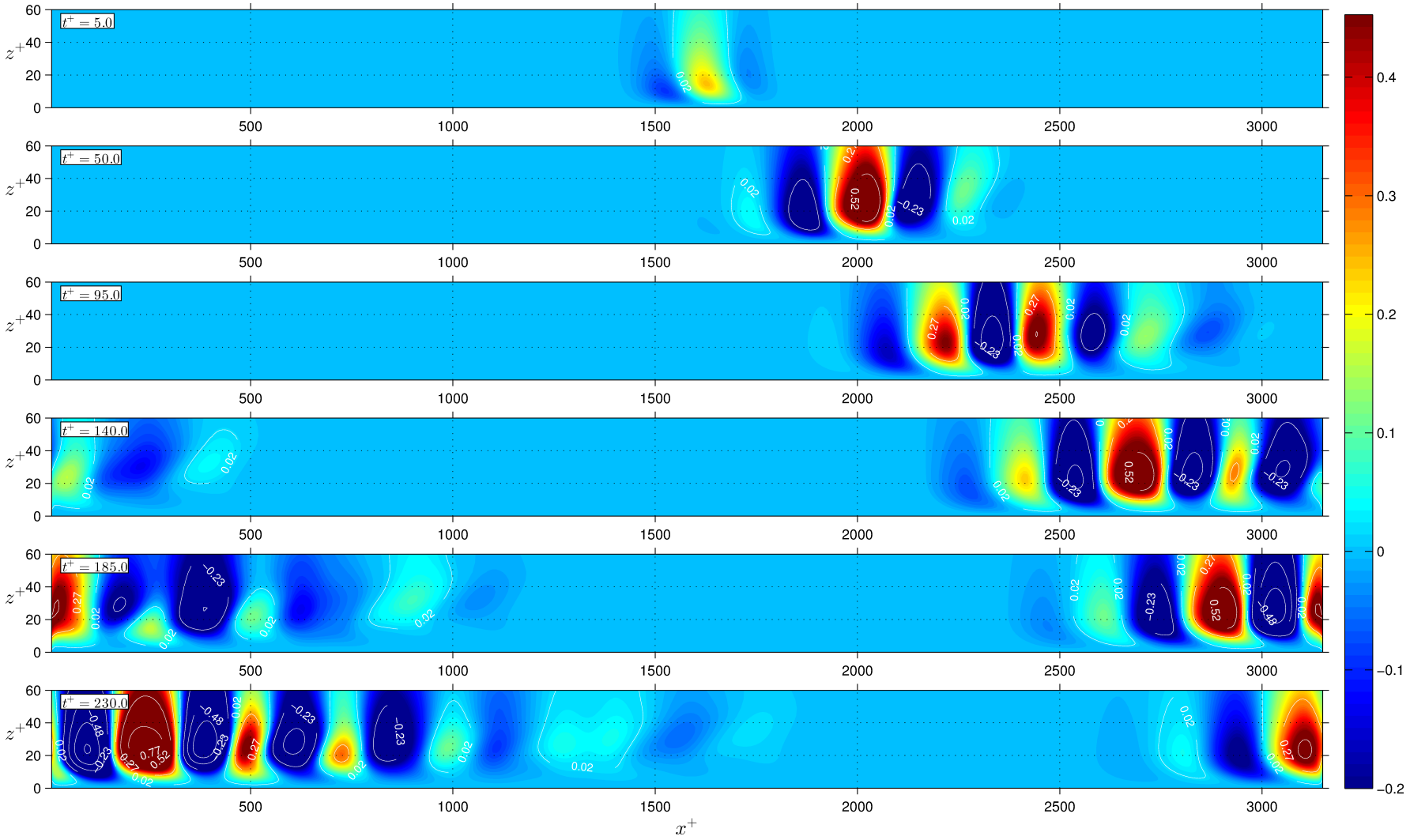

Figure 5.40: Side view of the temporal evolution of the wall-normal perturbation sinusoidal mode w_r (at $\beta y = \pi/2$); controlled perturbation, increase case 1: $\kappa_x^+ = 0.020$, $\lambda_{x,\mathrm{GSL}}^+ \approx 314.2$, $\omega^+ = 0.225$. Time snapshots taken at $t^+ = 5, 50, 95, 140, 185, 230$. Perturbation generated with $I_{2,w}$ as EM in a TBL at $Re_\tau = 200$ with a spacing $\lambda_y^+ = 243$. Normalization has been performed using $\max_t |w_\mathrm{i}|$, and the color-scale adjusted for detail enhancement.

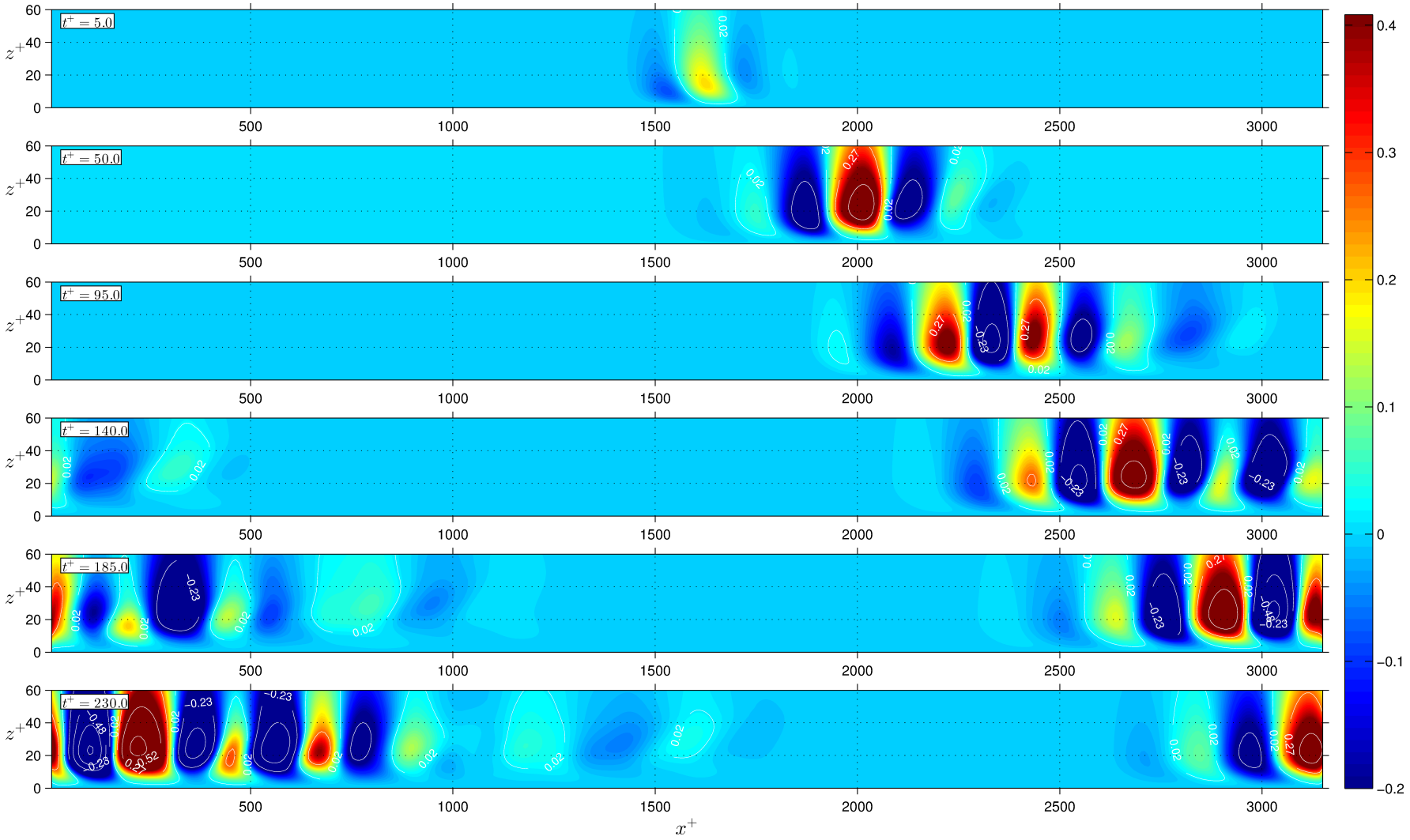

Figure 5.41: Side view of the temporal evolution of the wall-normal perturbation sinusoidal mode w_{i} (at $\beta y = \pi/2$); controlled perturbation, increase case 2: $\kappa_x^+ = 0.022$, $\lambda_{x,\text{GSL}}^+ \approx 285.6$, $\omega^+ = 0.240$. Time snapshots taken at $t^+ = 5, 50, 95, 140, 185, 230$. Perturbation generated with $I_{2,w}$ as EM in a TBL at $Re_\tau = 200$ with a spacing $\lambda_y^+ = 243$. Normalization has been performed using $\max_t |w_{\text{i}}|$, and the color-scale adjusted for detail enhancement.

Top and side views of the temporal evolution of the wall-normal perturbation velocity, with the sinusoidal and varicose modes combined, are presented in figures 5.42 to 5.45. Each side view has been extracted at the spanwise plane $\beta y = \pi/4$, whereas the planes used to construct the top view of each snapshot correspond to wall-normal planes containing the maximum values of the perturbation at the given time instant. These are indicated in the legend within each snapshot. These plots show, maybe somehow clearer, the two tendencies discussed previously. On the one hand, the monotonic decay of the initial structure as it evolves in time for the case linked with measure reduction as presented in figures 5.42 and 5.43. On the other hand, the seemingly continual formation of structures in the region close to the wall, as seen in figures 5.44 and 5.45.

The top view of the temporal evolutions confirm the presence of a more complex structure, compared against the uncontrolled case, of the wall-normal velocity perturbation. This feature is particularly more appreciable for the control case linked to measure increase. Nevertheless, in both control cases presented in figures 5.43 and 5.45, the perturbation exhibits a waviness structure, which corresponds to the periodicity of the basic state, i.e. to the wavelength of the given STWSV imposed. It seems apparent that this feature is the reason of the appearance of a train of regions of positive and negative w.

An additional noteworthy aspect is that, as it was conjectured previously, a distinction between the control cases bringing about measure reduction and those resulting in measure increase lies in the rate at which the structures of w are convected towards the TBL limit, upwards away from the wall. In the combination of κ_x^+ and ω^+ resulting in measure reduction (MR), the packet of w moves faster outwards, reaching the plane $z^+ \approx 49$ at $t^+ = 95$, just the third snapshot in figure 5.43. In turn, as seen in figure 5.45 for the control case which brings about measure increase (MI), the majority of the structures remain, essentially, below $z^+ \approx 27$, as conjectured in § 5.3.6, and somehow anticipated in the spatio-temporal evolution presented in figure 5.32b; this situation lasts until the last snapshot presented, $t^+ = 230$. Observing this plot it is apparent that there is not reduction at all, and the wavy structure of w keeps growing extending for more than 1000 inner units in the streamwise direction at the last time instant presented. Although other results are omitted for space reasons, this phenomenon was confirmed for other control cases near the region of $c^+ \approx 10$ in the DNS-based control map; in fact, as previously discussed, these are control points which bring about MI in the LNSE-based control map of the figure 5.30.

Again, if it is accepted that the lift-up term $w\, dU^B/dz$ plays an important role in the formation process of streaks, then the immediate consequence of structures of w being concentrated in the near-wall region is that the STWSV produces a reinforcement of the lift-up term, and therefore an intensification of near-wall coherent structures generation. However, up until this point the discussion has been focused on the wall-normal perturbation and the structures arising from the prescription of the STWSV. It is now required to explore the

streamwise and spanwise perturbation velocity structures arising from the prescription of flow-control.

In figures 5.46 and 5.47 are presented the top views of the streamwise perturbation velocity developing with the flow-control applied at the conditions referred to as control-MR case 2 ($\kappa_x^+ = 0.025$,$\omega^+ = 0.120$), and the control-MI case 2 ($\kappa_x^+ = 0.022$,$\omega^+ = 0.240$), respectively.

In the control case producing MR a weak wavy pattern is observed initially, structure which afterwards seems to stabilise, and then to undergo the normal transient growth that would be expected in the absence of control. The apparent weak transient growth is due to the fact that the perturbation represented in figure 5.46 is developing at $\lambda_y^+ = 243.3$. At this spanwise scales, although not explicitly mentioned previously for brevity, the transient growth occurs at a slower rate than at the optimal spanwise spacing. This may be due in part to the inter-play between non-normality of the LNSE operator and the degree of viscous dissipation at this scale, which diminishes the intensity of the algebraic growth and delays the transient growth. Nevertheless, as with the wall-normal perturbation velocity w, in this control-MR case the perturbation structure (in this case the streak), is advected monotonically outwards. This was also verified for other flow-control cases bringing about measure reduction. An additional observation is that, in this reduction case, the developed structure returns to its varicose mode dominant nature. This might be expected: as the streak is advected away from the wall, it ceases to fell the effect of the spanwise oscillation, returning to its regular streaky-structure. This seems to suggests that, at least for control points associated with MR, the perturbation is stable out the GSL induced by the STWSV.

In the control-MI case presented in figure 5.47 the structure obtained initially is a weak wavy pattern, in a similar fashion as in the previous control-MR case. Notwithstanding, the subsequent evolution of the streamwise perturbation velocity u is totally different from the control-MR case. The structure keeps growing in strength and extension as it evolves in time, in a similar manner as it was observed for w. Equally, the structure remains contained in the region $z^+ < 15$, approximately. Although the streamwise structure elongates in time, it does not decay as it evolves. Additionally, the wavy pattern seems to indicate that an instability which is not varicose nor sinusoidal dominant takes place, growing in time, and replacing the regular transient growth expected in the uncontrolled case.

In the temporal evolution of both u and w two different trends have been appreciated. Firstly, the structures obtained with control parameters producing MR (combinations of κ_x^+ and ω^+ achieving measure reduction), decay in time, monotonically, and are advected into the boundary layer, away from the bounding wall, faster than in the uncontrolled case. Secondly, those structures obtained with STWSV producing MI do not decay in time, but instead remain growing and extending in the streamwise direction as they evolve. In this case, the structures remain confined within a zone close to the wall, and the degree of advection is minimal, compared

with the uncontrolled case, and with the control cases bringing about MR. At this point it appears that these two trends are common to all the components of perturbation velocity. In order to assess if this is also true for the spanwise perturbation velocity v, figures 5.48 and 5.49 show the top view of the temporal evolution of v, for the control-MR and control-MI cases chosen as example, respectively. As it can be seen, in effect this is also the case for v, i.e. two marked distinct trends for cases linked with MR or MI, as explained above.

Thus, if as conjectured and proposed previously, it is accepted that the wall-normal velocity plays a major role in the process of streak (or other near-wall structures) generation, as part of the lift-up term, it seems that the temporal evolution of the structures portrayed in the figures discussed in this section could explain, at least phenomenologically, the two different responses of the LNSE-LOM-system to the flow-control based on STWSV. The phenomenological control mechanism proposed is: in those cases where the spanwise oscillation holds or produces pockets of wall-normal perturbation velocity in the near-wall region, these structures, through the lift-up term, enhance the production and generation of streamwise structures, which then keep growing in time. Therefore, by retaining the structures of the wall-normal and spanwise velocities in the near-wall region, the flow-control seems to be reinforcing the formation of streamwise structures, which eventually lead to, in the full non-linear turbulent flow phenomenon, an increase in the skin-friction drag. This might explain the correlation between the regions of MI in the control map for the measure μ_{N2}, and those regions of DI in the DNS-based drag reduction map. Following a similar rationale, the other trend of accelerated advection upwards away from the wall of the near-wall structures, might explain the correlation between regions of MR with those of DR. In this case, by advecting the near-wall perturbation structures, the STWSV may be reducing the impact of the lift-up term, and therefore the conversion of energy from the mean base flow into streamwise perturbation structures. A reduction of the amount and intensity of near-wall structures present in the near-wall region would then induced a drag-reduction effect, which in the LNSE-LOM-system case is being quantified by the MR phenomenon. This has been found to correlate to the DR regions of the DNS-based map, which supports this facet of the proposed phenomenological mechanism. In any case, it is clear that a further exploration into the previous phenomenological observations must be done, but extension of the present work precludes a more in-deep examination at this point.

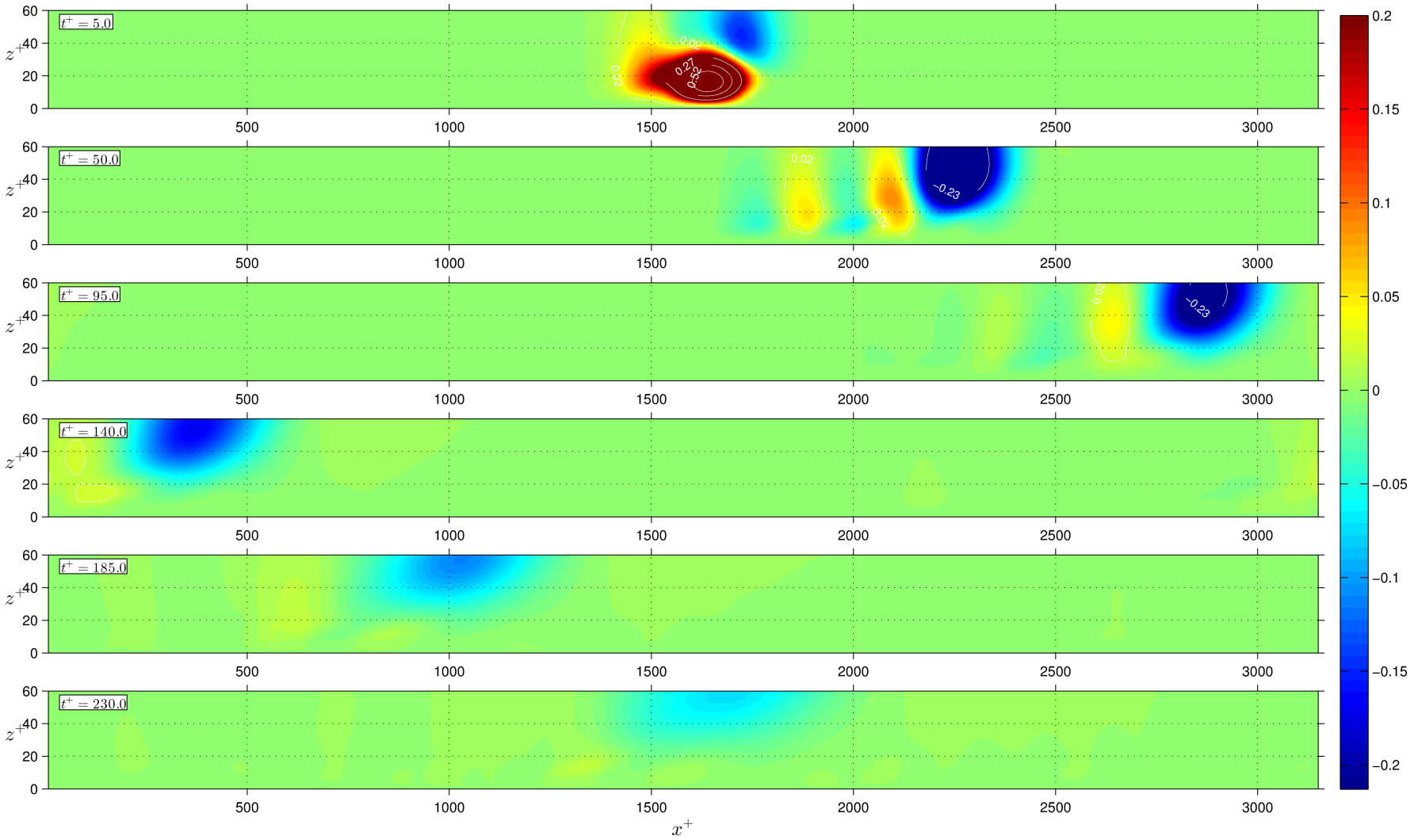

Figure 5.42: Side view of the temporal evolution of the wall-normal perturbation w for the control-MR case 2: $\kappa_x^+ = 0.025$, $\lambda_{x,\mathrm{GSL}}^+ \approx 251.3$, $\omega^+ = 0.120$. Combined sinusoidal and varicose modes taken at $\beta y = \pi/4$; time snapshots taken at $t^+ = 5$, 50, 95, 140, 185, 230. Perturbation generated with $I_{2,w}$ as EM in a TBL at $Re_\tau = 200$ with a spacing $\lambda_y^+ = 243$. Normalization has been performed using $\max_t |w|$, and the color-scale adjusted for detail enhancement.

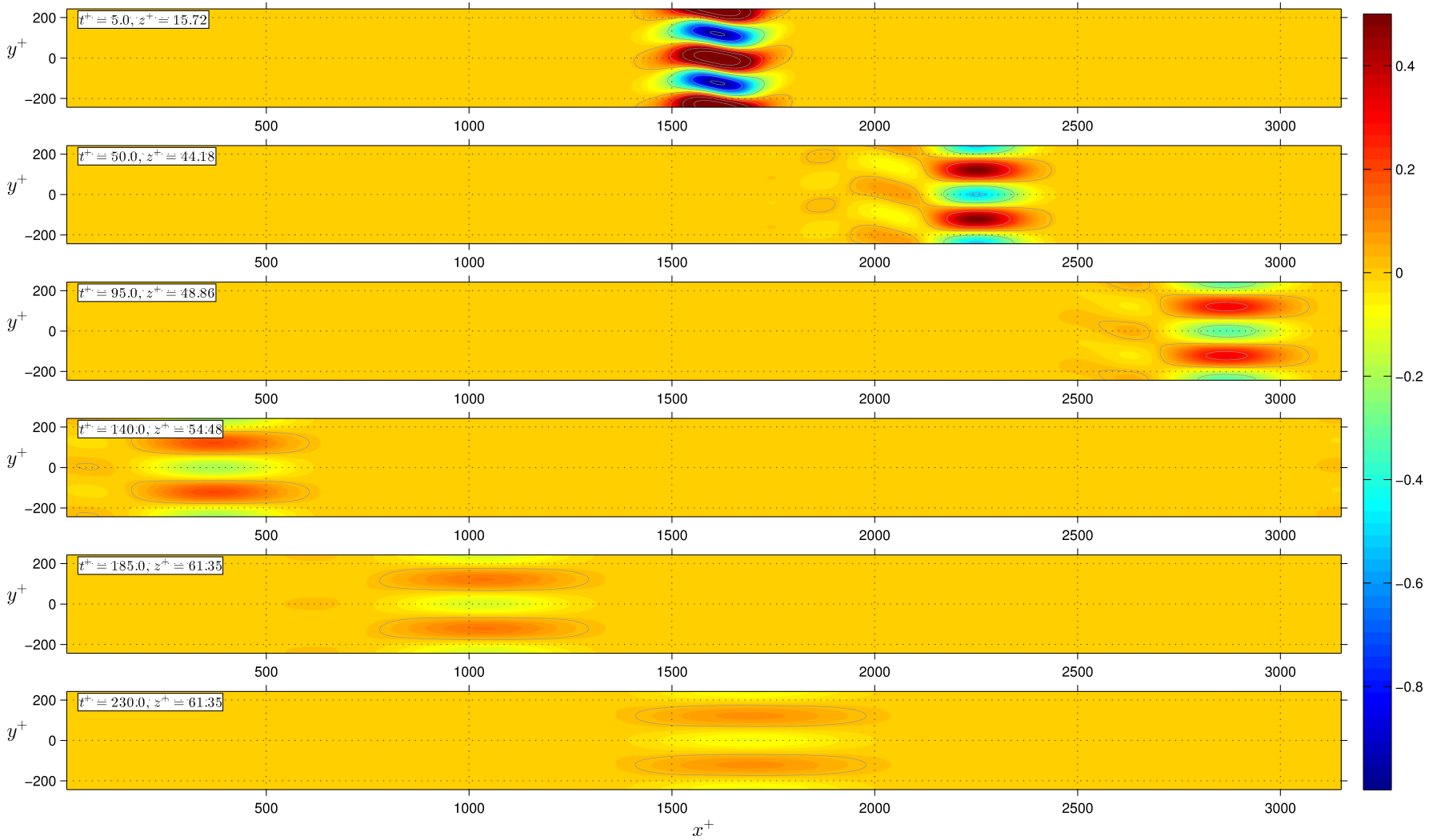

Figure 5.43: Top view of the temporal evolution of the wall-normal perturbation w for control-MR case 2: $\kappa_x^+ = 0.025$, $\lambda_{x,\mathrm{GSL}}^+ \approx 251.3$, $\omega^+ = 0.120$. Combined sinusoidal and varicose modes taken at planes containing the value $\max|w|$ at each time instant: $z^+ = 15.72, 44.18, 48.86, 54.48, 61.35$; time snapshots taken at $t^+ = 5,\ 50,\ 95,\ 140,\ 185,\ 230$. Perturbation generated with $I_{2,w}$ as EM in a TBL at $Re_\tau = 200$ with a spacing $\lambda_y^+ = 243$. Normalization has been performed using $\max_t|w|$, and the color-scale adjusted for detail enhancement.

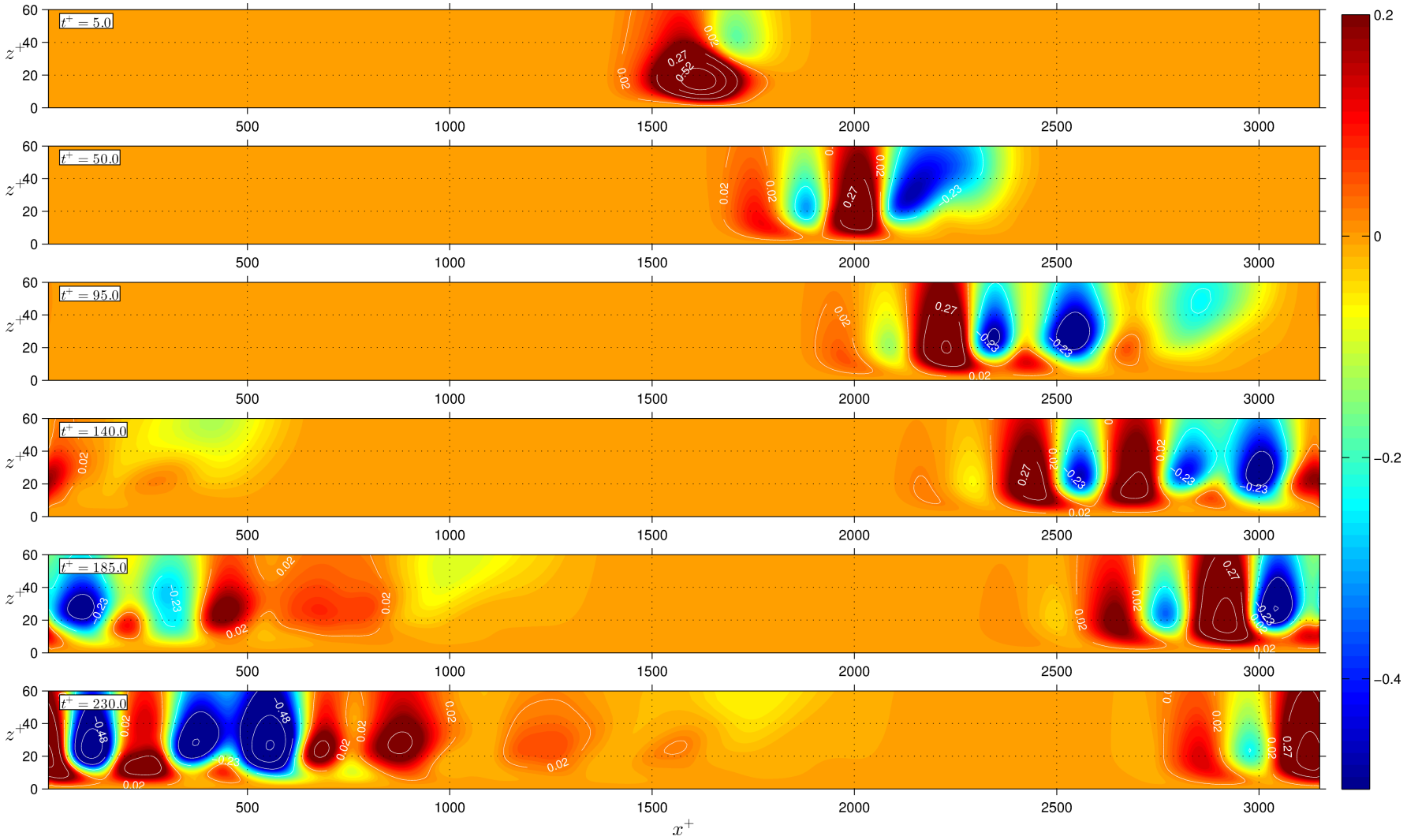

Figure 5.44: Side view of the temporal evolution of the wall-normal perturbation w for the control-MI case 2: $\kappa_x^+ = 0.022$, $\lambda_{x,\mathrm{GSL}}^+ \approx 285.6$, $\omega^+ = 0.240$. Combined sinusoidal and varicose modes taken at $\beta y = \pi/4$; time snapshots taken at $t^+ = 5$, 50, 95, 140, 185, 230. Perturbation generated with $I_{2,w}$ as EM in a TBL at $Re_\tau = 200$ with a spacing $\lambda_y^+ = 243$. Normalization has been performed using $\max_t |w|$, and the color-scale adjusted for detail enhancement.

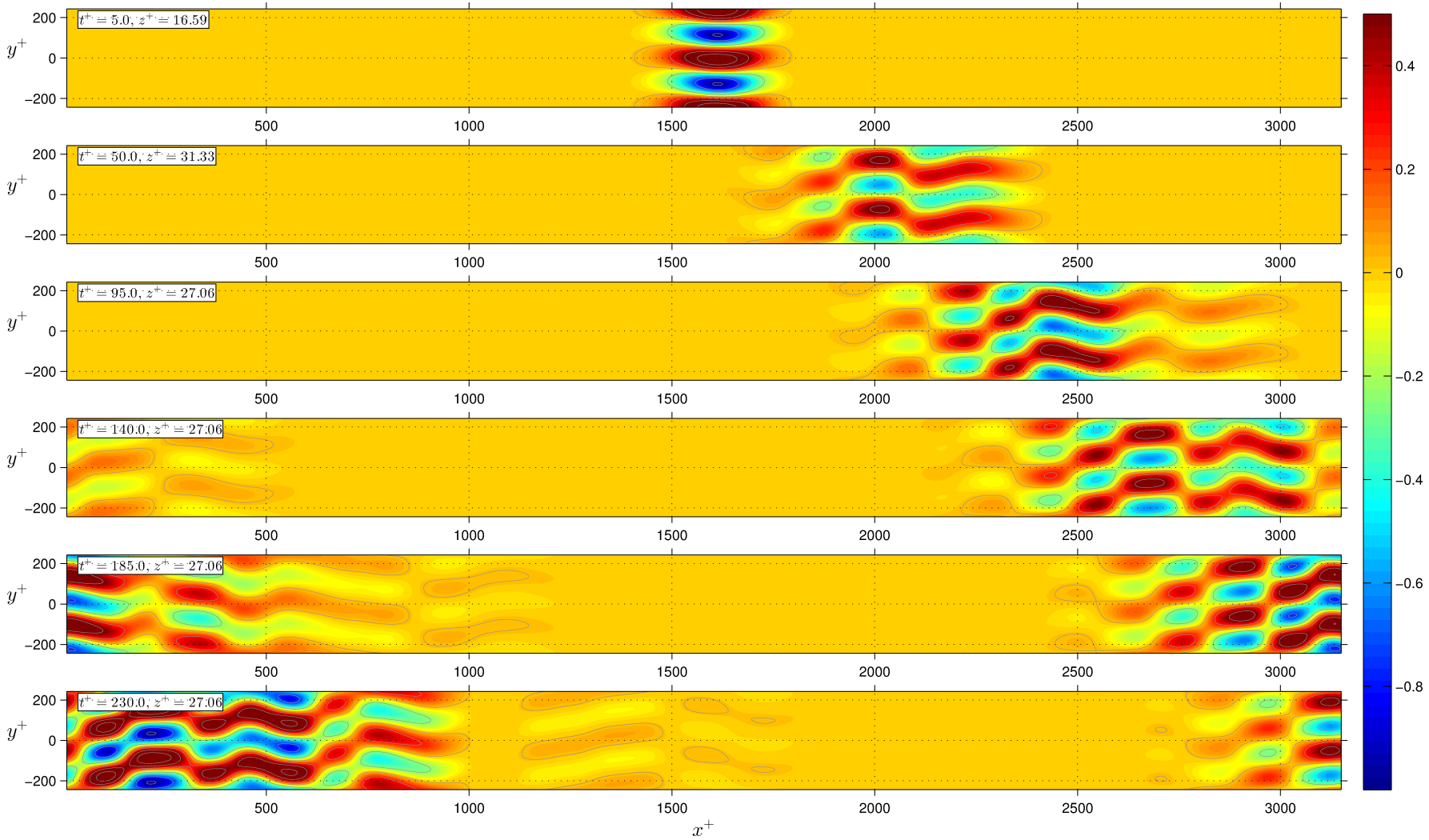

Figure 5.45: Top view of the temporal evolution of the wall-normal perturbation w for control-MI case 2: $\kappa_x^+ = 0.022$, $\lambda_{x,\mathrm{GSL}}^+ \approx 285.6$, $\omega^+ = 0.240$. Combined sinusoidal and varicose modes taken at planes containing the value $\max|w|$ at each time instant: $z^+ = 16.59, 31.33, 27.06$; time snapshots taken at $t^+ = 5,\ 50,\ 95,\ 140,\ 185,\ 230$. Perturbation generated with $I_{2,w}$ as EM in a TBL at $Re_\tau = 200$ with a spacing $\lambda_y^+ = 243$. Normalization has been performed using $\max_t|w|$, and the color-scale adjusted for detail enhancement.

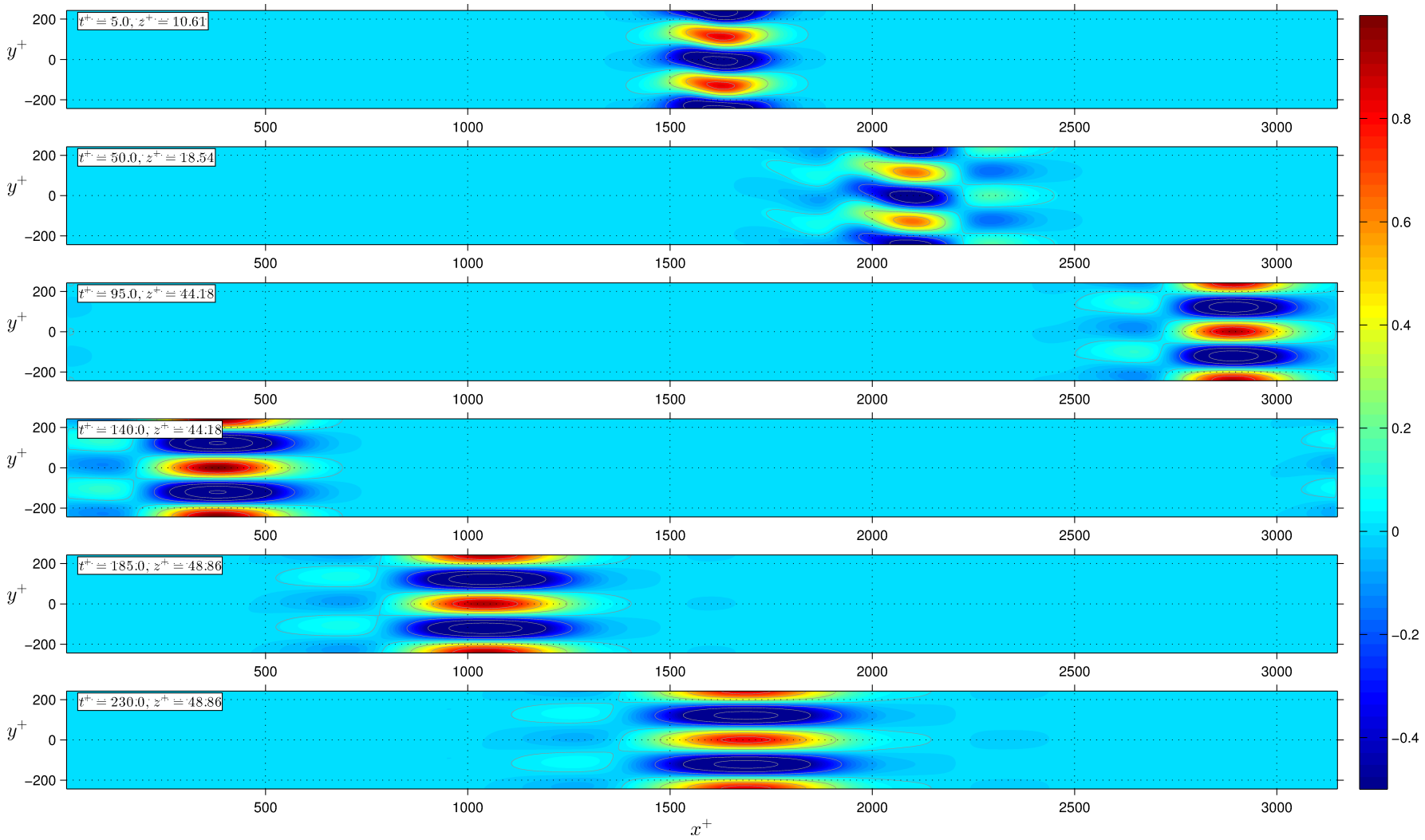

Figure 5.46: Top view of the temporal evolution of the streamwise perturbation w for the control-MR case 2: $\kappa_x^+ = 0.025$, $\lambda_{x,\mathrm{GSL}}^+ \approx 251.3$, $\omega^+ = 0.120$. Combined sinusoidal and varicose modes taken at planes containing the value $\max|u|$ at each time instant; perturbation generated with $I_{2,w}$ as EM in a TBL at $Re_\tau = 200$ with a spacing $\lambda_y^+ = 243$. Normalization has been performed using $\max_t|u|$, and the color-scale adjusted for detail enhancement.

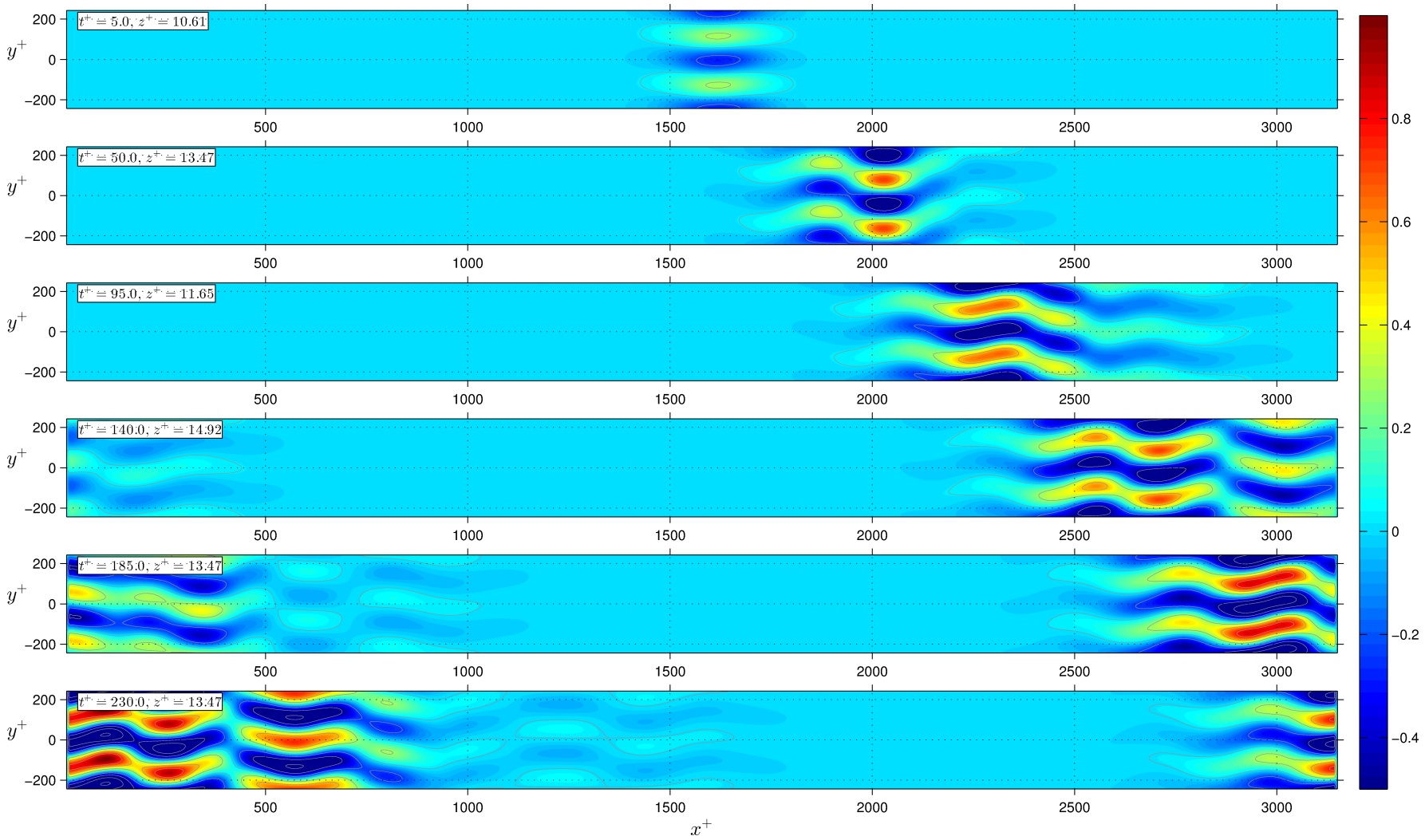

Figure 5.47: Top view of the temporal evolution of the streamwise perturbation u for control-MI case 2: $\kappa_x^+ = 0.022$, $\lambda_{x,\mathrm{GSL}}^+ \approx 285.6$, $\omega^+ = 0.240$. Combined sinusoidal and varicose modes taken at planes containing the value $\max|u|$ at each time instant; perturbation generated with $I_{2,w}$ as EM in a TBL at $Re_\tau = 200$ with a spacing $\lambda_y^+ = 243$. Normalization has been performed using $\max_t|u|$, and the color-scale adjusted for detail enhancement.

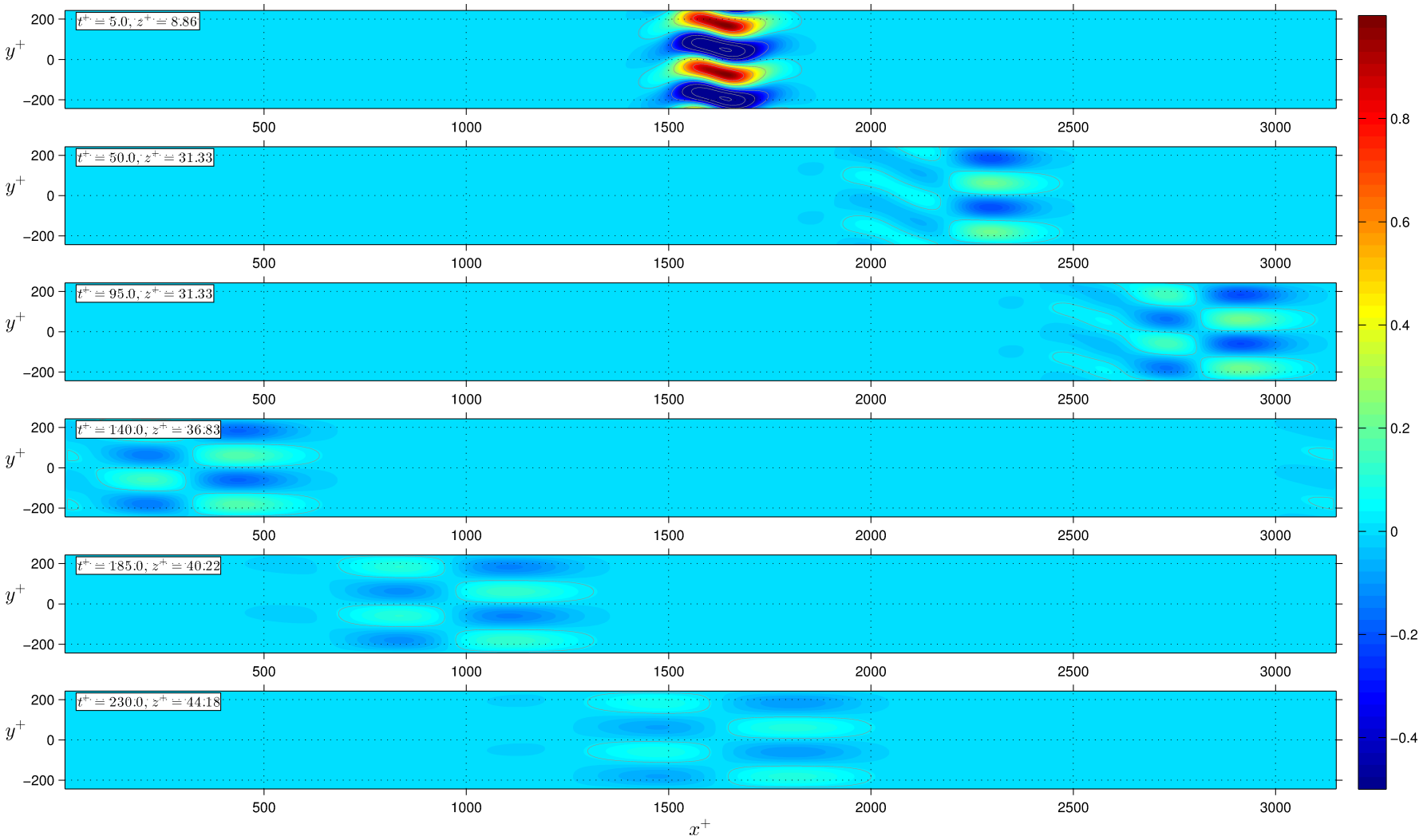

Figure 5.48: Top view of the temporal evolution of the spanwise perturbation v for the control-MR case 2: $\kappa_x^+ = 0.025$, $\lambda_{x,\mathrm{GSL}}^+ \approx 251.3$, $\omega^+ = 0.120$. Combined sinusoidal and varicose modes taken at planes containing the value $\max|v|$ at each time instant; perturbation generated with $I_{2,w}$ as EM in a TBL at $Re_\tau = 200$ with a spacing $\lambda_y^+ = 243$. Normalization has been performed using $\max_t|v|$, and the color-scale adjusted for detail enhancement.

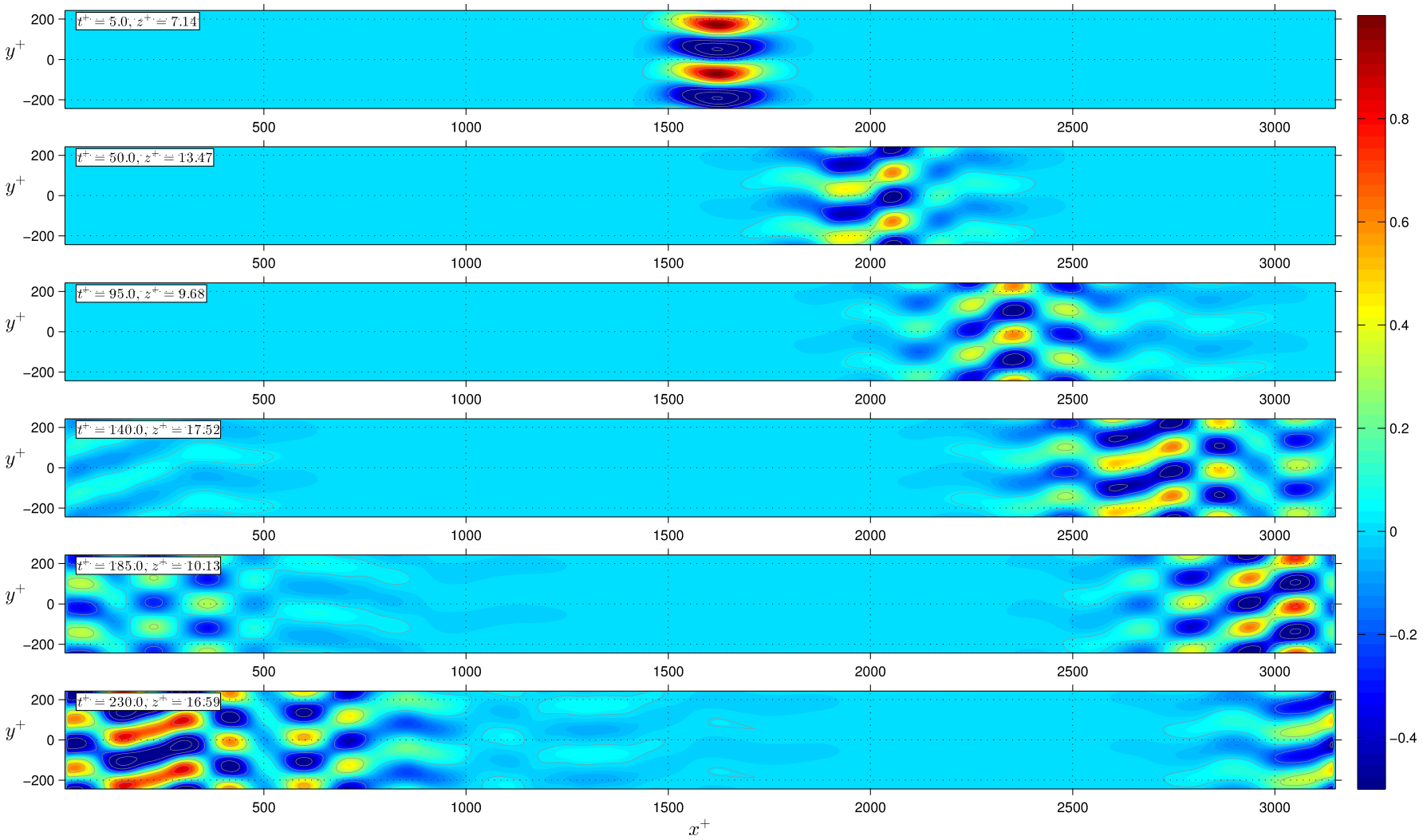

Figure 5.49: Top view of the temporal evolution of the spanwise perturbation v for control-MI case 2: $\kappa_x^+ = 0.022$, $\lambda_{x,\mathrm{GSL}}^+ \approx 285.6$, $\omega^+ = 0.240$. Combined sinusoidal and varicose modes taken at planes containing the value $\max|v|$ at each time instant; perturbation generated with $I_{2,w}$ as EM in a TBL at $Re_\tau = 200$ with a spacing $\lambda_y^+ = 243$. Normalization has been performed using $\max_t|v|$, and the color-scale adjusted for detail enhancement.

5.3.8 Controlled streak growth response at High Reynolds-number regime

One of the main benefits of following a linear approach is the ability to simulate the evolution of the near-wall streaks at higher Reynolds numbers than those permitted by DNS. Accordingly, the simulations presented previously were repeated using a turbulent boundary layer profile for a much higher Reynolds number $Re_\tau = 5000$, which corresponds to a displacement thickness Reynolds number $Re_{\delta_*} = 18210$. Owing to the Reynolds number independence of the optimal perturbation, determined with basis on the findings presented in § 4.4.3, the same parameters as defined previously were used for the EM $I_{2,w}$: $\sigma^+_{z,EM} = 3.9 \times 10^{-3}, \sigma^+_{x,EM} = 1.0^{-4}$ and $\lambda^+_y = 81.1$. The phase-averaging process for these high-Reynolds number tests was performed using 36 phases. The main goal of these tests was to verify if this feature was valid for an optimal perturbation evolving under the effect of the STWSV-control at high-Reynolds numbers.

Results for percentage change ϵ of μ_1 with $z^+_v = 12.5$ and calculated at $t^+ = 10$ are shown in figure 5.50. In figures 5.51 and 5.52 are shown the control map obtained for μ_{N2}, unscaled and linearly scaled (following the methodology presented in § 5.3.6), respectively. It can be seen that the magnitude of the streak-amplification change (ϵ) remains in general, within about $5 \sim 7\%$ of those values obtained for the lower Reynolds number case; this situation is portrayed, essentially, by all the control maps presented as can be seen by making a direct comparison between figures 5.27a and 5.50 for μ_1, and between figures 5.30b and 5.51 for μ_{N2}. In both cases, the contour maps are very much the same. Equally, by comparing the linearly scaled contour plots for μ_{N2} presented in figures 5.31b and 5.52, no significant change in the general layout of the MR and MI regions can be appreciated. Figure 5.53 shows the instability regions, in accordance to criterion previously introduced, at this high Reynolds number, although for a spanwise scale of $\lambda^+_y = 172$, i.e. twice the original optimal spanwise scale. This feature is then also consistently preserved at high Reynolds numbers.

This concurrence between the simulation results, arguably expected, strongly suggests that the effect of the spanwise flow actuation on the near-wall streaks is independent of the Reynolds number, if a correct scaling is made in terms of inner units. Of course, any such conclusion is subject to the validity of the simplifying approximations that were made in using the LNSE-LOM-system with a prescribed mean flow turbulent profile. Notwithstanding this, there are positive implications for the use of the wall motion flow control scheme in aerospace applications, where the high Reynolds number results are more pertinent. The linearized simulation results indicate that there may be no marked deterioration in the possible skin-friction reduction when the Reynolds number is increased above the relatively low values that have been considered in previous studies. Nevertheless, this optimistic assumption should be considered with reservations regarding the potential for a possible increasing role of large-scale structures in the turbulent boundary layer when the Reynolds number is higher [131]. No explicit attempt to model or identify such structures, which would be anticipated to develop

much further away from the wall than any of the streaks target of this study, has been made in this thesis.

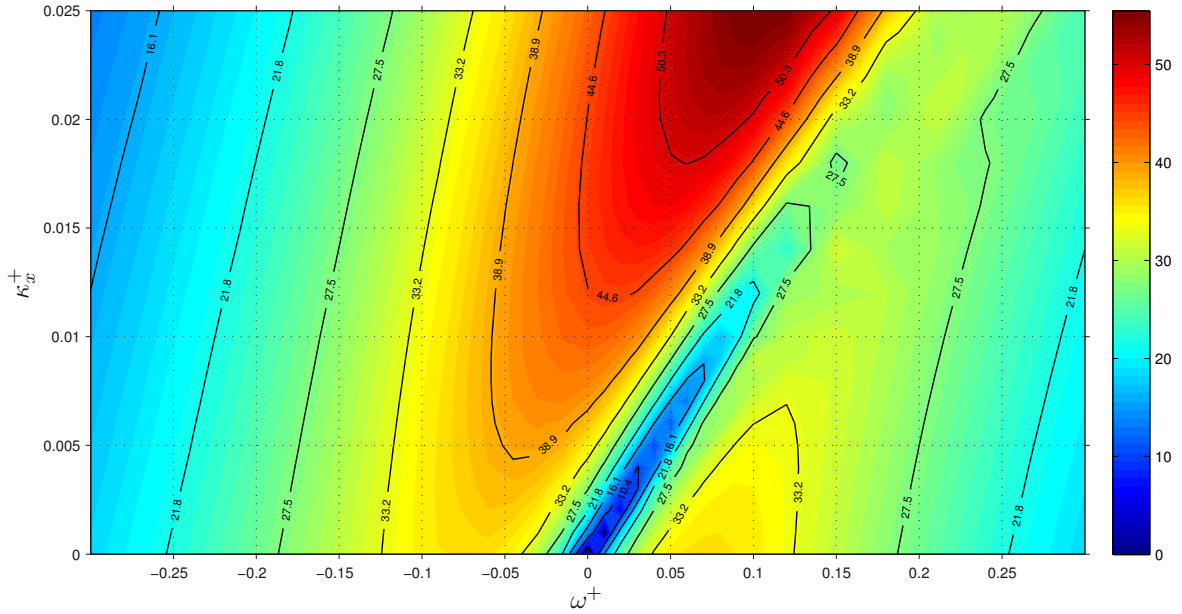

Figure 5.50: Contour plot of amplification measure change ϵ for μ_1 over actuation parameter space (ω^+, κ_x^+), obtained at $t^+ = 10$ as calculated using the linearized Navier-Stokes equations for a TBL at $Re_\tau = 5000$, and using $I_{2,w}$ as EM.

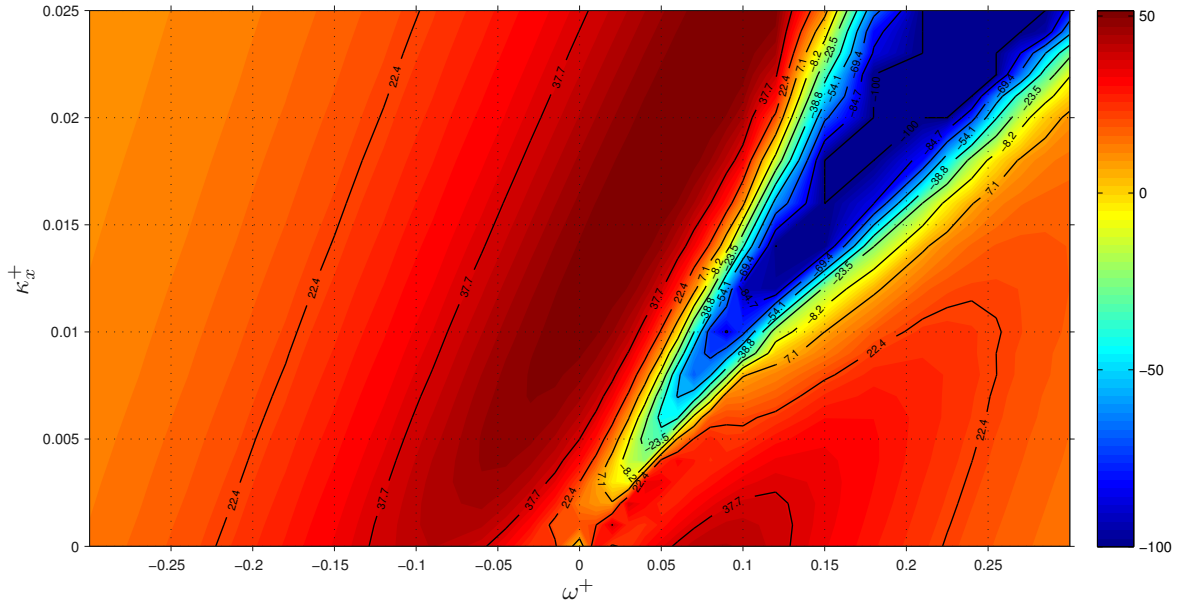

Figure 5.51: Contour plot of amplification measure change ϵ for μ_{N2} over actuation parameter space (ω^+, κ_x^+), as calculated using the linearized Navier-Stokes equations for a TBL at $Re_\tau = 5000$, and using $I_{2,w}$ as EM.

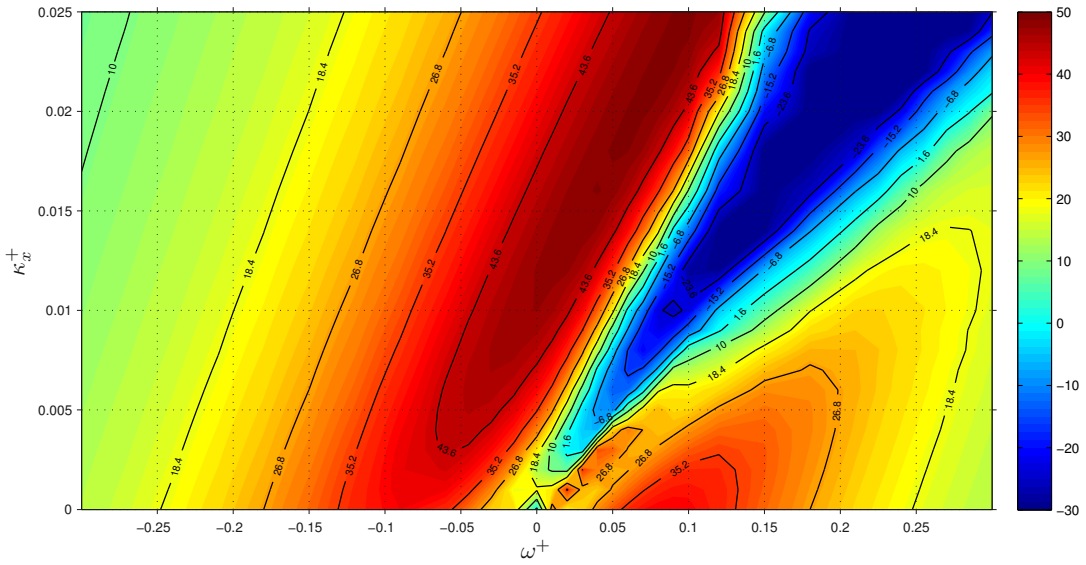

Figure 5.52: Contour plot of linearly scaled amplification measure change ϵ for μ_{N2} over actuation parameter space (ω^+, κ_x^+), as calculated using the linearized Navier-Stokes equations for a TBL at $Re_\tau = 5000$, and using $I_{2,w}$ as EM.

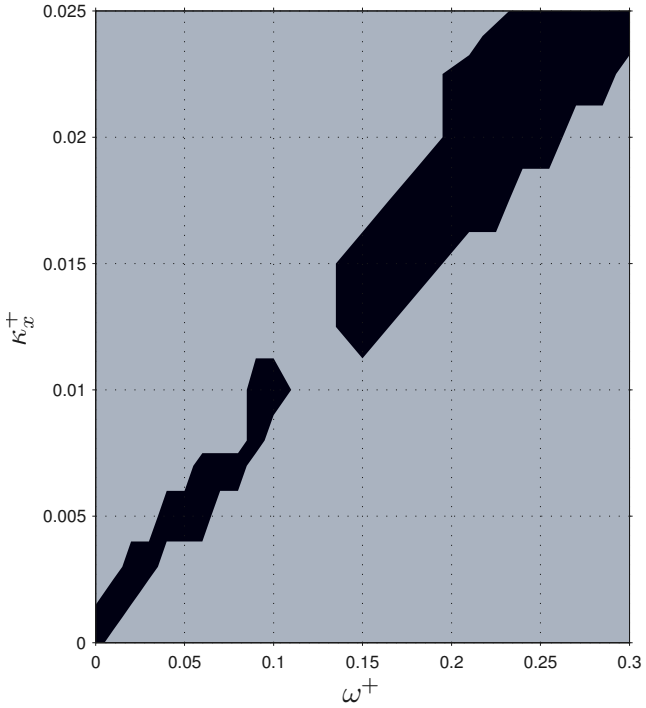

Figure 5.53: Regions of significant streak amplification ($> 50\%$) occurring over long time scales ($\tau_t^+ = 300$) due to streamwise-travelling wave actuation. Results generated for streamwise dependent condition $I_{2,w}$. Contour plot produced over a reduced actuation parameter space (ω^+, κ_x^+) of percentage change in streak amplification (ϵ) using maximum values of μ_1 for perturbation evolving at $\lambda_y^+ = 172.0$, as calculated by the LNSE-LOM-system. Results for a TBL at $Re_\tau = 5000$.

5.4 Conclusions

The most important conclusion to be drawn from the results presented in this chapter is that the main features of the drag-reduction/drag-increase map obtained by DNS ([57]) and shown in figure 5.21 are somehow contained within the linearized Navier-Stokes equations, in combination with the prescribed mean base flow here considered. The degree of success achieved by the formulation here adopted and implemented can be gauged by the general agreement obtained with results reported in experimental and DNS studies. For instance, as in DNS studies, an optimal oscillation frequency of period $T^+ \approx 100$ was found for the pure oscillating wall, in different control maps, with different excitation mechanisms and at different flow conditions. This response of the LNSE-LOM-system, under the action of spanwise oscillation, was fairly insensitive to the streamwise variation of the EM, which suggests that the three-dimensionality of the perturbation does not play an important role in the response to this type of flow control.

It has been found that two clearly distinct responses are exhibited by the LNSE-LOM-system once a flow control based on spanwise oscillation is applied. Firstly, for optimal perturbations developing at optimal spanwise scales λ_y^+, there is reduction in the streak intensity, which is present almost immediately after the application of the control. Owing to the time scales involved, most of the simulations were performed with the spanwise oscillation permanently present. For this reason, it was possible to observe levels of measure reduction (MR) comparable to those of drag reduction (DR), at just $t^+ = 10$. Secondly, for some perturbations evolving at spanwise scales greater than the optimal λ_y^+, it was possible to observe the appearance of instabilities which, incidentally, were always detected in regions where drag increase is observed in the DR/DI map by DNS. On the assumption that the linearized nature of the LNSE-LOM-system plays a major role in the response of the perturbations to the flow control by spanwise oscillation, additional properties of the evolution of the near-wall structures, some of them being streaks, were investigated. Considering properties that might have a significant influence on the correlation between DR/DI and MR/MI, an additional set was investigated using the LNSE-LOM-system adopted here. One specific property of interest was the time-integrated maximum of wall-normal velocity. This particular property was found to produce, in comparison to DNS-based control maps, exceptionally well correlated LNSE-based control maps, producing a superior agreement than those generated with the streamwise perturbation energy. In any case, the physical significance of this, if any, is still unclear.

It is important to acknowledge that for models based on linearized Navier-Stokes equations, and in the absence of a spanwise oscillating profile, the wall-normal optimal perturbation velocity only decays in time. For this reason the level of agreement found between the DNS results and the LNSE-LOM-system results seems to suggest that there exists a link between certain STWSV (especially those with wave speed close to

$c^+ \approx 10$) and an additional generation of wall-normal perturbation velocity, compared to the uncontrolled case, appearing at the regions where DNS-based control maps show DI. It was found that for the measure μ_{N2} there is also a good correlation between zones of larger increase of its temporal integration and the turbulent drag-increase, and also between zones of reduced time-integrated change of $|w|$ and regions of turbulent-drag reduction. It seems then apparent that, at least from the linearized point of view, the enhancement or inhibition of skin-friction drag is somehow related to the generation or suppression of wall-normal perturbation velocity. In any case, the precise nature of such a correlation and the role of $|w|$ in streak growth suppression needs to be the subject of a more in-depth study.

Finally, a phenomenological mechanism has been proposed to explain the apparent good correlation between the LNSE-based control maps and the DNS-based control maps. In this mechanism, under the assumption that the lift-up effect is the major element in the conversion of energy between the mean base flow and the streamwise near-wall structures (like the streaks), the STWSV-control inhibits skin-friction drag by advecting wall-normal perturbation structures away from the wall, into the region where the gradient of the mean base flow is smaller compared to the gradient in the near-wall region, which in turn provokes a reduction of the intensity of the lift-up effect. This would prevent the formation of near-wall streaks of high intensity, reducing so the level of skin-friction drag. On the other hand, for those cases where a MI is observed (which correlate to those regions of DI in the DNS-based control map), structures of the wall-normal and spanwise velocities are retained within the near-wall region, which, under the same rationale, increase the lift-up effect, and consequently reinforcing the formation of streamwise structures, which eventually would lead to, in the full non-linear phenomenon, increase in the friction drag. In conclusion, these results and the correlation found, suggest that the drag increase observed in certain regions of parameter space is generated via a linear instability over a restricted spanwise range of disturbances, specifically in the range $120 < \lambda_y^+ < 330$, approximately. It is highlighted, however, that a more in-deep examination of this mechanism is required.

5.5 Chapter summary

A complete mathematical model incorporating the laminar spanwise oscillating velocity profile was first presented. Different considerations regarding the numerical methodology to generate such a spanwise profile were discussed; an semi-analytical (ansatz) approach was selected as model to get the spanwise velocity profile defined by the GSL. The results of a large set of numerical tests involving different Reynolds numbers, excitation mechanisms, and spanwise scales were shown and similarities assessed to a drag-reduction map obtained by Quadrio et al. [57] using DNS; correlation between properties of our LNSE-LOM-system and the skin-friction drag change due to flow-control was found.

Chapter 6

Summary, conclusions and future work

6.1 Summary

In this thesis a linearized formulation of the Navier-Stokes operator, originally proposed by Davies and Carpenter [71], has been employed to explore two main aspects: the generation of near-wall streaks in turbulent boundary layers and the response of turbulent wall-bounded flows to spanwise oscillations of the bounding walls. For the purposes of the present work, these spanwise oscillations are considered as a flow-control mechanism.

The mathematical model and the numerical implementation adopted in this work were thoroughly tested against Tollmien-Schlichting waves results and optimal perturbation theory. A good performance was found to be provided by both the mathematical and numerical models.

The treatment adopted here for the linearized Navier-Stokes equations, which decomposed the fluid flow into a mean base flow plus some small perturbations, is a stability-theory type approach. Notwithstanding, the approach followed in this thesis abandoned the normal mode analysis in favour of a viscous initial-value-problem approach. In this regard, a thorough review on the turbulent streak generation process was presented and the concepts of exponential growth, algebraic growth and viscous dissipation of small scale perturbations were linked to the concept of transient growth. From the discussion in §4 it was clear that it is adequate to perform an optimization process to find a suitable set of parameters for the Low-Order-Model (LOM) here

adopted.

Regarding the near-wall streak generation process, results of a number of numerical experiments, using a large set of options for the LOM, were discussed and presented for two types of sources, here referred to as Excitation Mechanisms (EM): a body-force concept and an initial condition concept. The complete set of linearized Navier-Stokes equations plus the definition of an optimization problem and the selection of an EM was denominated as a LNSE-LOM-system, with the label LOM indicating that the methodology here adopted is a Low-Order-Model for the streak generation mechanism. In both cases of EM, satisfactory results were obtained for the streak generation process in terms of their ability to predict experimentally expected optimal spanwise scales.

For the flow control study a laminar Generalized Stokes Layer, introduced by Quadrio and Ricco [55], is adopted as model of the streamwise modulated waves of spanwise wall oscillations, labelled as Streamwise Travelling Waves of Spanwise Velocity (STWSV); the main aim regarding this flow control technique was to assess the correlation, if any existed, between predictions obtained with DNS modelling and prediction from the LNSE approach followed in this work. Based on a number of arguments thoroughly discussed in §5.2 and §5.1, this flow was incorporated into the linearized formulation as part of the base profile. A numerical model was selected based on computational efficiency and numerical accuracy. The success of the results presented later in §5 suggests the adequacy of the arguments and assumptions asserted in the construction of the mathematical and numerical models.

Finally, employing near-optimal initial conditions as EM for the LNSE-LOM-system an ample set of numerical experiments were conducted to evaluate the response of the linearized Navier-Stokes equations to the flow excitation of a spanwise oscillating wall. By comparing the results for the control maps, defined over an actuation parameter space ($\omega^+ - \kappa_x^+$), obtained with the linearized approach adopted here against the drag-reduction map obtained by DNS in other studies, it was possible to assess the relationship between streak evolution and disruption of the skin-friction drag. A good correlation between these responses was found for different properties of the near-wall streak.

The main and most relevant conclusions drawn from this study are presented below. Some suggestions about interesting new routes of work, based on the results contained in this document, are presented immediately after the conclusions.

6.2 Conclusions and additional considerations

Mechanisms of generation of streaks

The LNSE-LOM-system (adopted in this work) was able to reproduce two of the main types of growth mechanism: exponential and transient. The exponential growth was, for instance, successfully employed in the verification tests of code validation presented in §3.5. The transient growth mechanism was consistently dominant in the majority of the numerical tests on mechanisms of streaks generation, presented in §4.4.

In the LNSE model adopted here, in a similar fashion to others of a similar kind, an excitation mechanism is required. However, a question remains: does this excitation mechanism need to meet a specific property in order to predict near-wall structures resembling those experimentally observed? Aiming to address this point, two common methodologies of excitation, referred to as excitation mechanisms (EM), were examined: streak generation by a body-force and streak generation by prescription of an initial condition. Both methodologies showed successful generation of streaks, i.e. production of extended regions of streamwise perturbation velocity. However, also in both cases, the results showed that depending upon the selection of parameters, the response of the system could exhibit different responses in terms of transient growth. This clearly indicates that, as maybe subtly inferred by other previous works, the type of excitation used in linearized systems plays an important role in the characterization of the linear operator, although in terms of the production of streak-like regions, it could be argued that the system of LNSE is fairly independent of the excitation mechanism (EM), and a certain degree of natural selectivity is present in the LNSE operator.

Another extremely important facet in the present study, as in most works on short-term disturbances, was the selection of a norm to gauge the perturbation growth and therefore the streak intensity. A wide set of properties were considered to explore the implications of the selection of a given measure. Two main categories of measures were defined: global volumetric measures, tracking the evolution of structures over the entire domain, and planar localised measures, related with the development of structures at specific planes from the wall. In turn, these sets of measures were largely based on maximum streamwise momentum or total kinetic energy, both defined using perturbation fields. In any case, it has been a matter of speculation as to which type of measure is most suitable for the characterization of near-wall streaks. The results presented in 4.4 showed that, in fact, the linearized system was able to predict expected experimental features of near-wall structures, like the optimal spanwise spacing of streaks, using a wide set of combinations of measures and excitation mechanisms. This could explain the large amount of different measures used in this type of study which successfully offer valid predictions; two particular examples, different from the combination selected in this study, were presented: a body force as EM with a global streamwise momentum measure, and a prescribed

initial condition as EM with a global kinetic energy measure. Nevertheless, similarly to as briefly mentioned before for the type of EM, it cannot be argued that the response of the linearized NS operator, in terms of experimentally observed features of the near-wall streaks, is completely independent of such a selection of measure, and therefore a correct combination of measure and excitation mechanism needs to be found.

Evidently, the need to use a correct combination of an EM and a measure is a tuning. In any case, it was shown that regardless of the combination of EM and type of measure selected, an optimization process should be accomplished to bring about coherent values for the parameters defining a given excitation mechanism (EM). This is because the definition of the optimization problem is itself part of the system framework (as exemplified above for the case of OP). Four different definitions of the optimization problem were explored. In all cases considered, it was always possible to find a combination of measure, EM and optimization problem definition, that provided good correlations with experimentally expected results. This is arguably necessary in order to gauge the scope of validity of the LNSE-LOM-system model.

In light of the results from the numerical tests on near-wall streaks generation, and observing the different optimization and response maps obtained, it seems apparent that there exists a certain selectivity of the LNSE operator, although not one that will bring about experimentally observed streak scales without a tuning process. However, in the present work, such a tuning was easily obtained by performing optimization, which in the present work required: the selection of a functional excitation mechanism (EM), the selection of a measure, and, obviously, the search of an optimization problem, even as a Low Order Model (LOM in the present case), in terms of planar or volumetric measures. For the sake of simplicity, such a selection, in the present study, has been referred to as the LNSE-LOM-system. Following this methodology it was always possible to find EM parameters to make the response of the linearized system, regardless of the type of EM selected, to exhibit an optimum at around $\lambda_y^+ = 100 \pm 30$, and present in the region at $z^+ = 17 \pm 5$, for most of the different measures explored. In this sense the selection of 'almost' any type of LOM provided accurate results, although only if empirically tuned via the definition of the optimization problem. In any case, the versatility of the LOM adopted in this works was tested by using initial conditions requiring a reduced set of parameters to calibrate (e.g. the forcing time being one such parameter eliminated).

Particularly, excitation models defined by the optimization over visualization planes, specially with the measures μ_1 or μ_2 (introduced in 4.2), showed consistency and regularity defining the LOM. Optimal conditions found with this combination of LOM and measures provided results in good agreement with the expected range of values, as experimentally reported, in terms of optimal spatial scales. This type of optimization problem resembles the GOP defined in [64], where it has been argued that the optimization over visualization planes fits better into the optimal perturbation problem, for instance allowing direct comparisons against experimental

observations of near-wall streaks which, in any case, have usually been taken at fixed locations in the wall-normal direction.

Examining the different optimization maps obtained by optimization of local planar measures, and considering their success, again, in terms of expected spatial scales prediction for the optimal perturbation attained, even for different EMs, it seems evident that these measures are a preferred candidate when a LNSE-LOM-system is being defined. An explanation as to their apparent advantage over other measures can be argued to be associated with the effect of these measures over the optimisation process. By restricting attention to a given visualization plane, these measures effectively constrain the feasible optimization space, at least in comparison to the global volumetric measures, focusing on specific wall-normal regions, where specific spanwise scales and evolution time periods of the near-wall streaks are expected. It seems thus apparent that this is the key point in the success of those optimization problems, using the planar measures, to produce coherent structures bearing the most important features of the experimentally observed near-wall streaks. Nevertheless, the scope of this work precluded a more precise account of the implications of the selection of this kind of measures.

In summary, considering that the characteristic transient growth of the near-wall streaks can be linked to the non-normality of the linearized Navier-Stokes operator, it might be that an optimization definition is simply a way to adjust or tune the degree of non-normality exhibited by the LNSE operator, and therefore to provide suitable conditions (i.e. the parameters of the EM) for the lift-up effect to act strongly. In this manner, although there is still a degree of selectivity of the LNSE operator, this is enhanced by the optimization process, allowing to attain predictions of near-wall streaks spatial and temporal evolution in a fairly good agreement with experimentally observed values.

On the basis of the results obtained for the streak generation mechanisms, the initial conditions $I_{1,w}$ and $I_{2,w}$ were chosen as EM for the numerical experiments on flow control by spanwise oscillations presented and discussed in §5.3. For the majority of the numerical experiments on flow control, the selected parameters of the EM were attained by maximising the planar measure μ_1 using the optimization problem Type-II (introduced in 4.3.1).

Flow control by spanwise oscillations

The flow control technique targeted in the present study, and explored using the linearized approach, was the introduction of spanwise oscillations, modulated in the streamwise direction and time, of the wall bounding a turbulent flow. This technique has been named as the Streamwise Travelling Waves of Spanwise Velocity, or simply named as the STWSV or the STWSV-control. Its formulation was introduced in chapter § 5, where

also a complete account of the numerical experiments performed to assess this technique, from a linearized point of view, was presented.

With basis on the results obtained in this work and fully detailed in §5.3, it is clear that the main features of the drag-reduction/drag-increase control map obtained using DNS by Quadrio et al. [57] are somehow contained within the linearized Navier-Stokes operator including the control as an additional component of a prescribed mean base flow. The degree of success achieved by the formulation adopted here was evaluated in terms of general agreement with specific features of the DR/DI control map produced by DNS studies; one of these features being the correct prediction of an optimal oscillation frequency of period $T^+ \approx 100$, which was found for the case of a pure oscillating wall, akin to the DNS results. This and other features were replicated in different control maps obtained for the two different excitation mechanisms selected and at different flow conditions.

Nevertheless, it should be noted that predictions made for engineering purposes, as for aerospace applications, using the linear model presented in this work, will always require some form of semi-empirical calibration of the linearized model in order to be reliable. In the present case this calibration was carried out essentially in terms of the LNSE-LOM-system optimization. For instance, as described in §4.4 and summarised above, the parameters of the initial conditions employed as EM in the flow control study were obtained by maximization of μ_1 over the entire simulation time (i.e. problem $\{$Type-II,$\mu_1\}$) and at a visualization plane of $z_v^+ \approx 12$. The relative success in capturing features of the flow control technique explored, using these parameters, is itself an example of the adequacy of this approach.

Although the selection of optimization problem was a key element in the construction of the LNSE-based control maps, the response of the LNSE-LOM-system under the action of spanwise oscillation was fundamentally insensitive to the streamwise variation of the EM. This suggests that the three-dimensionality of the perturbations does not play an important role, if any, in the general response of the linearized Navier-Stokes operator to this type of flow control, i.e. the spanwise oscillations.

Regarding the parameters of the spanwise oscillations wave an exploration was performed to asses the impact of the wave phase in the development of the perturbation under control. A phase angle was defined in terms of two distinctive parameters: the initial spatial location of the perturbation and the time instant at which the control is switched on, here labelled as control activation time. Results of the numerical experiments clearly indicated that the relative position between different points of the wave and the centre of the perturbation played a major role in the development of the controlled perturbation, affecting the possible control scenario. In order to account for this effect, a phase averaging process was always implemented for the main set of numerical tests on flow control. On the other hand, through a 'thought experiment', presented and discussed

in § 5.3.3, the influence of the wave's transient build-up period on evolution of the perturbations was evaluated. Results of this experiment showed that if an inhibitory action exists due to the control being applied, this action occurs at early stages in the development of the streak, i.e. at the perturbation algebraic growth stage, whereas if a streak (or near-wall structure) enhancement is set by the control, this will occur at the later dissipative stage. Apart from these two observations, there was not possible to appreciate any significant change on the evolution of the control perturbation due to the control activation time, which seems to suggest that this is irrelevant to the near-wall structure control process. Nevertheless, it should be noted that this was a pure theoretical exercise as such a situation, a sudden appearance of spanwise oscillating velocity without any transient build-up, is not possible to occur.

The results of the main core of numerical experiments presented in chapter § 5 showed evidence of two well distinct responses of the LNSE-LOM-system to the flow control based on spanwise oscillations. Firstly, when the perturbations evolved at their optimal spanwise scale λ_y^+, there was always possible to see a reduction, for most of the control operational points (κ_x^+, ω), in the near-wall structures intensity. Secondly, for those structures evolving at spanwise scales greater than their optimal λ_y^+, it was also possible to observe the appearance of instabilities, defined as percentage change of the maximum streak intensity above 50%, which incidentally were always detected for those control points (κ_x^+, ω) laying in regions of the DNS-based control map where drag increase is obtained.

In those cases of perturbations evolving at their optimal λ_y^+, the effect of the flow control seems to be felt by the small perturbations almost immediately after their onset. In this work, and in accordance to the discussion presented in § 5.3.3, the STWSV-control was set to be permanently present during the evolution of the perturbation, and therefore the effect of the control was always observed to be evident at the early stages of its development. For instance, levels of measure reduction (MR) comparable to those of drag reduction (DR) were attained at early stages of the transient growth; control maps obtained at just $t^+ = 10$ had already some resemblance to the DR/DI map of DNS studies.

As mentioned above, for those perturbations modelled at higher values of spanwise spacing, compared to their optimal λ_y^+, a measure increase (MI) was observed at some control operational points (κ_x^+, ω), coinciding with those points associated to drag increase (DI) prediction in the DNS-based control maps. Although not thoroughly explored, this particular behaviour was seen for streaks developing at $2\,\lambda_{y,opt}^+ < \lambda_y^+ < 5\,\lambda_{y,opt}^+$, with $\lambda_{y,opt}^+$ being the optimal spanwise scale found by the respective LOM. This range corresponded to disturbances of about $120 < \lambda_y^+ < 330$, approximately.

In light of the similarities found between the control maps obtained here and the DR map by DNS, it was conjectured that a linear phenomenon plays a major role in the response to the flow control by spanwise

oscillation. With this assumption, it was also conjectured that additional measures of the linear streak response might also reflect similarities with the DNS results. Propelled by this rationale, other measures were investigated, though only results for two of them were presented. One specific measure of interest, not considered initially, was the integration in time of the maximum of wall-normal velocity. This particular measure was found to produce exceptionally good control maps (see figure 5.31b), giving an even better agreement with DNS results than those generated with the streamwise perturbation energy measure.

The level of correlation found between control maps (LNSE-based map vs DNS-based map) using the measure μ_{N2}, introduced in § 5.3.6, suggests that there might exist a causal link between the flow condition induced by certain streamwise travelling waves of spanwise velocity, particularly those having a wave speed around $c^+ \approx 10$, and the generation of wall-normal perturbation velocity. Using this measure, which is defined with basis on the time integral of $|w|$, there was possible to obtain a strong correlation between zones of larger increase of the percentage of change of measure in the LNSE-based maps and the turbulent drag-increase regions of the DNS-based control maps. A correlation was also observed between zones of reduced time-integrated change of $|w|$ and regions of turbulent-drag reduction. It thus seems apparent that the enhancement or inhibition of skin-friction drag, caused by the spanwise oscillations control, is somehow related to the generation or suppression of wall-normal perturbation velocity, particularly in the near-wall region ($z^+ < 30$). However, the precise nature of such a correlation, and the role of $|w|$ in streak growth suppression needs to be the subject of a more in-depth study.

It is in general accepted that the 'lift-up' effect is a major element of the streak generation process due to its importance in the dynamics of the fluid, especially in the near-wall region where, usually, the shear or gradient of the mean streamwise velocity is higher than in other parts of the flow; this lift-up effect is in general dictated by the term $w\,dU/dz$, with w being the wall-normal velocity. Taking into account this fact, and given the good correlation described before (found by using $|w|$), it thus seems plausible to propose, at least phenomenologically, a mechanism that explains the agreement between control maps for the two different responses exhibited by the LNSE-LOM-system to the flow-control. For instance, in those control cases where the spanwise oscillation produces, holds and/or retains structures of wall-normal perturbation velocity in the vicinity of the wall, the lift-up term might be enhanced producing thus a high level of generation of additional streamwise perturbation velocity structures, which then would not undergo the normal path of viscous decay, but instead start to grow and get intensified as they evolve in time, due precisely to the constant transfer of momentum produced by the $w\,dU/dz$ term. In our study, when perturbation velocity structures get an amplification above 50% with respect to the uncontrolled case, they are considered (labelled) as instabilities. The phenomenon of intensification of the near-wall structures would then be perceived as an increase of the skin-friction drag, which would be equivalent to the appearance of instabilities, especially in terms of the

streamwise momentum. Therefore, such an increase of the streamwise perturbation velocity, in a real-case scenario, can be associated to an increase of the skin-friction drag. Let now extend the phenomenological mechanism to consider the cases producing measure reduction, i.e. cases that correlate to drag reduction in DNS studies. In these cases, the flow control induces an 'accelerated' advection, as compared to the uncontrolled case, of the near-wall structures which are then drifted away from the wall. Among those advected structures are, obviously, the wall-normal perturbation velocity structures. This allow to construct a second part of the proposed mechanism: when the STWSV-control advects structures away from the wall, the final outcome of this situation would be a general reduction of the 'lift-up' effect, and therefore an inhibition of the streamwise perturbation velocity structures. This reduction in the production of streamwise perturbation velocity structures in a real-case scenario would be, to a certain degree, equivalent to a reduction of the skin-friction-drag. Under this rationale, as proposed in this simple mechanism, the correlation between regions of MR with those of DR, as well as the correlation between regions of MI with those of DI, is seemingly obvious. However, the proposed mechanism holds true only for those perturbations evolving at spanwise wavelengths greater than their optimal λ_y^+, where the observations described in the proposed mechanism were ascertained in a number of different numerical tests.

Aiming to examine even further the validity of the phenomenological control mechanism (discussed above), a series of tests were conducted to examine the spatio-temporal evolution, in the wall-normal direction, of the structures evolving in certain controlled cases. Results of these numerical experiments effectively showed that one of the main effects of the STWSV in cases producing amplification of the intensity of the perturbation structures is to keep structures of wall-normal perturbation velocity closer to the wall. As conjectured previously, the result of the flow-control in those cases was the augmentation of the level of streamwise perturbation velocity structures appearing in the near-wall region. This phenomenon was ascertained to occur within the buffer region of the boundary layer, i.e. below $z^+ < 30$. Equally, for those cases where the STWSV-control seems to produce measure reduction, it was possible to observe that, in general, all the perturbation velocity structures, including the wall-normal component, were advected upwards away from the wall, certainly at a much earlier stage in comparison with the uncontrolled case. Again, the second part of the proposed mechanism seems to hold true, as effectively a reduction of activity of the near-wall perturbation structures may be associated to the skin-friction reduction observed in DNS for these experiments. Nevertheless, the proposed phenomenological mechanism hereby proposed remain just an speculation which has to be explored in more depth.

Finally, it is noteworthy that the results of the numerical experiments, along with the correlation found between a LNSE-based control map and the DNS-based control map, suggest that the drag increase obtained in certain regions of the control parameter space is generated via a linear instability which occurs on disturbances evolving

over a restricted range of spanwise wavelengths, specifically in the range $120 < \lambda_y^+ < 330$, approximately.

6.3 Future work

Some exciting paths of future work, based on the outcomes of this work, have already been suggested above. The fact that results obtained with a linear approach replicate findings obtained by fully non-linear methodologies, like DNS, is itself attractive as to what degree this linear nature is present in the near-wall dynamics of turbulent flows. This reinforces the idea of a linear phenomena underlying and somehow dictating the turbulence dynamics, at least in the very near-wall region. It would be interesting to fully elicit such a relationship.

Regarding the mechanisms of streaks generation, it would be interesting to find additional flow properties, maybe based on turbulent statistics, to improve the degree of correlation between turbulence near-wall structures and the dynamics inherent to linear approaches. However, it should be kept in mind that this could be considered as an additional fitting. For the moment, it seems that only two main features are available to judge the quality of a particular perturbation: the optimal spanwise scale and the wall-normal trend of this spanwise spacing. Additional information on the characteristics of the near-wall turbulence is then required to assist, for instance, the selection of the optimization problem to be used in linearized approaches, like the LNSE-LOM-system adopted in this work. An immediate upshot of improving this correlation is that more reliable predictions could be achieved with the simpler and more computationally efficient linearized approaches.

Although promising results have been presented in this thesis, most of the observations have been phenomenological. There is still a great degree of ignorance as to the exact cause of the skin-friction reduction/increase when spanwise wall oscillations are imposed to turbulent flows. It is still also unclear how the skin friction is associated with the turbulent boundary layer. It is evident that, although a clear relevance of the linear nature has been highlighted, additional work is required to fully explain the intricate relationships arising in the dynamics of the near-wall turbulence.

In this work it was found that an instability appears, producing in some cases unbounded growth, for some specific combinations of the operational parameters for STWSV, at spanwise scales greater than $\lambda_{y,opt}^+$, but with some upper limit. Interestingly, the operational points for which this behaviour was observed always coincided with the region where drag increase was observed by DNS studies. This phenomena was not further explored in this work. It seems then that, given the correlation between instabilities and drag-increase, it is worth investigating the nature of the phenomenon, and the implications for engineering applications of this

kind of flow control.

Linearized approaches to the turbulence problem have the distinctive advantage of being computationally faster than some other numerical techniques. For instance, the computing time required in this work to fully construct a single control map in the case of spanwise oscillations, using approximately 600 different operational points, was of the order of $4 \sim 5$ hours, measured in wall-time clock, with a FORTRAN 90 code running on 12 cores of a standard HPC machine at present time (X86-64 Intel Xeon X5650 at 2.66 GHz). Additionally, results in this thesis are strong evidence of the important role played by linearity in the near-wall turbulence. Combining these two ideas, it would be worth exploring a hybrid numerical method involving fully non-linear calculations alongside linear estimations. Such hybrid methodology could be either in terms of exploiting temporal scale separation, or spatial scale separation, between the linear and non-linear phenomena. In any case, the main target would be to exploit the faster and improved performance of a linear solver along with a computationally intensive, but more accurate, non-linear model.

Maybe many more possibilities of future developments are hidden within the results of this work. The author of this thesis sincerely hopes that the explanations, discussion and results presented throughout this document can help any reader to expand the findings and ideas contained within.

Appendices

Appendix A

Error analysis of the Generalized Stokes Layer (GSL) profiles

The spanwise velocity profiles employed in chapter § 5 as GSL profiles were obtained using three different numerical approximations. A simple comparison of the general qualities of such profiles was presented in § 5.2.4. However, in order to select the most appropriate numerical approximation for the streak control study, an analysis of the accuracy and error of these approximations is required. Since there is not an 'exact' solution available to perform a more acute study of the quality of the profiles, a simple analysis of residuals of the numerical methodologies for the momentum equation (5.15) was performed. Isolating the GSL solvers, a number of numerical tests generating only GSL profiles have been performed, storing the nodal values for all the time steps. With the information of the GSL profiles for nodes in space and time, an evaluation on how well these nodal values fit in the GSL momentum equation is performed.

A nodal residual $R_{\epsilon,i}$ can be defined as

$$R_{\epsilon,i} = \frac{1}{Re_{\delta_*}} - \frac{\delta^t V_i + U_i \, \delta^x V_i}{\delta^{xx} V_i + \delta^{zz} V_i} \tag{A.1}$$

where V_i and U_i are nodal values for the spanwise and streamwise base flows, and operators δ^{α} and $\delta^{\alpha\alpha}$ represent numerical partial derivatives, of first and second order respectively, in a generic direction α. In the three cases, for the purposes of this accuracy analysis, schemes with spectral resolution were used to compute the derivatives required in equation (A.1). This residual, theoretically, should be equal to zero if an exact set of nodal values exist in the vicinity of a node i. Here, an estimator of the level of deviation from an exact

solution, at each computational time step, is defined as

$$\epsilon(t) = \max_{\Omega} \frac{|R_{\epsilon,i}|}{Re_{\delta_*}} \tag{A.2}$$

where Ω is the two-dimensional domain over which a set of nodal residuals exist. The normalization by Re_{δ_*} is arbitrary but intended to allow a valid comparison for different regimes.

A number of simulations were performed for domains of size $L_x^+ = 400.0$ for TBLs at $Re_{\delta_*} = 10000$ and 5000. In all the cases the number of grid points in wall-normal and streamwise directions was kept constant ($N_z = 128$, $N_x = 501$). Total simulation time was set to $t_\tau^+ = 200.0$. Figure A.1 shows the evolution in time of the error estimator ϵ defined in equation (A.2), for the three different methodologies. Examining this plot it is evident two different aspects: firstly, the strikingly accuracy of the ansatz solver proposed, which is almost three orders of magnitude better than the other two approaches; and secondly, it is now evident that, although subtle, there is a degradation in time of the accuracy of the solution obtained with the numerical scheme; even so, the level of accuracy of the spectral-FD solver is comparable to that obtained with the analytical model first proposed. In any case, regarding the detailed quality of the profiles, it is clear that the ansatz solver performs outstandingly.

A final evaluation is related to the computational time consumed by each solver. In figure A.2 it is shown the computational time consumed by each solver, for the different numerical simulations, including both regimes ($Re_{\delta_*} = 5000, 10000$). Surprisingly, the analytical solver was the more expensive one in terms of computational time. This indicates that the subroutine chosen to perform the Airy function computation is costly, compared with the other GSL solvers. However, also in this test the ansatz solution arises as the most favourable option to perform the numerical estimation of the GSL profiles.

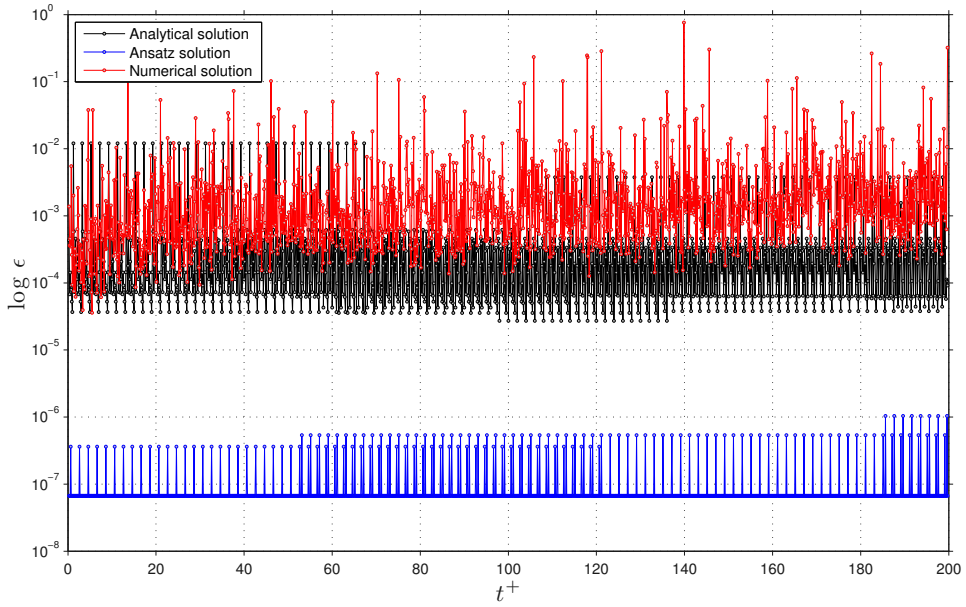

Figure A.1: Evolution of the error estimator ϵ in time; comparison between the GSL velocity profile, at $Re_{\delta_*} = 1 \times 10^4$, computed via (i) Analytical solution, (ii) Ansatz solution, and (iii) Numerical solution using our own code, for a STWSV with $c^+ = 2.0$. GSL distribution for $Re_{\delta_*} = 1 \times 10^4$, $A^+ = 12.0$, $\kappa_x^+ = 0.06$, $\omega^+ = 0.12$

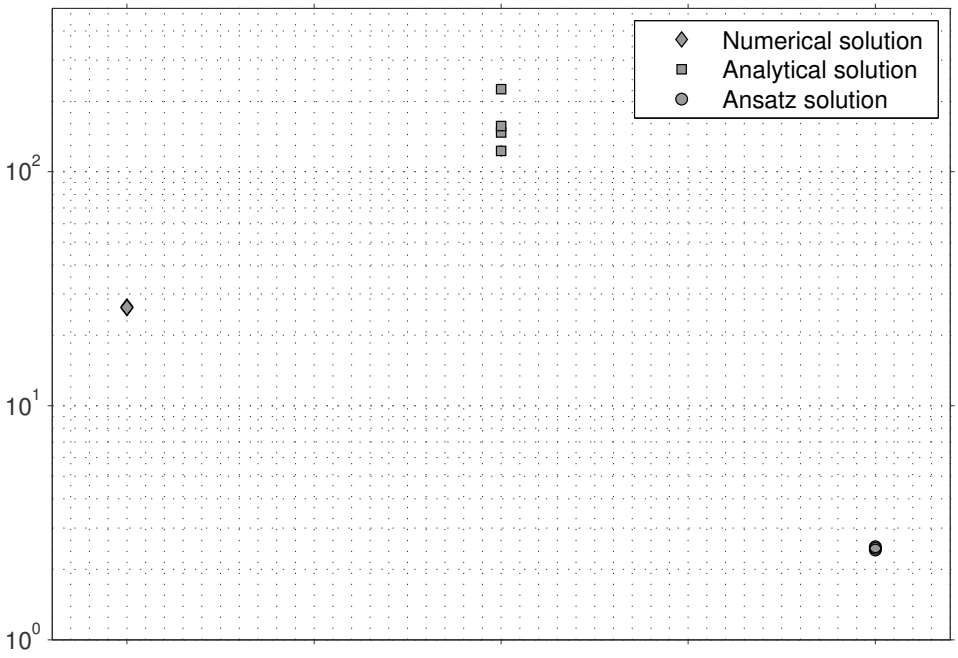

Figure A.2: Comparison of computational times consumed, in different numerical tests, for GSL estimation using (i) Analytical solution, (ii) Ansatz solution, and (iii) Numerical solution. Simulations performed for GSL at $Re_{\delta_*} = 5000$ and 10000

Appendix B

Numerical solution of Falkner-Skan equation using third-order and high-order-compact finite difference schemes

Appendix C

Modelling turbulent skin-friction control using linearized Navier–Stokes equations

Bibliography

[1] P. Carpenter, K. Kudar, R. Ali, P. Sen, and C. Davies. A deterministic model for the sublayer streaks in turbulent boundary layers for application to flow control. *Phil. Trans. R. Soc. A*, 365(1859):2419–2441, 2007. doi: 10.1098/rsta.2007.2016. URL http://journals.royalsociety.org/content/2h8845j2863grj82.

[2] P.W. Carpenter and E.L. Houghton. *Aerodynamics for Engineering Students*. Butterworth-Heinemann, Oxford, UK, 2003.

[3] C. Härtel and L. Kleiser. Analysis and modelling of subgrid-scale motions in near-wall turbulence. *Journal of Fluid Mechanics*, 356(-1):327–352, 1998.

[4] J.P. Bonnet. General Concepts on Structure Identification. In *Eddy Structure Identification; Series: CISM International Centre for Mechanical Sciences, Italy, May 23-26, 1994. Wien and New York, Springer-Verlag, 1996, p. 1-59*, pages 1–59, 1996.

[5] S.K. Robinson. A review of vortex structures and associated coherent motions in turbulent boundary layers. In *Structure of turbulence and drag reduction; Proceedings of the IUTAM Symposium, Zurich, Switzerland, July 25-28, 1989 (A91-55626 24-34). Berlin and New York, Springer-Verlag, 1990, p. 23-50. Research supported by USAF and U.S. Navy.*, pages 23–50, 1990.

[6] J. Kim. Second iutam symposium on structure of turbulence and drag reduction. In N.S. Berman and J.L. Zakin, editors, *Structure of Turbulence and Drag Reduction*, pages 600–604, IUTAM Symposium Zurich, Switzerland, July 1989. International Union of Theoretical and Applied Mechanics, Springer-Verlag.

[7] M.T. Landahl. Boundary layer turbulence regarded as a driven linear system. *Physica D: Nonlinear Phenomena*, 37(1–3):11 – 19, 1989. ISSN 0167-2789. doi: 10.1016/0167-2789(89)90113-9. URL http://www.sciencedirect.com/science/article/pii/0167278989901139.

[8] R.O. Kiesow and M.W. Plesniak. Near-wall physics of a shear-driven three-dimensional turbulent boundary layer with varying crossflow. *Journal of Fluid Mechanics*, 484(-1):1–39, 2003. doi: 10.1017/S0022112003004178.

[9] R. Adrian. Hairpin vortex organization in wall turbulence. *Physics of Fluids*, 19:041301, 2007. doi: 10.1063/1.2717527.

[10] S. Jakirlic and K. Hanjalic. A new approach to modelling near-wall turbulence energy and stress dissipation. *Journal of Fluid Mechanics*, 459(-1):139–166, 2002. doi: 10.1017/S0022112002007905.

[11] C. Baudet, O. Michel, and J.W. Williams. Detection of coherent vorticity structures using time-scale resolved acoustic spectroscopy. *Physica D: Nonlinear Phenomena*, 128(1):1–17, 1999. doi: 10.1016/S0167-2789(98)00321-2.

[12] A. M. Savill and J. C. Mumford. Manipulation of turbulent boundary layers by outer-layer devices: skin-friction and flow-visualization results. *Journal of Fluid Mechanics Digital Archive*, 191(-1):389–418, 1988. doi: 10.1017/S0022112088001624.

[13] M. Asai, M. Nishioka, and M. Minagawa. The instability and breakdown of a near-wall low-speed streak. *Journal of Fluid Mechanics*, 455(-1):289–314, 2002. doi: 10.1017/S0022112001007431.

[14] T. Theodorsen. Mechanism of turbulence. In *Proc. 2nd Midwestern Conf. on Fluid Mech., Ohio State University*, Columbus, Ohio, 1952.

[15] S.J. Kline, W. Reynolds, F.A. Schraub, and P. W. Runstadler. The structure of turbulent boundary layers. *Journal of Fluid Mechanics*, 30:741–773, 1967. doi: 10.1017/S0022112067001740.

[16] C. R. Smith and S. P. Metzler. The characteristics of low-speed streaks in the near-wall region of a turbulent boundary layer. *Journal of Fluid Mechanics Digital Archive*, 129(-1):27–54, 1983. doi: 10.1017/S0022112083000634. URL http://journals.cambridge.org/action/displayAbstract?fromPage=online&aid=376167&fulltextType=RA&fileId=S0022112083000634.

[17] M. T. Landahl. On sublayer streaks. *Journal of Fluid Mechanics Digital Archive*, 212(-1):593–614, 1990. doi: 10.1017/S0022112090002105.

[18] M. Zacksenhouse, G. Abramovich, and G. Hetsroni. Automatic spatial characterization of low-speed streaks from thermal images. *Experiments in Fluids*, 31:229–239, 2001. ISSN 0723-4864. URL http://dx.doi.org/10.1007/s003480100280. 10.1007/s003480100280.

[19] W. Schoppa and F. Hussain. Coherent structure generation in near-wall turbulence. *Journal of Fluid Mechanics*, 453(-1):57–108, 2002. doi: 10.1017/S002211200100667X.

[20] Y. Hwang and C. Cossu. Linear non-normal energy amplification of harmonic and stochastic forcing in the turbulent channel flow. *J. Fluid. Mech.*, 664:51–73, DEC 2010. ISSN 0022-1120. doi: {10.1017/S0022112010003629}.

[21] S. I. Chernyshenko and M. F. Baig. Streaks and vortices in near-wall turbulence. *Philosophical Transactions: Mathematical, Physical and Engineering Sciences*, 363(1830):1097–1107, 2005.

[22] J.M. Hamilton, J. Kim, and F. Waleffe. Regeneration mechanisms of near-wall turbulence structures. *Journal of Fluid Mechanics Digital Archive*, 287:317–348, 1995. doi: 10.1017/S0022112095000978. URL http://journals.cambridge.org/action/displayAbstract?fromPage=online&aid=353953&fulltextType=RA&fileId=S0022112095000978.

[23] J. Jiménez and A. Pinelli. The autonomous cycle of near-wall turbulence. *Journal of Fluid Mechanics*, 389:335–359, 1999.

[24] W. Schoppa and F. Hussain. Genesis and dynamics of coherence structures in near-wall turbulence. *Computational Mechanics Publications*, 1(Self-Sustaining Mechanisms of Wall Turbulence):385–422, 1997.

[25] S. Toh and T. Itano. Interaction between a large-scale structure and near-wall structures in channel flow. *Journal of Fluid Mechanics*, 524(-1):249–262, 2005. doi: 10.1017/S002211200400237X.

[26] S. Sanghi and N. Aubry. Mode interaction models for near-wall turbulence. *Journal of Fluid Mechanics Digital Archive*, 247(-1):455–488, 1993. doi: 10.1017/S0022112093000527.

[27] W. Schoppa and F. Hussain. Coherent structure dynamics in near-wall turbulence. *Fluid Dynamics Research*, 26:119–139(21), 2000. doi: 10.1016/S0169-5983(99)00018-0.

[28] W. Schoppa and F. Hussain. Formation of near-wall streamwise vortices by streak instability. *AIAA Journal*, 1998.

[29] A.E. Gill. A mechanism for instability of plane couette flow and of poiseuille flow in a pipe. *Journal of Fluid Mechanics*, 21(3):503–511, 1962.

[30] S.A. Orszag. Accurate solution of the orr-sommerfeld stability equation. *Journal of Fluid Mechanics*, 50(4):689–702, 1971.

[31] Z. Zhou. On the stability of distorted laminar flow(ii) - the linear stability analysis of distorted parallel shear flow. *Applied Mathematics and Mechanics*, 10(3):243–250, 1989.

[32] A.L. Braslow. *A history of suction-type laminar-flow control with emphasis on flight research*. In Monographs in aerospace history, no. 13. NASA History Division, Office of Policy and Plans, NASA Heaquarters, Washington, DC., 1999.

[33] P.W. Carpenter. Status of transition delay using compliant walls. In D.M. Brushnell, editor, *Viscous Drag Reduction in Boundary Layers*, volume 123 of *Progress in astronautics and aeronautics*, pages 79–113. AIAA, Washington, D.C., 1990.

[34] M. Gad-el-Hak. *Flow control: passive, active, and reactive flow management*. Cambridge University Press, Cambridge, UK, 2000.

[35] S.F. Tardu. Active control of near-wall turbulence by local oscillating blowing. *Journal of Fluid Mechanics*, 439:217–253, 2001. doi: 10.1017/S0022112001004542. URL http://journals.cambridge.org/abstract_S0022112001004542.

[36] M. Asai, Y. Konishi, Y. Oizumi, and M. Nishioka. Growth and breakdown of low-speed streaks leading to wall turbulence. *Journal of Fluid Mechanics*, 586(-1):371–396, 2007. doi: 10.1017/S002211200700688X.

[37] D. Lockerby. *Numerical simulation of boundary'layer control using MEMS actuation'*. PhD thesis, School of Engineering, The University of Warwick, March 2001.

[38] D. Lockerby, P.W. Carpenter, and C. Davies. Control of sublayer streaks using microjet actuators. *AIAA Journal*, 43(9):1878–1886, 2005.

[39] D.A. Lockerby, P.W. Carpenter, and C. Davies. Is helmholtz resonance a problem for micro-jet actuators? *Flow, Turbulence and Combustion*, 78(3):205–222, 2007. doi: 10.1007/s10494-006-9056-0. URL http://www.springerlink.com/content/u966rk46202262r9.

[40] M.J. Walsh and L.M. Weinstein. Drag and Heat-Transfer Characteristics of Small Longitudinally Ribbed Surfaces. *AIAA Journal*, 17:770–771, July 1979. doi: 10.2514/3.61216.

[41] M.J. Walsh. Turbulent boundary layer drag reduction using riblets. In V. Quan, S.F. Persselin, and T.T. Yang, editors, *AIAA, Aerospace Sciences Meeting*, jan 1982.

[42] W.E.. Reif and A. Dinkelacker. Hydrodynamics of the squamation in fast swimming sharks. *Neue Jahrb Geol Paläontol Abhandl*, 164:109–120, 1982.

[43] P. R. Viswanath. Aircraft viscous drag reduction using riblets. *Progress in Aerospace Sciences*, 38(6-7):571–600, 2002. ISSN 0376-0421. doi: 10.1016/S0376-0421(02)

00048-9. URL http://www.sciencedirect.com/science/article/B6V3V-479KFXM-5/2/d05a04bd4c4f41a25fba29ee4913fb9d.

[44] A.V. Johansson, P.H. Alfredsson, and J. Kim. Evolution and dynamics of shear-layer structures in near-wall turbulence. *Journal of Fluid Mechanics Digital Archive*, 224(-1):579–599, 1991. doi: 10.1017/S002211209100188X.

[45] S.-R. Park. *An experimental study of passive drag reduction in a turbulent boundary layer by a riblet surface*. PhD thesis, Maryland Univ., College Park., 1992.

[46] L. Sirovich and S. Karlsson. Turbulent drag reduction by passive mechanisms. *Nature*, 388:753–755, August 1997.

[47] K. Nourmohammadi, P.K. Hopke, and J.J. Stukel. Turbulent air flow over rough surfaces. II - Turbulent flow parameters. *ASME Transactions Journal of Fluids Engineering*, 107:55–60, March 1985.

[48] J. Jiménez. Turbulent Flows Over Rough Walls. *Annual Review of Fluid Mechanics*, 36:173–196, 2004. doi: 10.1146/annurev.fluid.36.050802.122103.

[49] J.H. Fransson, A. Talamelli, L. Brandt, and C. Cossu. Delaying Transition to Turbulence by a Passive Mechanism. *Physical Review Letters*, 96(6):064501–1–064501–4, feb 2006. doi: 10.1103/PhysRevLett.96.064501.

[50] A. Baron and M. Quadrio. Turbulent boundary layer over riblets: Conditional analysis of ejection-like events. *International Journal of Heat and Fluid Flow*, 18:188–196, April 1997. doi: 10.1016/S0142-727X(96)00087-2.

[51] K.-S. Choi. Drag reduction mechanisms and near-wall turbulence structure with riblets. In *Structure of turbulence and drag reduction; Proceedings of the IUTAM Symposium, Zurich, Switzerland, July 25-28, 1989 (A91-55626 24-34). Berlin and New York, Springer-Verlag, 1990, p. 553-560. Research supported by British Aerospace, PLC and Department of Trade and Industry of England.*, pages 553–560, 1990.

[52] K-S. Choi. Near-wall structure of a turbulent boundary layer with riblets. *Journal of Fluid Mechanics Digital Archive*, 208(-1):417–458, 1989. doi: 10.1017/S0022112089002892.

[53] K-S. Choi and B.R Clayton. The mechanism of turbulent drag reduction with wall oscillation. *International Journal of Heat and Fluid Flow*, 22(1):1–9, 2001. ISSN 0142-727X. doi: 10.1016/S0142-727X(00)00070-9. URL http://www.sciencedirect.com/science/article/pii/S0142727X00000709.

[54] M. Quadrio and P. Ricco. Initial response of a turbulent channel flow to spanwise oscillation of the walls. *Journal of Turbulence*, 4, 2003.

[55] M. Quadrio and P. Ricco. Critical assessment of turbulent drag reduction through spanwise wall oscillations. *Journal of Fluid Mechanics*, 521(-1):251–271, 2004. doi: 10.1017/S0022112004001855.

[56] G.E. Karniadakis and S.J. Sherwin. 8. algorithms for incompressible flows. *Spectral/hp Element Methods for Computational Fluid Dynamics*, 1:400–455(56), June 2005.

[57] M. Quadrio, P. Ricco, and C. Viotti. Streamwise-travelling waves of spanwise wall velocity for turbulentdrag reduction. *Journal of Fluid Mechanics*, 627:161–178, 2009.

[58] P. Ricco and M. Quadrio. Wall-oscillation conditions for drag reduction in turbulent channel flow. *International Journal of Heat and Fluid Flow*, 29(4):891–902, 2008.

[59] J.-I. Choi, H. J. Sung, and C.-X. Xu. Drag reduction by spanwise wall oscillation in wall-bounded turbulent flows. *AIAA Journal*, 40:842–850, May 2002. doi: 10.2514/2.1750.

[60] W.J. Jung, N. Mangiavacchi, and R. Akhavan. Suppression of turbulence in wall-bounded flows by high-frequency spanwise oscillations. *Physics of Fluids*, 4:1605–1607, August 1992. doi: 10.1063/1.858381.

[61] G.E. Karniadakis and Kwing-So Choi. Mechanisms on transverse motions in turbulent wall flows. *Annual Review of Fluid Mechanics*, 35(1):45–62, 2003. doi: 10.1146/annurev.fluid.35.101101.161213. URL http://www.annualreviews.org/doi/abs/10.1146/annurev.fluid.35.101101.161213.

[62] G.E. Karniadakis and S.J. Sherwin. 8. algorithms for incompressible flows. *Spectral/hp Element Methods for Computational Fluid Dynamics*, 1:400–455(56), Jun 2005. URL http://www.ingentaconnect.com/content/oso/1934890/2005/00000001/00000001/art00008.

[63] K.M. Butler and B.F. Farrell. Optimal perturbations and streak spacing in wall-bounded turbulent shear-flow. *Physics of Fluids a-Fluid Dynamics*, 5(3):774–777, 1993.

[64] S.I. Chernyshenko and M.F. Baig. The mechanism of streak formation in near-wall turbulence. *Journal of Fluid Mechanics*, 544(-1):99–131, 2005. doi: 10.1017/S0022112005006506.

[65] H.J.H. Clercx. A spectral solver for the navier-stokes equations in the velocity-vorticity formulation for flows with two nonperiodic directions. *Journal of Computational Physics*, 137:186–211(26), October 1997. doi: 10.1006/jcph.1997.5799.

[66] D.L. Young, Y.H. Liu, and T.I. Eldho. A combined bem-fem model for the velocity-vorticity formulation of the navier-stokes equations in three dimensions. *Engineering Analysis with Boundary Elements*, 24:

307–316(10), April 2000. doi: 10.1016/S0955-7997(00)00010-2. URL http://www.ingentaconnect.com/content/els/09557997/2000/00000024/00000004/art00010.

[67] M.F.M. Speetjens and H.J.H. Clercx. A spectral solver for the navier-stokes equations in the velocity-vorticity formulation. *International Journal of Computational Fluid Dynamics*, 19:191–209(19), March, 2005. doi: 10.1080/10618560412331283808. URL http://www.ingentaconnect.com/content/tandf/gcfd/2005/00000019/00000003/art00001.

[68] W.Z. Shen and T.P. Loc. Numerical method for unsteady 3d navier-stokes equations in velocity-vorticity form. *Computers and Fluids*, 26:193–216(24), February 1997. doi: 10.1016/S0045-7930(96)00040-0. URL http://www.ingentaconnect.com/content/els/00457930/1997/00000026/00000002/art00040.

[69] D.C. Lo, K. Murugesan, and D.L. Young. Numerical solution of three-dimensional velocity-vorticity navier-stokes equations by finite difference method. *International Journal for Numerical Methods in Fluids*, 47:1469–1487, Apr 2005. doi: 10.1002/fld.822.

[70] S.C.R. Dennis and J.D. Hudson. Methods of solution of the velocity-vorticity formulation of the navier-stokes equations. *Journal of Computational Physics*, 122:300–306(0), December 1995. URL http://www.ingentaconnect.com/content/ap/cp/1995/00000122/00000002/art01215.

[71] C. Davies and P.W. Carpenter. A novel velocity-vorticity formulation of the navier-stokes equations with applications to boundary layer disturbance evolution. *Journal of Computational Physics*, 172:119–165(47), September 2001. doi: 10.1006/jcph.2001.6817. URL http://www.ingentaconnect.com/content/ap/cp/2001/00000172/00000001/art06817.

[72] M. Togneri. *A high-order finite difference investigation of boundary layer perturbations*. PhD thesis, Cardiff University, 2010.

[73] C. Davies. Numerical simulation of boundary-layer disturbance evolution. *Philosophical Transactions: Mathematical, Physical and Engineering Sciences*, 363(1830):pp. 1109–1118, 2005. ISSN 1364503X. URL http://www.jstor.org/stable/30039636.

[74] C.G. Speziale. On the advantages of the vorticity velocity formulation of the equations of fluid-dynamics. *Journal of Computational Physics*, 73(2):476–480, DEC 1987. ISSN 0021-9991. doi: 10.1016/0021-9991(87)90149-5.

[75] G. Kawahara, J. Jiménez, M. Uhlmann, A. Pinelli, et al. The instability of streaks in near-wall turbulence. *Center for Turbulence Research, Annual Research Briefs*, pages 155–170, 1998.

[76] S.S. Joshi, J.L. Speyer, and J. Kim. A systems theory approach to the feedback stabilization of infinitesimal and finite-amplitude disturbances in plane Poiseuille flow. *J. Fluid Mech.*, 332:157–184, FEB 10 1997. ISSN 0022-1120.

[77] J. Kim and J. Lim. A linear process in wall-bounded turbulent shear flows. *Physics of Fluids*, 12(8): 1885–1888, 2000. doi: 10.1063/1.870437. URL http://link.aip.org/link/?PHF/12/1885/1.

[78] A. Asaithambi. Numerical solution of the Falkner-Skan equation using piecewise linear functions. *Appl. Math. and Comput.*, 159(1):267–273, 2004.

[79] A. Asaithambi. Solution of the falkner-skan equation by recursive evaluation of taylor coefficients. *J. of Comput. and Appl. Math.*, 176(1):203–214, 2005.

[80] T. Cebeci and H.B. Keller. Shooting and parallel shooting methods for solving the Falkner-Skan boundary-layer equation. *J. of Comput. Phys.*, 7(2):289–300, 1971. ISSN 0021-9991. doi: 10.1016/0021-9991(71)90090-8.

[81] A. Asaithambi. A second-order finite-difference method for the Falkner-Skan equation. *Appl. Math. and Comput.*, 156(3):779–786, 2004.

[82] C. Davies. *Evolution of Tollmien-Schlichting waves over a compliant panel*. PhD thesis, Department of Engineering, The University of Warwick, January 1995.

[83] M. Togneri and C. Davies. A high order finite-difference solver for investigation of disturbance development in turbulent boundary layers. *Computers and Fluids*, 46(1):472–478, 2011. ISSN 0045-7930. doi: 10.1016/j.compfluid.2010.12.008. URL http://www.sciencedirect.com/science/article/B6V26-51P9T54-5/2/14035e9e30893905667d4fb89cfe1220. 10th ICFD Conference Series on Numerical Methods for Fluid Dynamics (ICFD 2010).

[84] H Schlichting and K. Gersten. *Boundary Layer Theory*. Springer-Verlag, 2001.

[85] R. Ali and P. Carpenter. Klebanoff modes in boundary layers over compliant surfaces. *APS Division of Fluid Dynamics Meeting Abstracts*, pages A3+, Nov 2001.

[86] R. Jordinson. The flat plate boundary layer. part 1. numerical integration of the orr—sommerfeld equation. *Journal of Fluid Mechanics*, 43(04):801–811, 1970. doi: 10.1017/S0022112070002756. URL http://dx.doi.org/10.1017/S0022112070002756.

[87] V.G. Falkner and S.W. Skan. Some approximate solutions of the boundary-layer equations. *Phil. Mag.*, 12:865–, 1931.

[88] D. R. Hartree. On an equation occurring in falkner and skan's approximate treatment of the equations of the boundary layer. *Mathematical Proceedings of the Cambridge Philosophical Society*, 33(02):223–239, 1937. doi: 10.1017/S0305004100019575. URL http://dx.doi.org/10.1017/S0305004100019575.

[89] M. Hogberg and D. Henningson. Secondary instability of cross-flow vortices in falknercooke boundary layers. *Journal of Fluid Mechanics*, 368:339–357, 1998. URL http://dx.doi.org/10.1017/S0022112098001931.

[90] D. Coles. The law of the wake in the turbulent boundary layer. *Journal of Fluid Mechanics*, 1(02):191–226, 1956. doi: 10.1017/S0022112056000135. URL http://dx.doi.org/10.1017/S0022112056000135.

[91] A.J. Musker. Explicit expression for the smooth wall velocity distribution in a turbulent boundary-layer. *AIAA Journal*, 17(6):655–657, 1979. ISSN 0001-1452. doi: {10.2514/3.61193}.

[92] H. M. Nagib and K. A. Chauhan. Variations of von Kármán coefficient in canonical flows. *Physics of Fluids*, 20(10):101518, October 2008. doi: 10.1063/1.3006423.

[93] I. Marusic, B. J. McKeon, P. A. Monkewitz, H. M. Nagib, A. J. Smits, and K. R. Sreenivasan. Wall-bounded turbulent flows at high Reynolds numbers: Recent advances and key issues. *PHYSICS OF FLUIDS*, 22(6), JUN 2010. ISSN 1070-6631. doi: {10.1063/1.3453711}.

[94] D. B. Spalding. A single formula for the "law of the wall". *Journal of Applied Mechanics*, 28(3):455–458, 1961. doi: 10.1115/1.3641728. URL http://link.aip.org/link/?AMJ/28/455/1.

[95] H.M. Nagib, K.A. Chauhan, and P.A. Monkewitz. Approach to an asymptotic state for zero pressure gradient turbulent boundary layers. *Philosophical Transactions of the Royal Society A: Mathematical, Physical and Engineering Sciences*, 365(1852):755–770, 2007. doi: 10.1098/rsta.2006.1948. URL http://rsta.royalsocietypublishing.org/content/365/1852/755.abstract.

[96] G.D. Smith. *Numerical solution of partial differential equations: finite difference methods*. Oxford applied mathematics and computing science series. Clarendon Press, 1985. ISBN 9780198596509. URL http://books.google.co.uk/books?id=hDpvljaHOrMC.

[97] S. Rionero and G. Romano. *Trends and applications of mathematics to mechanics: STAMM 2002*. Springer, 2005. ISBN 9788847002692. URL http://books.google.co.uk/books?id=lBuEMSQvAg4C.

[98] C. Canuto. *Spectral methods: fundamentals in single domains*. Scientific computation. Springer, 2006. ISBN 9783540307259. URL http://books.google.co.uk/books?id=DFJB0kiq0CQC.

[99] P.S. Pacheco. *Parallel programming with MPI*. Morgan Kaufmann Publishers, 1997. ISBN 9781558603394. URL http://books.google.co.uk/books?id=GufgfWSHt28C.

[100] P Wesseling. von Neumann stability conditions for the convection-diffusion equation. *IMA J. Numer. Anal.*, 16(4):583–598, OCT 1996. ISSN 0272-4979. doi: {10.1093/imanum/16.4.583}.

[101] J Frank, W Hundsdorfer, and JG Verwer. On the stability of implicit-explicit linear multistep methods. *APPLIED NUMERICAL MATHEMATICS*, 25(2-3):193–205, NOV 1997. ISSN 0168-9274. doi: {10.1016/S0168-9274(97)00059-7}. Workshop on Innovative Time Integrators, CTR MATH & COMP SCI, AMSTERDAM, NETHERLANDS, OCT 30-NOV 01, 1996.

[102] P.J. Schmid and D.S. Henningson. *Stability and transition in shear flows*. Applied mathematical sciences. Springer, 2001. ISBN 9780387989853. URL http://books.google.co.uk/books?id=5eNoy2VdXo8C.

[103] J. Watson. On spatially-growing finite disturbances in plane poiseuille flow. *Journal of Fluid Mechanics*, 14(02):211–221, 1962. doi: 10.1017/S0022112062001172. URL http://dx.doi.org/10.1017/S0022112062001172.

[104] M. Gaster. On the generation of spatially growing waves in a boundary layer. *Journal of Fluid Mechanics*, 22(03):433–441, 1965. doi: 10.1017/S0022112065000873. URL http://dx.doi.org/10.1017/S0022112065000873.

[105] A. Michalke. On spatially growing disturbances in an inviscid shear layer. *Journal of Fluid Mechanics*, 23(03):521–544, 1965. doi: 10.1017/S0022112065001520. URL http://dx.doi.org/10.1017/S0022112065001520.

[106] Ira J. Walker, David S. Torain II, and Morris H. Morgan III. An eigenvalue search method using the orr–sommerfeld equation for shear flow. *Journal of Computational and Applied Mathematics*, 236(11):2795–2802, 2012. ISSN 0377-0427. doi: 10.1016/j.cam.2012.01.012. URL http://www.sciencedirect.com/science/article/pii/S0377042712000131.

[107] T.J. Bridges and P.J. Morris. Differential eigenvalue problems in which the parameter appears nonlinearly. *Journal of Computational Physics*, 55:437, Sep 1984. doi: 10.1016/0021-9991(84)90032-9.

[108] G. Danabasoglu and S. Biringen. A chebyshev matrix method for the spatial modes of the orr–sommerfeld equation. *International Journal for Numerical Methods in Fluids*, 11(7):1033–1037, 1990. ISSN 1097-0363. doi: 10.1002/fld.1650110709. URL http://dx.doi.org/10.1002/fld.1650110709.

[109] Lloyd N. Trefethen, Anne E. Trefethen, Satish C. Reddy, and Tobin A. Driscoll. Hydrodynamic stability without eigenvalues. *Science*, 261(5121):578–584, 1993. doi: 10.1126/science.261.5121.578. URL http://www.sciencemag.org/content/261/5121/578.abstract.

[110] T. Ellingsen and E. Palm. Stability of linear flow. *Physics of Fluids*, 18(4):487–488, 1975. doi: 10.1063/1.861156. URL http://link.aip.org/link/?PFL/18/487/1.

[111] K.M. Butler and B.F. Farrell. Three-dimensional optimal perturbations in viscous shear flow. *Physics of Fluids*, 4(8):1637–1650, Aug 1992. doi: 10.1063/1.858386.

[112] L.N. Trefethen and M. Embree. *Spectra and pseudospectra: the behavior of nonnormal matrices and operators*. Princeton University Press, 2005. ISBN 9780691119465. URL http://books.google.co.uk/books?id=7gIbT-Y7-AIC.

[113] Dan S. Henningson and Satish C. Reddy. On the role of linear mechanisms in transition to turbulence. *Physics of Fluids*, 6(3):1396–1398, 1994. doi: 10.1063/1.868251. URL http://link.aip.org/link/?PHF/6/1396/1.

[114] W. C. Reynolds and W. G. Tiederman. Stability of turbulent channel flow, with application to malkus's theory. *Journal of Fluid Mechanics*, 27(02):253–272, 1967. doi: 10.1017/S0022112067000308. URL http://dx.doi.org/10.1017/S0022112067000308.

[115] SC Reddy and DS Henningson. Energy growth in viscous channel flows. *Journal of fluid mechanics*, 252:209–238, Jul 1993. ISSN 0022-1120. doi: {10.1017/S0022112093003738}.

[116] L. Haringrkan Gustavsson. Energy growth of three-dimensional disturbances in plane poiseuille flow. *Journal of Fluid Mechanics*, 224:241–260, 1991. doi: 10.1017/S002211209100174X. URL http://dx.doi.org/10.1017/S002211209100174X.

[117] P. J. Schmid. Nonmodal stability theory. *Annual Review of Fluid Mechanics*, 39(1):129–162, 2007. doi: 10.1146/annurev.fluid.38.050304.092139.

[118] Satish C. Reddy, Peter J. Schmid, and Dan S. Henningson. Pseudospectra of the orr–sommerfeld operator. *SIAM Journal on Applied Mathematics*, 53(1):15–47, 1993. doi: 10.1137/0153002. URL http://link.aip.org/link/?SMM/53/15/1.

[119] M. T. Landahl. A note on an algebraic instability of inviscid parallel shear flows. *Journal of Fluid Mechanics Digital Archive*, 98(-1):243–251, 1980.

[120] L. S. Hultgren and L. H. Gustavsson. Algebraic growth of disturbances in a laminar boundary layer. *Phys. of Fluids*, 1981.

[121] Mohamed Gad el Hak and A. K. M. Fazle Hussain. Coherent structures in a turbulent boundary layer. part 1: Generation of "artificial" bursts. *Physics of Fluids*, 29(7):2124–2139, 1986. doi: 10.1063/1.865600. URL http://link.aip.org/link/?PFL/29/2124/1.

[122] Carlo Cossu, Gregory Pujals, and SebastieN Depardon. Optimal transient growth and very large–scale structures in turbulent boundary layers. *Journal of Fluid Mechanics*, 619:79–94, 2009. doi: 10.1017/S0022112008004370. URL http://dx.doi.org/10.1017/S0022112008004370.

[123] CD Tomkins and RJ Adrian. Energetic spanwise modes in the logarithmic layer of a turbulent boundary layer. *J. Fluid Mech.*, 545:141–162, DEC 25 2005. ISSN 0022-1120. doi: 10.1017/S0022112005006397.

[124] F. Auteri, A. Baron, M. Belan, G. Campanardi, and M. Quadrio. Experimental assessment of drag reduction by traveling waves in a turbulent pipe flow. *Physics of Fluids*, 22(11):115103, 2010. doi: 10.1063/1.3491203. URL http://link.aip.org/link/?PHF/22/115103/1.

[125] C. Viotti, M. Quadrio, and P. Luchini. Streamwise oscillation of spanwise velocity at the wall of a channel for turbulent drag reduction. *Physics of Fluids*, 21(11), 2009.

[126] M. Quadrio and P. Ricco. The laminar generalized Stokes layer and turbulent drag reduction. *Journal of Fluid Mechanics*, 667:135–157, January 2011. doi: 10.1017/S0022112010004398.

[127] Ahmed M.M. Khodier. A finite difference scheme on nonuniform grids. *International Journal of Computer Mathematics*, 77(1):145–152, 2001. doi: 10.1080/00207160108805057. URL http://www.tandfonline.com/doi/abs/10.1080/00207160108805057.

[128] J.D. Swearingen and R.F. Blackwelder. The growth and breakdown of streamwise vortices in the presence of a wall. *Journal of Fluid Mechanics*, 182:255–290, 1987. doi: 10.1017/S0022112087002337. URL http://dx.doi.org/10.1017/S0022112087002337.

[129] P. Andersson, L. Brandt, A. Bottaro, and D.S. Henningson. On the breakdown of boundary layer streaks. *Journal of Fluid Mechanics*, 428:29–60, feb 2001.

[130] V.G. Chernoray, V.V. Kozlov, L. Löfdahl, and H.H. Chun. Visualization of sinusoidal and varicose instabilities of streaks in a boundary layer. *J. Vis.*, 9(4):437–444, December 2006. ISSN 1343-8875. doi: 10.1007/BF03181783. URL http://dx.doi.org/10.1007/BF03181783.

[131] Nicholas Hutchins and Ivan Marusic. Large-scale influences in near-wall turbulence. *Philosophical Transactions of the Royal Society A: Mathematical, Physical and Engineering Sciences*, 365(1852): 647–664, 2007. doi: 10.1098/rsta.2006.1942. URL http://rsta.royalsocietypublishing.org/content/365/1852/647.abstract.